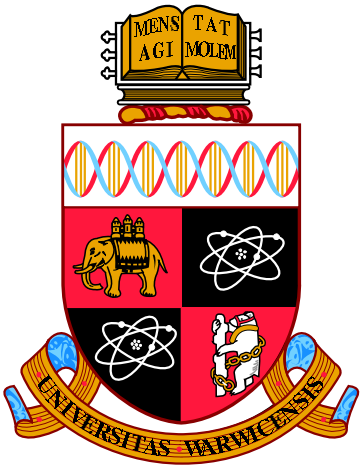

Development of EMAT and piezoelectric transducers for high temperature ultrasonic thickness measurements

by

Natasha Lunn

Thesis

Submitted to The University of Warwick

for the degree of

Doctor of Engineering in Non-Destructive Evaluation

Department of Physics

September 2018

THE UNIVERSITY OF WARWICK

Contents

List of Tables

List of Figures

Acknowledgments

First and foremost, I would like to thank my academic supervisor Professor Steve Dixon for providing me with the opportunity to work on this project, and for his invaluable support and guidance. I would like to thank my industrial supervisor Dr. Mark Potter for his continued support during this project. I wish to acknowledge the funding provided by the Research Centre for Non-Destructive Evaluation (RCNDE) and by my sponsor company, Sonemat Ltd., which have made this work possible.

I would like to extend my thanks to everyone within the Warwick Ultrasound Group, especially those that I have had the pleasure of sharing an office with. Special mentions to: Dr. Charley Fan who provided invaluable help with numerous aspects of this project, Dr. Samuel Hill all his help with PZFlex modelling and Dr. Susan Burrows who assisted in helping me in the laboratory. An honourable mention goes to Jonathan Harrington who provided his support and time in machining many of the critical components in this project, and Jeanette Chattaway who performed delicate brazing for me on numerous occasions.

Lastly, I must thank my family and friends for their love and encouragement over the years, especially my fiancé Daniel Worwood; you are my rock.

Declarations

I declare that the work presented in this thesis is my own, except where stated otherwise, and was carried out entirely at the University of Warwick or in conjunction with the sponsoring company, Sonemat Ltd., during the period between October 2014 and September 2018, under the supervision of Prof. Steve Dixon. The research reported here has not been submitted, either wholly or in part, in this or any other academic institution, for admission to a higher degree. Parts of this work and other work not reported in this thesis have appeared in other forms, listed here.

List of Publications

1. N.Lunn, S.Dixon and M.D.G Potter. "High temperature EMAT design for scanning or fixed point operation on magnetite coated steel". *NDT & E International*. Vol. 89, 74-80. April 2017.

2. N.Lunn, M.D.G Potter and S.Dixon. "Shear wave EMAT thickness measurements of low carbon steel at 450 °C without cooling." AIP Conference Proceedings. Vol. 1806. No. 1. Atlanta (Georgia). 050009.

3. N.Lunn, S.Dixon and M.D.G Potter. "High temperature piezoelectric transducer for continuous online thickness monitoring". 57th Annual British Conference of Non-Destructive Testing (NDT 2018), Nottingham, UK, Sept. 2018.

Abstract

Improving reliability of components operating at high temperature, such as pipelines, boilers and reactors, within a range of industries is of importance in the asset management process. This thesis concerns the development and testing of ultrasound transducers for use at elevated temperatures, up to 500 °C, without the use of active cooling. Ultrasound thickness measurement applications employing these high temperature transducers includes both portable-type non-destructive testing (NDT) inspections and permanent condition monitoring, primarily towards detection of corrosion and erosion.

The development and optimisation of an electromagnetic acoustic transducer (EMAT) design which generates and detects bulk radially polarised shear waves utilising a high temperature permanent magnet and a ceramic encapsulated spiral coil is discussed. This design was optimised for use on magnetite coated mild steel samples; it was shown that the magnetostriction mechanism tends to dominate, depending upon sample properties, producing large signals even at elevated temperatures. High temperature laboratory trials (up to 500 °C) demonstrated the non-linear change in signal amplitude with increasing temperature on magnetite coated mild steel samples, attributed to the complex non-linear relationship between magnetostrictive strains and applied external magnetic field. The EMAT provided good signal amplitude, even at relatively large sample-EMAT lift-off (up to 8.0 mm), demonstrating the applicability of this EMAT for high temperature scanning inspections. A long-term industrial field trial on a high temperature pipeline ($\approx$ 350 °C) in a refinery exhibited the suitability of this design for high temperature continuous monitoring applications.

A piezoelectric transducer with a novel compression-type design was optimised for application at high temperature, with the use of a waveguide, high temperature piezoelectric element and high temperature backing material; the optimisation of these components is discussed. This transducer design incorporates compression applied via a central bolt, to achieve acoustic coupling between the components, avoiding the use of adhesive layers, to generate bulk longitudinal waves. With the application of a bismuth titanate piezoelectric element, the transducer was able to generate signals on stainless steel whilst withstanding high temperatures (up to 500 °C) continuously without cooling.

Abbreviations

AC	Alternating Current
AGC	Automatic Gain Control
AlN	Aluminium Nitride
BVD	Butterworth-Van Dyke
BIT	Bismuth Titanate
BW	Bandwidth
CMUT	Capacitive Micromachined Ultrasonic Transducer
CVD	Chemical Vapour Deposition
DC	Direct Current
EMAT	ElectroMagnetic Acoustic Transducer
ECT	Eddy Current Testing
FEA	Finite Element Analysis
LGS	Langasite Crystal
LN	Lithium Niobate
MPT	Magnetostrictive Patch Transducer
NDE	Non-Destructive Evaluation
NDT	Non-Destructive Testing
Pk-Pk	Peak-to-Peak Voltage
PN	Lead Metaniobate

PPM Periodic Permanent Magnets

PR Pulser-Receiver

PZT Lead Zirconate Titanate

ReCOB Rare-Earth Element Calcium Oxyborate

SNR Signal-to-Noise Ratio

UT Ultrasound Testing

Nomenclature

Latin:

A_0	Initial ultrasound wave amplitude
A_x	Ultrasound wave amplitude at distance x
$\mathbf{B}$	Magnetic flux density
$\mathbf{B_S}$	Static magnetic flux density
$\mathbf{B_D}$	Dynamic magnetic flux density
c^E	Mechanical compliance at constant electric field
c_{ijkl}	Elastic stiffness tensor
c	Anisotropy parameter for cubic crystallographic materials
d	Piezoelectric charge constant
$\mathbf{D}$	Electric displacement
$\mathrm{D_{ih}}$	Average diameter of an inhomogeneity
$\mathrm{D_p}$	Diameter of piezoelectric disc
$\mathrm{D_W}$	Diameter of transducer waveguide
e	Piezoelectric constant
$\mathbf{E}$	Electric field

f	Frequency
f_{C}	Centre frequency
f_{L}	-3dB bandwidth lower frequency
f_{p}	Piezoelectric parallel resonance frequency
f_{s}	Piezoelectric series resonance frequency
f_{U}	-3dB bandwidth upper frequency
$\mathbf{F}$	Lorentz force
$\mathbf{F}_{\mathrm{M}}$	Magnetisation force
g	Piezoelectric constant
h	Piezoelectric constant
$\mathbf{H}$	Magnetic field strength
$\mathbf{J}_{\mathrm{f}}$	Free current density
$\mathbf{J}_{\mathrm{e}}$	Image current density
k	Wavenumber
k_p	Piezoelectric electromechanical coupling coefficient
k_t	Piezoelectric electromechanical coupling factor
K	Stiffness per unit area
L_T	Bolt thread length
m	Mass of an electron
$\mathbf{M}$	Magnetisation
n_e	Electron density

$\hat{\mathrm{n}}$	Unit vector normal to sample surface
P	Electric polarisation
P_n	Electric polarisation
q	Particle electrical charge
Q_m	Piezoelectric mechanical quality factor
R_{12}	Ultrasound reflection coefficient - material 1 to 2
s_H	Elastic compliance at constant magnetic field
$\mathbf{S}$	Elastic strain
t	Time
t_p	Thickness of piezoelectric disc
T_{12}	Ultrasound transmission coefficient - material 1 to 2
T	Temperature
$\mathrm{T_C}$	Curie temperature
$\mathrm{T_{max}}$	Maximum operating temperature
$\mathbf{U}$	Surface displacement of ultrasound wave
v	Particle velocity
v_L	Longitudinal ultrasound velocity
v_S	Shear ultrasound velocity
$\mathbf{v_e}$	Mean electron velocity
V	Voltage
z	Out of plane surface displacement
Z	Electrical impedance
Z_a	Acoustic impedance

Greek:

α	Material ultrasonic attenuation coefficient
α_{T}	Linear coefficient of thermal expansion
ϵ	Strain
ϵ_0	Permittivity of free space
ϵ_{m}	Material permittivity
ϵ_{r}	Relative permittivity
γ	Electrical conductivity
δ	Electromagnetic skin depth
κ	Thermal conductivity
λ	Wavelength
λ_L	Lamé constant 1
λ_m	Magnetostrictive constant
μ_0	Magnetic permeability of free space
μ_{i}	Particle displacement (i^{th} component)
μ_{m}	Material permeability
μ_{L}	Lamé constant 2
μ_{r}	Relative permeability
μ^{σ}	Magnetic permeability at constant stress
$\boldsymbol{\xi}$	Displacement vector
ρ	Material density

σ	Stress
τ	Mean time between electron-ion collisions
υ	Phase velocity
ϕ	Scalar potential
ψ	Vector potential
ω	Angular frequency
$\mathbf{\Gamma}_{\mathrm{ij}}$	Christoffel matrix

Chapter 1

Introduction

1.1 Industrial Motivation

A variety of components operate continuously at elevated temperatures (e.g. pipelines, boilers, reactors, pressure vessels and heat exchangers) over a range of industries, most notably power generation, petrochemical and metal processing. Defects (e.g. cracks, wall thinning, media corrosion, and cavitation erosion [1]) may result in compromised integrity, and the risk of in-service catastrophic failure poses not only a severe hazard for human life, but potentially extensive economic losses due to plant shut-down and repair costs. Therefore, performing regular service maintenance inspections is a vital aspect of the asset management process for many industries operating high temperature components; ideally, this would be achieved at elevated temperatures as in-service inspections or via permanently installed structural health monitoring techniques. In addition, on-line monitoring permits plants to remain in operation for longer periods, thereby reducing the number of periodic shutdowns and the associated risk of damage from thermal cycling, whilst also enabling shutdowns to be completed in a shorter time frame.

Despite the clear advantages and industrial demand for on-line inspection at elevated temperatures, the vast majority continue to be performed at lower or ambient temperatures [2, 3]. The lack of widespread application of high temperature inspections is due to a number of factors, such as: poor performance of high temperature commercial sensors, time consuming sample preparation (e.g. grinding or sandblasting oxidised surface layers), difficulty in scanning large areas and reliability issues with respect to lifetime of a sensor. Although progress is being made in the field, detailed extensively in the sections below, there is no generally applicable solution to high temperature inspection that is widely commercially available [2, 4].

This body of work centres on two types of high temperature ultrasound transducer, specifically the design, fabrication and testing of an electromagnetic acoustic transducer (EMAT) and a piezoelectric ultrasound transducer, for continuous operation at temperature up to 500 °C. The aim of this EngD project is to address some issues with current high temperature EMAT and piezoelectric transducer solutions, towards presenting improved sensor designs suitable in many typical applications at elevated temperature, such as thickness measurements of high temperature pipelines. It is anticipated that the research presented here will result in novel high temperature transducer products, which can be commercialised by the sponsor company of this EngD project, Sonemat Ltd [5].

1.2 Contribution to Knowledge

The work achieved in this EngD and presented here contributes further knowledge to the field of ultrasonics within the non-destructive testing and evaluation (NDT&E) community, specifically with regard to the performance of novel high temperature ultrasonic transducers. Innovations in transducer design for both EMATs and piezoelectric transducers are demonstrated, and these enhance the current state-of-the-art high temperature capabilities of ultrasonic transducers with respect to their long-term high temperature performance and ability to offer significant advantages for both transducer manufacturers and end-users. These transducers can be directly employed by industry to advance high temperature thickness measurement condition monitoring applications, particularly relevant for corrosion and erosion of pipelines. The list of publications arising from this research is given below:

List of Publications

1. N.Lunn, S.Dixon and M.D.G Potter. "High temperature EMAT design for scanning or fixed point operation on magnetite coated steel". *NDT & E International*. Vol. 89, 74-80. April 2017.

2. N.Lunn, M.D.G Potter and S.Dixon. "Shear wave EMAT thickness measurements of low carbon steel at 450 °C without cooling." AIP Conference Proceedings. Vol. 1806. No. 1. Atlanta (Georgia). 050009.

3. N.Lunn, S.Dixon and M.D.G Potter. "High temperature piezoelectric transducer for continuous online thickness monitoring". 57th Annual British Conference of Non-Destructive Testing (NDT 2018), Nottingham, UK, Sept. 2018.

1.3 Non-Destructive Testing and Evaluation

Within an industrial engineering context, NDT&E describes a range of approaches to investigate the structural integrity of a component without causing permanent damage, as is often the case with other characterisation methods (e.g. creep tests, fatigue, point bending tests, hardness testing); this type of assessment proves beneficial in both manufacturing quality assurance and in-service maintenance environments. Generally, in manufacturing industries, NDT techniques are used to ensure parts are manufactured to the appropriate quality assurance standards, such as with regards to material composition, and size and location of defects present in the as-manufactured state (e.g. cracks, voids, inclusions, porosity). In brief, the objective of in-service NDT is to assist a structural assessment of a component to ensure reliability for its planned lifetime.

A range of NDT&E techniques are employed within industry, including: visual methods [6–8], dye penetrant testing [9, 10], eddy current testing [11–13], magnetic flux leakage [14, 15], ultrasonic testing [16–18], thermography [19, 20] and radiography [21–23]. A review of these techniques is not given here, but further details on these techniques can be found within the references provided. The benefits and limitations of the different techniques must be taken into consideration when deciding upon a technique for a particular application, and often these methods are considered complimentary to meet the requirements and limitations of an inspection; within the field of NDT&E there is not a technique that accommodates the demands of every inspection. The following sections provide a detailed review of different NDT techniques for application in industries with components operating at elevated temperatures.

1.4 Ultrasound Testing

Ultrasound testing (UT) encompasses a wide range of techniques which are able to propagate ultrasound waves both in the bulk and on the surface of a variety of materials, towards investigating certain properties of that material [16]; ultrasound describes sound waves which have a frequency above 20 kHz. Ultrasonic inspection is the NDT technique employed within this work, as such a detailed discussion of ultrasound wave propagation theory and ultrasound inspection method relevant to this thesis are presented in chapter 2. This section aims to provide the reader with a concise overview of ultrasound testing with respect to the high temperature NDT literature review provided in the following sections.

In brief, ultrasound transducers are used to convert electrical energy to acoustic energy and vice versa, and pulser-receivers (PR) are used typically to drive the transducer with the required electrical signal and provide the necessary amplification of received signals. Different methods exist for generating and detecting ultrasound in materials, including: piezoelectric transducers [24], electromagnetic acoustic transducers (EMATs) [25] and laser ultrasound methods [26]. Each method has benefits and limitations, which should be taken into account in relation to the requirements of a particular application.

The analysis of the interaction between ultrasound propagating through a material can be used to infer information about that material; for example, by measuring the attenuation of signals, amplitude of reflected waves and time of flight of signals, material properties can be determined, in addition to information on the presence, size, location, orientation and depth of defects [16]. The size of detectable material features is limited by the wavelength of the ultrasound, such that reducing the wavelength (i.e. increasing the frequency) enables detection of smaller features; however, there is a compromise as higher frequency ultrasound waves tend to be more attenuated by the material [27], which can cause a large reduction in detectable signals.

Simple schematic diagrams of two typical inspection formats, through transmission and pulse-echo, are presented in Figure 1.1 on a bulk sample with and without a defect present; here basic representation of the received ultrasound signals in the form of A-scans (signal voltage, V, vs. time, t) are given to illustrate how signals are interpreted to detect defects within a sample. Through-transmission describes the method of transmitting and receiving ultrasound from two separate transducers at different sides of a component, whilst pulse-echo describes the use of a single transducer which transmits and receives the ultrasound on one side. The time of arrival of the transmitted or reflected ultrasound waves provides information on sample thickness and presence and size of defects, if the speed of ultrasound in the material is known.

Ultrasound testing methods have been successfully employed in a wide range of NDT applications, including: thickness measurements [28, 29], stress measurements [30, 31], corrosion and erosion detection [32, 33], surface and near-surface defect detection [34, 35], weld inspection [36, 37], composite inspection [38, 39] and adhesive joint inspection [40, 41]. Such inspections are performed using different types of ultrasound waves, such as: bulk waves (longitudinal and shear), surface waves (Rayleigh) and a variety of different guided waves. Bulk waves are ultrasound wave modes which propagate throughout the bulk of a material, and are

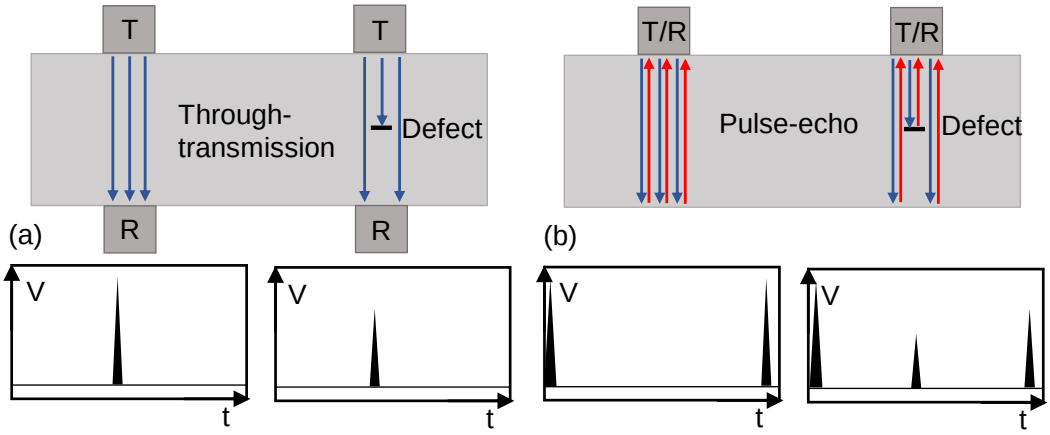

Figure 1.1: Schematic diagrams of typical ultrasound inspections on a bulk sample with and without a defect present and their corresponding rectified A-scan (signal voltage, V, vs. time, t): (a) through transmission, (b) pulse-echo. T = transmitting transducer, R = receiving transducer.

detailed further in section 2.1.3. Rayleigh waves propagate along the surface of a relatively thick material, penetrating to a depth of one wavelength, exhibiting an elliptic orbit motion [42]. Guided waves are ultrasound waves whose propagation is geometrically constrained by the materials in which they are propagating which are typically thin structures (e.g. plates and pipes).

1.5 Piezoelectric Transducers

Piezoelectric transducers are arguably the most commonly used type of ultrasound transducer in the fields of NDT&E, medicine and fluid flow measurements. They provide a number of benefits for conversion of electrical energy into ultrasound energy, including: high conversion efficiency, rugged construction and ability to manufacture the active piezoelectric element into variety of shapes and sizes. This section provides an overview of the basic operating principles of piezoelectric transducers, along with a detailed review of their application at elevated temperatures.

1.5.1 Piezoelectric Materials

Piezoelectric transducers are able to convert electrical energy into mechanical energy, and vice versa, via the direct and inverse piezoelectric effects; the theory of piezoelectricity is discussed in greater detail in section 2.3. In brief, piezoelectricity refers to the ability of piezoelectric crystals to generate an electric field on external application of stress (direct effect), and to exhibit a mechanical deformation when

they experience an electric field (inverse effect). The application of piezoelectricity provides a method for generation and detection of ultrasound waves, as illustrated in the schematic diagram in Figure 1.2.

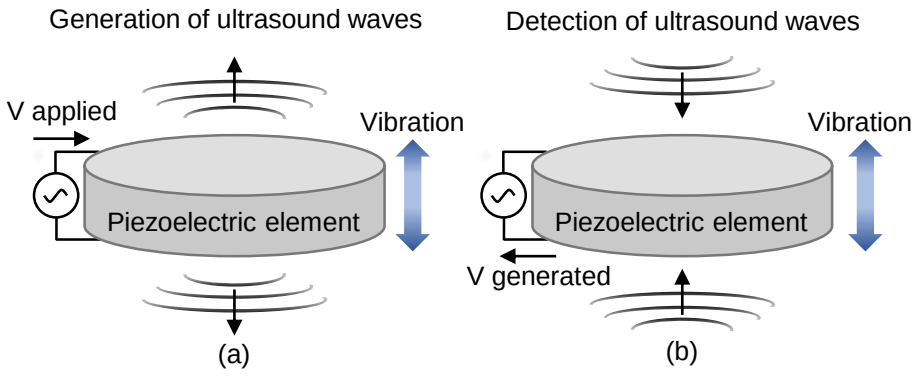

Figure 1.2: Schematic diagram of the basic operation of piezoelectric transducers: (a) generation of ultrasound via the direct piezoelectric effect, (b) detection of ultrasound via the indirect piezoelectric effect.

Piezoelectricity is dependent on crystallographic structure and asymmetry, such that phase transformations can result in complete loss of piezoelectric properties. One such phase transformation exhibited by many commonly used piezoelectric materials occurs at the Curie temperature (T_C), unique for each piezoelectric material, resulting in loss of crystallographic asymmetry and, therefore, piezoelectricity; for example, the widely used piezoelectric material lead zirconate titanate ($Pb[Zr_xTi_{1-x}]O_3$ ($0 \leq x \leq 1$), PZT) has a T_C of $\approx 360\,^{\circ}C$.

PZT exhibits a perovskite unit cell crystal structure, as illustrated in Figure 1.3, which features a titanium (Ti^{4+}) or zirconium (Zr^{4+}) ion inside an octahedron of oxygen (O^{2-}) ions, with a cube of lead (Pb^{2+}) ions surrounding it. The left diagram illustrates the symmetric crystal structure of PZT above the T_C, where no net polarisation exists and piezoelectricity is not exhibited. The right diagram shows the crystal structure below the T_C, where the central ion is shifted from the geometric centre of the unit cell; the shifting of the central ion generates a net polarisation (P) within the unit cell, such that piezoelectricity is exhibited.

Neighbouring unit cells will tend to have aligned polarisations, which creates a domain structure within a piezoelectric material; however, the polarisation direction of individual domains is random relative to surrounding domains, such that net polarisation over the bulk of the material is not observed. Therefore, to make a functioning transducer from a piezoelectric material, these domains must be

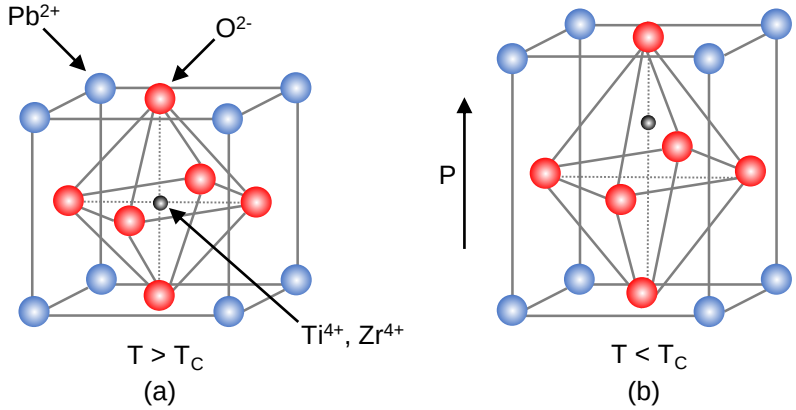

Figure 1.3: The perovskite crystal structure of PZT: (a) symmetric crystal structure above T_C, (b) polarised crystal structure exhibited below T_C where the central ion is shifted from the geometric centre of the unit cell generating a net polarisation (P)

aligned. Domain alignment is achieved via application of a large DC voltage across the element in the required polarisation direction, commonly carried out at elevated temperatures to facilitate domain movement. The temperature is decreased whilst the voltage is retained, and this forms a polarised piezoelectric ceramic element.

A criterion for long term operation of a piezoelectric material at elevated temperatures is that the maximum operating temperature should not exceed $\approx$ 75 % of the T_C [2]. An approach to allow long term operation of piezoelectric transducers at elevated temperatures is the selection of an appropriately high T_C piezoelectric material for a specific application. A wealth of literature exists on high T_C piezoelectric materials and it remains a topical research area; a number of detailed review papers have been published [43–47].

Table 1.1 displays the T_C of high temperature piezoelectric materials often referenced in the literature. Although discussed in greater detail in section 2.3, in brief the piezoelectric coefficient d, also referred to as the piezoelectric charge constant, quantifies the mechanical strain experienced by a piezoelectric material per unit of electric field applied. For d_{33}, the first subscript indicates the direction of the applied electric field, whilst the second subscript indicates the direction of the induced strain; hence, d_{33} is the piezoelectric coefficient when the electric field and induced strain are parallel, which typically denotes the case for through-thickness resonance of a piezoelectric element. The coefficient d_{33} is a key figure of merit used to compare different piezoelectric transducers, where a higher value is generally preferred.

Table 1.1: Piezoelectric properties of some piezoelectric materials of interest for application at elevated temperatures, where T_C denotes the Curie temperature T_C and d_{33} denotes the piezoelectric coefficient.

Material	T_C (°C)	d_{33} (pC/N)	Refs.
PZT-5A	365	370	[48]
$PbNb_2O_6$	570	81	[49]
$Bi_4Ti_3O_{12}$	675	20	[50]
$LiNbO_3$	1150	6	[51]
AlN	None known	5	[52]
$La_3Ga_5SiO_{14}$	None known	-	
$YCa_4O(BO_3)_3$	None known	-	

Lead metaniobate ($PbNb_2O_6$, PN) exhibits excellent piezoelectric properties for broadband transducer applications owing to its large anisotropy and very low mechanical quality factor (Q_m), in addition to a high T_C of 570 °C it is has been researched and utilised for high temperature applications [49, 53, 54]. Unfortunately, conventional ceramic processing methods yield low density polycrystalline PN, due to rapid grain growth, and while doping achieves a higher density and an increase in the piezoelectric constant (d_{33}) it results in a decrease of the T_C [54]. A common composition of PN is a 10% doping with Ba, resulting in a T_C of $\approx$ 400 °C [43]. Another limiting factor of PN at elevated temperatures is its high electrical conductivity above 300 °C.

Bismuth titanate ($Bi_4Ti_3O_{12}$, BIT) is a well studied piezoelectric material exhibiting piezoelectric properties similar to that of quartz, namely low d_{33} and high conductivity, although it exhibits a high T_C of $\approx$ 675 °C [47] allowing application at high temperature [55–57]. Doping can provide improvement to piezoelectric properties, such as an increase in d_{33}. Sodium modified bismuth titanate (NBIT) is well commercialized and has a high T_C of $\approx$ 600 °C.

Single crystal lithium niobate ($LiNbO_3$, LN) has been extensively studied as a replacement for PZT for high temperature applications [55, 58–61] due to its high electromechanical coupling factor which is similar to that of PZT, high mechanical quality factor and extremely high T_C of $\approx$ 1150 °C. However, LN exhibits pyroelectricity, a phenomenon describing the ability of piezoelectric materials to generate a voltage on heating or cooling, along with high conductivity and, most notably, LN undergoes chemical decomposition via oxygen loss to the environment at temperatures above $\approx$ 300 °C [62, 63].

Aluminium nitride (AlN) has received attention in recent decades due to piezoelectric properties demonstrated in thin film form at temperatures up to 1150 °C [55, 64–67]; AlN has no known T_C. A benefit of AlN over other piezoelectric materials is its ability to operate continuously in a neutral atmosphere at high temperatures, where many other piezoelectric materials will be reduced and exhibit high conductivity [44].

Langasite crystal ($La_3Ga_5SiO_{14}$, LGS) is a relatively new type of piezoelectric material first discovered in 1980 which has an electromechanical coupling factor roughly three times greater than quartz [62]. Langasite has received attention for application at high temperature as no phase transformation is observed up to its melting point at ≈ 1470 °C [68–70]. Yet, langasite exhibits low resistivity and high dielectric loss at elevated temperatures which restricts application to below 800 °C [71].

Oxyborate crystals ($ReCa_4O(BO_3)_3$, where Re = rare-earth element, ReCOB) are a relatively new type of piezoelectric material first reported in the early 1990s. Similarly to langasite crystals, no phase transition is observed before their melting point at ≈ 1500 °C. Oxyborate crystals have similar piezoelectric properties to those of langasite, whilst exhibiting high resistivity at elevated temperatures [72]. Oxyborate crystals investigated for application at high temperature include yttrium calcium oxyborate (YCOB) [73, 74] and gadolinium calcium oxyborate (GdCOB) [72, 75].

Piezoelectric composites consisting of an active piezoelectric material and a non-piezoelectric passive material, such as a polymer or ceramic, have been researched for use in high temperature applications in attempts to improve piezoelectric properties; Lee et. al. [76] published an extensive review paper on the topic of high temperature piezoelectric composites. For example, LN-cement composites have been researched for use up to 400 °C [77], BT-PZT sol-gel sprayed film composites have been tested up to 440 °C [78] and PZT-epoxy (glass sphere modified epoxy) [79] composites have been found to operate at up to with 250 °C improved thermal stability.

1.5.2 Transducer Design

Piezoelectric transducers are constructed to allow maximum transmission and reception of ultrasound waves via the application of a piezoelectric effect from a piezoelectric element, this involves the use of a number of important components, as shown in Figure 1.4. As mentioned above, the piezoelectric element is a critical component for operation of piezoelectric transducers as it provides the conversion of

electrical energy into mechanical energy. A disc shaped piezoelectric ceramic is often used, with thin electrodes deposited on either side to which a live and ground wire are connected by various methods, such as: soldering, conductive epoxy and wire bonding. The piezoelectric element is physically coupled, often by a thin adhesive layer, to a highly attenuative backing material, which acts to damp the oscillating piezoelectric disc towards increasing the bandwidth of the transducer; the effect of backing material on transducer performance is discussed in detail in section 6.5. Commonly for NDT applications, a wear plate is adhered to the front face of the piezoelectric element to provide protection.

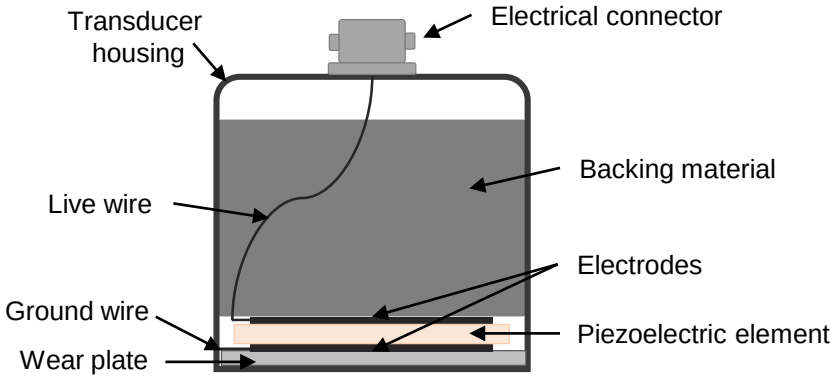

Figure 1.4: Schematic diagram of a conventional single element piezoelectric transducer.

The piezoelectric element employed in high temperature transducers is not the only component to account for as other polymer-based components, which generally cannot withstand temperatures much above 100 - 300 °C for long periods [80, 81], form a complete piezoelectric transducer including, backing materials and adhesive layers. If the transducer is expected to survive high temperatures continuously, high temperature materials can be employed to replace polymer-based components. The backing material provides control over the transducer bandwidth, resolution and sensitivity, and commonly a tungsten-epoxy composite material is used as this provides a relatively close acoustic impedance match with piezoelectric materials and high acoustic attenuation. Reports of high temperature backing materials include tin-tungsten composites [82], porous carbon-carbon composites [60], compressed aluminium foil [60] and porous zirconia ceramic [83]. Solder glasses which have a low glass transition temperature (T_g) have been used to replace polymer-based adhesive joints between the piezoelectric element and backing material [84].

1.5.3 Physical Coupling

Piezoelectric transducers require mechanical coupling of the transducer to the test specimen to permit transmission of ultrasound. Mechanical coupling remains a major drawback at high temperatures, due to the difficulties in acquiring and maintaining mechanical coupling with the complexities present in high temperature environments. Generally, NDT applications require either short term contact of the transducer with a specimen, such as spot-check thickness measurements, or long term permanent installation of the transducer to the specimen, such as on-line monitoring of a known defect. For industrial applications ultrasound couplants should ideally be low hazard and inexpensive, such that most room temperature couplants are based on water or water-based gels and pastes, although these are not suitable for use at elevated temperatures. For short term applications high temperature couplants can be used, such as proprietary pastes and fluids produced by Olympus (e.g. H-2 $T_{max} \approx 400\,^{\circ}C$), Sonotech (Pyrogel® 100 $T_{max} \approx 430\,^{\circ}C$), Echo Ultrasonics (EchoTherm Extreme™ $T_{max} \approx 675\,^{\circ}C$). Although these high temperature couplants can operate at their stated temperatures, they often evaporate or dry out rapidly above $300\,^{\circ}C$ and are thus suitable only for instantaneous measurements [85]. Care must also be taken to ensure an undesired chemical reactions does not occur between the couplant and sample at high temperature.

Published literature exists on a variety of different techniques for long term permanent installation of a transducer to a hot specimen, including: brazing, welding, solder, dry coupling, ceramic adhesives, or direct deposition of the piezoelectric material via sol-gel methods or other chemical deposition techniques. Critical factors to consider with respect to adopting a long term coupling method are achieving good ultrasound transmission at the transducer-specimen interface, safety and material compatibility, long term thermal stability and ability of the interface to withstand thermal cycling [2, 86].

Research into the use of brazes, welds and solders to form a permanent joint at the specimen-transducer interface was driven by the ability to achieve efficient ultrasound transmission, as in some cases the bond-line can be considered virtually indistinguishable from the parent metal [2], in addition to reducing the number of interfaces the ultrasound passes through. Moreover, selection of the brazing alloy will allow the joint to be soft enough at the operating temperature to provide a degree of strain relief against differential thermal expansion. Muto *et al.* [87] have successfully employed brazing for continuous monitoring of plate thickness at up to $550\,^{\circ}C$ and investigating $475\,^{\circ}C$ embrittlement of two phase stainless steel. Arakawa *et al.* [88] have used a brazing coupling method to monitor growth of a known fatigue

crack at 300 °C. The main concern with brazing techniques is avoiding heating the piezoelectric element beyond its maximum operating temperature during deposition of the brazing material.

Dry coupling creates an interface between the transducer and specimen by joining them under high pressure, commonly referred to as clamping. It must be noted that very high pressures ($\approx$ 300 MPa [89]) are required to remove air at the interface, even between highly polished surfaces, where even very small air pockets (> 0.01 pm) considerably reduce the ultrasound energy entering the specimen [85]. Soft metallic foil, such as gold, can be used to improve ultrasound transmission. Long term success (> 5 years) has been observed with gold foil clamping in ultrasonic flowmeters up to 600 °C on liquid sodium [3]. Maintaining a constant coupling pressure long term at high temperature could prove problematic in some applications due to thermal expansion effects.

Ceramic adhesives have the ability to withstand exceedingly high temperatures (> 1000 °C) whilst providing the ease of application of a liquid couplant together with the permanence and high quality coupling of brazing and welding [85]. Ceramic adhesives have been shown to operate long term (500 days) at 400 °C bonded directly to a LN single crystal [90], in addition to operating at up to 1000 °C bonding LN single crystal to stainless steel [59]. Ceramic adhesive bond-line thickness must be taken into consideration to ensure a strong bond to avoid cracking, whilst keeping ultrasound attenuation to a minimum [90].

The use of sol-gels is a novel approach to deposit high temperature ultrasonic transducers directly onto test specimens avoiding some common physical coupling issues. Sol-gel is a chemical preparation technique in which a sol transforms into a gel, via agglomeration of solid nanoparticles dispersed in a liquid to form a continuous three-dimensional network, and this method is used for fabricating ceramic materials [91, 92]. A key benefit of sol-gel and other direct deposition techniques is their ability to coat complex shapes, such as curved surfaces on high temperature pipelines. Burrows *et al.* [57] prepared bismuth titanate via a sol-gel method for direct deposition onto a stainless steel shim and thickness measurements were made on steel samples up to 225 °C, and Kobayashi *et al.* [78] published work on a bismuth titante-PZT composites prepared via sol-gel, which can be sprayed onto complex surfaces, with ultrasonic testing up to 440 °C. A chemical vapour deposition (CVD) technique was used to deposit thick films of AlN, which was able to generate and detect ultrasound up to 900 °C [93]. Despite recent advances in direct piezoelectric deposition techniques, these technologies are relatively new and are yet to provide a complete solution to the complex issues of high temperature inspections [3].

1.5.4 Waveguides

An alternative approach, or one used in conjunction with higher T_C piezoelectric material, is to isolate the piezoelectric element from the heat source via a waveguide. The use of a waveguide allows operation of a piezoelectric element far below its T_C, as the waveguide has a variable temperature profile along its length due to cooling via air or an active cooling material (e.g. water). Although, the size and shape of the waveguide has an effect on the temperature drop which can be sustained across a waveguide. For example, it has been calculated [4] that a thin (0.5 mm radius wire or 1 by 15 mm strip) stainless steel (thermal conductivity, $\kappa = 15\,\mathrm{W/mK}$) waveguide is able to maintain a temperature drop from 600 °C to 50 °C over a distance of 0.2 - 0.3 m under natural convection cooling, yet for a larger radius waveguide (10 mm radius) a much longer (≈ 1 m) waveguide is required to sustain the same temperature drop.

Implementation of a waveguide can allow the use of commercially available standard piezoelectric transducers, reducing the complexity and cost of an inspection. Waveguides are often referred to as delay lines or buffer rods in the literature, and have been employed in a variety of high temperature applications, including thickness measurement of hot plates up to 960 °C [94], ultrasonic imaging of defects up to 340 °C in liquid sodium [95] and sound velocity and attenuation measurements of molten glass at a temperature range of 1000-1200 °C [96]. The schematic diagrams in Figure 1.5 illustrate a number of different waveguide geometries used to isolate piezoelectric transducers from high temperature environments.

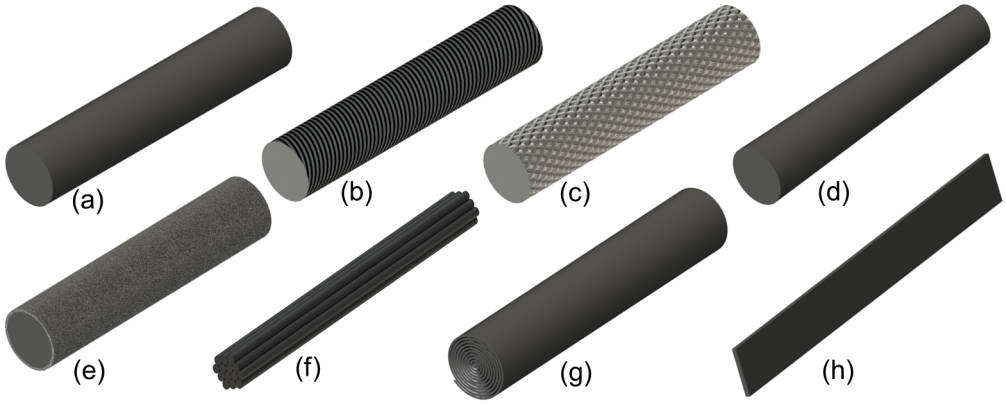

Figure 1.5: Schematic diagrams of different waveguide geometries used to isolate piezoelectric transducers from high temperature environments: (a) simple rod, (b) threaded rod, (c) knurled rod, (d) tapered rod, (e) clad rod, (f) wire bundle, (g) spiralled plate, (h) thin rectangular strip

A complication of buffer rod waveguides is the generation and detection of spurious echoes, often termed trailing echoes, which interfere with desired signals. These trailing echoes are formed in buffer rod waveguides of a finite diameter due to waveguide-air boundary effects, namely mode conversion, reverberation and diffraction [97, 98]. Use of large diameter, short buffer rod waveguides is a simple method to remove trailing echoes, however, this is impractical owing to size and weight limitations in many applications. Other methods to remove trailing echoes involve alterations to the waveguide-air boundary to greatly reduce the amplitude of reflections, these include waveguides whose surface have been modified by a threaded [99, 100] or knurled [101] pattern; although these methods are effective at removing the trailing echoes, they create additional noise into the signal. Alternative methods also include cladding [102, 103] of the waveguide rod with a material of different acoustic properties, and tapering [96, 104] the rod such that the diameter at both ends varies.

Dispersion is a critical issue to overcome with the application of waveguides, and this describes the phenomenon that occurs when the velocity of an ultrasonic wave is dependent on the frequency [42, 97]. This results in a propagating ultrasound wave pulse (containing multiple frequencies) spreading out in space and time, such that the individual frequency components propagate with different velocities. Dispersion is typically observed with guided waves, although not with ultrasound waves in large, bulk samples. Due to the distribution of the ultrasound wave, dispersion is a problem when attempting to collect accurate ultrasound measurements.

As a result of dispersion in waveguides, a variety of studies have been performed to investigate different waveguide geometries towards reducing the effects of dispersion. Lynnworth *et al.* [105, 106] have published details of wire bundle waveguides, which allow propagation of the minimally dispersive fundamental longitudinal wave mode L(0,1); the waveguides were formed as bundles of wires to retain strong ultrasound signals. Heijnsdijk and van Klooster [107] registered a patent for a coiled foil waveguide, where the thickness of the foil is selected to be much less than the smallest wavelength to be propagate though the waveguide; this aims to generate the propagation of essentially non-dispersive compressional ultrasound wave modes, which mimic a plane wave propagating along the foil. Cegla *et al.* [4, 108] have published the use of long, thin, rectangular waveguides to propagate non-dispersive guided shear-horizontal (SH) waves for crack detection up to 500 °C, and the long term performance was evaluated for four weeks at 750 °C without signal degradation. Laws *et al.* [109, 110] reported the use of a steerable waveguide phased array for fluid flow measurement application in hostile environments, which consisted of

five parallel stainless steel rectangular strips of finite width. Deviations from typical Lamb wave dispersion behaviour were observed due to coupling across the finite width of the strips, such that Lamb-like ultrasound guided waves were generated.

Commercial high temperature piezoelectric transducers are available which employ waveguides or delay line. Ionix Advanced Technologies Ltd. [111] have a range of HotSense^{TM} transducers which utilise a proprietary piezoelectric material attached to a delay line, that can be clamped to high temperature components. These can be used at temperatures up to 380 °C for monitoring thickness, cracks, range sensing and level sensing. KANDE international [112, 113] have developed a piezoelectric system also employing a relatively short delay line which can be welded to a high temperature component. These transducers have been used for thickness monitoring and crack detection at temperatures up to 600 °C. Permasense Ltd. [114] have a WT sensor series of high temperature piezoelectric transducers which are able to operate continuously at up to 600 °C via application on a long thin waveguide permanently attached, such that the piezoelectric element and electronics are kept away from the hot component. The transducers are employed for long term condition monitoring, providing information on wall thickness to monitor corrosion or erosion.

1.6 Electromagnetic Acoustic Transducers

EMATs are an attractive solution for high temperature inspection issues, namely due to their non-contact nature, as ultrasound transmission occurs electromagnetically. Application of EMATs at elevated temperatures circumvents many mechanical coupling problems associated with piezoelectric transducers, such as sample preparation, achieving good ultrasound transmission and thermal cycling. EMATs can be operated at high temperature for portable, spot-check type measurements, continuous monitoring via permanent installation or scanning inspections.

EMATs use a combination of static and dynamic magnetic fields to generate and detect ultrasound waves principally through two mechanisms, the Lorentz force and magneto-elastic mechanisms (e.g. magnetostriction) [25]; the mechanism that operates or dominates depends upon the EMAT design, and the electrical and magnetic properties of the sample. The theory of EMAT operating principles are discussed here in brief, greater detail is given in section 2.2.

Lorentz force describes the EMAT generation and detection mechanism which operates on electrically conducting samples, as illustrated in Figure 1.6. When an alternating current pulse is driven through a coil, eddy currents are generated within

the electromagnetic skin depth of the sample; although the skin depth is discussed in more detail in section 2.2.2, it essentially describes the depth of penetration of an electromagnetic field into a sample, and it is inversely proportional to the eddy current frequency [115]. As described in section 2.2.2, the generated eddy currents can be approximated as an image current at the surface of the sample, which effectively mirrors the current through the EMAT coil. The image current interacts with the static magnetic field provided by a magnet, to produce a Lorentz force on the free conducting electrons. Momentum exchange between the electrons and the lattice via collisions generates ultrasound within the sample. EMATs can detect ultrasound through the reciprocal process.

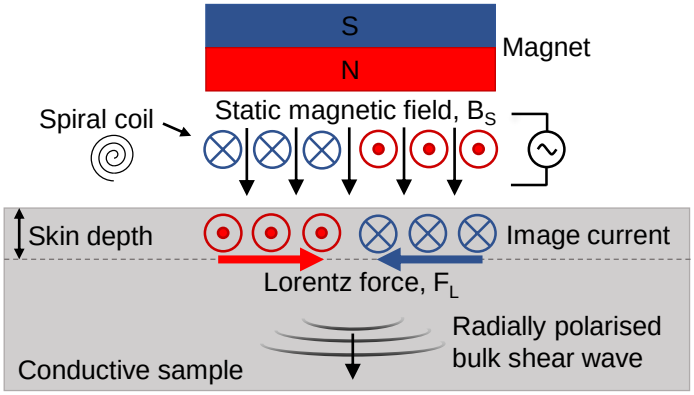

Figure 1.6: Schematic diagram of the Lorentz force mechanism operating on an electrically conductive sample; a spiral coil and magnet with static magnetic field B_S directed into the sample generates and detects radially polarised shear waves. Note: $\odot$ represents current travelling into the page, and $\otimes$ represents current travelling out of the page.

The Lorentz force mechanism diagram in Figure 1.6 depicts the spiral coil EMAT with a single magnet with its static magnetic field directed into the sample and a flat, spiral coil; this spiral coil EMAT design generates and detects radially polarised shear waves, and is the EMAT configuration used within this work. It is important to note that a variety of EMAT coil designs (e.g. spiral, racetrack, meander line) and magnet arrangements can be used to excite and detect different wave modes within a sample using the Lorentz force mechanism [25], including: longitudinal, shear, Rayleigh waves, Lamb waves and guided wave modes.

The magnetostrictive properties of a sample can be used to generate and detect ultrasound waves. This is of particular importance for high temperature applications, as a number of steel grades form a layer of oxide (magnetite) in a high temperature reducing environment. Magnetite exhibits magnetostriction and this

effect can often greatly enhance EMAT sensitivity depending on a number of factors [116, 117], including: strength of the static magnetic field, degree of bonding between the oxide coating and steel substrate, coating thickness and composition. Subject to these factors, the magnetostriction mechanism is able to generate signals in the region of two orders of magnitude greater on magnetite coated steel, when compared to bare steel samples. This variation is attributed to the fundamental difference between the generation and detection of ultrasound via magnetostriction when a highly magnetostrictive oxide coating is present, compared to the contribution from both the Lorentz force and magnetostriction on bare steel. Essentially, the Lorentz force mechanism produces a surface force acting on a conductive sample, whilst the magnetostrictive mechanism produces a shear body force across the entire magnetostrictive coating thickness on magnetite coated samples.

Magnetostriction is a reversible property of materials with magnetocrystalline anisotropy, resulting in a strain on exposure to a magnetic field, termed Joule magnetostriction; the reverse is the Villari effect [118]. The magnetostriction mechanism operating on a material coated with a magnetostrictive layer (e.g. magnetite coated steel) is provided in Figure 1.7 for a spiral coil EMAT. A static magnetic field B_S directed into the sample is provided by a magnet, and it acts to align the magnetic domains within the magnetostrictive material. An alternating current is applied through the coil to generate a dynamic magnetic field (B_D), depending on its frequency and strength relative to (B_S), this acts to rotate the magnetic domains with B_D; this results in oscillating magnetostrictive strains within the coating, which generate ultrasound waves into the bulk of the sample, if there is a good mechanical coupling at the interface. Reception of ultrasound waves occurs via a reciprocal process, whereby the wave causes oscillating strain of magnetic domains within the magnetostrictive coating, which generates a dynamic field detectable by the coil.

1.6.1 Coil Design

Conventional room temperature EMAT coils are often either made from hand wound wire coils or printed circuit board coils, both of which contain polymer-based materials. A key complication of EMAT operation at elevated temperatures is breakdown of the EMAT coil wire insulation or the printed circuit board substrate material, which are usually a polymer-based materials that cannot withstand temperatures above 150 °C [119]. Hand wound wire coils require embedding to retain their shape, and this often involves the use of Kapton® tape, which is a polyimide film developed by DuPont™ [120]. Although some grades of Kapton® tape have a relatively high maximum operating temperature (up to $\approx 300\,^{\circ}C$) compared to most polymer

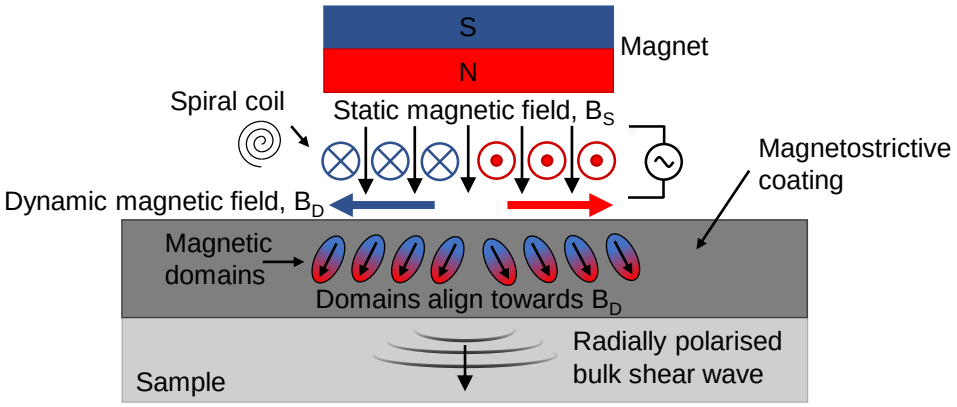

Figure 1.7: Schematic diagram of magnetostriction mechanism on a sample with a magnetostrictive coating, e.g. magnetite coated steel.

materials, it is often too low for many industrial high temperature applications. Approaches to allow EMAT operation at high temperature involves active cooling, selection of high temperature components or a combination of both.

Hernandez-Valle *et al.* [121], when based at the Ultrasonics group at the University of Warwick, published a detailed account of the high temperature spiral coil design used at temperatures up to 600 °C. A hand wound coil was used, where two different sized (0.315 mm and 0.27 mm) bare copper wires were uniformly wound to form two spiral coils with 18 turns next to each other. After winding the 0.27 mm diameter wire was removed, which left a uniform gap between the turns. This gap was filled with a high temperature alumina-based ceramic adhesive (Ceramabond™) to form the coil insulation. This coil winding method is used in this work, and described in more detail in section 3.3.2

1.6.2 Electromagnets

Another key complication of EMAT operation at elevated temperatures is the degradation of magnetic properties of the magnet. To overcome the effects of heat on magnetic properties, researchers have employed the use of both electromagnets, discussed here, and permanent magnets, discussed in section 1.6.3. Early EMAT designs for high temperature applications employed water-cooled DC electromagnets to generate the magnetic field required. Cole [122] investigated the effect of temperature on electromagnetic generation and reception of surface acoustic waves using a water-cooled DC E-core electromagnet on mild steel at temperatures up to 1000 °C. Whittington *et al.* [123] used an oil-cooled DC electromagnet to detect a silicate inclusion in a mild steel bar at 650 °C. Yamahuchi *et al.* [124] carried out on-line

through-transmission thickness measurements of steel tubes and pipes successfully using a tunnel-type electromagnet for temperatures up to 1000 °C. Electromagnets are capable of generating strong magnetic fields which enable EMAT operation at high temperature, however, the main drawback of EMATs constructed with electromagnets is their large size, resulting in bulky transducers.

Limited published literature exists on the use of EMATs without a form of active cooling, primarily due to difficulties in maintaining sufficient magnetic field strengths at elevated temperatures. Hernandez-Valle *et al.* [121, 125] successfully tested a high temperature pulsed electromagnet EMAT capable of thickness and material property measurements up to 600 °C on low-carbon steel without cooling, although the EMAT was in contact with the hot sample for less than two minutes. The EMAT operated in pulse-echo mode via generation and reception of bulk shear waves, employing an alumina ceramic encapsulated spiral copper coil, and a pulsed electromagnet fabricated from an E-shaped iron core with a ceramic encapsulated energising coil. Uchimoto [126] presented at the 2016 Review of Progress in Quantitative Nondestructive Evaluation (QNDE) on the use of an air-core pulsed electromagnet, in order to overcome the Curie temperature limitations of electromagnets with iron cores. A prototype shear wave EMAT was tested and signals were obtained at temperatures up to 700 °C, and the decrease in shear wave velocity with increasing temperature was recorded.

1.6.3 Permanent Magnets

With the development of relatively small rare-earth magnets, capable of generating magnetic field densities similar to those generated by DC electromagnets, compact EMATs constructed with permanent magnets became commonplace [127]. The preferred choice of permanent magnet is usually neodymium-iron-boron (NdFeB) or samarium-cobalt (SmCo: $SmCo_5$ and Sm_2Co_{17}), due to their large magnetic energy product (BH_{max}) values compared to other permanent magnets, such as Alnico (iron alloys with addition of Al, Ni and Co) and ferrite magnets. The high temperature application of a permanent magnet is limited by its T_C, which is ≈ 315 °C for NdFeB, ≈ 730 °C for $SmCo_5$ and ≈ 830 °C for Sm_2Co_{17} [128]; it is important to note that T_C value of a material depends on the alloy grade composition and processing conditions. The Curie temperature is not to be confused with the realistic maximum operating temperature, due to the significant loss of magnetic properties observed when magnets are heated towards their T_C; the Curie temperature is the temperature at which complete loss of magnetic properties is observed, and heating beyond this temperature will result in an irreversible loss of magnetic properties. Generally,

under practical conditions, the maximum operating temperature is considered to be $\approx 80\,^{\circ}\mathrm{C}$ for NdFeB [129], and $\approx 300\,^{\circ}\mathrm{C}$ for SmCo [130].

Subsequently, water-cooled permanent magnet EMATs were employed in high temperature applications [127]. EMATs are more efficient at detection due to inefficient momentum transfer from conduction electrons to the lattice, when considering the significant difference in their mass. Such that water-cooled EMATs have been applied at high temperature as detectors in combination with laser generation of ultrasound, and this is discussed in section 1.7.1. The published work on generation and detection of ultrasound with water-cooled permanent magnets EMATs is presented here.

Boyd *et al.* [131] reported an EMAT pulser and receiver system for on-line time-of-flight measurements on a continuous caster strand of stainless steel using water-cooled permanent magnet EMATs. A signal was detected on steel with a surface temperature of $\approx 1130\,^{\circ}\mathrm{C}$, although the EMAT was in contact with the hot steel for only a few seconds to record the waveform, with a cooling time of two to five minutes between measurements. Lee *et al.* [132] studied the temperature dependence of the ultrasound velocities and attenuation in aluminium, ferromagnetic steel and stainless steel samples at temperatures up to $800\,^{\circ}\mathrm{C}$ using water-cooled permanent magnet shear and longitudinal EMATs. Dixon *et al.* [133] demonstrated a water-cooled permanent magnet EMAT capable of acting as both generator and detector of bulk shear waves using a spiral coil; this EMAT was able to measure wall thickness of a steel galvanising kettle at temperatures in excess of $450\,^{\circ}\mathrm{C}$. Burrows *et al.* [134] published the use of a water-cooled permanent magnet EMAT in pulse-echo mode for thickness measurements on ferromagnetic low carbon steel at temperatures approaching $770\,^{\circ}\mathrm{C}$.

The majority of published literature on high temperature EMATs concerns bulk ultrasound waves for thickness measurements. Guided waves can be employed in inspection or condition monitoring of large structures from a single access point, as they can propagate large distances without significant attenuation, although dispersion complicated signal interpretation [135, 136]. Recently, Kogia *et al.* [137] published details of a water-cooled permanent magnet guided wave EMAT system, generating and detecting non-dispersive shear horizontal (SH_0) waves, which is capable of operating up to $500\,^{\circ}\mathrm{C}$ on ferromagnetic and stainless steel plates. The EMATs were constructed with both NdFeB and SmCo, for comparison, in a periodic permanent magnets (PPM) configuration, with an alumina ceramic encapsulated race-track EMAT coil using constantan (Cu-Ni alloy) wire.

1.7 Laser Ultrasound

The use of lasers to generate and detect ultrasound within materials is well-established and has been utilised in a range of non-destructive evaluation applications, such as thickness measurements, detect flaws and materials characterisation [26]. Advantages of laser ultrasonics include: non-contact nature, in-situ measurements for industrial applications, broadband systems, scanning capability, large ultrasound signals orders of magnitude higher than contact piezoelectric transducers and the tiny footprint allows inspection of curved and complex shapes. The key advantage of laser ultrasonics for applications at elevated temperatures is the capacity of truly remote operation, where optical components can be located well away from a hot specimen, whereas EMAT-sample lift-off must be kept within millimetres in most cases. However, the main barrier for industrial application of laser based ultrasonic systems is their relatively high cost compared to other inspection methods.

1.7.1 Laser Generation of Ultrasound

Pulsed lasers can be used to generate ultrasound in a range of samples; laser generation is described in terms of two extreme regimes, namely the thermoelastic and ablative regimes, the laser energy density determines which regime dominates [138]. Schematic diagrams of the two laser generation regimes are displayed in Figure 1.8. In brief, within the thermoelastic regime, the optical power absorbed by the material is converted to heat, leading to rapid localized temperature increase which results in thermal expansion of a local region, thereby generating ultrasound within the material. In the ablative regime, the laser energy is focused onto the sample surface and at sufficiently high energy densities a plasma will form, which may consist of the vaporised sample and/or air breakdown, depending on the sample and experimental conditions. For both regimes, laser generated ultrasound is not truly non-destructive, but for most industrial applications the damage is on a microscopic scale and is negligible. The ultrasonic waveforms which result from laser generation are relatively complex as all ultrasonic modes are simultaneously generated, such that a waveform will contain longitudinal, shear and surface wave modes.

Many studies have been published on laser-EMAT combinations for operation at elevated temperatures [134, 139–143]. Interest in the laser-EMAT combination for high temperature application arose as lasers are a strong source of ultrasound and EMATs are efficient in reception, thereby providing an inspection technique which is non-contact and relatively insensitive to surface finish. Generally, a Q-switched Nd:YAG laser is used for ultrasound generation, whilst a water-cooled

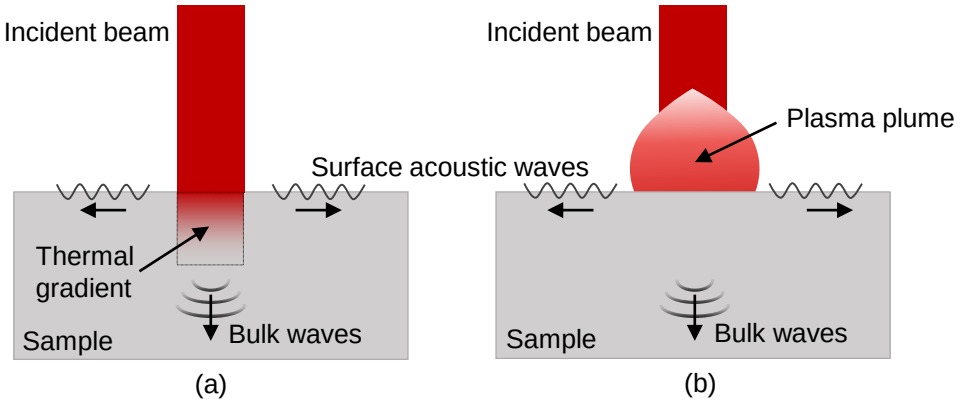

Figure 1.8: Laser ultrasound generation regimes: (a) thermal expansion, (b) ablation.

permanent magnet EMAT provides ultrasound reception. For example, Idris *et al.* [141] designed and tested a laser-EMAT system for measurements of elastic properties on mild steel, a copper alloy and aluminium-silicon alloys up to 1100 °C, where the water-cooled EMAT was exposed to the heat source for the time needed to record a signal. More recently, Baillie *et al.* [142, 143] designed and tested a prototype system to detect defects in steel at temperatures up to 800 °C on pilot scale rolling mill.

1.7.2 Laser Detection of Ultrasound

Laser detection is performed by illuminating a point on the sample with a continuous wave laser, and as ultrasonic waves produce small surface displacements in the order of 10 nm, the displacements lead to a Doppler shift which can be detected. Laser detectors fall into two categories: interferometric detection (e.g. Fabry-Pérot, Michelson and vibrometers) and amplitude variation detection, such as knife-edge detectors. A schematic diagram of a Michelson reference beam interferometer is provided in Figure 1.9. Within a Michelson interferometer, a laser source beam is divided by a beam splitting mirror to form a probe beam and a reference beam, where the beam splitter directs the probe beam towards the sample and the reference beam to a reference mirror where is reflected to a photodetector, where both beams are recombined. Ultrasonic waves can be detected as they cause surface displacements, which introduce small variations in the path length of the probe beam, resulting in a phase difference change between the probe and the reference beams.

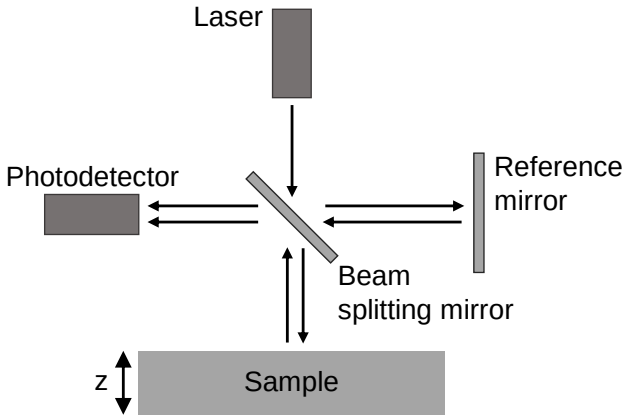

Figure 1.9: Schematic diagram of a Michelson reference beam interferometer used to detect out-of-plane surface displacement, z.

Calder *et al.* [144] determined elastic constants of a stabilised plutonium alloy at temperatures up to 500 °C using a high-energy Nd-glass laser as the ultrasound generator and a continuous wave laser interferometer as detector. Dewhurst *et al.* [145] measured the temperature dependence of the longitudinal ultrasonic velocity in iron and dural (Al-Cu-Mg alloy) at temperatures in excess of 1000 °C, using a Q-switched Nd:YAG laser for generation and a modified Michelson laser interferometer for detection. Scruby and Moss [146] reported an extensive study to determine the temperature dependence of ultrasonic velocity and attenuation, in addition to generation and reception sensitivity of the system, in ferritic and austenitic steel samples at temperatures up to 1000 °C; the system utilised a Q-switched Nd:YAG laser for generation and a Michelson reference beam interferometer for detection.

There are potential disadvantages for some laser reception systems, for instance the Michelson reference beam interferometer used in [144–146], as their sensitivity is greatest when the sample surface is highly polished. Scruby and Moss [146] reported rapid sensitivity loss on rough or dirty surfaces due to increased absorption of the light, and via convection currents that cause speckles to broaden and move across the photo-detector. The authors estimated a loss of sensitivity of 20 dB at 1000 °C, such that an alternative laser detector was proposed, namely the confocal Fabry-Pérot interferometer, which is speckle insensitive [147, 148] thus less sensitive to surface condition, convection and motion.

Nakano and Nagai [149] detected and measured the length of fatigue cracks in stainless steel at temperatures up to 1000 °C using a Q-switched Nd:YAG laser and confocal Fabry-Pérot interferometer system. Demonstration of these laser detection systems has been achieved in industrial environments, for example, Monchalin *et al.*

[150] carried out on-line wall thickness measurement of tubes at 1000 °C travelling at 4 m/s, and Lévesque *et al.* [151] developed an on-line inspection system for the steel tube making process which measured wall thickness and austenite grain size.

More recently, Quintero *et al.* [152] were the first to experimentally determine the feasibility of laser ultrasound inspection of ceramic matrix composites for use in jet engine technology, as the temperatures reached precludes the possibility of using sensors placed in direct contact with the specimen. Flat coupons of silicon-carbide (SiC) fibres in a SiC matrix were scanned with a Nd:YAG laser for generation on one side and a Michelson interferometer for detection on the other. The authors were able to detect interlaminar defects caused by impacts and monitor crack opening under tensile load, whilst achieving good signal stability at temperatures up to 1200 °C. Laser ultrasound has also been proposed for inspection of Zircaloy cladding tubes used in the nuclear sector, which can degrade and threaten fuel integrity while in service at elevated temperatures; Yeh *et al.* [153] presented the use of Nd:YAG laser for generation and a laser Doppler for detection of guided waves within Zircaloy tubes at temperatures up to 300 °C, where the dispersion spectra was used to infer material properties, such as the elastic modulus.

1.8 Electrostatic Transducers

Electrostatic transducers, also referred to as capacitive transducers, including capacitive micromachined ultrasonic transducers (CMUTs), are designed to generate and detect ultrasound waves in low impedance media (e.g. air, water, blood) [154, 155]. Electrostatic transducers operate via application of a large bias DC voltage between a thin membrane and a contoured conductive backing plate, which rigidly stretches the membrane; a schematic diagram of an electrostatic transducer is provided in Figure 1.10. Oscillation of the membrane occurs on application of an alternating current, which in turn generates ultrasound waves within the surrounding medium. The reciprocal process allows detection of ultrasound waves, where an incident wave results in vibration of the membrane to produce an electrical signal.

Electrostatic transducers have been employed in a range of applications, including: air-coupled NDT [156], flow measurement [157] and medical diagnostics and therapy [158]. Capacitance transducers have the advantage of relatively large bandwidths, and are well matched to low impedance media by avoiding losses due to internal reflections, unlike standard piezoelectric ceramic transducers. In particular, CMUTs are made of small unit cells which can be manufactured to produce large arrays, allowing larger amounts of ultrasound energy to be transmitted, and their

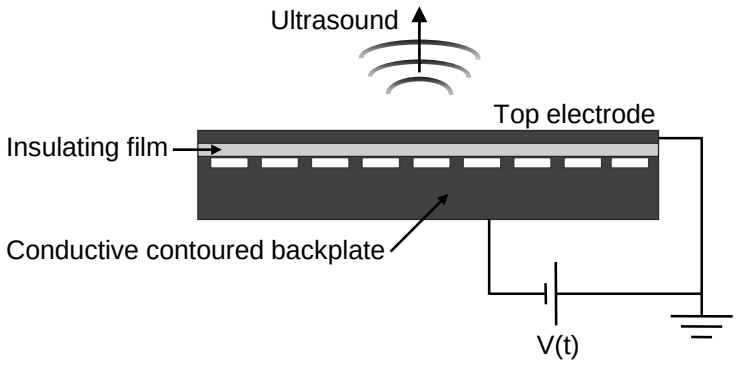

Figure 1.10: Schematic diagram of an electrostatic transducer for generation and detection of ultrasound, with a bias voltage V(t).

fabrication is relatively straightforward as the same techniques are used as those for standard integrated circuit technology based on silicon [159].

The application of electrostatic transducers at elevated temperatures has been reported. Basford and Hutchins [160] investigated the use of an air-coupled capacitance transducer for imaging injection moulded and green-state ceramics in through-transmission mode at temperatures up to 150 °C; a metallised Mylar membrane was used along with high temperature ceramic and Teflon coated wire. Subsequently, Wright and Hutchins [161] published details of an air-coupled capacitance transducer capable of operating at up to 600 °C, which was used to monitor the pyrolytic removal of organic binder from injection moulded silicon nitride ceramics; a high temperature Mico film was used as the membrane. Schröder *et al.* [162] also studied high temperature capacitive transducers, and employed the use of micromachining techniques to investigate the high temperature performance of different materials for the backplate and insulating components. The most successful transducer was constructed from a titanium foil membrane with a silicon backplate with a thermally grown insulating layer of silicon dioxide; this device was able to operate long term at 500 °C.

1.9 Magnetostrictive Patch Transducers

Magnetostrictive patch transducers (MPTs) utilize magnetostriction as a coupling mechanism to generate and detect guided ultrasound waves in plates and pipes [163]. Generally, a MPT is comprised of a magnetostrictive material (patch) bonded to a sample, a coil of wire and a permanent magnet, as illustrated in the basic schematic

diagram in Figure 1.11. Essentially, MPTs can be thought of as EMATs where a magnetostrictive coating is applied to the sample. The same magnetostriction mechanism principles apply for MPTs for EMATs operating on materials coated with a magnetostrictive layer, as described in more detail in section 1.6. There are a variety of different coil and magnet arrangements, which are able to generate different ultrasound wave modes; for example, a permanent magnet arrangement and a meander coil wrapped around a pipe along with a magnetostrictive patch, are able to generate pure torsional guided wave modes [164].

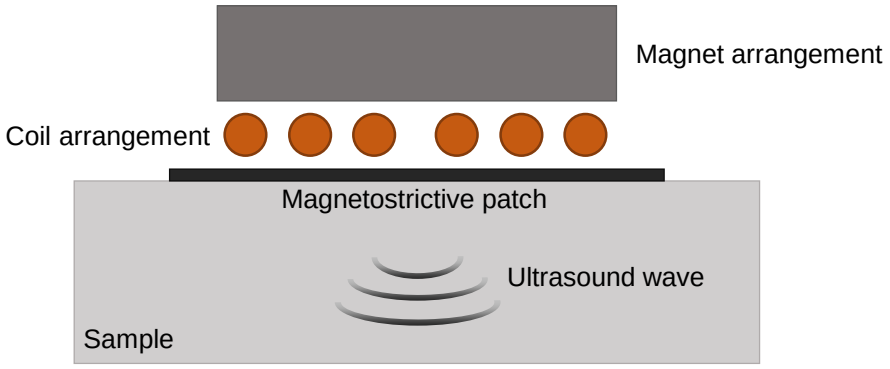

Figure 1.11: Schematic diagram of the main components of a magnetostrictive patch transducer: magnet arrangement, coil arrangement and magnetostrictive patch bonded to a sample.

Recently, MPTs have been of interest for high temperature inspection as all components can be made to withstand elevated temperatures. Ashish *et al.* [165] reported initial trials of MPT capable of generating and receiving axisymmetric longitudinal guided waves at 350 °C continuously for 10 hours; the MPT was fabricated on a waveguide rod welded to the test piece, utilising a Metglas® patch, a transmitting coil and receiving coil wound onto the rod and SmCo magnets. Heo *et al.* [166] developed a 3mm thick MPT that can be embedded for permanent installation between the surface of a pipe and its insulation layer, for monitoring the wall thickness of high temperature pipelines in secondary systems of nuclear power plants using SH bulk waves; the MPT consisted of an iron-cobalt (FeCo) alloy patch, transmitting and receiving meander coils and SmCo permanent magnets and was tested at 300 °C for 24 hours. MPTs appear to be a promising condition monitoring technique for high temperature components, yet, the requirement of physical bonding of the magnetostrictive patch to the sample is their main drawback.

1.10 Eddy Current Testing

Eddy current testing (ECT) is an extensively used non-contact NDT technique [13] for inspection on electrically conducting materials, with applications including: automated inspection systems for production lines (e.g. bar, wire and tubes), detection of defects, coating thickness measurement, material identification and microstructural characterisation. Different types of ECT are used in industry, including: single and dual eddy current probes, pulsed eddy current testing [167] and eddy current arrays [168, 169]. Eddy current testing is a relatively inexpensive, repeatable, non-contact inspection method, which is notably sensitive to small surface and near surface discontinuities. The main drawbacks of eddy current testing are that inspection is limited to electrically conductive materials and high sensitivity to variations in probe-sample lift-off and probe tilt angle [12].

A basic schematic diagram of conventional eddy current testing, in which a single eddy current probe is placed in contact with an electrically conducting sample, is provided in Figure 1.12. The excitation coil within an eddy current probe is subject to an alternating electric current which generates a primary alternating magnetic field, and when this is positioned near to a conductive sample, eddy currents are induced within the electromagnetic skin depth of the sample [12]. The eddy currents generate a secondary alternating magnetic field to counteract the primary alternating magnetic field; the secondary magnetic field is measurable due to electrical impedance changes observed in the excitation coil [13]. The phase and amplitude changes in the measured impedance when an eddy current probe is scanned over a sample can provide useful information, such as change in thickness and size and position of discontinuities. It is crucial to note that eddy current testing is predominantly a surface and near-surface inspection technique due to the skin depth effect, with typical skin depths on the order of a few hundred microns for metallic samples at typical industrial inspection frequencies (100 kHZ - 5 MHz) [13].

Although ECT systems are predominantly employed for room temperature applications, there are a few reports of their use at elevated temperatures [170–174]. For instance, Klümper-Westkamp *et al.* [173] developed a prototype eddy current sensor, the coils of which are approved up to 500 °C, for monitoring the material microstructure development of steel alloys during heat treatment. Urayama *et al.* [172] reported the use of a dual EMAT Eddy current (EMAT/EC) probe, which was employed to monitor wall thickness loss at temperatures up to 300 °C. Commercial high temperature eddy current probes are available [175–177], some of which are reported to operate at up to 380 °C continuously. Many variables alter eddy current

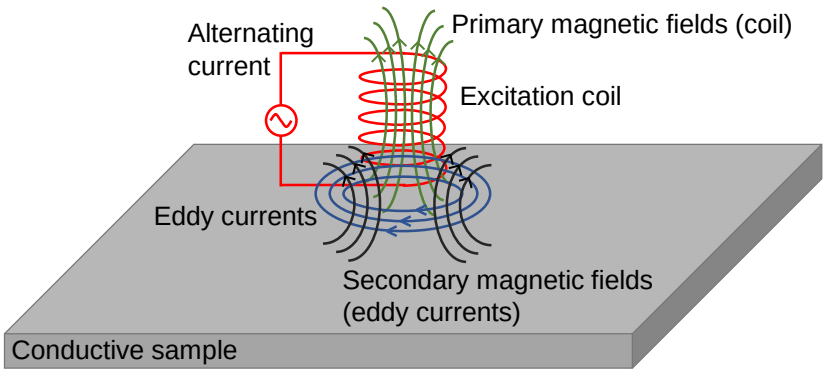

Figure 1.12: Schematic diagram of eddy current generation within an electrically conductive sample via application of an alternating current through an excitation coil near the sample surface.

response even at ambient conditions, including: permeability, conductivity, sample-probe lift-off, depth of penetration and frequency [178]. The complexity of the eddy current response is increased with the change in these variables at elevated temperatures, such that adoption of high temperature eddy current testing systems is often limited.

1.11 Thermography

Thermographic inspection involves monitoring the temperature gradient on the surface of a specimen as it is heated or cooled, and as discontinuities within a sample can alter the heat flow, temperature fluctuations at the surface can be detected and analysed to provide useful information about a sample[179]. A schematic diagram of the basic experimental set-up often used in conventional flash thermography is given in Figure 1.11, where one or multiple heat sources (e.g. heater, flash lamp) are used to heat the sample and a heat sensing device, often an infra-red (IR) camera, is used to detect the thermal gradients generated. A variety of different thermographic inspection techniques have been established, including: transient thermography [180], lock-in thermography [181], and pulsed eddy current thermography [182]. Thermography is employed in a range of inspection applications [183, 184], including: concrete structures (e.g. buildings and bridges), coatings, adhesive bonds and composite materials.

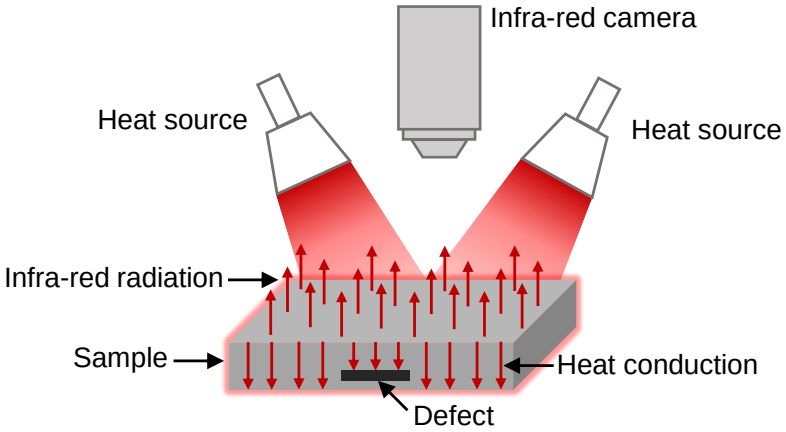

Figure 1.13: Schematic diagram of the experimental set-up of conventional flash thermography; heat sources are used to establish thermal gradients within a sample which are detected by an infra-red camera.

Thermography is often performed on samples at room temperature, however, there are cases of thermographic inspection at elevated temperatures. Shen *et al.* [1] demonstrated a thermal inspection system, using an IR camera, capable of detecting defects in stainless and carbon steel pipes at temperatures up to 150 °C. Kim *et al.* [185] developed a thermographic inspection system, utilising an IR camera and a cooling fan, to detect wall-thinned defects on a carbon steel pipe, similar to those used in secondary systems in nuclear power plants, at temperatures up to 150 °C. Thermography is non-contact, can allow inspection of large areas, and in certain cases provides simple visual representation of defects; however, for high temperature applications it can be difficult to interpret data if a material has variable emissivity, sensitivity can be effected by reflections and background radiation and, most crucially for industrial application, thermographic inspection systems can be relatively expensive.

Chapter 2

Theory and Background

This chapter considers the theory underlying the research carried out on the use of both bulk longitudinal and shear waves for thickness measurements using EMATs and piezoelectric transducers. First, the theory of ultrasonic wave propagation is discussed in section 2.1. This leads onto a review of the theory of generation and detection mechanisms of EMAT on different materials in section 2.2. The operating principles of piezoelectric ultrasound transducers are discussed in section 2.3. Finally, a brief note on signal-to-noise ratio (SNR) is provided in section 2.4, and finite element analysis (FEA) is introduced in section 2.5.

2.1 Ultrasonic Wave Propagation

Ultrasound testing was introduced briefly in section 1.4 with reference it its application in NDT. This section aims to introduce the theoretical background to ultrasound waves and their propagation in solid materials by consideration of: the theory of elasticity, the propagation of ultrasound in elastic materials, discussion of bulk longitudinal and shear waves, the interaction of bulk waves and interfaces, the principles of attenuation of bulk waves, and the effect of temperature on ultrasound propagation.

2.1.1 Theory of Elasticity

Ultrasound waves produce a deformation within a material by disturbing particles from their equilibrium position, and internal restoring forces return the particles to their equilibrium position, resulting in oscillatory motion; this relationship can be mathematically described at any point in time by considering strain (ϵ) as the material deformation and stress (σ) as the internal restoring force [42]. The strain

and stress are represented as rank two tensors using Cartesian coordinates (x, y, z) in three dimensions by:

$$\epsilon_{ij} = \begin{pmatrix} \epsilon_{xx} & \epsilon_{xy} & \epsilon_{xz} \\ \epsilon_{yx} & \epsilon_{yy} & \epsilon_{yz} \\ \epsilon_{zx} & \epsilon_{zy} & \epsilon_{zz} \end{pmatrix}, \tag{2.1}$$

$$\sigma_{ij} = \begin{pmatrix} \sigma_{xx} & \sigma_{xy} & \sigma_{xz} \\ \sigma_{yx} & \sigma_{yy} & \sigma_{yz} \\ \sigma_{zx} & \sigma_{zy} & \sigma_{zz} \end{pmatrix}. \tag{2.2}$$

The strain and stress tensors are symmetric to conserve the static equilibrium of the material, resulting in six independent components given by:

$$\epsilon_{ij} = \begin{pmatrix} \epsilon_1 & \frac{1}{2}\epsilon_6 & \frac{1}{2}\epsilon 5 \\ \frac{1}{2}\epsilon_6 & \epsilon_2 & \frac{1}{2}\epsilon_4 \\ \frac{1}{2}\epsilon_5 & \frac{1}{2}\epsilon_4 & \epsilon_3 \end{pmatrix} = \begin{pmatrix} \epsilon_1 \\ \epsilon_2 \\ \epsilon_3 \\ \epsilon_4 \\ \epsilon_5 \\ \epsilon_6 \end{pmatrix}, \tag{2.3}$$

$$\sigma_{ij} = \begin{pmatrix} \sigma_1 & \frac{1}{2}\sigma_6 & \frac{1}{2}\sigma_5 \\ \frac{1}{2}\sigma_6 & \sigma_2 & \frac{1}{2}\sigma_4 \\ \frac{1}{2}\sigma_5 & \frac{1}{2}\sigma_4 & \sigma_3 \end{pmatrix} = \begin{pmatrix} \sigma_1 \\ \sigma_2 \\ \sigma_3 \\ \sigma_4 \\ \sigma_5 \\ \sigma_6 \end{pmatrix}. \tag{2.4}$$

The strain and stress components are represented here by a single subscript index, as shown by the reduced subscript index notation listed in table 2.1.

Table 2.1: Conversion table from regular indices to reduced indices

Reduced indices	Regular indices
1	11
2	22
3	33
4	23 = 32
5	31 = 13
6	12 = 21

Relatively small deformations caused by an ultrasound wave, namely deformations that are below the linear elastic limit of a material, can be described by Hooke's law [186, 187], such that the strain observed is linearly proportional to the applied stress, as given by equation 2.5; it is assumed that this assumption applies for the materials considered within this work.

$$\sigma_{ij} = c_{ijkl}\epsilon_{kl} \tag{2.5}$$

Einstein notation is used here to represent a summation over repeated indices, such that the subscript indices (i, j, k, l) denote any of the three spatial directions (x, y, z). The linear proportionality constant of Hooke's law is given by c_{ijkl}, which is a fourth-order elasticity tensor representing the elastic constants of a solid material. The elasticity tensor c_{ijkl} has 81 components, although it can be shown that a maximum of 36 independent elastic constants can be used to describe a material [188], thereby reducing the elasticity tensor to a rank two tensor with 36 independent components, as shown by Hooke's law in equation 2.6.

$$\begin{pmatrix} \sigma_1 \\ \sigma_2 \\ \sigma_3 \\ \sigma_4 \\ \sigma_5 \\ \sigma_6 \end{pmatrix} = \begin{pmatrix} c_{11} & c_{12} & c_{13} & c_{14} & c_{15} & c_{16} \\ c_{21} & c_{22} & c_{23} & c_{24} & c_{25} & c_{26} \\ c_{31} & c_{32} & c_{33} & c_{34} & c_{35} & c_{36} \\ c_{41} & c_{42} & c_{43} & c_{44} & c_{45} & c_{46} \\ c_{51} & c_{52} & c_{53} & c_{54} & c_{55} & c_{56} \\ c_{61} & c_{62} & c_{63} & c_{64} & c_{65} & c_{66} \end{pmatrix} \cdot \begin{pmatrix} \epsilon_1 \\ \epsilon_2 \\ \epsilon_3 \\ \epsilon_4 \\ \epsilon_5 \\ \epsilon_6 \end{pmatrix} \tag{2.6}$$

Typically, real engineering materials are produced by working processes, such as rolling or extrusion, which tend to create elastic anisotropy within the polycrystalline structure [189]. Here the cubic crystals of aluminium and steel are considered as these materials are used within this body of work. Essentially, the individual aluminium and steel crystals exhibit a cubic structure, however, aggregates of these cubic crystallites can observe macroscopic symmetry which is isotropic, cubic or orthorhombic [189]. The crystallographic alignment of an aggregate of grains within a material, which is altered by working process, dictates whether macroscopic isotropy or anisotropy is exhibited.

The majority of components of the elasticity tensor are zero for elastic isotropic materials due to certain symmetry considerations and approximations [42, 190]. This produces only two independent elastic constants for elastic isotropic materials, such that the elasticity tensor, c_{ij}, can be represented as:

$$c_{ij} = \begin{pmatrix} c_{11} & c_{12} & c_{12} & 0 & 0 & 0 \\ c_{12} & c_{11} & c_{12} & 0 & 0 & 0 \\ c_{12} & c_{12} & c_{11} & 0 & 0 & 0 \\ 0 & 0 & 0 & c_{44} & 0 & 0 \\ 0 & 0 & 0 & 0 & c_{44} & 0 \\ 0 & 0 & 0 & 0 & 0 & c_{44} \end{pmatrix}, \tag{2.7}$$

where the two independent elastic constants c_{12} and c_{44} are referred to as the Lamé constants λ_L and μ_L ($c_{12} = \lambda_L$ and $c_{44} = \mu_L$), and these are related to c_{11} by:

$$c_{11} = \lambda_L + 2\mu_L. \tag{2.8}$$

The elasticity tensor, c_{ij}, in equation 2.7 can also be used to describe materials that exhibit cubic symmetry, where c_{11}, c_{12} and c_{44} are all independent variables, such that cubic crystals can be described by three independent elastic constants. The anisotropy of materials with cubic symmetry is quantified by the anisotropy parameter, c, given by:

$$c = c_{11} - c_{12} - 2c_{44}. \tag{2.9}$$

The elasticity tensor for materials with orthorhombic symmetry is described by nine independent elastic constants, and is given by:

$$c_{ij} = \begin{pmatrix} c_{11} & c_{12} & c_{13} & 0 & 0 & 0 \\ c_{12} & c_{22} & c_{23} & 0 & 0 & 0 \\ c_{13} & c_{23} & c_{33} & 0 & 0 & 0 \\ 0 & 0 & 0 & c_{44} & 0 & 0 \\ 0 & 0 & 0 & 0 & c_{55} & 0 \\ 0 & 0 & 0 & 0 & 0 & c_{66} \end{pmatrix}. \tag{2.10}$$

The theory of elasticity yields a full characterisation of the static properties of a mechanical system, however, a dynamic theory must be introduced to represent ultrasound wave propagation in solid materials; this is detailed in section 2.1.2.

2.1.2 Propagation of Ultrasonic Bulk Waves

The previous section detailed the relationship between stress and strain for the static condition, neglecting the time varying nature of ultrasonic oscillations. The equations of motion defined by Newton's and Hooke's law, given in equation 2.5, can be used to derive the wave equation for ultrasound waves propagating in a solid elastic isotropic medium; this provides a means by which the polarisation and characteristic wave speeds of longitudinal and shear bulk ultrasound waves modes can be calculated. Newton's second law in tensor notation is given by [190]:

$$\frac{\partial \sigma_{ij}}{\partial x_j} = \rho \frac{\partial^2 u_i}{\partial t^2}, \tag{2.11}$$

which correlates stress, σ_{ij}, to particle displacement, u_i, where u_i is the i^{th} component of the displacement of the particle and ρ is material density. Application of the elastic relations detailed in section 2.1.1 to equation 2.5 for isotropic elastic materials gives:

$$\begin{aligned} \sigma_{ij} &= (c_{11} - 2c_{44})\epsilon_{kk}\delta_{ij} + 2c_{44}\epsilon_{ij} \\ &= (c_{11} - 2c_{44})\epsilon_{kk}\delta_{ij} + c_{44}\left(\frac{\partial ui}{\partial x_j} + \frac{\partial uj}{\partial x_i})\right), \end{aligned} \tag{2.12}$$

where δ_{ij} is the Kronecker delta. Following this, equation 2.12 can be substituted into Newton's law given by equation 2.11 to generate the wave equation for ultrasound waves propagating in an isotropic elastic three dimensional solid [190]:

$$\rho \frac{\partial^2 u_i}{\partial t^2} = \frac{\partial}{\partial x_i}\left[(c_{11} + 2c_{44})\frac{\partial u_i}{\partial x_i}\right] + c_{44}\frac{\partial^2 u_i}{\partial x_j^2} + c_{44}\frac{\partial}{\partial x_i}\left(\frac{\partial u_i}{\partial x_j}\right). \tag{2.13}$$

The wave equation can be simplified to vector notation given in equations 2.14 and 2.15, respectively. The vector notation of the wave equation is presented in equation 2.16, where the displacement field is denoted by the vector $\mathbf{u}$ with components u_i u_j. and u_k.

$$\nabla = \left(\frac{\partial}{\partial x_i} + \frac{\partial}{\partial x_j} + \frac{\partial}{\partial x_k}\right) \tag{2.14}$$

$$\nabla^2 = \left(\frac{\partial^2}{\partial x_i^2} + \frac{\partial^2}{\partial x_j^2} + \frac{\partial^2}{\partial x_k^2}\right) \tag{2.15}$$

$$\rho \frac{\partial^2 \mathbf{u}}{\partial t^2} = (c_{11} + c_{44})\nabla(\nabla \cdot \mathbf{u}) + c_{44}\nabla^2 \mathbf{u} \tag{2.16}$$

As the particle displacement is presented here in vector form, and any vector field can be expressed by the gradient of a scalar potential, ϕ, and the curl of a vector potential, ψ, it can be written as:

$$\mathbf{u} = \Delta\phi + \Delta \times \boldsymbol{\psi}. \tag{2.17}$$

Utilising the notation in equation 2.17, it is possible to isolate the vector notation of the wave equation expressed in equation 2.16 into two independent variables, such that one is a totally scalar term and the other a totally vector terms:

$$\nabla\left(\rho\frac{\partial^2\phi}{\partial t^2} - c_{11}\nabla^2\phi\right) + \nabla \times \left(\rho\frac{\partial^2\boldsymbol{\psi}}{\partial t^2} - c_{44}\nabla^2\boldsymbol{\psi}\right) = 0. \tag{2.18}$$

To satisfy this condition, both the scalar and vector terms of the must be independently zero, allowing the formation of two equations, the first for longitudinal waves and the second for shear waves, given by [190]:

$$\rho\frac{\partial^2\phi}{\partial t^2} = c_{11}\nabla^2\phi, \tag{2.19}$$

$$\rho\frac{\partial^2\boldsymbol{\psi}}{\partial t^2} = c_{44}\nabla^2\boldsymbol{\psi}. \tag{2.20}$$

Alternatively, the propagation of a uniform plane wave can be described using the Christoffel equation [42, 188]:

$$k^2\Gamma_{ij}v_j - \rho\omega^2 v_i = 0, \tag{2.21}$$

where k is the wave number, Γ_{ij} is the Christoffel matrix, ρ is the density, ω is the angular frequency, and v is the phase velocity. This equation is expressed in full tensor form by:

$$k^2\begin{pmatrix}\Gamma_{11} & \Gamma_{12} & \Gamma_{13}\\ \Gamma_{21} & \Gamma_{22} & \Gamma_{23}\\ \Gamma_{31} & \Gamma_{32} & \Gamma_{33}\end{pmatrix}\begin{pmatrix}v_i\\ v_j\\ v_k\end{pmatrix} - \rho\omega^2\begin{pmatrix}v_i\\ v_j\\ v_k\end{pmatrix} = 0. \tag{2.22}$$

The Christoffel matrix, Γ_{ij}, has elements that are functions of the wave propagation direction and the elastic constants of the material, such that the matrix for isotropic and anisotropic materials are different [188]. For isotropic materials, the Christoffel equation can be formed by substituting the elasticity tensor, c_{ij}, for isotropic materials given in equation 2.7 to form a purely diagonal matrix:

$$k^2 \begin{pmatrix} c_{44} & 0 & 0 \\ 0 & c_{44} & 0 \\ 0 & 0 & c_{11} \end{pmatrix} \begin{pmatrix} v_i \\ v_j \\ v_k \end{pmatrix} - \rho\omega^2 \begin{pmatrix} v_i \\ v_j \\ v_k \end{pmatrix} = 0. \tag{2.23}$$

2.1.3 Longitudinal and Shear Bulk Waves

As detailed in section above, the wave equation demonstrates that two types of ultrasonic waves can be supported in bulk isotropic elastic materials, namely longitudinal and shear waves. The longitudinal wave represented by equation 2.19 is defined by a scalar quantity with no change in angle or rotation, such that there is a volume change as the wave propagates through the material. Longitudinal waves propagate via oscillating regions of particle displacement through compression and rarefaction in the same direction of propagation, as shown in Figure 2.1(a). The longitudinal wave velocity, v_L, can be calculated using equation 2.24 [190].

$$v_L = \sqrt{\frac{c_{11}}{\rho}} = \sqrt{\frac{(\lambda_L + 2\mu_L)}{\rho}} \tag{2.24}$$

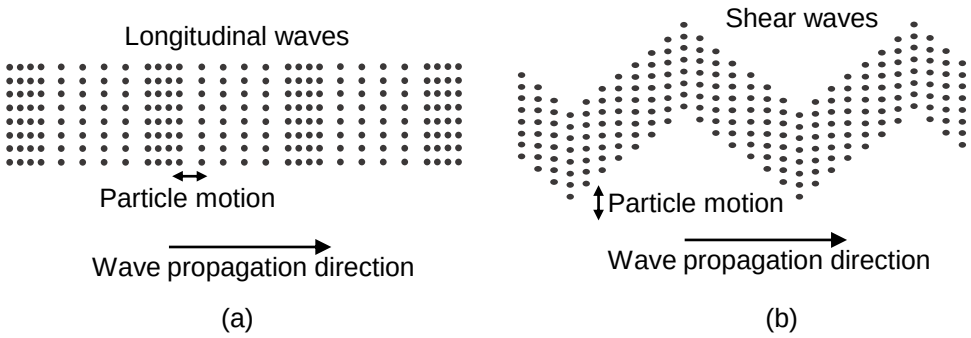

Figure 2.1: Schematic diagram of bulk wave modes in a solid material: (a) longitudinal waves where the particle displacement is parallel to the direction of propagation, and (b) shear waves where the particle displacement is perpendicular to the direction of propagation.

The shear wave represented by equation 2.20 is defined by the vector potential with two orthogonal states of polarization, typically defined as shear horizontal (SH) and shear vertical (SV), and with no change in material volume as the wave propagates through the material. Shear waves propagate via oscillation of the par-

ticles in the polarisation direction, such that it is perpendicular to the direction of propagation, as shown in Figure 2.1(b). The shear wave velocity, v_S, can be found with equation 2.25 [190]. For isotropic materials SH and SV waves will travel with identical velocities. Bulk shear waves can also exhibit radial polarisation, as detailed in section 2.2.

$$v_S = \sqrt{\frac{c_{44}}{\rho}} = \sqrt{\frac{\mu_L}{\rho}} \tag{2.25}$$

2.1.4 Ultrasonic Waves at Material Interfaces

Ultrasound waves propagate continuously through a medium, however, when a medium with alternating acoustic properties is encountered the ultrasound wave can exhibit a number of interactions at the interface: including transmission, reflection, refraction and mode conversion. The extent of the interaction of a wave with an interface between two media depends upon the acoustic properties of both media, namely the acoustic impedance, Z_a, given by equation 2.26 where v_L is the longitudinal acoustic wave velocity, in addition to the angle of incidence and type of incident ultrasound wave.

$$Z_a = \rho v_L \tag{2.26}$$

The ultrasound pressure transmission coefficient, T_{12}, and reflection coefficient, R_{12}, can be calculated using equations 2.27 and 2.28 for an ultrasound wave propagating through a medium with acoustic impedance Z_{a1} which is normally incident on an interface with a medium of acoustic impedance Z_{a2}; this relationship assumes the two media are semi-infinite and there is perfect contact at the interface. Using these coefficient definitions, it can be found that if Z_{a2} is less than Z_{a1}, then $R_{12} < 0$ leading to a reflected wave from the interface that will exhibit a π radian phase change. If the interfacing media are such that $Z_{a1} >> Z_{a2}$, then the boundary can be assumed to be free, resulting in almost complete reflection of the incident ultrasound wave; for example, this is usually the case with a steel-air interface, as Z_{steel} is $\approx 46 \times 10^6$ Rayl whilst Z_{air} is $\approx 0.0004 \times 10^6$ Rayl.

$$T_{12} = \frac{2Z_2}{Z_1 + Z_2} \tag{2.27}$$

$$R_{12} = \frac{Z_1 - Z_2}{Z_1 + Z_2} \tag{2.28}$$

Mode conversion describes the phenomenon that occurs at an interface between two media when an incident wave can partially or wholly convert to a different particle displacement polarisation. For an infinite isotropic medium, the equations 2.19 and 2.20 demonstrate that the longitudinal and shear bulk wave modes are uncoupled, such that mode conversion can occur as the wave modes convert to a coupled state due to the boundary conditions. For instance, a longitudinal wave mode incident on an interface can undergo mode conversion to both reflected and transmitted shear vertical wave modes, in addition to reflected and transmitted longitudinal modes.

2.1.5 Attenuation of Bulk Waves

Attenuation of ultrasound waves refers to the amplitude loss observed as the wave propagates though a medium. Ultrasound attenuation can be attributed to geometric and/or intrinsic attenuation. Geometric attenuation refers to the amplitude loss that results from a wave spreading out as it propagates, whilst intrinsic attenuation is due to absorption or scattering effects. It is crucial to appreciate the effect of ultrasound attenuation, as the sensitivity can be greatly reduced in certain cases, leading to poor signals. The general equation which describes the effect of intrinsic attenuation is given by:

$$A_x = A_0 e^{-\alpha x}, \tag{2.29}$$

where A_x is the wave amplitude after travelling distance x within the material, A_0 is the initial wave amplitude at $x = 0$ and α is the attenuation coefficient. The attenuation coefficient is frequency dependent as the mechanisms for intrinsic attenuation are dependent upon the ultrasound frequency; generally, an increase in frequency is associated with an increase in attenuation.

Absorption describes the direct conversion of ultrasound energy within a material to heat via various mechanisms, although is generally estimated as a form of damping on particle oscillation as the wave propagates; it is typically found that absorption is directly proportional to frequency. Scattering attenuation is a result of amplitude loss due to wave interactions (e.g. reflection, refraction and mode conversion) with inhomogeneities present in a material, such as: grain boundaries, voids, porosity, inclusions and phase changes. The extent of attenuation via scattering mechanisms depends upon the relationship between the average diameter of an inhomogeneity (D_{ih}), the ultrasound wavelength (λ), and can be classified by three regimes:

$$\text{Rayleigh}: \quad \lambda \gg D_{ih} \quad \alpha \propto D_{ih}^3 \omega^4 \tag{2.30}$$

$$\text{Stochastic}: \quad \lambda \approx D_{ih} \quad \alpha \propto D_{ih} \omega_2 \tag{2.31}$$

$$\text{Diffuse}: \quad \lambda \ll D_{ih} \quad \alpha \propto \frac{1}{D_{ih}} \tag{2.32}$$

where ω is the angular frequency, using $\omega = 2\pi f$ where f is ultrasound frequency. The constants of proportionality for the relations presented in equations 2.30 - 2.32 are dependent upon the material properties, such as: average grain size, distribution of grain sizes, grain shape and other microstructure characteristics. Consequently, formulating expressions for accurate calculation of attenuation coefficients is relatively complex due to the large variation in these properties within and between different materials.

2.1.6 Effect of Temperature on Ultrasound Propagation

The density and the elastic constants of a solid medium are directly dependent on the average interatomic separation of the particles. When the solid is subjected to an increase in temperature, it usually follows that the average interatomic separation increases via thermal expansion, thereby, reducing the density and elastic constants of the material. The density of a solid material as a function of the temperature can be calculated using [191]:

$$\rho_T = \frac{\rho_{RT}}{1 + 3\alpha_T \Delta T}, \tag{2.33}$$

where ρ_T is the density at temperature T, ρ_{RT} is the density at room temperature (20 °C), α_T is the linear coefficient of thermal expansion for the material and ΔT is the temperature difference between T and room temperature.

Dates *et al.* [192] investigated the change in elastic moduli in mild steel samples for a range of temperatures between room temperature up to 750 °C, and found the values decreased at a gradual rate, where the shear and bulk modulii were measured to reduce by 35 % and 39 %, respectively. The decrease in elastic constants resulted in a decrease in the measured ultrasound wave velocity.

2.2 EMAT Operating Principles

As described in section 1.6, EMATs are non-contact transducers capable of generating and detecting a variety of ultrasound wave modes via electromagnetic coupling on electrically conductive and magnetic samples. EMATs generally consist of a coil with a specific geometry, which is driven with an alternating current, and a magnet which provides a static magnetic field. EMATs operate via three mechanisms, namely Lorentz force, magnetisation force and magnetostriction; the mechanism which dominates depends upon the conductive and magnetic properties of the sample. This section aims to provide detail on the fundamental operating principles of each mechanism, with emphasis on Lorentz force and magnetostriction, as these are exploited within this work.

2.2.1 Maxwell's Equations

EMATs exploit electromagnetic coupling to generate and detect ultrasound in electrically conductive and magnetic materials, negating mechanical coupling between the transducer and sample which is required by piezoelectric transducers. The electromagnetic interaction can be described by Maxwell's equations [193]:

$$\nabla \cdot \mathbf{D} = \rho_f, \tag{2.34}$$

$$\nabla \cdot \mathbf{B} = 0, \tag{2.35}$$

$$\nabla \times \mathbf{E} = -\frac{\partial \mathbf{B}}{\partial t}, \tag{2.36}$$

$$\nabla \times \mathbf{H} = \mathbf{J_f} + \frac{\partial \mathbf{D}}{\partial t}, \tag{2.37}$$

where $\mathbf{D}$ is the displacement vector, ρ_f is the free charge density, $\mathbf{B}$ is the magnetic field, $\mathbf{E}$ is the electric field, $\mathbf{H}$ is the magnetic field strength and $\mathbf{J_f}$ is the free current density. The following constitutive relationships, which express the displacement and magnetic field strength in relation to the elastic and magnetic fields, are required to fully describe the electromagnetic interaction:

$$\mathbf{D} = \epsilon_m \mathbf{E}, \tag{2.38}$$

$$\mathbf{H} = \mu_m^{-1} \mathbf{B}, \tag{2.39}$$

where ϵ_m is the material permittivity using $\epsilon_m = \epsilon_r \epsilon_0$ and μ_m is the material permeability using $\mu_m = \mu_r \mu_0$.

2.2.2 The Skin Effect

For ultrasound generation, the EMAT coil is excited with an alternating current pulse close to the surface of an electrically conductive sample. Such a time varying current produces a dynamic electromagnetic wave, which induces an electric field within the sample via Faraday's law (equation 2.36). The electric field establishes eddy currents within the sample, which in turn generates a magnetic field to impede the propagation of the electromagnetic wave further into the sample via Lenz's law. Due to the attenuation of the electromagnetic wave, eddy currents are only induced within a particular distance from the sample surface; the depth of penetration is termed the electromagnetic skin-depth, δ. The skin-depth of a plane wave within a electrically conductive sample can be calculated by [115]:

$$\delta = \sqrt{\frac{2}{\omega \mu_m \gamma}}, \tag{2.40}$$

where μ is material permeability and γ is material conductivity. Note that magnetic permeability of a material is a function of both frequency and magnetic field strength. From equation 2.40, it is clear that the skin-depth is inversely proportional to the frequency, permeability and conductivity. The electromagnetic wave decays exponentially within the sample, and the skin-depth gives a value of the distance within the sample at which the eddy current density reaches $\frac{1}{e}$ ($\approx 37\,\%$, where e is Euler's number) of its original value at the surface [25]. Metallic samples at typical ultrasound NDT inspection frequencies (e.g. 1-5 MHz) exhibit very small skin-depths, such that for bulk samples the skin-depth can be assumed to be much smaller than the sample thickness; this provides the basis for the assumption of an image current, which is essentially confined to the sample surface and mirrors the current driven through the EMAT coil.

2.2.3 Lorentz Force

The Lorentz force mechanism describes the ultrasound generation mechanism when using EMATs on electrically conductive samples. As detailed in this section, ultrasound generation occurs due to the exchange of momentum between the free conducting electrons, which experience a Lorentz force, and the ions of the material lattice. The Lorentz force describes the force, $\mathbf{F}$, experienced by a particle with charge q within an electric and magnetic field [25]:

$$\mathbf{F} = q\left(\mathbf{E} + \mathbf{v} \times \mathbf{B}\right), \tag{2.41}$$

where $\mathbf{v}$ is the velocity of the charged particle. The free conducting electrons (i.e. electrons around or above the Fermi energy) carry the current in metallic samples, such that the equation of motion becomes [25]:

$$m\frac{\mathrm{d}\mathbf{v_e}}{\mathrm{d}t} = -e\left(\mathbf{E} + \mathbf{v_e} \times \mathbf{B}\right) - \frac{m\mathbf{v_e}}{\tau} \tag{2.42}$$

where m is the mass of an electron, e is the charge of an electron, $\mathbf{v_e}$ is the mean electron velocity and τ is the mean time between electron-ion collisions (order of $10^{-14}\,\mathrm{s}$ at room temperature for metals [25]). The momentum originating from the excitation of the free electrons is transferred to the lattice of ions within the conductive material through collisions, resulting in the generation of ultrasound waves within the sample. The force per unit volume on the ions reduces to:

$$\mathbf{F} = -n_e e\mathbf{v_e} \times \mathbf{B} \tag{2.43}$$

where n_e is the electron density. The relationship in equation 2.43 assumes the conductive sample has an overall neutral charge and that the time period of the electric field is much larger than the electron-ion mean collision time. This can be reduced further, giving:

$$\mathbf{F} = \mathbf{J_e} \times \mathbf{B} \tag{2.44}$$

where J_e represents the image current density within the sample.

The expression in equation 2.44 demonstrates how the interaction between the image current density and the magnetic fields generates a Lorentz force on the electrons, the momentum of which is transferred to the ions via electron-ion collisions to generate ultrasound waves; this inefficient momentum transfer accounts for the relatively low efficiency EMATs exhibit in generation, due to the enormous mass difference between ions and electrons.

The Lorentz force is perpendicular to both to the magnetic field and the image current. The direction of the Lorentz force applied to the electrons, and therefore the direction and polarisation of the generated ultrasound wave, can be manipulated by altering directions of the magnetic field and image current. When applying the Lorentz force relation to EMATs, $\mathbf{B}$ accounts for the total magnetic flux density, including both contributions of the static magnetic field ($\mathbf{B_S}$) from the permanent magnet and the dynamic magnetic field ($\mathbf{B_D}$) from the excitation current through the coil (i.e. $\mathbf{B} = \mathbf{B_S} + \mathbf{B_D}$); note, the magnetic flux density established within a material is dependent on its magnetic properties. It is critical

to account for the contributions from the different magnetic fields, as the direction of the Lorentz force depends on their orientation to the excitation current. For instance, the schematic diagram in Figure 2.2(a) illustrates the Lorentz force direction from a static magnetic field directed into the sample, whilst Figure 2.2(b) illustrates the Lorentz force direction from a dynamic magnetic field, both with an excitation current directed out of the page.

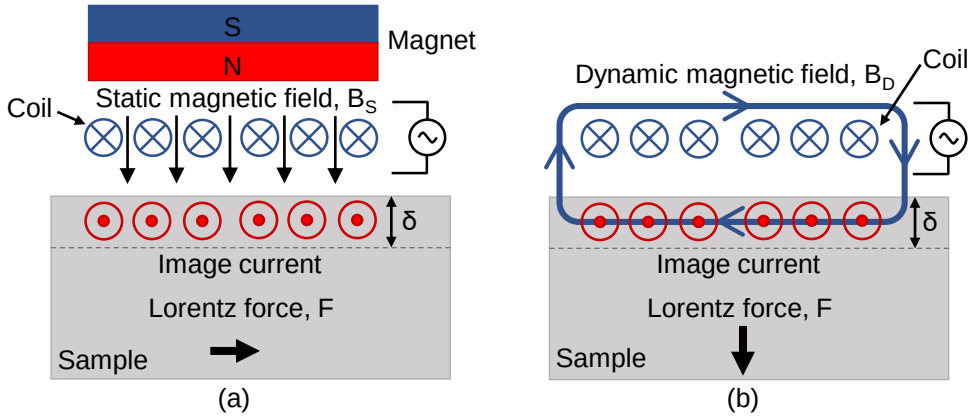

Figure 2.2: Schematic diagram highlighting the direction of the Lorentz force interaction between the image current and: (a) static magnetic field directed into the sample, (b) dynamic magnetic field generated by the excitation current through the EMAT coil.

The Lorentz force due to the static magnetic field generates ultrasound waves which oscillate with the same frequency as the excitation current, yet the Lorentz force produced by the dynamic magnetic field generates ultrasound waves which oscillates at twice the frequency of the excitation current [25]. The Lorentz force is typically dominated by the contribution from the static magnetic field, as the dynamic magnetic field is often considerably weaker, such that the dynamic field is ignored in most cases. However, if the coil is driven with a sufficiently large current, the dynamic magnetic field alone can be used to generate ultrasound [194, 195], which has advantages is particular applications.

2.2.4 Ultrasound Detection

The method by which EMATs detect ultrasound in electrically conductive material is discussed here, where EMATs can be considered as velocity sensors. In detection, the ultrasound wave disturbs the lattice ions and electrons, and in the presence of a static magnetic field orientated perpendicular to the particle displacement, this results in a Lorentz force on the ions and electrons. The free conducting electrons

have a far lower mass than the ions, such that they exhibit a much greater acceleration; therefore, it is the free conducting electrons which give rise to ultrasound detection, rather than the oscillation of the lattice ions. Analogous to the generation mechanism, these electrons produce an electromagnetic field that induces an image current within a current carrying coil near to the sample surface, thereby providing a means to detect the ultrasound wave.

It has been deduced that EMATs act as particle velocity detectors [196, 197]. A wave travelling towards the material surface with the displacement, $\mathbf{U}(t, z)$, can be expressed as:

$$\mathbf{U}\left(t, z\right) = S_0 e^{i(\omega t - kz)}, \tag{2.45}$$

where t is the time, z is the distance in the direction of propagation, ω is the angular frequency of the ultrasonic wave and k is the wave number. At the sample surface, the displacement vector, $\boldsymbol{\xi}$, describes the sum of the incident wave which travels towards the surface, and the reflected wave travelling away:

$$\begin{aligned} \boldsymbol{\xi} &= U_0 e^{i\omega t}\left(e^{-ikz} + e^{ikz}\right) \\ &= U_0 e^{i\omega t} 2\cos\left(kz\right). \end{aligned} \tag{2.46}$$

Ohm's law can be applied to express the eddy current density, $\mathbf{J}(z)$, shown in equation 2.47, where γ is the conductivity of the sample. The current density can be also be expressed by equation 2.48, as the electric field is proportional to the product of the rate of change of the displacement and the static magnetic field.

$$\mathbf{J}\left(z\right) = \gamma \mathbf{E} \tag{2.47}$$

$$= \gamma \frac{\partial \boldsymbol{\xi}}{\partial t} \mathbf{B} \tag{2.48}$$

If the displacement is perpendicular to the static magnetic field, the magnitude of the current density is given by equation 2.49; this can be integrated over the skin depth, δ, to calculate an average value of the current density within the skin depth, as shown in equation 2.50.

$$|\mathbf{J}(z)| \ = i\omega\gamma U_0 e^{i\omega t}\left(2\cos(kz)\right) \tag{2.49}$$

$$\mathbf{J}(z) = \frac{1}{\delta}\int_0^{\delta} i\omega\gamma U_0 e^{i\omega t}\left(2\cos(kz)\right) dz \tag{2.50}$$

As described above, eddy currents are confined within the electromagnetic skin depth from the sample surface, which infers that z $\leqslant \delta$. Since the ultrasound wavelength is typically much greater than the skin depth (kδ << 1, hence cos($k\delta$) $\approx$ 1), the eddy current density at the surface of the sample can be approximated by:

$$\mathbf{J}(z) = i\omega\gamma 2U_0 e^{i\omega t}, \tag{2.51}$$

$$= 2\gamma \frac{\partial \mathbf{U}(t,0)}{\partial t}. \tag{2.52}$$

Consequently, the eddy current density is detected by the EMAT, which is described in equation 2.52 as a function of the time derivative of the displacement (i.e. particle velocity).

2.2.5 Magnetisation Force

The magnetisation force mechanism arises when ferromagnetic materials are exposed to an external magnetic field. The dynamic magnetic field generated by the EMAT interacts with the internal magnetism of a ferromagnetic sample and the static magnetic field, which results in re-orientation of magnetic moments within the sample to generate a magnetisation force [25, 198]. The expression for the magnetisation force, $\mathbf{F_M}$, is given by:

$$\mathbf{F_M} = \int_V \nabla^* (\mathbf{M} \cdot \mathbf{H}) \, \mathrm{d}V + \frac{1}{2\mu_0} \int_S \hat{\mathbf{n}} M_n^2 \mathrm{d}S, \tag{2.53}$$

where $\mathbf{F_M}$ it is split into two components: a volume force $\mathbf{F_V}$ (first integrand), and a surface force, $\mathbf{F_S}$ (second integrand). The ∇^* signifies that the gradient is operating only on $\mathbf{H}$, $\mathbf{M}$ is the magnetisation, $\hat{\mathbf{n}}$ is a unit vector normal to the sample surface, and M_n is the normal component of the magnetisation at the surface. The first integrand is typically referred to as the magnetization force, as the second integrand appears because of a steep change of the electromagnetic fields at the surface and disappears within the sample [25].

In EMAT configurations with the static biasing magnetic field tangential to the sample, it has been shown that the components of the Lorentz force and magnetisation force normal to the sample are out of phase with comparable amplitudes, such that these forces act to oppose each other. As such, EMATs are generally accepted as poor generators of longitudinal waves in ferromagnetic materials.

2.2.6 Magnetostriction

The magnetostriction mechanism can be observed when EMATs operate on all ferromagnetic, ferrimagnetic and antiferromagnetic materials due to their magnetic properties [199], which originate from magnetic moments due to the spins of electrons in incomplete occupied inner orbitals of their atoms. Two types of magnetostriction exist: spontaneous magnetostriction and field induced magnetostriction. Spontaneous magnetostriction describes the phenomenon which occurs when a ferromagnetic material is cooled through its Curie temperature and exhibits spontaneous magnetisation, which results in an associated mechanical strain. This can be described by considering neighbouring atomic magnetic dipoles that tend to align towards the same direction to form a magnetic domain below the materials T_C, as illustrated in Figure 2.3(a); magnetic domains form to minimise the internal magnetostatic energy of the material [128]. These magnetic domains are separated by domain walls, in which the magnetisation direction of the atoms rotates coherently from one direction to the other, such that neighbouring magnetic domains exhibit a different magnetic field direction. The spontaneous magnetisation of the domain along its particular magnetisation direction creates a spontaneous strain, and the average deformation across the bulk of the ferromagnetic material is the average of all the individual magnetic domains; this effect is termed spontaneous magnetisation. For isotropic materials, spontaneous magnetisation results in a change of volume of the material, although the shape remains the same.

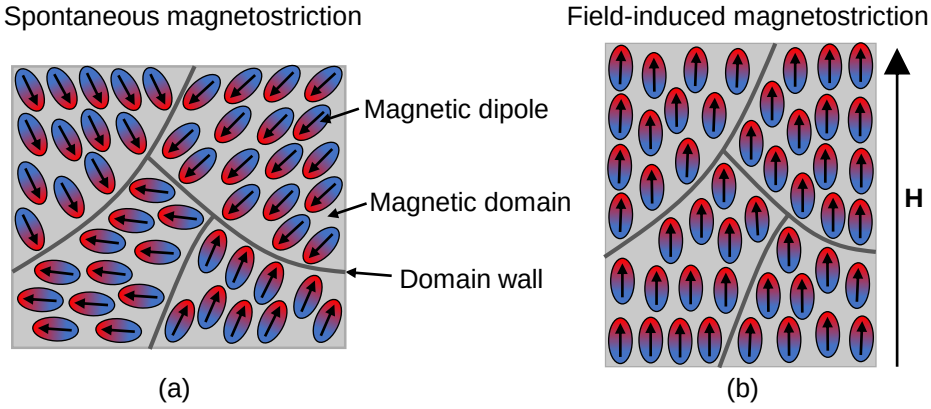

Figure 2.3: Schematic diagram illustrating magnetostriction in polycrystalline materials below T_C: (a) spontaneous magnetostriction where magnetic domains form with randomly orientated magnetisation directions, and (b) field induced magnetostriction where magnetic domains align with an external magnetic field, **H**. Adapted from [200]

Field induced magnetostriction is also observed below the T_C of a ferromagnetic material, as a result of an applied external magnetic field, **H**. The application of a magnetic field creates a preferred magnetisation direction, to which all magnetic domains tend to align via domain wall movement and domain rotation [128], as pictured in Figure 2.3(b). This produces an overall strain along the direction of the applied magnetic field, which is referred to as longitudinal magnetostriction; as volume is conserved, there is an associated transverse magnetostriction which is half the magnitude and opposite in sign to the train along the magnetisation direction [201]. The magnetostrictive strain will increase with an increase in the applied magnetic field until the point at which the sample is magnetically saturated, such that all magnetic domains are aligned with the external field. At this point, magnetostriction reaches a maximum value, referred to as the saturation magnetostriction. Magnetostrictive strains are typically very small (order of 10^{-6}), and can be classified as expansion (positive magnetostriction) or contraction (negative magnetostriction) and this is material dependent [201]. When the term magnetostriction is used within this thesis, it refers to field induced magnetostriction.

Joule magnetostriction denotes the deformation of a sample due to an applied magnetic field, as illustrated by the magnetic moments on a simple crystalline lattice in Figure 2.4 [200]. Above T_C the magnetic moments are disordered, as shown in Figure 2.4(a), such that magnetostriction is not observed. As described above, cooling below T_C, neighbouring atoms tend to align their magnetic moments, shown in Figure 2.4(b). Application of an external magnetic field results in rotation of magnetic moments to align the external field direction and deformation of the material, as displayed in Figure 2.4(c).

Magnetostriction is a reversible property, and the reciprocal process is known as the Villari effect; this describes the change in magnetisation which is induced by a mechanical deformation, and the simple schematic diagrams in Figure 2.5 [200] highlight the effect. When a sample with positive magnetostriction is below the T_C as shown in Figure 2.5(a), and is exposed to a stress parallel to the magnetisation direction as shown in Figure 2.5(b), a shift in the inter-atomic distances in the lattice occurs. This results in an alternative magnetisation direction which is more energetically favourable, such that the magnetic moments rotate to align with this direction, which typically creates a reduction of the magnetisation for polycrystalline materials [200].

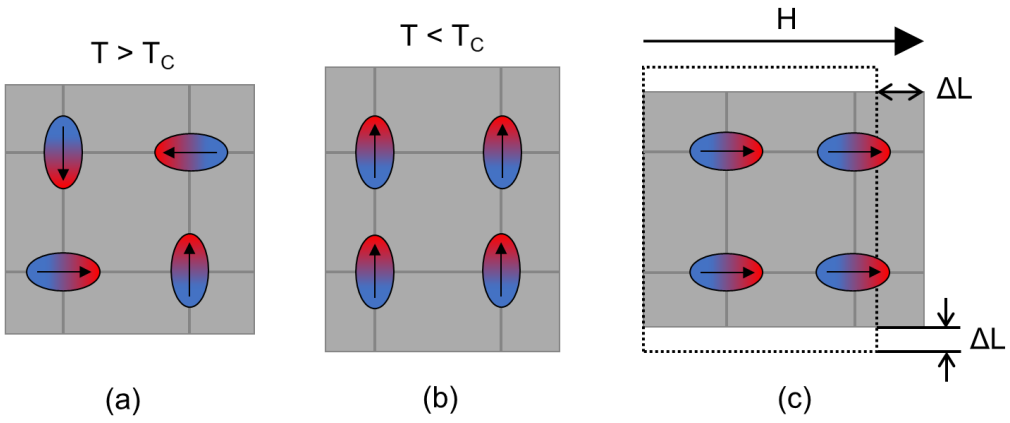

Figure 2.4: Schematic diagram of Joule magnetostriction: (a) disordered magnetic moments above T_C, (b) ordering of magnetic moments within a domain below T_C, and (c) alignment of magnetic moments with an external magnetic field, **H**, resulting in a magnetostrictive strain. Adapted from [200].

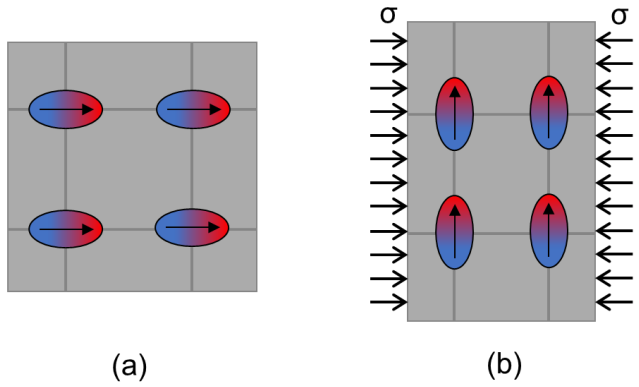

Figure 2.5: Schematic diagram of the Villari effect: (a) magnetic moments aligned within a magnetic domain below T_C, and (b) application of an external stress, σ, results in a change in the magnetisation via rotation of the magnetic moments to a more favourable direction. Adapted from [200].

EMATs can exploit Joule magnetostriction, whereby a dynamic field superposed on a static biasing magnetic field, with a resultant total dynamic field, produces dynamic strains which generate ultrasound waves within the material. The detection of ultrasound waves applies the Villari effect, such that the mechanical deformation caused by the wave generates a change in magnetisation of the material, which can be detected by the coil due to the variation in the magnetic flux density.

In general, magnetostrictive constitutive relations are non-linear, where magnetostrictive strain is a non-linear function of the magnetic field strength. The non-linear behaviour of magnetostrictive materials has been observed experimentally [199, 202]; for instance, the typical static magnetostrictive curve (magnetostrictive strain versus magnetic field strength) is shown in Figure 2.6 for iron. Generally, iron undergoes a positive magnetostriction at low magnetic field strengths, to a maximum value, then decreases consistently such that a negative saturation magnetostriction is reached.

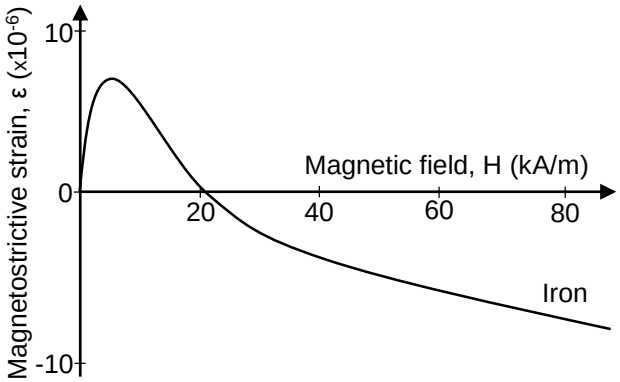

Figure 2.6: Static magnetostriction curve of iron, showing the non-linear behaviour of magnetostriction. Adapted from [199, 202]

Despite the non-linear nature of magnetostriction, it is possible to approximate the coupled magnetostrictive equations by comparison with piezoelectricity to form linear relations [203], giving:

$$\epsilon = s^H \sigma + \lambda_m \mathbf{H}, \tag{2.54}$$

$$\mathbf{B} = \lambda_m^T \sigma + \mu^\sigma \mathbf{H}, \tag{2.55}$$

where s^H represents the elastic compliance matrix (6×6) at constant magnetic field, λ_m expresses the magneto-mechanical coupling matrix (6×3) referred to as the magnetostrictive constant, and μ^σ is the magnetic permeability matrix (3×3) at constant stress. Equation 2.54 describes Joule magnetostriction, whilst equation 2.55 describes the Villari effect.

These linear relations are considered to be valid for EMATs operating within the so-called strong bias field approximation, whereby a small dynamic magnetic field, $\mathbf{H}_{\mathrm{D}}$, is superimposed on a much greater static bias field, $\mathbf{H}_{\mathrm{S}}$, such that $\mathbf{H}_{\mathrm{D}} \leqslant \mathbf{H}_{\mathrm{S}}$. As illustrated in Figure 2.7, the strong bias field approximation is valid with a small oscillation of $\pm\mathbf{H}_{\mathrm{D}}$ at the EMAT operation point $\mathbf{H}_{\mathrm{S}}$.

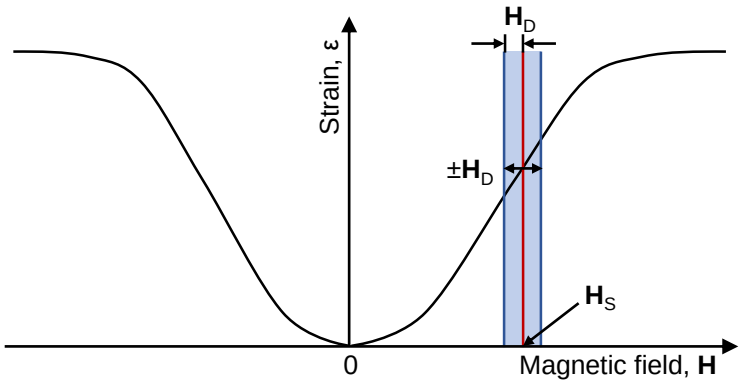

Figure 2.7: Schematic figure of the strong bias field approximation for magnetostriction, where a linear relation can be approximated if a dynamic magnetic field, $\mathbf{H}_{\mathrm{D}}$, is superimposed on a static bias magnetic field, $\mathbf{H}_{\mathrm{S}}$.

The generation and detection efficiency originating from the magnetostriction mechanism is strongly dependent on the material properties of the magnetostrictive sample, such as: magnetic permeability, magnetostrictive coefficients, electrical resistivity and elastic constants [204, 205]. The efficiency is also effected by the strength and direction of the bias magnetic field relative to the dynamic magnetic field. Moreover, the efficiency can vary as a function of temperature, as the factors mentioned are temperature dependent. It has been found that the contribution of the magnetostriction mechanism to the transduction efficiency is dominant at lower static bias field, where a non-linear response is observed with respect to the bias magnetic field, although at high fields the Lorentz force contribution is dominant, with a linear response with increasing bias magnetic field; this relationship is illustrated by the schematic in Figure 2.8 [204, 205].

It is crucial to determine which transduction mechanism dominates for an EMAT configuration on a particular sample, as the performance can vary widely depending upon these factors. For EMAT configurations involving the bias magnetic field directed normal to the sample surface, there was a dispute in the literature to whether the Lorentz force [206, 207] or the magnetostriction mechanism [25, 208] dominates. Kitley [209] carried out a detailed study of EMAT operation on fer-

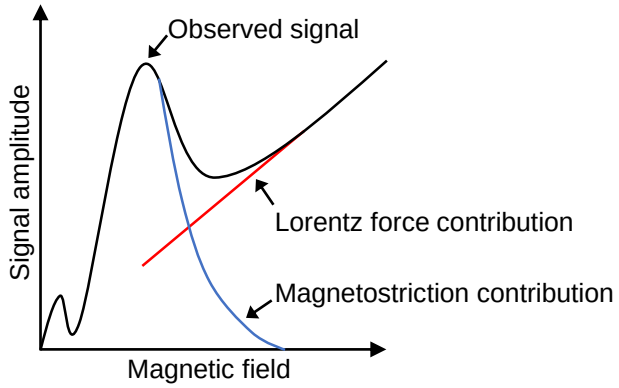

Figure 2.8: Schematic of the dependence of transduction efficiency for Lorentz force and magnetostriction mechanisms in iron. Adapted from [204, 205].

romagnetic samples, and demonstrated that the Lorentz force dominates on low tensile carbon steel, mild steel and cast iron samples with a normal bias field EMAT configuration. However, the magnetostriction mechanism was found to dominate for nickel and invar (nickel-steel alloy) samples. Ribichini *et al.* [210] further confirmed these findings, such that the magnetostriction mechanism on a variety of steel samples was not found to contribute more than 5-10 % of the overall observed signal for normal bias field EMATs; yet, it was suggested this is not the case for materials with a magnetostrictive coating, such as oxide (magnetite) coated steels. The work in this thesis centres on normal bias field EMAT operation on magnetite coated steel samples, where it is expected that the magnetostriction mechanism will dominate over the Lorentz force mechanism.

2.2.7 Radially Polarised Bulk Shear Wave EMAT

The normal bias field spiral coil EMAT configuration is used throughout this work, which generates and detects radially polarised bulk shear waves; a simple schematic diagram illustrating the EMAT configuration and direction of ultrasonic displacement is shown in Figure 2.9. This EMAT configuration is one of the simplest and most commonly used, it consists of a single cylindrical permanent magnet with the static bias field directed normally into the sample and a single flat spiral (pancake) coil with the required number of turns. Applications of this EMAT include: thickness measurements [211], ultrasonic texture measurement of rolled metal sheets [212] and the birefringent acoustoelastic stress measurement [213].

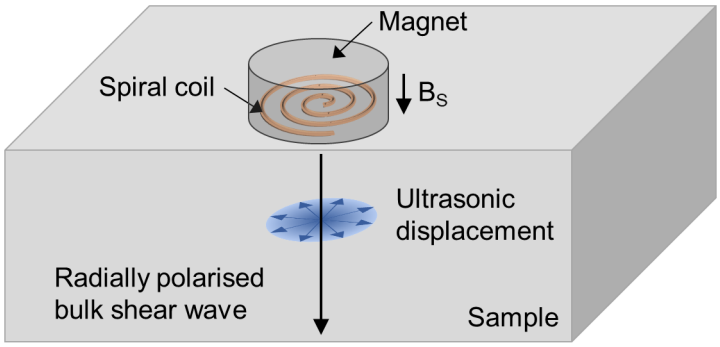

Figure 2.9: Schematic diagram of a normal bias field spiral coil EMAT configuration which generates and detects radially polarised bulk shear waves.

A schematic diagram of this EMAT configuration operating on a conductive sample via the Lorentz force mechanism was shown in section 1.6 in Figure 1.6, where the radial polarised image current generates a radially polarised Lorentz force, which results in a radially polarised ultrasonic displacement in truly isotropic materials. The ultrasound waves generated are bulk shear waves as the ultrasonic displacement is perpendicular to the direction of propagation, which is directed into the sample. Similarly, a schematic diagram of this EMAT operating on a sample with a magnetostrictive coating was shown in section 1.6 in Figure 1.7. The spiral coil generates a radially polarised dynamic magnetic field, which generates radially polarised strains within the magnetostrictive coating, which launches radially polarised shear waves within the bulk of the sample.

The performance of this EMAT configuration is tested at room temperature and at elevated temperatures on a purely electrically conductive material (i.e. aluminium) and a material with a magnetostrictive coating (i.e. magnetite coated steel); this work is presented and discussed in chapters 3 and 4.

2.3 Piezoelectric Transducer Operating Principles

Piezoelectric transducers were introduced in section 1.5, with emphasis on their design considerations for high temperature application. This section aims to present the theory of piezoelectric transducer operating principles, with emphasis on piezoelectricity, the resonance behaviour of piezoelectric elements used in transducers, equivalent circuits used for modelling and the damping of the piezoelectric element.

2.3.1 Piezoelectricity

Piezoelectricity describes the electromechanical interaction in crystalline materials which do not exhibit a centre of symmetry, such materials are referred to as piezoelectric [214]. The direct piezoelectric effect is the generation of a voltage across a piezoelectric material on application of an external mechanical stress; this is employed in piezoelectric transducers to detect ultrasound waves. The indirect (or converse) piezoelectric effect is the reverse, whereby piezoelectric materials exhibit mechanical strain as a result of an applied electric field; this is utilised in piezoelectric transducers to generate ultrasound waves. Quartz is an example of a naturally occurring piezoelectric material, however, polarisation is required for most crystalline materials with asymmetry for piezoelectricity to be observed, as discussed in section 1.5.1.

Piezoelectricity can be expressed by the following linear constitutive equations as described in the IEE standard [215], which assumes the piezoelectric material undergoes an elastic deformation that is sufficiently small such that non-linear effects can be neglected [216]:

$$\mathbf{D} = d\sigma + \epsilon^{\sigma}\mathbf{E}, \tag{2.56}$$

$$\mathbf{S} = c^{E}\sigma + d^{T}\mathbf{E}, \tag{2.57}$$

where $\mathbf{D}$ is the electric displacement vector, d is the piezoelectric charge constant matrix, σ is the elastic stress matrix, ϵ^{σ} is the material permittivity matrix at constant stress, $\mathbf{E}$ is the electric field vector, $\mathbf{S}$ represents the elastic strain matrix and c^{E} is the mechanical compliance matrix at constant electric field. The piezoelectric constitutive equations can be expressed via four different representations depending on which set of variables is chosen as independent, as shown in Table 2.2; equations 2.56 and 2.57 are the constitutive equations when $\mathbf{E}$ and σ are taken as independent variables. The piezoelectric constants (d, e, g and h) can be represented by the following equations:

Table 2.2: Piezoelectric constants and their relative independent and dependent variables from the four different constitutive equations.

Independent variables	Dependent variables	Piezoelectric constants
E, σ	**D**, **S**	d
E, **S**	**D**, σ	e
D, σ	**E**, **S**	g
D, **S**	**E**, σ	h

$$d = \left(\frac{\partial S}{\partial \mathbf{E}}\right)_{\sigma} = \left(\frac{\partial \mathbf{D}}{\partial \sigma}\right)_{\mathbf{E}}, \tag{2.58}$$

$$e = -\left(\frac{\partial \sigma}{\partial \mathbf{E}}\right)_{\mathbf{S}} = \left(\frac{\partial \mathbf{D}}{\partial S}\right)_{\sigma}, \tag{2.59}$$

$$g = \left(\frac{\partial S}{\partial \mathbf{D}}\right)_{\sigma} = -\left(\frac{\partial \mathbf{E}}{\partial \sigma}\right)_{\mathbf{D}}, \tag{2.60}$$

$$h = -\left(\frac{\partial \sigma}{\partial \mathbf{D}}\right)_{\mathbf{S}} = -\left(\frac{\partial \mathbf{E}}{\partial S}\right)_{\mathbf{D}}. \tag{2.61}$$

The reference directions for the constitutive equations are illustrated in Figure 2.10(a), where directions 1, 2 and 3 are equivalent to the Cartesian coordinates system x, y and z. Directions 4, 5 and 6 describe rotations about the 1, 2, and 3 directions, respectively. Figure 2.10(b) displays the typical disc geometry of piezoelectric elements in conventional single element piezoelectric transducers, where the disc diameter, D_p is much greater than the thickness, t_p, ($D_p >> t_p$). Here, the poling direction of the piezoelectric disc is along direction 3. The upper and lower surfaces of the disc are usually deposited with a thin layer of conductive material (e.g. silver) to form two electrodes. This disc geometry is assumed throughout this thesis, as this is the type of piezoelectric element used within this work.

The piezoelectric constant, d_{ij}, is a figure of merit, which expresses their ability to act as a generator of ultrasound, also known as the piezoelectric charge constant. The value of d_{ij} can be described in two ways: the polarisation generated per unit of mechanical stress, or the mechanical strain experienced per unit of electric field. There are two subscripts associated with d_{ij}, the first denotes the polarisation direction when the applied electric field is zero (i.e. poling direction). The second subscript represents the direction of the applied mechanical stress or the induced strain. The parameter d_{33} is used to describe disc shaped piezoelectric materials, where the poling direction is parallel to the applied mechanical stress (i.e. direction 3, also known as the z-axis) and the induced strain is also along the same direction.

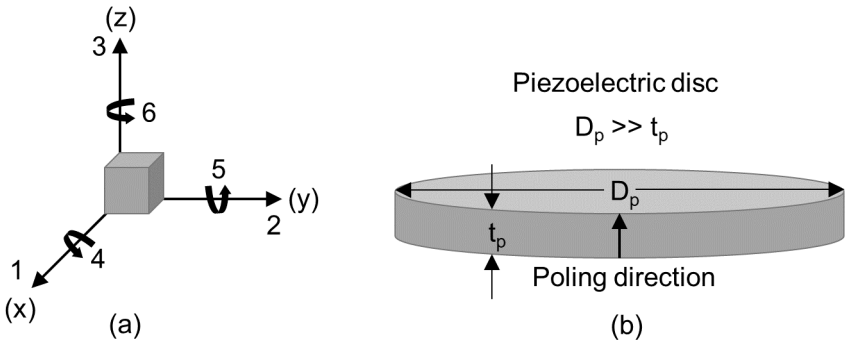

Figure 2.10: Schematic diagrams of: (a) reference directions (1, 2, 3, 4, 5 and 6) for piezoelectric materials, and (b) polarisation of a piezoelectric disc along the 3 axes, where the diameter, D_p, is much larger than the thickness, t_p.

Similarly, the piezoelectric constant g_{ij} is a figure of merit of piezoelectric transducers expressing their ability to detect ultrasound, often referred to as the piezoelectric voltage constant. The value of g can also be described in two ways: the electric field generated per unit of applied mechanical stress, or the mechanical strain experience per unit of electric displacement applied. The first subscript implies the direction of the generated electric field, whilst the second subscript indicates the direction of the applied mechanical stress. The parameter g_{33} is used to describe disc shaped piezoelectric materials, where the electric field generated by the applied mechanical strain are both along direction 3, parallel to the poling direction (i.e. direction 3, or z).

The piezoelectric electromechanical coupling coefficient, k, is often used to express the efficiency of energy conversion for piezoelectric materials, and it is defined for both the direct and inverse piezoelectric effects by equations 2.62 and 2.63, respectively. The value of k is between 0 and 1, although it is often less than 1 due to losses in the conversion process. The term k_t denotes the electromechanical coupling efficient for thickness resonance of thin discs with the electric field and vibrations in direction 3.

$$k_p = \sqrt{\frac{\text{Stored mechanical energy}}{\text{Input electrical energy}}} \tag{2.62}$$

$$k_p = \sqrt{\frac{\text{Stored electrical energy}}{\text{Input mechanical energy}}} \tag{2.63}$$

2.3.2 Resonance Behaviour

Piezoelectric transducers employ the resonance behaviour of piezoelectric elements to achieve oscillations which result in generation or detection of ultrasound, which can be through thickness or radial. Considering the classical case of a mass and spring, a piezoelectric element can oscillate mechanically at its fundamental (first) frequency, and at various harmonics [16]. The fundamental frequency of the through thickness oscillation in a piezoelectric disc rigidly fixed at its edges is illustrated in Figure 2.11. The particles at material boundaries oscillate simultaneously, either outwards or inwards, whilst at the median plane the particles are at rest. The displacement of the particles at a series of different points in time results in a group of sinusoidal curves with different amplitudes, constituting a standing wave [16]. This can be considered as two waves travelling in opposite directions through the plate at the same frequency. The thickness oscillation of a plate can be described by a plane wave that is reflected at one boundary with opposite phase, and reflected again at the other boundary, also with opposite phase. Thus, the plane wave undergoes a phase shift equal to one wavelength, such that it interacts with itself in phase.

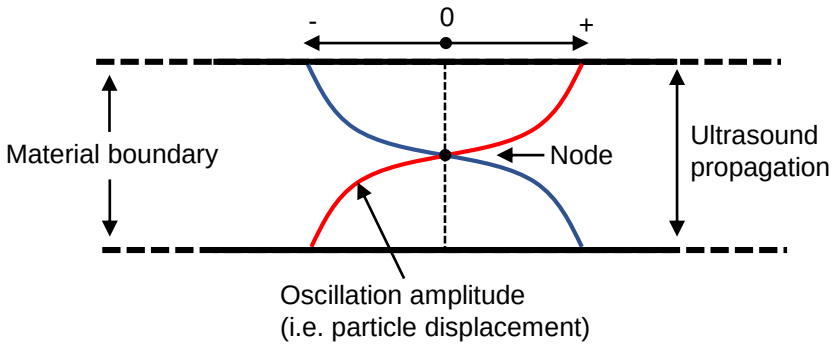

Figure 2.11: Schematic of the fundamental through thickness resonance of a piezoelectric element.

From this analysis, the thickness of the piezoelectric element, t_p, is equal to half the wavelength, λ, of the ultrasound as shown in equation 2.64. The frequency of the fundamental through thickness resonance, f_0, can be expressed by equation 2.65, where v_L is the speed of sound in the piezoelectric material.

$$t_p = \frac{\lambda}{2} \tag{2.64}$$

$$f_0 = \frac{v_L}{2t_p}, \tag{2.65}$$

The resonance behaviour of a piezoelectric disc is achieved by driving it with an alternating current pulse at a frequency similar to its fundamental resonance frequency. Generally, if the frequency of the driving pulse is low the piezoelectric acts as a parallel plate capacitor, such that charge is stored at the two electrodes on either face. If the driving pulse is at the resonance frequency the piezoelectric disc dissipates energy in the form of mechanical vibrations. Typically for piezoelectric transducers, this is the fundamental through thickness resonance of a piezoelectric disc poled in direction 3, where the electric field applied is also along direction 3.

The resonance of the piezoelectric disc can be analysed by measuring the electrical impedance, Z, with change in frequency; Z is a measure of opposition that a device or circuit presents to current, I, when a voltage, V, is applied and can be defined by substituting it into Ohm's law:

$$Z = \frac{V}{I}. \tag{2.66}$$

When a sinusoidal voltage is applied to a circuit with capacitors and inductors, the current response is sinusoidal with a phase shift, such that the impedance is a complex quantity; this can be expressed in polar form by equation 2.67, or in Cartesian form by 2.68:

$$Z = |Z|\ e^{i\theta}, \tag{2.67}$$

$$Z = R + iX, \tag{2.68}$$

where $|Z|$ is the impedance magnitude, θ is the phase shift between the current and voltage, R is the real part of the impedance (resistance), X is the imaginary part of the impedance (reactance) and i is the imaginary unit. The impedance values of an ideal resistor, Z_{R}, ideal inductor, Z_{L}, and ideal capacitor, Z_{C}, are represented by:

$$Z_{\mathrm{R}} = R, \tag{2.69}$$

$$Z_{\mathrm{L}} = i\omega L, \tag{2.70}$$

$$Z_{\mathrm{C}} = \frac{1}{i\omega C}, \tag{2.71}$$

where R is the resistance, L is the inductance and C is the capacitance. The impedance of a resistor is purely real, whilst the impedance of both inductors and capacitors is purely imaginary.

The impedance of a device can be calculated by applying a sinusoidal voltage to the device in series with a resistor, and measuring the voltage across both the resistor and the device. This measurement is performed across a range of frequencies of the applied voltage, to obtain the impedance magnitude and phase. An AC impedance analyser can be used to evaluate the resonance behaviour of piezoelectric elements and piezoelectric transducers. The schematic in Figure 2.12 represents the typical impedance magnitude and phase of a piezoelectric disc at the fundamental through thickness resonance.

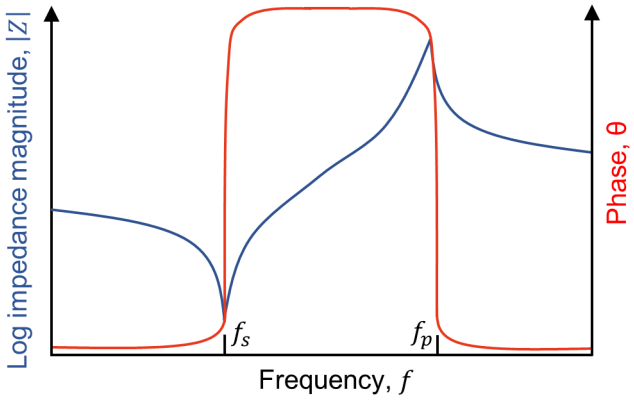

Figure 2.12: Schematic of the typical impedance magnitude and phase versus frequency at through thickness resonance for a piezoelectric disc, highlighting the series resonance frequency, f_s, and the parallel resonance frequency, f_p.

As shown in Figure 2.12, increasing the frequency results in the piezoelectric disc approaching a minimum value of impedance magnitude, which approximates the series resonance frequency, f_s, if resistance via mechanical losses are neglected; this minimum impedance magnitude frequency is referred to as the resonance frequency, f_r. The piezoelectric material properties and geometry determine this resonance frequency, as described by equation 2.65. Further increasing the frequency results in a maximum impedance magnitude, approximated by the parallel resonance frequency, f_p, again if resistance via mechanical losses are ignored.

Piezoelectric transducers generally behave as capacitors, and an ideal capacitor has a purely capacitive phase of $-90°$ between the voltage and current. However, as the piezoelectric disc or transducer resonances when driven at its resonance frequency, energy dissipates and the system becomes more resistive which increases the

phase; this increase in phase at resonance results in a peak in the phase spectrum around the resonance frequency, as shown in Figure 2.12. The magnitude of the phase peak provides an indication of the energy dissipation of the system, and is related to the efficiency of a piezoelectric disc or transducer.

The phase data measured for a piezoelectric disc or a piezoelectric transducer can be used to estimate the bandwidth (BW) and centre frequency (f_{C}). The -3 dB bandwidth technique [217] can be used to determine the upper frequency, f_U, and lower frequency, f_L, relative to the range of frequencies where the amplitude is 0.707 times that of the peak maximum value of the phase shift data. Along with the frequency of the peak maximum, f_0, the -3 dB bandwidth an be calculated using equation 2.72. The centre frequency can be estimated using equation 2.73.

$$BW = \frac{f_U - f_L}{f_0} \times 100 \tag{2.72}$$

$$f_{\mathrm{C}} = \frac{f_U - f_L}{2} \tag{2.73}$$

The electromechanical coupling factor, k_t, can be calculated if the series resonance frequency and parallel resonance frequencies are known from the impedance analysis by [215]:

$$k_t^2 = \frac{\pi}{2}\frac{f_s}{f_p}\tan\left[\frac{\pi}{2}\left(\frac{f_p - f_s}{f_p}\right)\right] \tag{2.74}$$

2.3.3 Equivalent Circuit

Piezoelectric systems can be represented by equivalent circuits which aid in the design and characterisation of piezoelectric transducers. The simplest equivalent circuit is given by the Butterworth-Van Dyke (BVD) model [215] of an unloaded piezoelectric element at series resonance, as shown in Figure 2.13, which consists of an inductor, L_1, a capacitor, C_1 and a resistor, R_1, (i.e. RLC circuit) in series with a parallel capacitor, C_0. Here, L_1, C_1 and R_1 represent mechanical damping, mass and mechanical compliance of the piezoelectric element, whilst C_0 represents the capacitance between the two surface electrodes of the piezoelectric element [218]. The mechanical quality factor, Q_m, of the piezoelectric element can be estimated by equation 2.75, which gives an indication of the total energy stored in the piezoelectric element in relation to the energy dissipated at resonance. The series and parallel resonances can be estimated from the BVD model via equations 2.76 and 2.77, respectively.

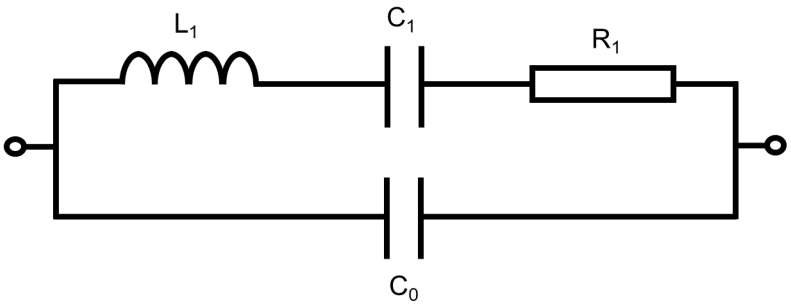

Figure 2.13: Butterworth-Van Dyke (BVD) model of an unloaded piezoelectric element at resonance.

$$Q_m = \frac{\sqrt{L_1/C_1}}{R_1} \tag{2.75}$$

$$f_s = \frac{1}{2\pi\sqrt{L_1 C_1}} \tag{2.76}$$

$$f_p = \frac{1}{2\pi\sqrt{L_1 \frac{C_1 C_0}{C_1 + C_0}}} \tag{2.77}$$

The BVD model fails to provide accurate analysis for piezoelectric materials with significant losses, or more complex systems. Alternative equivalent circuit models can be used, such as the Sherrit model [219] which assumes complex numbers for the circuit components, rather than real as for the BVD, or the Guan model [220] which attempts to model the energy dissipation with greater accuracy by including an additional series and parallel resistance to the BVD circuit.

Furthermore, the mechanical boundary conditions will be altered significantly when a piezoelectric element is bonded to a mechanical structure (i.e. loaded), which will result in a change in the electrical impedance and equivalent circuit. The Guan model accounts for these changes via additional RLC circuits with components R_n, L_n and C_n in parallel which equate to the n^{th} resonance, to account for the multiple resonances observed.

2.3.4 Damping

Piezoelectric materials used in transducers (e.g. PZT) typically exhibit low ultrasonic attenuation, such that when the element is excited by a driving pulse it undergoes significant resonance, the decay of which is dictated by the transfer of acoustic energy from the element. As the element continues to resonate after excitation, the ultrasonic pulse generated by the element is lengthened. Longer ultrasound pulses have a decreased axial resolution, that is their ability to distinguish between features within the material; this is often described in terms of bandwidth (i.e. shorter pulse length), where increased bandwidth is desirable for many NDT applications involving reflection of ultrasound from material features.

As a result, most piezoelectric transducers employ a backing material which is adhered to the piezoelectric element to damp the ringing behaviour, both during generation and detection. To achieve significant damping backing materials must be highly attenuative, such that the ultrasound entering the material is rapidly absorbed and is not reflected back to the element. Also, it is crucial that backing materials exhibit an acoustic impedance similar to that of the piezoelectric disc to maximise transmission of the ultrasound from the element to the backing. However, there is a compromise in transducer design, with respect to the choice of backing material, between the desired bandwidth and the sensitivity, where increased bandwidth is accompanied by a decrease in sensitivity.

2.4 Signal-to-Noise Ratio

For reference the signal-to-noise ratio (SNR) is introduced here, which is referred to as a figure of merit for the high temperature transducers developed within this work. SNR is a measure of a desired signal compared to the level of background noise, where SNR is defined as the ratio of signal power to the noise power, which is typically expressed in decibels (dB). The SNR is calculated using equation 2.78, where S_{max} is the maximum amplitude of the desired signal and N_{Max} is the amplitude of the noise for a region of signal adjacent to the desired echo.

$$SNR = 20 \log_{10} \left(\frac{S_{max}}{N_{max}} \right) \tag{2.78}$$

It is important to note in this work, when the SNR is quoted for a particular waveform, noise refers to both coherent and background/random noise in the baseline of the signal, such that all signals surrounding the desired signal are con-

sidered noise; for example, coherent noise signals may arise from mode conversion on reflection from the backwall. In this way, the SNR is used as a figure of merit to access the performance of a transducer on a particular sample, where only the desired backwall signals used for ultrasound thickness measurements are of interest. When the SNR is provided for a particular waveform, the region used to calculate the maximum noise value is labelled on the corresponding A-scan. The error in the SNR calculation originates from the error in determining the signal and noise amplitudes, and this is directly effected by the quantisation error in the signal acquired when recording the data with a digital oscilloscope.

2.5 Finite Element Analysis

Finite Element Analysis (FEA) is a effective tool to analyse ultrasound wave propagation. It can be used to model complex ultrasound signals, as it allows visualisation of ultrasound interactions, including interaction with defects. Most notably, FEA can be employed to model conditions which are difficult to obtain experimentally. FEA using the commercial software package PZFlex is employed within this body of work to model the ultrasound wave propagation within the piezoelectric transducer, and interaction of the generated signals with a sample. PZFlex is a time domain solver that has been developed to model large wave propagation problems, with emphasis on modelling piezoelectric materials.

The fundamental principle of FEA is the discretisation of the system being modelled into a large number of sub-domains, often referred to as elements. The elements within the model are connected at the nodes forming a mesh of the system. As the structure of these elements is much simpler than the system, the differential wave equations can be solved for each individual element, and this is applied over the whole mesh. If the solutions for each element are consistent with adjoining elements, the solution for the entire system can be calculated, including wave properties such as particle displacement, velocity and pressure at each element within the mesh. However, the main drawback is that this process can be computationally expensive, and often simplifications and assumptions have to be made to reduce the model simulation time. The maximum ultrasound frequency of interest in the model and the minimum ultrasound wave speed in any material in the model determine a limit on the element size, although a smaller element size is often required to avoid artefacts, such as numerical dispersion. Depending on geometry, the computational demand of a model can be reduced by employing planes of symmetry or simplifying the system to two dimensions, as this reduces the total number of elements.

Chapter 3

Development of a High Temperature EMAT

This chapter presents the development of a high temperature EMAT. The experimental set-up of the ultrasound measurements is described in section 3.1. An overview of the details of the samples used throughout this chapter and chapter 4 is given in section 3.2. The optimisation process for critical components of this high temperature EMAT design are given in section 3.3, namely the permanent magnet (see section 3.3.1) and the high temperature EMAT coil (see section 3.3.2), and a detailed overview of the assembly of the final high temperature EMAT design is provided in section 3.3.3. Finally, the performance of this EMAT design on different materials is compared in section 3.4, with particular emphasis on the enhancement on the signal amplitude via the magnetostriction mechanism for operation on magnetite coated mild steel samples.

3.1 Pulser-Receiver System

The ultrasound measurements presented in chapters 3 and 4 were obtained using the pulse-echo experimental set-up illustrated in Figure 3.1, unless otherwise stated. The results were recorded using a digital oscilloscope (Tektronix, DPO2014) for single shot data, and averaged data (32×) to improve signal to noise ratio (SNR). A pulser-receiver (PR) system (Sonemat, PR5000) was used to provide a spike driving current pulse, at 450 V with a 100 ns pulse width, to excite the coil in generation, and wideband low noise signal amplification in detection. The PR system was attached to a variable transformer (RS Components), also referred to as a variac, which allows one to change the voltage supply to the pulser receiver, varying it from the

mains supply voltage at $\approx 240\,\mathrm{V}$. For example, with a variable setting at 100% the maximum driving current pulse was $\approx 35\,\mathrm{A}$, whilst at 10% the maximum driving current pulse was $\approx 14\,\mathrm{A}$, this was determined by recording the voltage across a $0.1\,\Omega$ resistor in the discharge current path as the EMAT coil was pulsed. The variation of the driving current amplitude ensures the amplifier is within a linear range during detection, as large signals generated using magnetite coated steel samples are able to saturate the amplifier, and this should be avoided for quantitative measurements. For direct evaluation and comparison of the same sample under different conditions, an identical variac voltage percentage setting was used. When this PR system is used with a spiral coil EMAT with a static bias field directed normal to the sample surface it generates and receives bulk shear waves within the sample, and the subsequent first to fifth backwall echoes are referred to as S1, S2, S3, S4 and S5, respectively.

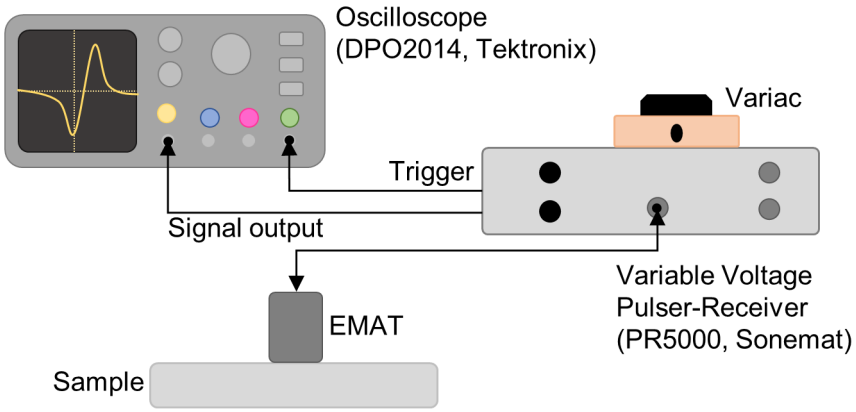

Figure 3.1: Schematic diagram of the experimental set-up used to obtain pulse-echo ultrasound measurements with the EMAT.

The current pulse generated by the PR system set to 100% voltage, and was measured using a high voltage oscilloscope probe (P5100, Tektronix), and the measured current pulse is displayed in Figure 3.2(a). To measure the relationship between the variac percentage and the maximum current, the voltage was recorded at a number of different variac percentages, and the maximum current pulse was calculated; the results are presented in Figure 3.2(b). It is clear there is a non-linear relationship between the variac percentage and the maximum driving current pulse, where the current changes more significantly at lower variac percentages and the current changes much less at above $\approx 40\%$.

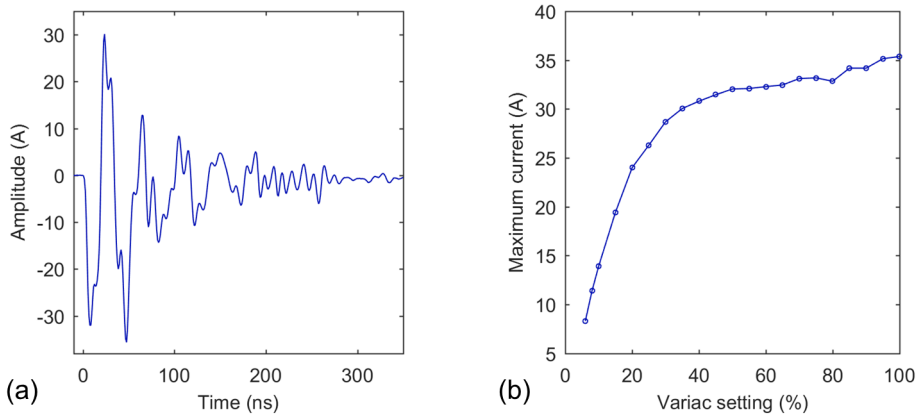

Figure 3.2: Sonemat PR5000 pulser-receiver: (a) current pulse with 450 V,nd (b) with a variac attached showing the variable voltage percentage and the corresponding maximum driving current pulse.

3.2 Samples

The ultrasound measurements presented in chapters 3 and 4 were obtained on a number of samples, including aluminium, mild steel and magnetite coated mild steel. Two industrial magnetite coated low carbon steel pipe samples were used, termed sample A and B, pictured in Figure 3.3(a) and (b). The magnetite thickness was 0.1 - 0.2 mm; this variation arises from the nature of growth of high temperature oxide scales in an industrial environment, where growth conditions can change due to a number factors, such as local surface condition, temperature and base steel composition. Average magnetite coating thickness was determined using a micrometer at a number of positions with and without the coating. Sample A had a stepped inner diameter, the maximum step at 6.8 mm $\pm$ 0.1 mm and minimum step at 2.6 mm $\pm$ 0.1 mm; both of these steps were tested to evaluate change in EMAT performance with sample thickness. Sample B had a uniform thickness of 6.8 mm $\pm$ 0.1 mm. Both samples A and B had an outer pipe diameter of 150 mm. In addition, a 12.0 mm $\pm$ 0.1 mm thick magnetite coated mild steel plate, termed Sample C, was also used. Sample C had one face coated with magnetite and on the opposite face the magnetite was removed by grinding and polishing, to leave a bare mild steel surface. Two aluminium plate samples were used, one a 10.0 mm $\pm$ 0.1 mm thick and the other 50.0 mm $\pm$ 0.1 mm thick.

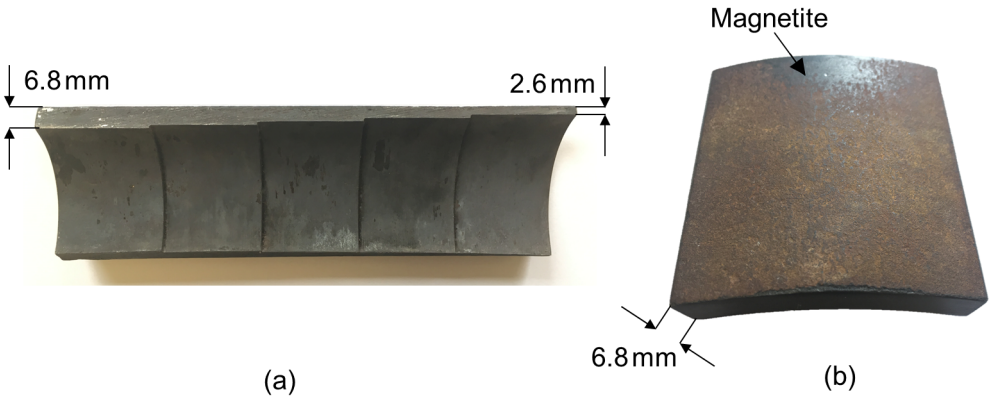

Figure 3.3: Industrial magnetite coated mild steel pipe samples sections: (a) sample A which has a stepped inner diameter with a maximum step thickness of 6.8 mm and a minimum step thickness of 2.6 mm, and (b) sample B with a thickness of 6.8 mm.

3.3 High Temperature EMAT Design Optimisation

The development and optimisation of the two main components in this high temperature EMAT design are discussed here. First the permanent magnet used is discussed in section 3.3.1, following a discussion on the optimisation of the ceramic encapsulated EMAT coil in section 3.3.2. This leads on to a detailed account of the final assembly of the high temperature EMAT in section 3.3.3.

3.3.1 Permanent Magnet

The use of both electromagnets and permanent magnets in EMATs for application at elevated temperatures was discussed in detail in section 1.6. Although electromagnets are a viable option for very high temperature applications, it was estimated that operation up to temperatures of $\approx 550\,^{\circ}\mathrm{C}$ would be sufficient for a majority of high temperature pipelines in power generation and petrochemical industries, for which this high temperature EMAT is designed. As such, the high temperature EMAT was constructed with the use of a permanent magnet with a high maximum operating temperature, avoiding the use of bulky electromagnets which limits their use in some applications.

As described in section 1.6.3, NdFeB permanent magnets are commonly used in room temperature EMATs due to their strong magnetic field strengths, but they typically have a maximum operating temperature (T_{max}) of $\approx 80\,^{\circ}\mathrm{C}$, with a Curie temperature of $\approx 315\,^{\circ}\mathrm{C}$. As NdFeB magnets cannot withstand temperatures of up to $550\,^{\circ}\mathrm{C}$, an alternative magnet material was selected. This high temperature

magnet has two different grades, one of which has a T_{max} of 450 °C and the other has a T_{max} of 550 °C, and are here referred to as a high temperature permanent magnet (HT-PM450 and HT-PM550), supplied by Sonemat Ltd.

For comparison at room temperature, a NdFeB magnet of the same dimensions (25 mm cube) as the HT-PM450 magnet were tested on the 50 mm thick aluminium sample, where the Lorentz force is the only EMAT generation and detection mechanism. A spiral EMAT coil was made from a 0.2 mm polymer encapsulated copper wire, hand wound, with a spaced 0.2 mm for 20 turns, and the coil was encapsulated in Kapton tape, with a 0.1 mm copper foil between the coil and magnet to avoid ultrasound reflections from generation within the magnet. The magnetic flux density (**B**) was measured with a gaussmeter (GM1-ST, AlphaLab Inc.), with the end of the probe placed at a central position on the face of the magnet closest to the sample, where five readings were used to calculate an average value rounded to two significant figures. The A-scans using NdFeB (blue) and HT-PM450 (red) magnet are displayed in Figure 3.4, showing the first three backwall echoes (S1, S2 and S3). The magnetic flux density, peak-to-peak (Pk-Pk) voltage and SNR for S1 are given in Table 3.1 for both the NdFeB and the HT-PM450 magnets.

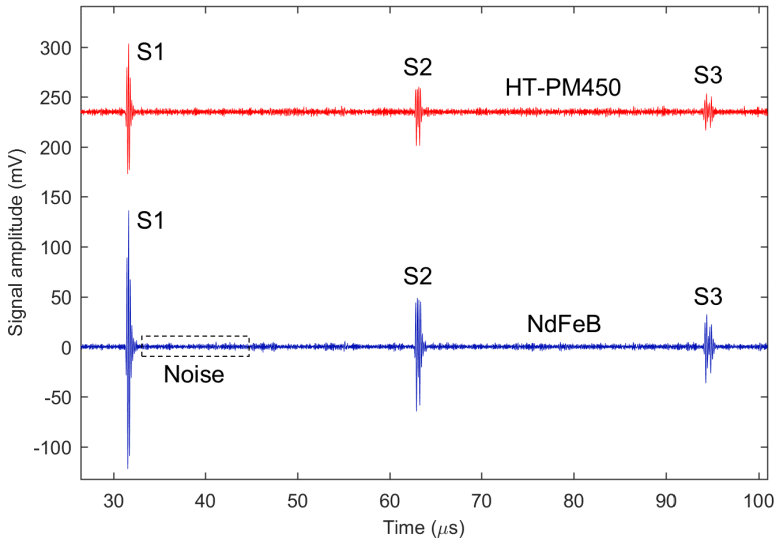

Figure 3.4: Signal amplitude at room temperature on a 50 mm thick aluminium sample using: (blue) NdFeB magnet and (red) HT-PM450 magnet, showing the first three backwall echoes (S1, S2 and S3) with a label of the coherent noise region used to calculate the SNR.

Table 3.1: Measured magnetic flux density (**B**), and Pk-Pk voltage and SNR values using NdFeB and HT-PM450 magnets for S1 on an aluminium sample at room temperature.

Magnet	Magnetic Flux Density, **B** (T)	Pk-Pk Voltage (mV)	SNR (dB)
NdFeB	0.53	260	29.7
HT-PM450	0.37	130	22.7

The measured magnetic flux density of the NdFeB magnet at 0.53 T larger than that of the HT-PM450 at 0.37 T. This corresponded to a significantly larger peak-to-peak voltage and SNR of S1 for NdFeB of 260 mV and 29.7 dB, compared to 130 mV and 22.7 dB for HT-PM450. These results were expected for an aluminium sample, as the Lorentz force is the only generation and detection mechanism, where the signal in pulse-echo mode is the Lorentz force is proportional to the magnetic flux density squared ($\mathbf{B}^2$). However, these results show that the high temperature permanent magnet of the same dimensions is able to produce signals of sufficient amplitude for ultrasound thickness measurements, at least at room temperature.

Following this, three different high temperature permanent magnets were tested and compared for use in the high temperature EMAT design. Both the cubic magnet (25 mm) and the large cylindrical magnet (35 mm diameter and 20 mm height) were material HT-PM450, whilst the small cylindrical magnet (20 mm diameter and 20 mm height) were a slightly different material composition HT-PM550, and all three magnets are pictured in Figure 3.5(a), (b) and (c), respectively. The operation of each magnet with the same EMAT coil (0.2 mm wire with 0.2 mm spacing at 20 turns, described above) was compared on the 10.0 mm aluminium sample and the 6.8 mm thick step of the magnetite coated mild steel (sample A). The A-scans for the cubic magnet (blue), large cylindrical magnet (red) and small cylindrical magnet (green) are presented in Figures 3.6 and 3.7 for the 10.0 mm aluminium and sample A, respectively. The corresponding peak-to-peak voltage and SNR values of S1, and magnetic flux density, are presented in Table 3.2.

The measured magnetic flux density of the cubic magnet at 0.37 T was larger than the other magnets, with the small cylindrical magnet slightly less at 0.34 T and that of the large cylindrical magnet significantly less than expected at 0.25 T. The relative values of the magnetic flux densities corresponded to the measured peak-to-peak voltage values on the aluminium sample, where the cubic magnet at 120 mV was larger than the other magnets, with the small cylindrical magnet slightly less at 90 mV and that of the large cylindrical magnet significantly less than expected at

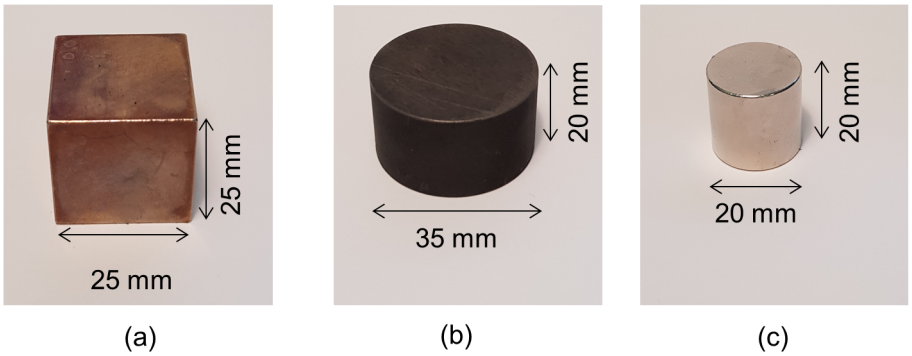

Figure 3.5: Images of the high temperature permanent magnets: (a) cubic magnet (HT-PM450), (b) large cylindrical magnet (HT-PM450) and (c) small cylindrical magnet (HT-PM550).

Table 3.2: Measured magnetic flux density (**B**), and Pk-Pk voltage and SNR values using different HT-PM magnets for S1 on a 10.0 mm aluminium sample and sample A at room temperature.

Magnet and Dimensions (mm)	T_{max} (°C)	**B** (T)	Aluminium		Magnetite coated steel	
			Pk-Pk (mV)	SNR (dB)	Pk-Pk (mV)	SNR (dB)
Cubic - 25	450	0.37	120	42.5	280	33.6
Cylindrical (35 D, 20 h)	450	0.25	90	35.4	590	32.1
Cylindrical (20 D, 20 h)	550	0.34	60	24.4	470	31.8

60 mV. These results were expected for an aluminium sample, as the Lorentz force is the only generation and detection mechanism where the signal in pulse-echo mode is the Lorentz force is proportional to the magnetic flux density squared ($\mathbf{B}^2$).

However, for the magnetite coated mild steel sample A the relative values of the magnetic flux densities failed to correspond to the measured peak-to-peak voltage values. The large cylindrical magnet with the lowest magnetic flux density observed the greatest peak-to-peak voltage value of 590 mV, followed by the small cylindrical magnet at 470 mV, compared to the cubic magnet which observed the lowest peak-to-peak voltage of 280 mV, despite having the largest measured magnetic flux density. Also, note that the shape of the shear wave signals in sample A (see Figure 3.7) are different to those in aluminium, where the signals appear to be longer in the time domain.

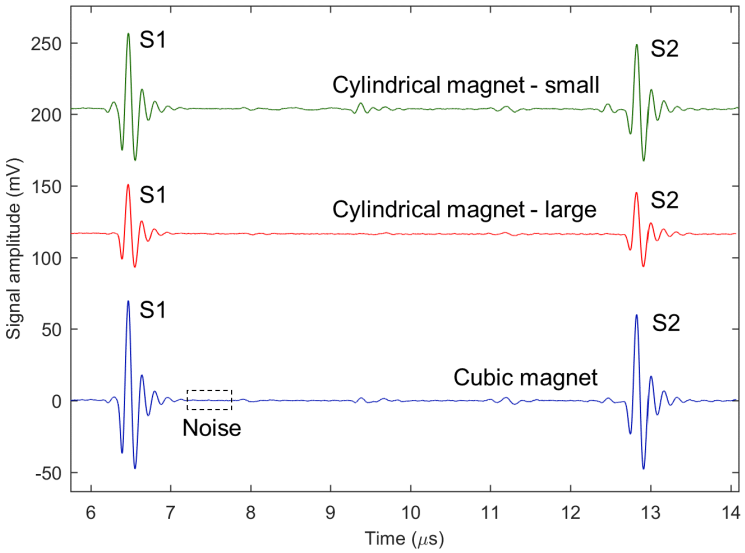

Figure 3.6: Signal amplitude at room temperature on a 10.0 mm thick aluminium sample using: (blue) cubic magnet (HT-PM450), (red) large cylindrical magnet(HT-PM450) and (green) small cylindrical magnet (HT-PM550), showing the first two backwall echoes (S1 and S2).

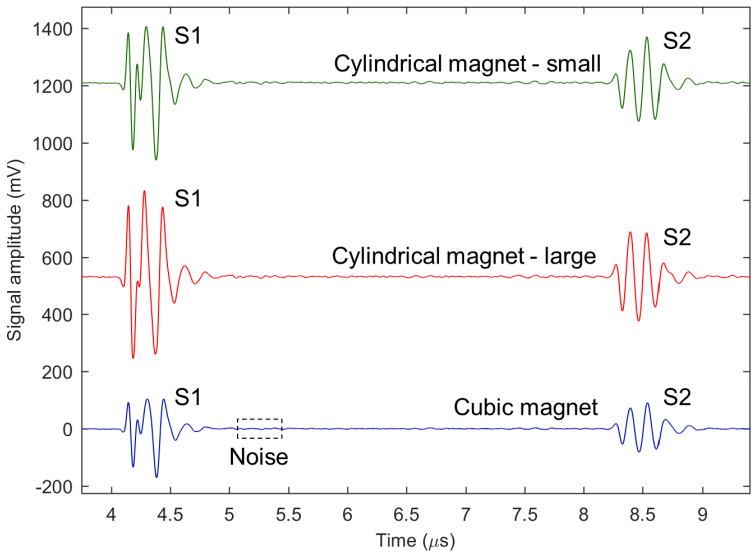

Figure 3.7: Signal amplitude at room temperature on sample A using: (blue) cubic magnet (HT-PM450), (red) large cylindrical magnet(HT-PM450) and (green) small cylindrical magnet (HT-PM550), showing the first two backwall echoes (S1 and S2).

The difference in the signals compared to aluminium is due to the magnetostrictive generation and detection mechanism dominating on magnetite coated samples, as opposed to the Lorentz force which is the sole mechanism operating on aluminium samples. As detailed in section 2.2.6, the magnetostrictive strain coefficient of iron is non-linear with respect to the applied external magnetic field, which observes a peak at lower magnetic flux densities. Although the magnetostrictive strain coefficients reported in literature typically are measured at DC, and this is not the case in the EMAT operation, this could explain the observed behaviour here. Therefore, it could be assumed that there is a peak in the signal amplitude with the external applied magnetic field when the magnetostrictive mechanism dominates. This peak could explain how the large cylindrical magnet with a lower magnetic flux density produces a much greater signal on sample A than the cubic magnet, where the lower magnetic flux value of the large cylindrical magnet is closer to the peak maximum and the cubic magnetic field is above this value.

Long-term high temperature trials were carried out with the cubic magnet (HT-PM450). The magnet was put into a furnace at 450 °C for 11 weeks, a total of 1850 hours. The magnet was cooled to room temperature at nine intervals and for each measurement the magnetic flux density was measured at the same face where five readings were used to calculate an average value rounded to three significant figures. The time at 450 °C and the corresponding magnetic flux density is plotted in Figure 3.8, where the error bars represent the standard deviation. The magnetic flux density of the cubic magnet (HT-PM450) before heating was measured at 0.362 T and decreased slightly after 1850 hours at 450 °C to 0.354 T.

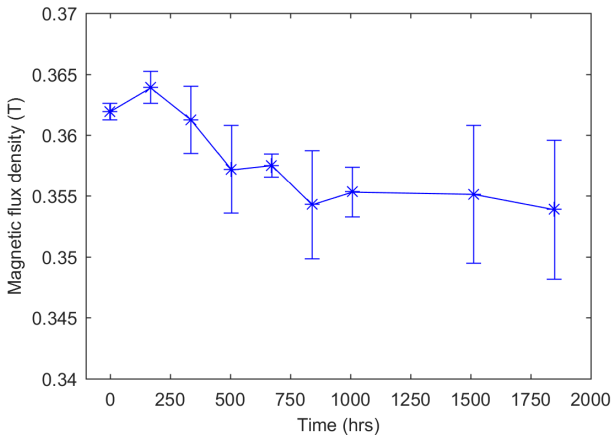

Figure 3.8: Time the cubic magnet (HT-PM450) was held at 450 °C and the corresponding magnetic flux density measured at room temperature, where the error bars represent the standard deviation.

3.3.2 High Temperature Coil

Following work from Hernandez-Valle [121], which provides a detailed account of the high temperature spiral coil design used at temperatures up to 600 °C, a similar approach was used in this work to construct an EMAT coil to operate at high temperatures without active cooling. The approach behind this high temperature coil design is to remove all polymer based materials, replacing them with ceramic materials which are able to withstand very high temperatures. The spiral EMAT coil is constructed from a bare copper wire, although if this were to be wound as a typical EMAT coil for room temperature operation (i.e. a tight spiral coil) a short circuit would occur. To avoid this, a space is fixed between each turn of the coil, achieved by winding two bare copper wires tightly together to form two concentric spirals, one of which is later removed. This space between turns of the spiral coil is filled with a high temperature ceramic adhesive, which serves as electrical insulation.

This section describes preliminary room temperature tests carried out using the high temperature permanent magnet with flat, spiral shaped EMAT coils with varying parameters, including: wire diameter, turn spacing and number of turns. These tests were performed at room temperature in order to select the optimal coil parameters for use in the high temperature EMAT, and so the coils were fabricated from polymer encapsulated copper wire. However, there are limitations on the use of polymer encapsulated wires at the elevated temperatures, as described in section 1.6.1, due to breakdown of the insulation or the printed circuit board substrate material, which are usually a polymer-based materials that cannot withstand temperatures above 150 °C; note that ceramic PCBs are becoming commercially available. Hand wound wire coils require embedding to retain their shape, and this often involves the use of Kapton tape. Although some grades of Kapton tape have a relatively high maximum operating temperature (up to $\approx$ 300 °C compared to most polymer materials), it is often too low for many industrial high temperature applications.

The high temperature EMAT is designed for use in a pulse-echo configuration, such that the EMAT performs as both the generator and detector of ultrasound. In this case, the effect of the EMAT coil wire must be taken into account with respect to the received signal amplitude. The coil wire can be considered as an inductive component, with an associated resistance and a small parasitic capacitance. In generation, the coil impedance should ideally be low to allow higher driving current through the coil, which is required to generate larger ultrasound signals, but this requires more turns which leads to an increase in the coil impedance. Moreover, in detection, the induced signal amplitude is proportional to the number of turns in

the coil, such that it is desirable to have a coil with high impedance. As a result of these conflicting factors, a number of different spiral coils were made with various parameters and compared with each other to determine the optimal parameters for the highest received pulse-echo signal amplitude.

For reference, three different coils are discussed here and their performance on aluminium is compared. The coils were hand wound as described above, leaving a space between the turns, and they were encapsulated in a single layer of Kapton tape. The cubic magnet (HT-PM450) detailed in section 3.3.1 was used with each coil with a 0.1 mm copper foil taped to the face of the magnet, to avoid reflections from within the magnet being picked up by the coil and appearing in the waveforms. Table 3.3 details the three coils, termed A, B and C here for reference, giving the wire diameter, spacing, number of turns and coil diameter, with the corresponding peak-to-peak voltage and SNR of the first backwall echo on a 10.0 mm thick aluminium sample; the A-scans for each coil operating on the aluminium sample are shown in Figure 3.9.

Table 3.3: Comparison of three different spaced coils with varying coil parameters, and the corresponding peak-to-peak voltage and SNR of the S1 echo on a 10.0 mm thick aluminium sample.

Coil	Wire Diameter (mm)	Spacing (mm)	Turns	Coil Diameter (mm)	Pk-Pk (mV)	SNR (dB)
A	0.15	0.15	18	12	16	17.9
B	0.20	0.20	20	17	69	25.0
C	0.315	0.20	15	16	32	21.6

From these results, it is clear that coil B constructed from 0.2 mm diameter wire with a 0.2 mm spacing at 20 turns produces the greatest peak-to-peak voltage at 69 mV with a SNR of 25 dB. This was followed by coil C constructed from 0.315 mm diameter wire with a 0.2 mm spacing at 15 turns with a peak-to-peak voltage of 32 mV and a SNR of 21.6 dB. The lowest signal was produced by coil A, constructed from 0.15 mm diameter wire with a 0.15 mm spacing at 18 turns, giving a peak-to-peak 16 mV and a SNR of 17.9 dB. As a result of the comparisons of these different coils, coil B was chosen as a suitable coil design for use in the high temperature EMAT, and this is the coil used throughout the high temperature trials discussed in chapter 4.

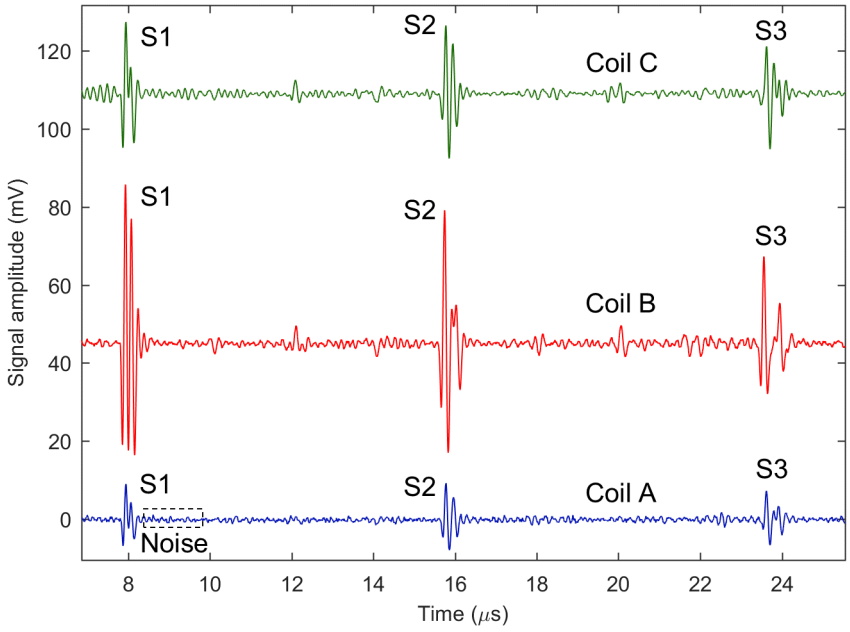

Figure 3.9: Signal amplitude at room temperature on a 10.0 mm thick aluminium sample using: (blue) coil A with 0.15 mm diameter wire, 0.15 mm spacing and 18 turns, (red) coil B with 0.2 mm diameter wire, 0.2 mm spacing and 20 turns and (green) coil C with 0.315 mm diameter wire, 0.2 mm spacing and 15 turns, showing the first three backwall echoes (S1, S2 and S3) with a label of the coherent noise region used to calculate the SNR.

Another coil was constructed, termed coil D, to compare the difference between a spaced and non-spaced coil of the same wire diameter and number of turns. Coil D was construed from 0.2 mm diameter wire with no spacing between the turns with a total of 20 turns, such that it was compared to coil B. The A-scans of these coils on a 50 mm aluminium sample, with the cubic magnet (HT-PM450), are given in Figure 3.10.

These results demonstrate that the spaced coil used in this high temperature EMAT design appears to produce larger signals, at least at the same number of turns and wire diameter, compared to non-spaced coils. For the first sample backwall echo (S1) coil B with a 0.2 mm spacing produced a peak-to-peak voltage of 130 mV with a SNR of 22.7 dB, compared to a coil D with no spacing with a peak-to-peak voltage of 63 mV and a SNR of 18.6 dB. It is also clear to note that the second (S2) and third (S3) backwall echoes are much more predominant with the spaced coil B, where S3 is not detectable for coil B.

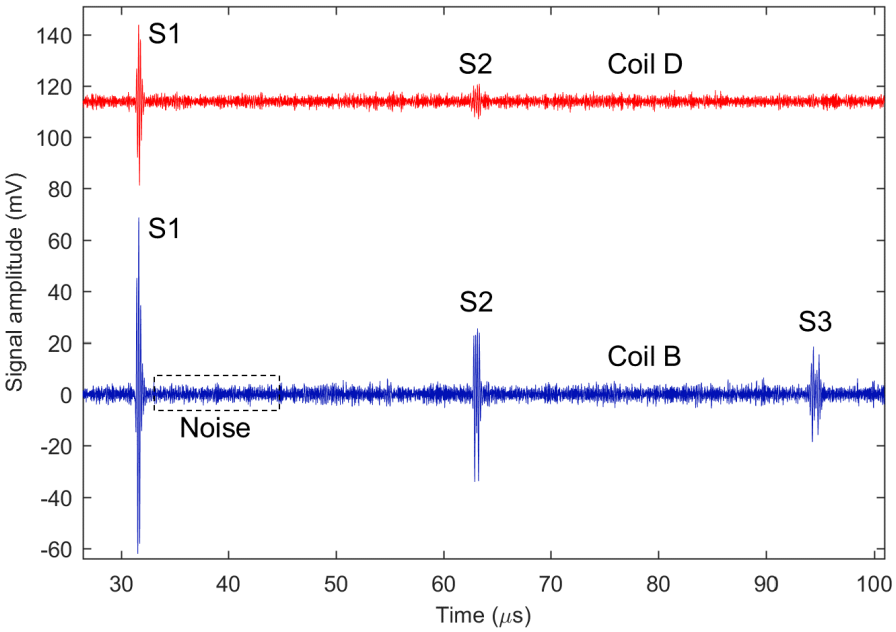

Figure 3.10: Signal amplitude at room temperature on a 50 mm thick aluminium sample using: (blue) coil B with 0.2 mm diameter wire, 0.2 mm spacing and 20 turns, and (red) coil D with 0.2 mm diameter wire, no spacing and 20 turns, showing the first three backwall echoes (S1, S2 and S3) with a label of the coherent noise region used to calculate the SNR.

With regards to constructing a spaced spiral EMAT coil for use at high temperature, not only must a ceramic adhesive be used to act as the wire insulation, but ceramic substrates are required in order to completely encapsulate the coil to provide protection during inspection. Following previous work by Baillie [143] on different types and thickness values of ceramic substrates, 0.5 mm thick alumina ceramic substrates (ADS-96R, Coorstek) were chosen to encapsulate the EMAT coil. The work demonstrated that with water-cooled EMATs at high temperatures a ceramic substrate is suitable to provide protection to the EMAT coil without significantly impairing the proper functioning of the transducer, assuming the substrate is not too thick, which would equate to both larger sample-EMAT and sample-magnet lift-offs and reduced sensitivity.

Two slightly different substrates were purchased to construct the coils in this work, both were laser machined to the desired shape, here 25 mm diameter discs, one with a machined central hole at 0.5 mm diameter and one without. The purpose of the hole is to provide an exit point for one of the coil wire ends to avoid short circuit across the entire coil. The other coil wire end is left to protrude from the side of the

coil. This is shown more clearly in the photograph spaced spiral coil in Figure 3.11. The image shows the spiral coil (0.2 mm diameter bare copper wire, 0.2 mm spacing at 20 turns) connected to the ceramic disc substrate with the ceramic adhesive and the ceramic adhesive between the turns to act as electrical insulation. The ceramic adhesive used in this study is an alumina based ceramic (Pelco® High Performance Ceramic Adhesive 16026, Agar Scientific Ltd.), set from a dispersion of aluminium oxide in an inorganic silicate aqueous solution, which appears as a high viscosity paste, although this can be altered by addition of water. This ceramic adhesive is specially formulated for bonding and sealing ceramics, metals and quartz for applications demanding electrical and thermal insulation at high continuous service temperature, providing low electrical and thermal conductivity. It has a maximum continuous service temperature of 1650 °C.

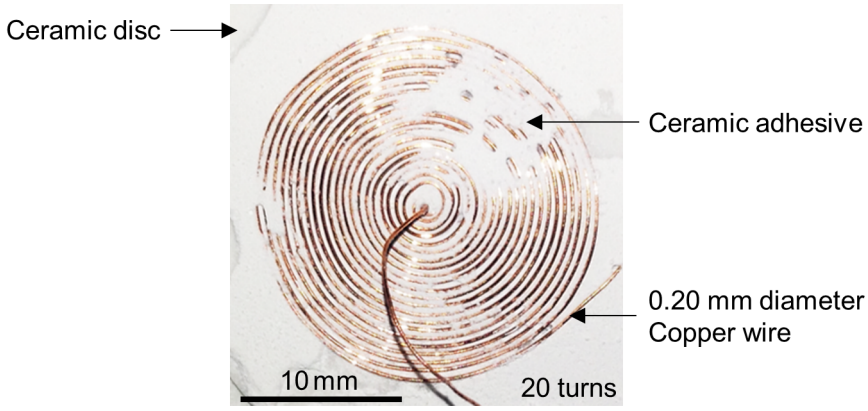

Figure 3.11: Image of the high temperature spaced spiral coil before complete encapsulation, showing the bare copper wire and the ceramic adhesive acting as electrical insulation.

A cross-sectional schematic of the encapsulated EMAT coil is shown in Figure 3.12, which highlights how the spiral coil is sandwiched between two 0.5 mm thick ceramic discs with ceramic adhesive binding all the components together. The overall thickness of the encapsulated coil is ≈ 2 mm, although this can vary slightly depending on how the ceramic adhesive sets. For reference, the inductance of this coil was measured (to 3 significant figures) at 5.0 MHz as 3.00 μH with 2.15 Ω resistance using an impedance analyser (4294A, Agilent).

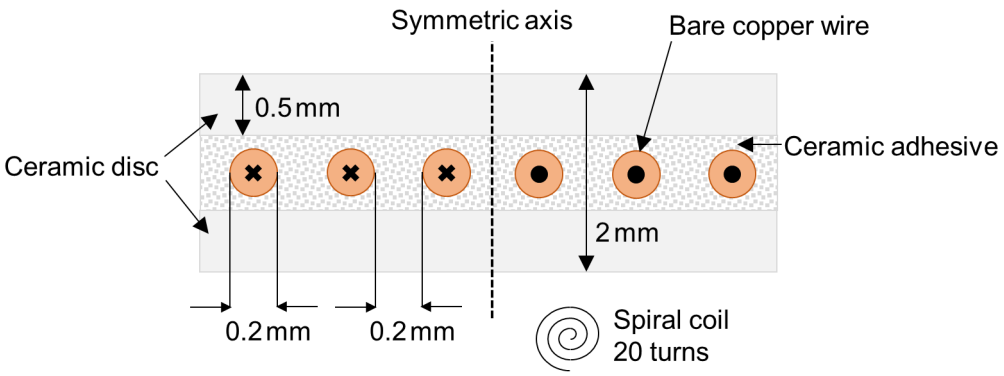

Figure 3.12: Schematic diagram showing the cross-section of the high temperature spaced EMAT coil encapsulated between ceramic discs using ceramic adhesive.

3.3.3 EMAT Assembly

The high temperature permanent magnet and coil are critical components which allow this EMAT design to operate continuously at temperatures up to 550 °C. However, the method by which the EMAT components are assembled to form the final design influences the high temperature performance. This section details the development of the assembly methods used to construct the final high temperature EMAT design.

From preliminary high temperature trials with early prototypes, it was found that the method of electrical connection had a significant impact on the long-term viability of the EMAT at elevated temperatures. Electrical connection of the live and ground wires to the BNC connector for room temperature EMATs are typically formed using a combination of soldering and contact connection. Although it depends on the alloy used for the solder joint, conventional solder alloys would not survive temperatures up to 550 °C as required by this design, such that alternative high temperature methods of electrical connection were evaluated. Initially, it was thought that contact connection may be suitable; however, after a small number of cycles exposing the EMAT up to 450 °C it became clear that the electrical connection was impaired, due to oxidation of the copper wire and metallic contact surfaces. Therefore, an improved electrical connection method was sought, which would remove the effects of surface oxidation from impeding the electrical connection despite long term exposure to high temperatures in the presence of oxygen.

Following this, it was concluded that the next viable option would be achieving electrical connection via brazed joints, which would prevent the issue of oxidation and ensure a durable bond between the EMAT coil live and ground wires and the

BNC connector. Brazing describes the act of joining metals by melting them and applying a filler metal into the joint. In this EMAT design two different brazed joints were required: a copper-to-copper brazed joint for the live wire connection between the EMAT coil and the core of the coaxial cable, and the other a copper-to-stainless-steel brazed joint for the ground wire connection between the EMAT coil and the outer sheath of the coaxial cable. After multiple trials at temperatures up to 500 °C without any loss in signal, brazing was adopted as the method of electrical connection for this high temperature EMAT design.

A schematic diagram of the high temperature EMAT design is provided in Figure 3.13, showing a cross-section through the EMAT. The high temperature magnet and ceramic encapsulated spiral coil are held in the transducer housing, which is an important part of this design as it provides shielding from electrical noise, protects the coil and magnet during inspection and holds all the components together. Stainless steel was chosen as the material for the transducer housing due to its oxidation and corrosion resistance at high temperature.

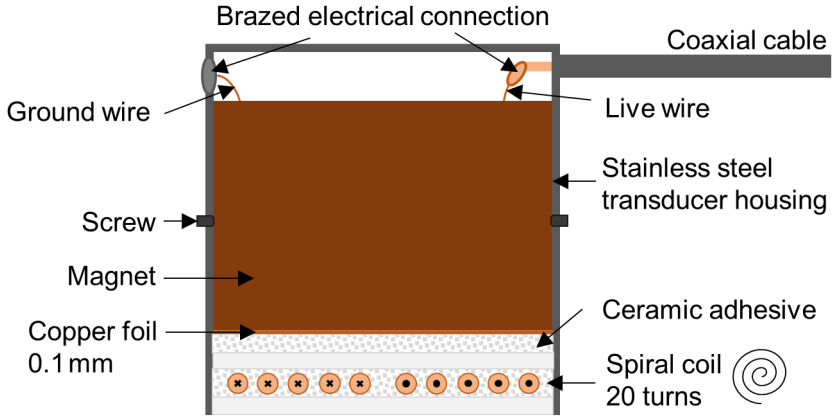

Figure 3.13: Schematic diagram providing a cross-sectional view of the high temperature EMAT design. Not to scale.

The coaxial cable consists of an outer sheath which is a thin walled tube of stainless steel, with an outer diameter of 5.0 mm and an inner diameter of 4.4 mm giving a wall thickness of 0.3 mm. This outer sheath is brazed to a 5.0 mm through hole at the top of the transducer housing, as shown in Figure 3.13, and the end of the sheath is brazed to the BNC connector. The ground wire emitting from the encapsulated coil is brazed to the stainless steel transducer housing, which is electrically connected to the outer sheath by brazing. The three brazed joints in this design ensure that the ground wire electrical connection can withstand high temperatures continuously. Inside the stainless steel sheath a ceramic fibre tube (XS-116,

Omega), with a 1.5 mm nominal diameter, made from Silica that is braided without organic, glass or metal inserts and has a maximum continuous operating temperature of 983 °C, is used to as electrical insulation. The ceramic fibre electrically insulates the 1.0 mm diameter bare copper core wire, which is brazed to the live wire emitting from the coil within the top of the transducer casing, as shown in Figure 3.13. The end of the inner core wire is soldered to the central pin in the BNC connector. It is important to note that in this design the BNC connector has polymer components, such that it cannot withstand very high temperatures. For the trials carried out in this work the BNC connector has been cooled by ambient air conditions; this is explained in more detailed in chapter 4.

The encapsulated EMAT coil is positioned such that its front face is flush with the bottom of the housing to minimise sample-EMAT lift-off. A 0.1 mm copper foil is placed at the back of the encapsulated coil, then a layer of ceramic adhesive is applied and the magnet is inserted. The magnet is further held in position by four M1 grub screws which are connected to the transducer housing by four threaded M1 holes. Once all components are held in place, the ceramic adhesive is cured for 2 hours at room temperature, then heat cured at 100 °C for 2 hours to achieve final electrical and mechanical properties.

The final high temperature EMAT developed in this work is pictured in Figure 3.14. This EMAT was constructed using the small cylindrical magnet (HT-PM550), which allows the dimensions of the housing to be as small as possible; here the housing is cylindrical in shape with a diameter of 30 mm and height of 40 mm and a wall thickness of 2 mm.

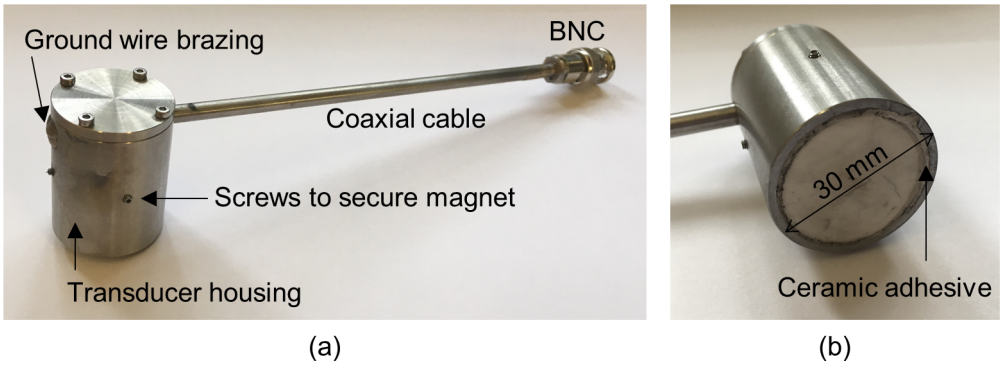

Figure 3.14: Final high temperature EMAT images: (a) full view showing the EMAT, coaxial cable and BNC connector, and (b) zoomed view showing the ceramic encapsulated coil at the front face of the EMAT.

3.4 EMAT Operation on Different Materials

A comparison of the high temperature EMAT performance at room temperature on different materials was carried out using the experimental set-up in section 3.1 on the following samples: aluminium plate (10.0 mm thick), mild steel plate (12.0 mm thick, bare steel face of sample C) and magnetite coated mild steel plate (12.0 mm thick, magnetite coated face of sample C). Sample C was chosen to compare against aluminium as it is was a flat sample, unlike the other magnetite coated samples which were curved pipe samples. Direct comparison between curved and flat samples cannot be achieved as there is a difference in the sample-EMAT lift-off across the coil diameter due to the curvature, which would result in a variation in the penetration of the dynamic magnetic field, produced by the EMAT coil, across the sample surface. The A-scan for the aluminium and mild steel sample are given in Figure 3.15, while the A-scan for the magnetite coated mild steel sample is given in Figure 3.16.

Direct comparison between the peak-to-peak voltage and SNR values of the aluminium and mild steel with the magnetite coated steel is not possible, as the variac setting on the PR system was decreased significantly for the magnetite sample to avoid saturation of the amplifier, due to the significant signal enhancement provided by the magnetostriction mechanism which dominates on magnetite coated samples. The variac was set to 100% for the aluminium and mild steel sample corresponding to ≈ 35 A maximum driving current through the coil, whilst the variac was set to 2% for the magnetite coated steel sample corresponding to ≈ 5 A maximum driving current. The variac setting used and the corresponding peak-to-peak voltage and SNR values of the first backwall echo (S1) are presented in Table 3.4.

Table 3.4: Comparison of EMAT performance on different materials, showing the PR variac setting used and the corresponding peak-to-peak voltage and SNR values of the first backwall echo (S1).

Sample	Variac (%)	Pk-Pk (mV)	SNR (dB)
Aluminium	100	31	20.6
Mild steel	100	25	18.3
Magnetite coated mild steel	2	705	38.5

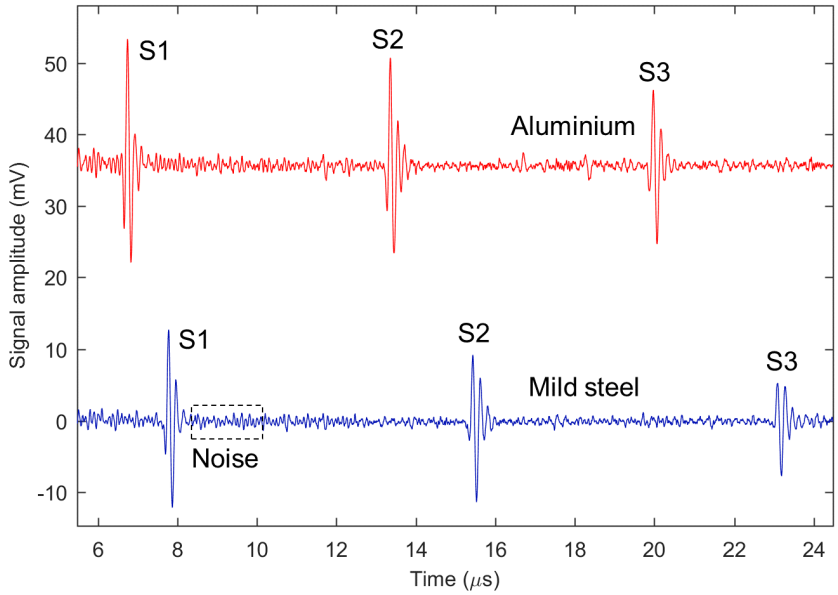

Figure 3.15: Signal amplitude at room temperature for: (blue) 12 mm thick mild steel sample, and (red) 10.0 mm thick aluminium sample, showing the first three backwall echoes (S1, S2 and S3) with a label of the coherent noise region used to calculate the SNR.

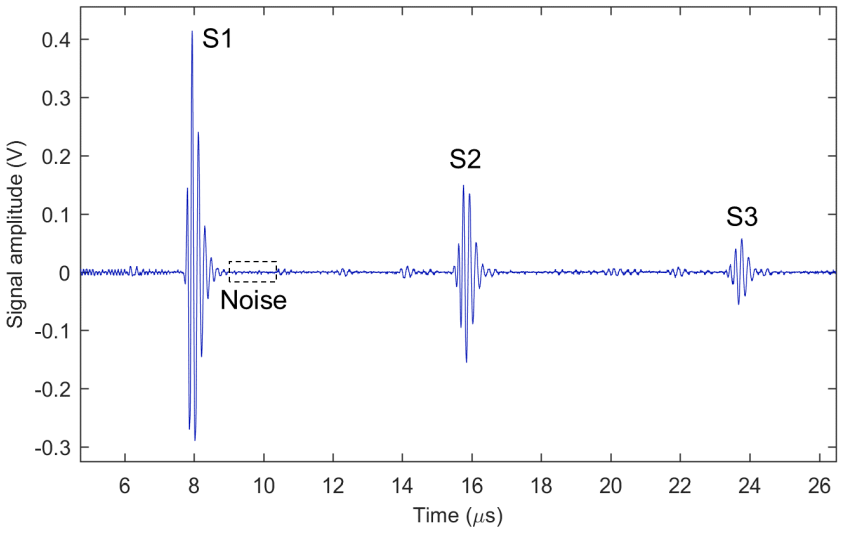

Figure 3.16: Signal amplitude at room temperature for a 12 mm thick magnetite coated mild steel sample, showing the first three backwall echoes (S1, S2 and S3) with a label of the coherent noise region used to calculate the SNR. Small amplitude mode converted signals are detectable between the main backwall echoes.

The peak-to-peak voltage of S1 for aluminium is 31 mV with a SNR of 20.6 dB, which is slightly higher than bare mild steel which has a peak-to-peak voltage of 25 mV with a SNR of 18.3 dB. Despite application of a much lower maximum driving current through the EMAT coil on the magnetite coated mild steel, a much larger peak-to-peak voltage is observed than is seen in both aluminium and bare steel at 705 mV with a SNR of 38.5 dB. These results highlight the significant enhancement of the signal amplitude produced by the magnetostriction mechanism on this type of magnetite coated sample, at least when the oxide is relatively thick and well adhered to the steel beneath.

The theory behind the EMAT magnetostriction mechanism was discussed in detail in sections 1.6 and 2.2.6, but is discussed briefly here in reference to the increased signal amplitude observed when compared to aluminium and bare steel. The operation of EMATs on magnetite coated steel samples can be considered to be similar to piezoelectric transducers. In that generation and detection of ultrasound waves within the sample is achieved via physical coupling of an oscillating element, here in the form of a magnetostrictive magnetite coating that is well adhered to the base steel, which is comparable to an acoustically coupled piezoelectric element used in a piezoelectric transducer. Note, this mechanism is also similar to the way in which magnetostrictive patch transducers operate, as discussed in section 1.9.

As such, the EMAT magnetostriction mechanism with a magnetite coating is significantly different to the Lorentz force, which is the sole operating mechanism on aluminium samples. For the magnetostrictive mechanism on magnetite coated samples, the oscillation of the ions/atoms in the bulk of the sample is generated by the oscillating strains of the coating itself, unlike the Lorentz force mechanism which occurs by transfer of momentum from free conducting electrons in the image current to the ions/atoms of the bulk material, which is known to be relatively inefficient due to the large difference in mass between free electrons and ions/atoms. Therefore, it can be assumed that the large difference observed in the signal amplitude between aluminium and magnetite coated mild steel is due to the increased efficiency of generating the ultrasound by oscillation of magnetostrictive strains in the coating, as a result of the dynamic magnetic field produced by the EMAT coil.

However, the EMAT magnetostrictive mechanism is highly non-linear due to the non-linear relationship between magnetostrictive strain coefficients and the applied biasing magnetic field of the EMAT, as discussed in section 2.2.6. Moreover, the difference between the signal amplitude with and without the coating for a given grade of steel can vary significantly, depending on the physical and chemical properties of the magnetite coating, such as chemical composition, coating thickness,

degree of bonding to the base steel and residual stress. Similarly to piezoelectric transducers, the degree of bonding between the magnetite coating and base steel is critical, when the coating is not well adhered the ultrasound, energy will not couple into the bulk of the sample.

When considering the signal amplitude on the bare mild steel sample, it appears slightly less than that of aluminium largely due to the fact that mild steel has a lower conductivity than aluminium. As such, the Lorentz forces generated at the surface by the image current are lower; this is despite stronger static fields in the steel generated by the permanent magnet, due to the magnetic permeability of steel. As detailed in 2.2.6, there has been some dispute in the literature on the extent to which the EMAT magnetostriction mechanism contributes to the signal amplitude on bare steel, although it was found by Ribichini *et. al* that overall the contribution should be only between 5-10% for bare mild steel [210], where the Lorentz force dominates. It is was also found that when the Lorentz force dominates, small changes in signal amplitude between different materials is a result of differences in conductivity and magnetic permeability.

The vast majority of industrial mild steel pipelines which operate continuously for long periods over 200 °C in a reducing atmosphere tend to develop a thin, well-adhered magnetite surface coating. As this type of coating has been shown to greatly enhance the efficiency of EMAT operation, these types of samples will be exploited to provide sufficient SNR for ultrasound thickness measurements at elevated temperatures, when continuous operation is required without any form of active cooling, as described in detail in chapter 4.

3.5 Summary

This chapter reviews the developmental stages in optimising the EMAT for use at temperatures up to 550 °C without active cooling. First the pulse-echo ultrasound experimental set-up is described (see section 3.1), which was used throughout the work presented in this thesis on the high temperature EMAT, in both chapters 3 and 4. A pulser-receiver system was used such that bulk shear waves were generated in the sample by the EMAT. A variac was attached to the pulser-receiver unit to control the maximum drive current though the coil. This avoids saturation of the amplifier for use on magnetite coated mild steel samples, where the magnetostriction mechanism has the ability to generate ultrasound with significantly larger signal amplitude compared to the Lorentz force mechanism.

Although electromagnets are a viable option for very high temperature applications up to $\approx 750\,^{\circ}\mathrm{C}$, it was estimated that operation up to temperatures of $\approx 550\,^{\circ}\mathrm{C}$ would be sufficient for a significant amount of high temperature pipelines in power generation and petrochemical industries, for which this high temperature EMAT is designed. As such, the high temperature EMAT was constructed with the use of a permanent magnet up to an operating temperature of 550 °C, whilst avoiding the use of bulky electromagnets (see section 3.3.1). Two different grades of this high temperature permanent magnet were compared on aluminium and magnetite coated steel samples at room temperature, each with a different dimension and magnetic flux density values. It was found that the large cylindrical shape magnet, with the lowest measured magnetic flux density performed best on magnetite coated steel, while it performed worst on aluminium. This result highlights the non-linear relationship between the signal amplitude of ultrasound generated from the magnetostriction mechanism with change in the applied magnetic flux density of the biasing magnetic field. The permanent magnet was exposed to 450 °C for a total of 1850 hours, and whilst it did show a slight decrease in the magnetic flux density over this period the results demonstrate the feasibility of application of this magnet grade for use in the high temperature EMAT design.

Following this, the optimisation and ceramic encapsulation of the EMAT coil was discussed in detail (see section 3.3.2). The method of fabricating an EMAT coil capable of withstanding elevated temperatures continuously without cooling was adopted from previous work by Hernandez-Valle [119, 121]. A number of different coil parameters were tested, and the best performing coil was found to be one with constructed with a 0.20 mm diameter wire, 0.20 mm spacing and 20 turns; this is the coil design employed within the final high temperature EMAT design.

Subsequently, the methods used to assemble the final high temperature EMAT design were discussed, including incorporation of the permanent magnet and encapsulated coil within a stainless steel transducer housing and the high temperature coaxial cable. Of key importance was the discussion on the high temperature performance of the electrical connection. Early high temperature trials demonstrated that contact connection was not suitable for continuous application at elevated temperature due to oxidation of the contacting surface. Therefore, brazing was chosen as the method to electrically connect the live and ground wires to the coaxial cable and BNC connector, which was shown to be resistant to the effects of oxidation at high temperatures.

Finally, the performance of the final high temperature EMAT design was tested at room temperature on different materials, namely: aluminium, mild steel and magnetite coated mild steel. It was found that although a much lower driving current was used with the magnetite coated steel to avoid saturation of the amplifier, the signal amplitude was far greater compared to both aluminium and mild steel. This was attributed to the increased efficiency of the magnetostrictive mechanism on magnetite coated steels, whereby the oscillation of the ions/atoms in the sample bulk is generated by the oscillating strains of the coating itself, similar to the method in which piezoelectric transducers and magnetostrictive patch transducer operate. This is different to the Lorentz force mechanism, where ultrasound is generated by transfer of momentum from free conducting electrons in the image current to the ions/atoms of the bulk material, and this is known to be relatively inefficient due to the large difference in mass between free electrons and ions/atoms. As many industrial mild steel pipelines which operate continuously over 200 °C in a reducing atmosphere tend to develop a well-adhered magnetite coating. These types of samples will be exploited to provide sufficient SNR for ultrasound thickness measurements at elevated temperatures; this work is presented in the following chapter.

Chapter 4

High Temperature Performance of EMAT

This chapter details the high temperature testing of the EMAT design presented in chapter 3. Initially, a series of laboratory furnace trials were performed using this EMAT at high temperatures, as described in section 4.1. The performance of the EMAT was evaluated for different magnetite coated mild steel samples (see sections 4.1.1 and 4.1.2), including temperature dependent analyses of the change in signal amplitude, shear wave velocity, shear wave attenuation and frequency content of the signals. The performance of this EMAT design on aluminium was also investigated (see section 4.1.3). The sample-EMAT lift-off performance at elevated temperatures is evaluated in 4.1.4 and initial trial results on the longer-term high temperature performance of the EMAT are given in 4.1.5. This leads onto a discussion of a longer-term field trial on high temperature magnetite coated mild steel pipelines located in a refinery (see section 4.2).

4.1 Laboratory Furnace Trials

Following the development and optimisation of the high temperature EMAT design at room temperature, detailed in chapter 3, the EMAT was subject to a series of high temperature trials in a laboratory environment to investigate performance at elevated temperatures on a number of different samples. These trials were performed using the experimental set-up described in section 3.1, unless otherwise stated.

During these trials, the sample, EMAT and high temperature cable were held at temperature without any form of cooling, except the BNC connector which exited the furnace (ITEMP 14/15, Pyro Therm Furnaces) from a small, thermally

insulated hole in the furnace door. Before each high temperature measurement was taken the sample, EMAT and cable were heated to the required temperature for a dwell time of at least 3 hours. The temperature at the sample surface was recorded using a K-type thermocouple clamped to the sample. On heating, the furnace temperature controller reading was lower than the actual sample surface temperature. The temperature difference was attributed to a thermal gradient established within the furnace, where the lower furnace regions are warmer due to the position of the heating elements. The furnace thermocouple is fixed at the top of the furnace, whereas the sample was placed at the base of the furnace. Table 4.1 shows the furnace and sample surface temperatures recorded for the 6.8 mm step on sample A. The sample and EMAT bulk temperatures were between these values, depending on thermal diffusivity, dwell time and furnace position.

Table 4.1: Furnace temperature and corresponding sample surface temperature.

Furnace Temperature (°C)	Sample Surface Temperature (°C)
25	26
50	55
150	171
250	278
350	378
425	458

Note that for all laboratory trials discussed in this section, the EMATs were constructed using the cubic magnet (HT-PM450) and ceramic encapsulated coils with 0.20 mm wire diameter with 0.20 mm spacing and 20 turns. Also note, when the furnace was set to 425 °C the actual sample surface temperature was measured at 458 °C, which is slightly higher than the maximum operating temperature of the permanent magnet (HT-PM450). For the remainder of the section, the temperatures in the A-scan labels are for the furnace temperature setting, except the temperature when the furnace was set to 425 °C which is quoted as 450 °C. Also, when a parameter (e.g. peak-to-peak voltage or SNR) is plotted against temperature the actual surface temperature values are used.

4.1.1 Performance on Magnetite Coated Mild Steel: Sample A

This section details the high temperature trials using the EMAT on sample A, introduced in section 3.2, which is a section from an industrial mild steel pipe onto which has grown a magnetite coating due to exposure to high temperatures. The inner diameter of the pipe was machined to different thicknesses, the maximum step thickness was 6.8 mm whilst the minimum step thickness was 2.6 mm. The signal amplitude for the first and second backwall echoes (S1 and S2) at range of temperatures from 25 °C to 450 °C on the 6.8 mm step of sample A are shown in Figure 4.1; the corresponding peak-to-peak voltage and SNR of the first echo (S1) against temperature are displayed in Figures 4.2(a) and 4.2(b), respectively, and the values are listed in Table 4.2. The y-axis lower limits in Figures 4.2(a) and 4.2(b) are set not to zero to emphasize the appreciable change in peak-to-peak voltage and SNR between 25 °C and 450 °C, as these differences are substantial considering the increased noise recorded at higher temperatures.

Table 4.2: Peak-to-peak voltage and SNR for first backwall echo (S1) on magnetite coated mild steel (sample A, 6.8 mm thick) for temperatures between 25 °C and 450 °C.

Temperature (°C)	Pk-Pk Voltage (V)	SNR (dB)
25	0.33	34.9
50	0.34	36.3
150	0.51	38.2
250	0.57	36.6
350	0.52	35.9
450	0.41	34.5

The first two backwall echoes are clearly identifiable from room temperature up to 450 °C. It is evident that there is a non-linear change in signal amplitude with increasing temperature, with a maximum signal amplitude at approximately 300 °C. Most importantly for high temperature measurements, there is a greater signal amplitude of 0.41 V at 450 °C compared to 0.33 V at 25 °C. Although, due to the increased levels of noise at the baseline of the signal at elevated temperatures, this equates to a SNR of 34.5 dB at 450 °C, which is slightly lower than the SNR value of 34.9 dB calculated at 26 °C.

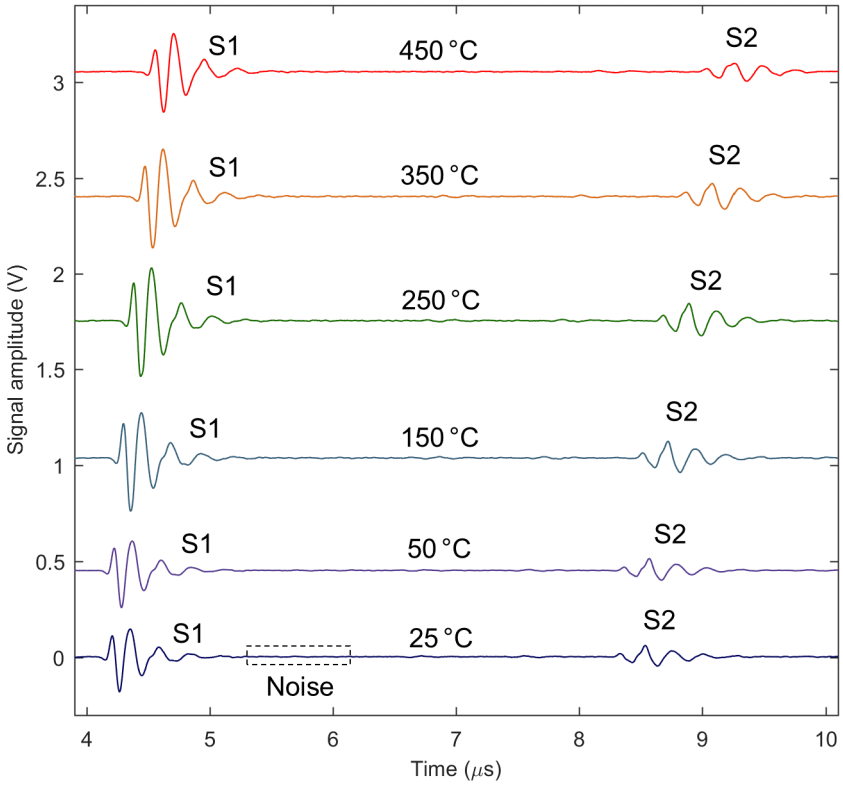

Figure 4.1: Signal amplitude on a magnetite coated mild steel sample (sample A, 6.8 mm thick step) at: (dark blue) 25 °C, (purple) 50 °C, (light blue) 150 °C, (green) 250 °C, (orange) 350 °C and (red) 450 °C, for the first two backwall echoes (S1 and S2) with a label of the coherent noise region used to calculate the SNR.

This non-linear behaviour could be attributed to the dominance of the magnetostrictive mechanism, where magnetostrictive strain coefficients [205] and ultrasound signal amplitude vary non-linearly with change in the applied magnetic field; this relies on the assumption that the field strength of the EMAT magnet decreases with increasing temperature, given that magnetic flux density measurement at elevated temperatures was not measured. This follows from previous research [117] showing the non-linear change in signal amplitude with change in EMAT static magnetic field, for magnetite coated steel pipes, where a maximum signal amplitude was observed at lower magnetic fields of ≈ 0.35 T at room temperature. Further complexity is introduced when considering reports in the literature [221, 222] of a general trend of decrease in magnetostrictive strain coefficients for magnetite with increasing temperatures towards T_C of magnetite at ≈ 570 °C.

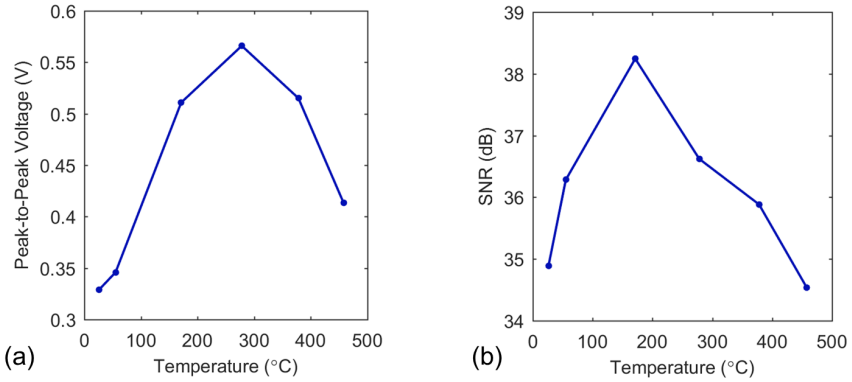

Figure 4.2: First backwall echo (S1) at temperatures between 25 °C and 450 °C on magnetite coated mild steel (sample A, 6.8 mm thick) showing: (a) peak-to-peak voltage and (b) SNR.

Recent literature on modelling and experimental validation of EMAT magnetostrictive behaviour has focused on the magnetostriction contribution on bare steels [210, 223], found to be between 5% and 10% depending on steel grade, where the Lorentz force is dominant. To the best of the authors' knowledge, a comprehensive study of high temperature operation of EMATs on magnetite coated steels, where magnetostriction is the dominant mechanism, has not been reported in the literature. This is most likely due to the complex non-linear nature of the magnetostrictive mechanism on such materials and the number of dependent variables, further complexity is also added at elevated temperatures due to the temperature related effects, such as the temperature dependence of magnetostrictive strains.

The change in shear wave velocity and shear wave signal attenuation with temperature for the 6.8 mm step on sample A are plotted in Figures 4.3(a) and 4.3(b), respectively; the values were calculated in the time domain. A thickness correction for thermal expansion was applied using equation 4.1 [121], where d is sample thickness at temperature T, d_0 is the sample thickness at $T_0 = 25\,^{\circ}\mathrm{C}$ and $\alpha_T(T)$ is the thermal expansion coefficient of steel at temperature T. The time of flight difference, Δt, between the first and second echoes (S1 and S2) was calculated by finding the difference between the time point of maximum signal amplitude of both echoes. The errors originate from determination of the sample thickness and time of flight between successive backwall echoes. The shear wave velocity was calculated from equation 4.2. The shear wave signal attenuation obtained directly from the time domain waveform was calculated using equation 4.3, where A_1 and A_2 represent the maximum signal amplitude of the first and second echoes, respectively, however diffraction effects were neglected.

$$d = d_0[1 + \alpha_T(T)(T - T_0)] \tag{4.1}$$

$$v = \frac{2d}{\Delta t} \tag{4.2}$$

$$\alpha_T = \frac{1}{2d} 20 \log_{10} \left(\frac{A_1}{A_2} \right) \tag{4.3}$$

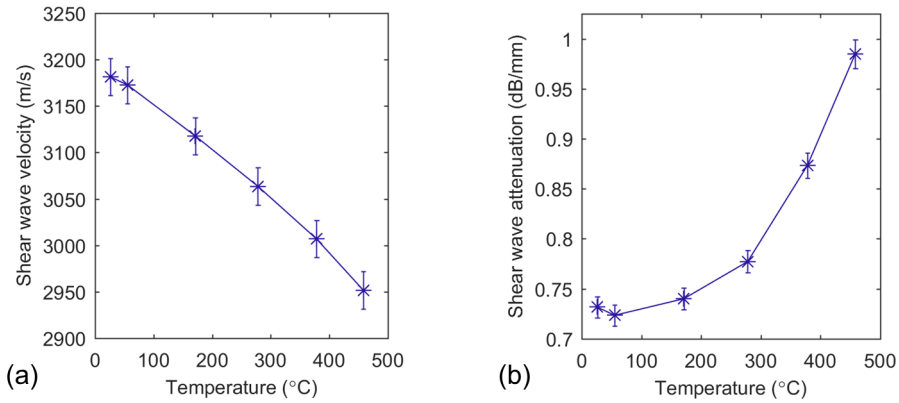

Figure 4.3: At temperatures between 25 °C and 450 °C on 6.8 mm thick sample A: (a) shear wave velocity and (b) shear wave attenuation, including a thickness correction for thermal expansion.

The shear wave velocity displays a steady decrease with increasing temperature, observed from the increase in echo arrival time, corresponding to a change in velocity from 3180 m/s at 25 °C to 2950 m/s at 450 °C; the velocity decrease is primarily as a result of change in the elastic constants with increasing temperature. The shear velocity values calculated are similar to those reported in literature for low carbon steel [146, 192]. The change in velocity with temperature is an important consideration for thickness measurement calibration, as if not taken into account errors will occur during inspection. The shear wave signal attenuation undergoes an increase at elevated temperatures, from 0.73 dB/mm at 25 °C to 0.98 dB/mm at 450 °C. In general, ultrasound attenuation within a sample is the result of a various mechanisms, including absorption, scattering and diffraction effects. Over this temperature range, increased attenuation is attributed to greater scattering from increased thermal phonon-phonon interactions, rather than change in the microstructure [224]. Despite the increase in attenuation, both the first and second echo signal amplitude at 450 °C are adequate for thickness measurements

The frequency content of the signals was examined via a fast Fourier transform (FFT) of a windowed (tapered cosine) section of a backwall echo. The first backwall echo frequency content is shown in Figure 4.4(a) for 25 °C - 450 °C. The first and second back-wall echo frequency content at 450 °C are displayed in Figure 4.4(b). The signal is relatively broadband, with a centre frequency of ≈ 5.5 MHz. A significant reduction in the higher frequency content of the second back-wall echo is observed, likely due to greater attenuation of higher frequencies, which is more distinct with increasing temperature. This is highlighted by the frequency dependent attenuation coefficient, calculated using equation 4.3, where A_1 and A_2 represent the FFT magnitude of the first and second backwall echoes, respectively; these results are displayed in Figure 4.5 at 25 °C, 250 °C, and 450 °C.

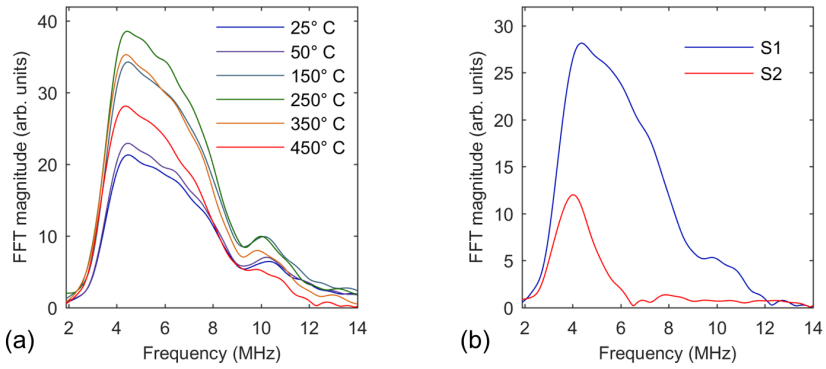

Figure 4.4: FFT magnitude calculated on sample A (6.8 mm thick) for: (a) the first backwall echo (S1) at temperatures between 25 °C to 450 °C, and (b) the first (S1) and second (S2) backwall echoes at 450 °C.

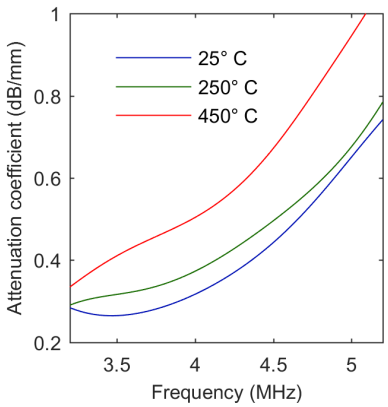

Figure 4.5: Frequency dependent attenuation coefficient calculated for sample A (6.8 mm thick) at 25 °C, 250 °C and 450 °C.

Signal amplitudes on the minimum step of sample A, with a thickness of 2.6 mm, are presented in Figure 4.6 for 25 °C and 450 °C. The initial excitation noise from the driving pulse is included to indicate the loss of the first backwall echo (S1) within the noise, such that the second to fifth backwall echoes (S1 - S5) are displayed. The excitation noise with a dead time of $\approx 2\,\mu$s is longer than usual for this type of spiral EMAT coil, most likely due to the rigid encapsulation of the coil within the ceramic adhesive. For the second backwall echo (S2) the peak-to-peak voltage at 450 °C is 0.56 V with a SNR of 25.9 dB, while at 25 °C a lower peak-to-peak voltage of 0.53 V at SNR 22.1 dB was measured; despite the loss of the first backwall echo, subsequent echoes can be resolved in the time domain and their signal amplitudes are more than adequate for thickness measurements. However, because of dead time issues in the pre-amplifier, radially polarised EMATs are rarely used on samples below 3 mm thick when one needs to observe the first backwall echo.

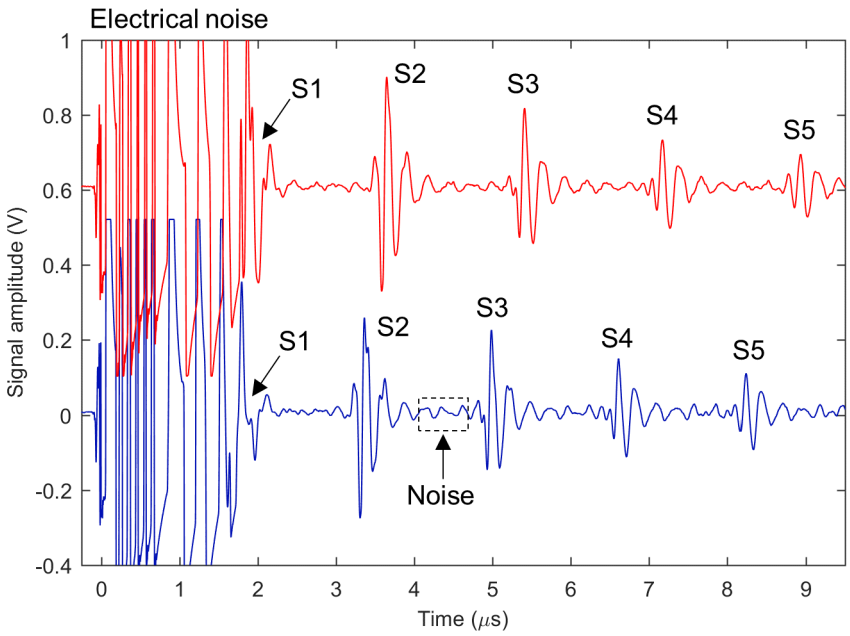

Figure 4.6: Signal amplitude on a magnetite coated mild steel sample (sample A, 2.6 mm thick step) at: (blue) 25 °C and (red) 450 °C, for the second to fifth backwall echoes (S2 and S5) as the first backwall echo (S1) is lost within the electrical noise generated by the driving current, with a label of the coherent noise region (dominated by mode converted signals) used to calculate the SNR.

4.1.2 Performance on Magnetite Coated Mild Steel: Sample B

In order to further highlight the complex nature of the magnetostriction mechanism on magnetite coated mild steels, the high temperature performance of a different magnetite coated sample is included here, namely sample B (6.8 mm thickness), which was introduced in section 3.2. The sample was tested using the experimental set-up described in section 3.1, with a variac setting of 6% to avoid saturation of the amplifier. The signal amplitude for the first and second backwall echoes (S1 and S2) at 25 °C and 450 °C on sample B are shown in Figure 4.7; the corresponding peak-to-peak voltage and SNR of the first echo (S1) against temperature are displayed in Figures 4.8(a) and 4.8(b), respectively. The y-axis lower limits in Figures 4.8(a) and 4.8(b) are set not to zero to emphasize the appreciable change in peak-to-peak voltage and SNR between 25 °C and 450 °C, as these differences are substantial considering the increased noise recorded at higher temperatures.

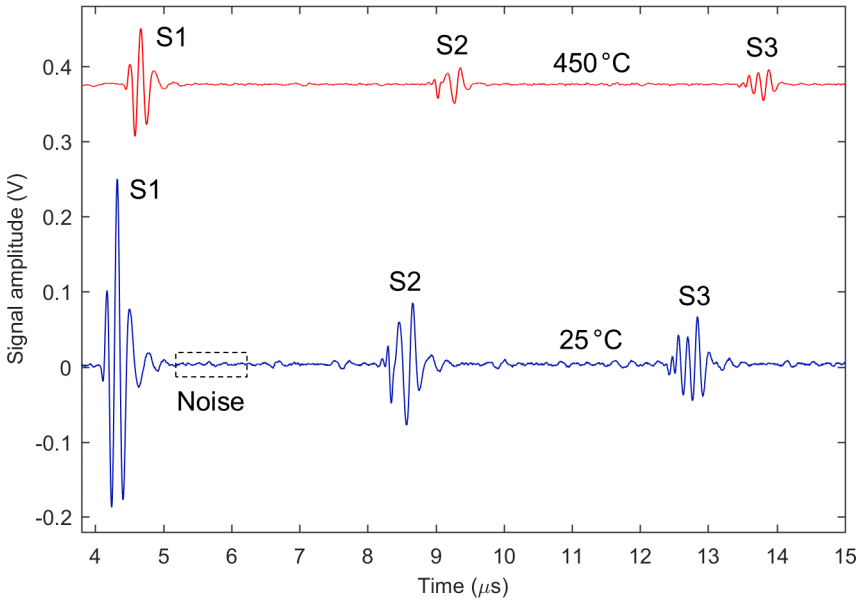

Figure 4.7: Signal amplitude on a magnetite coated mild steel sample (sample B, 6.8 mm thick) at: (blue) 25 °C and (red) 450 °C, for the first two backwall echoes (S1 and S2) with a label of the coherent noise region used to calculate the SNR. Acoustic birefringence [225] can be identified, due to peak splitting of the S2 and S3.

The peak-to-peak voltage at 25 °C was measured as 0.44 V which was significantly larger than that measured for 450 °C at 0.14 V, this corresponded to a SNR at 25 °C of 34.9 dB and at 450 °C of 30.5 dB. Although there is an overall

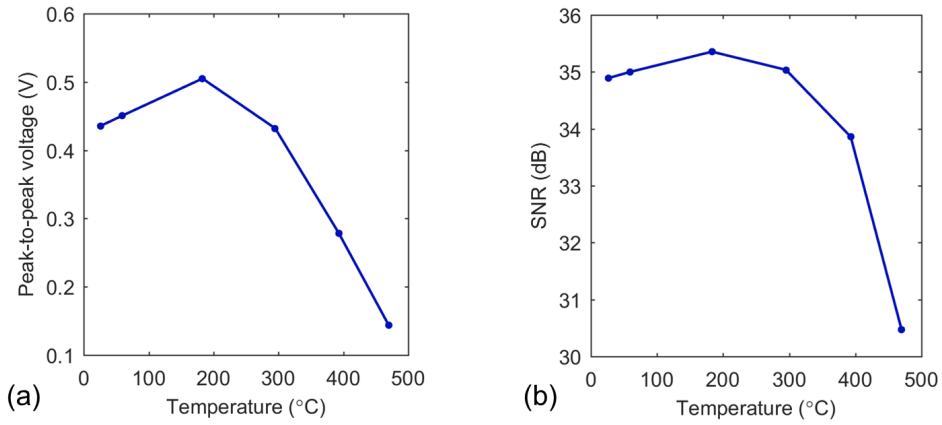

Figure 4.8: First backwall echo (S1) at temperatures between 25 °C and 450 °C on magnetite coated mild steel (sample B, 6.8 mm thick) showing: (a) peak-to-peak voltage and (b) SNR.

decrease in the signal at the same variac setting for sample B between 25 °C and 450 °C, the relationship between both peak-to-peak voltage and SNR is non-linear, as demonstrated in Figure 4.8, where there appears to be a maximum in both the peak-to-peak voltage and SNR at ≈ 200 °C. Although there is clearly a non-linear relationship between signal amplitude and temperature on this magnetite coated steel sample, it appears different to that observed on sample A where there is a significantly greater signal amplitude found at 450 °C compared to 25 °C and the maximum value appears at ≈ 300 °C. This difference could be due to the difference in properties of the magnetite coating between the samples, such as variations in coating thickness, degree of bonding to the base steel and magnetostrictive strain coefficients (e.g. from differences in residual stress). There is a difference in shape of the various backwall signals, where there appears to be elongation when comparing the first (S1) and third (S3) echoes due to peak splitting, and this has been attributed to acoustic birefringence [225]. The origin of acoustic birefringence on this sample is a result of the various metal processing methods used to form the pipe, such as rolling and extruding, which create two polarisation directions in the metal with slightly different velocities. The effects of acoustic birefringence can largely be ignored if the first backwall echo (S1) is used for analysis and thickness measurements.

The difference between the signals observed on sample B is further highlighted when considering the frequency content; the FFT magnitude of the first backwall echo (S1) at 450 °C on sample B is given in Figure 4.9. The signal appears to have a slightly higher centre frequency of ≈ 5.6 MHz, where the maximum FFT

magnitude frequency is clearly higher. Although, there appears to be less signal content at high frequencies for sample B compared to sample A. In general, for application of this EMAT design on magnetite coated samples it is critical that the differences in variation that can be found between samples is recognized.

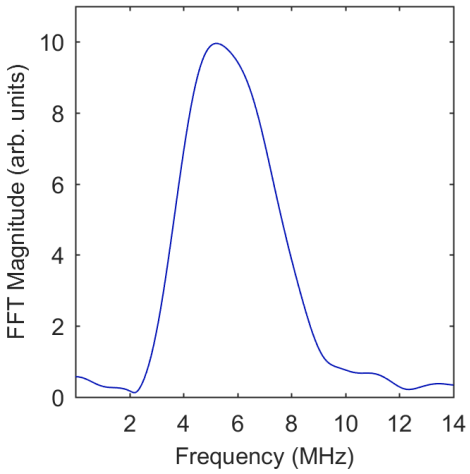

Figure 4.9: FFT magnitude calculated on sample B (6.8 mm thick) for the first backwall echo (S1) at 450 °C.

4.1.3 Performance on Aluminium

The high temperature performance of this EMAT design was evaluated on a 10.0 mm thick aluminium sample to compare results with the magnetite coated steel samples, as the signal in aluminium is solely due to the Lorentz force mechanism. Greatly decreased signal amplitudes were generated on aluminium compared to the magnetite coated samples at high temperature, when using the Sonemat PR5000 pulser-receiver system with the same EMAT drive current. This difference is due to the relatively large signals generated via the magnetostriction mechanism on these magnetite coated steel samples, compared to the Lorenz force mechanism on aluminium, such that a direct comparison with identical hardware and drive current was not possible.

To produce the most suitable signal on aluminium, an alternative pulser-receiver system was used. A conventional flaw detector (Masterscan D-70, Sonatest) was used as the pulser-receiver with a drive voltage of 450 V and 100 ns pulse width, along with an EMAT averaging adapter (GS2020, Sonemat), which gave increased SNR performance via a 128 running average and automatic gain control (AGC). This set-up produced a maximum driving current pulse amplitude of 12 A. The

data was recorded using a digital oscilloscope. The A-scans for the first and second backwall echoes (S1 and S2) across a range of temperatures from 25 °C to 450 °C on the 10.0 mm aluminium sample are shown in Figure 4.10; the corresponding peak-to-peak voltage and SNR of the first backwall echo against temperature on aluminium are displayed in Figures 4.11(a) and 4.11(b), respectively.

The first backwall echoes in aluminium are distinguishable from room temperature up to 350 °C, whereas the first backwall echo at 450 °C is not clearly defined. The results show a steady decrease in signal amplitude with increasing temperature in aluminium, with a peak-to-peak voltage of 0.23 V with a SNR of 17.3 dB at 25 °C and 0.11 V with a SNR of 10.5 dB at 350 °C. The AGC may have changed the peak-to-peak voltage amplitudes differently with increasing temperature, the value of gain used by the AGC is not known; this may affect the direct comparison between the A-scans at different temperatures, however, it could be assumed for the case with aluminium that as the signals are all relatively low, the gain was set to a maximum value for at all temperatures.

As the Lorentz force is the sole generation and detection mechanism when EMATs operate on aluminium, we can contribute a proportion of the loss in signal amplitude at elevated temperatures to a decrease in the Lorentz force, in addition to increased ultrasound attenuation. In pulse-echo mode, the Lorentz force is proportional to the square of magnetic field, which is dominated by the static magnetic field at the coil driving currents used in this study. Hence, the Lorentz force most likely decreases from a reduction in the EMAT magnet field strength at elevated temperatures. Therefore, it can be estimated that the non-linear change in signal amplitude with increasing temperature observed on magnetite coated steel samples is due to the dominance of the magnetostriction mechanism.

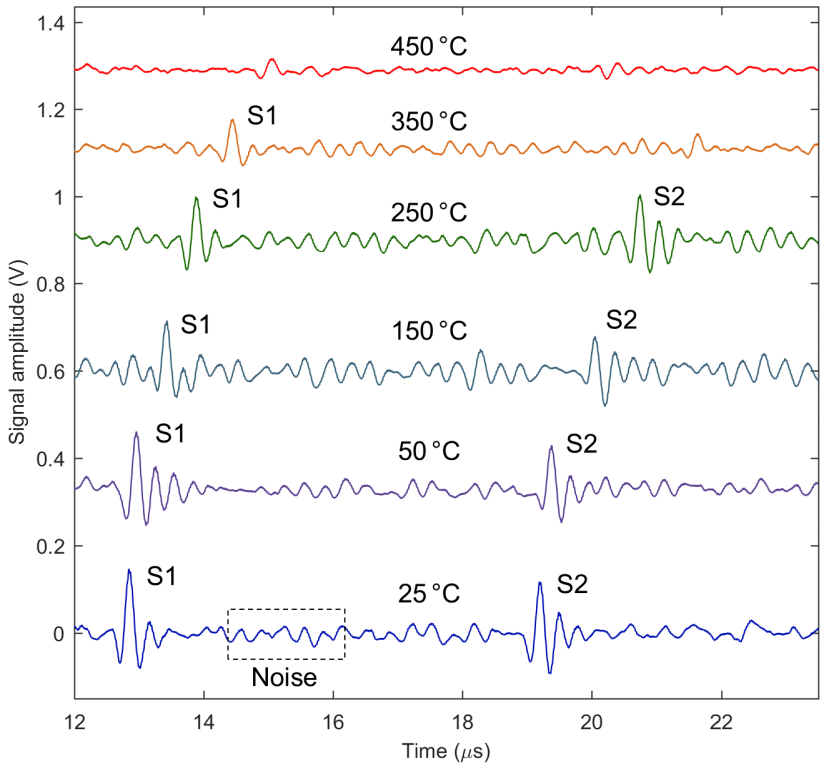

Figure 4.10: Signal amplitude on 10.0 mm thick aluminium sample at: (dark blue) 25 °C, (purple) 50 °C, (light blue) 150 °C, (green) 250 °C, (orange) 350 °C and (red) 450 °C, for the first two backwall echoes (S1 and S2) with a label of the coherent noise region used to calculate the SNR.

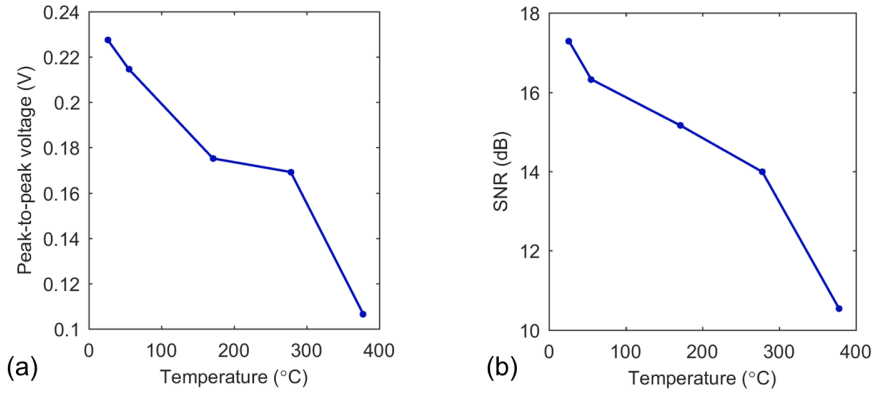

Figure 4.11: First backwall echo (S1) at temperatures between 25 °C and 450 °C on aluminium (10.0 mm thick) showing: (a) peak-to-peak voltage and (b) SNR.

4.1.4 Lift-Off Performance

One of the advantages of using EMATs at high temperature compared with piezoelectric transducers is their non-contact nature, such that a degree of lift-off between the sample and EMAT can be maintained due to electromagnetic coupling of ultrasound, and this can be useful in scanning applications. However, typically the lift-off tolerance of EMATs is relatively small, often on the order of less than 1.0 mm, depending on the configuration of the EMAT and the properties of the sample, and the signal amplitude decays exponentially with increasing lift-off. Despite this, initial lift-off tests at room temperature using this EMAT design on magnetite coated steel samples demonstrated that relatively large lift-off values could be tolerated whilst still providing good SNR. Therefore, a series of trials were carried out to evaluate the high temperature lift-off performance of this EMAT design on magnetite coated steel samples.

Using the experimental set-up detailed in 3.1, lift-off measurements were made at 450 °C on sample B (6.8 mm thickness), with the variac set at 100%. The sample-EMAT lift-off was maintained by positioning of a stack of alumina ceramic discs (0.5 mm thickness) for lift-off values of zero to 10.0 mm in increments of 1.0 mm. The first three backwall echoes (S1, S2 and S3) are shown for 4.0 mm,6.0 mm and 8.0 mm lift-off in Figure 4.12, whilst the peak-to-peak voltage against lift-off for S1 at each lift-off value tested is provided in Figure 4.13.

The exponential decay in signal amplitude with increasing lift-off is clear from these results. However, it is evident that relatively large signals are measured even at lift-off values generally considered large for EMATs, especially considering the effect of decreasing signal amplitude on sample B at 450 °C. For comparison, the peak-to-peak voltage at zero lift-off was 0.92 V compared to 0.0069 V (6.9 mV) at 10.0 mm. The SNR were calculated as 27.1 dB, 21.9 dB and 14.7 dB for 4.0 mm, 6.0 mm and 8.0 mm, respectively. Despite the decrease in signal amplitude at increasing lift-off values, these signals are adequate for thickness measurements at 450 °C at all the lift-off values tested. This demonstrates the applicability of this EMAT for high temperature scanning inspections of magnetite coated mild steel pipelines without plant shutdown.

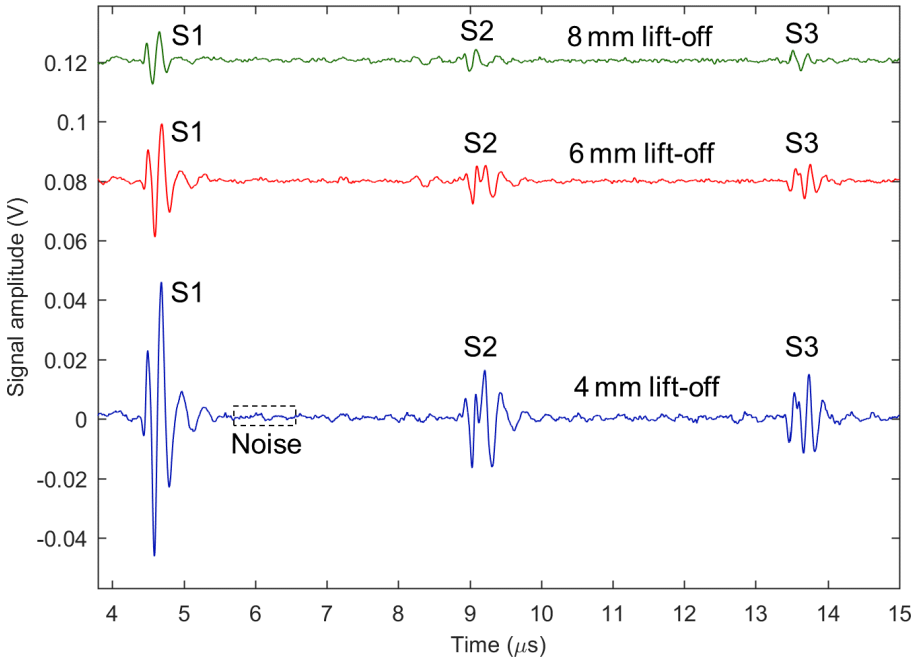

Figure 4.12: Signal amplitude on sample B (6.8 mm thickness) at 450 °C with different sample-EMAT lift-off values: (blue) 4.0 mm, (red) 6.0 mm and (green) 8.0 mm, for the first three backwall echoes (S1, S2 and S3) with a label of the coherent noise region used to calculate the SNR.

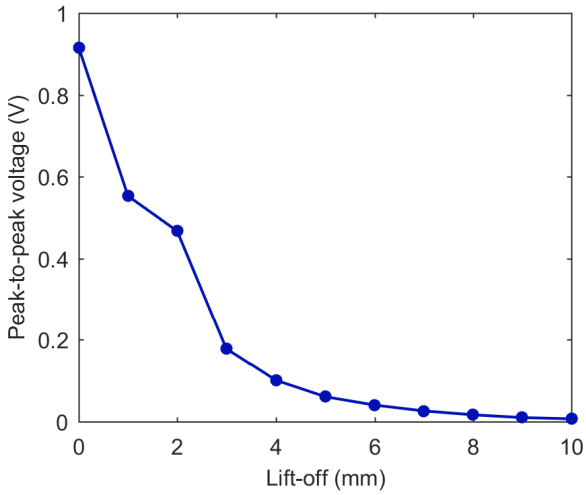

Figure 4.13: Peak-to-peak voltage of the first backwall echo (S1) against sample-EMAT lift-off measured on sample B (6.8 mm thickness) at 450 °C.

4.1.5 Long-Term Performance

A preliminary trial was carried out to study the longer-term performance of this EMAT design at elevated temperatures, wherein the EMAT was held in a furnace for 1 month, using the setup described in section 3.1. A measurement was recorded on a magnetite coated mild steel sample (sample C, 12.0 mm) at 450 °C before and after 1 month of continuous exposure of the EMAT to 450 °C, where the variac was set to 2% to avoid saturation of the amplifier. The A-scans recorded are shown in Figure 4.14 for the first three backwall echoes (S1, S2 and S3). The sample was not heated during this time to minimize changes to the magnetite coating thickness, as long-term exposure to 450 °C may cause magnetite coating growth; this had the potential to cause signal variation not attributed to changes in EMAT performance.

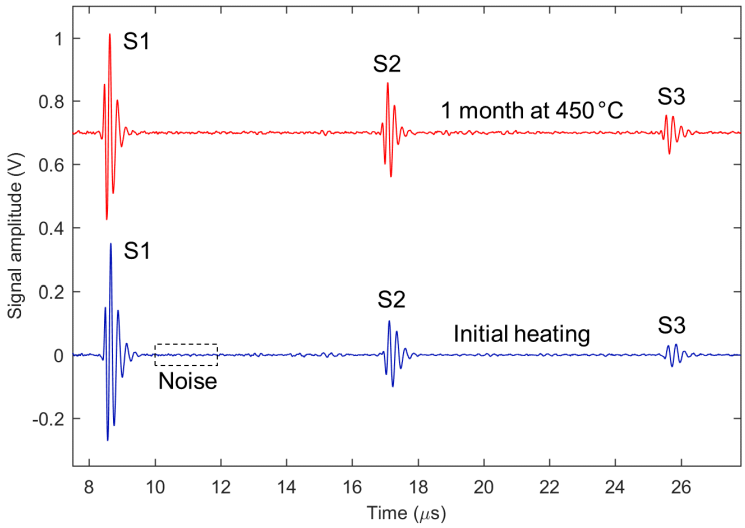

Figure 4.14: Signal amplitude at 450 °C on sample C (12.0 mm thickness) for: (blue) EMAT on initial heating and (red) EMAT after 1 month of continuous exposure to 450 °C, showing the first three backwall echoes (S1, S2 and S3) with a label of the coherent noise region used to calculate the SNR.

For S1 the measured peak-to-peak voltage was 0.59 V on initial heating with a SNR of 33.0 dB, compared to 0.59 V and a slighter lower SNR of 32.9 dB after heating. Effort was made to place the EMAT on the same sample position for measurements before and after heating, however, the positioning may not have been identical; this could have led to a difference in the signal amplitude, due to difference in properties of the magnetite coating. No significant loss in performance was observed, indicating the potential application of this high temperature EMAT design for continuous inspection at elevated temperatures.

4.2 Industrial Field Trial: Pembroke Refinery

Following the success of laboratory furnace trials using the high temperature EMAT on magnetite coated samples, longer term industrial field trials were necessary to evaluate the performance of the EMAT in a real engineering environment over a longer period. This includes investigating effects from temperature fluctuations and thermal cycling, but also was an opportunity to access the performance of the EMAT on different industrial samples, where the magnetite coating may vary (e.g. in thickness and degree of bonding to the base steel), which would have a large impact on the amplitude of the signal produced by the magnetostriction mechanism. In collaboration with Sonomatic Ltd. [226] and Valero Energy [227] an industrial field trial at Pembroke refinery was implemented.

For the field trial, two magnetite coated steel pipes were identified, such that two high temperature EMATs were fabricated and tested in the laboratory prior to the trial. The EMATs were constructed with magnets from the same batch as the small cylindrical HT-PM550, with ceramic encapsulated coils (0.20 mm wire diameter, 0.20 mm spacing and 20 turns) and the live and ground wire connections were brazed; the fabrication details are discussed in detail in section 3.3.3. The EMATs were heated to 450 °C in the laboratory and their performance was recorded after a 3 hours dwell, with a view to comparing the performance after the trial under near identical conditions; these tests were carried out on magnetite coated mild steel sample B (6.8 mm thickness) with the variac set at 20%. The recorded waveforms are presented in Figure 4.15, and the EMATs have been labelled as EMAT-North and EMAT-South, corresponding to the location of the inspections.

For the first backwall echo (S1) with the EMAT-North the peak-to-peak voltage was measured at 0.59 V with a SNR of 32.8 dB, whilst the EMAT-South peak-to-peak voltage was 0.46 V with a SNR of 30.4 dB. There is a relatively significant difference between the signal amplitudes and SNRs of the two EMATs, the result of which is difficult to determine. This may be a result of variation in stand-off between the coil and sample between the two EMATs, due to the precise location of the coil within the transducer housing. However, this may be a result of differences between the encapsulated coils, for example some coil turns may have short-circuited if the ceramic adhesive failed to set correctly, although this is not likely. This could also be due to variations in the magnetic flux density provided by the magnet, especially considering high temperature related effects. Or, this may be due to slight variations of the positioning of the EMAT on sample B, due to variations in the magnetite coating properties across the surface of the sample.

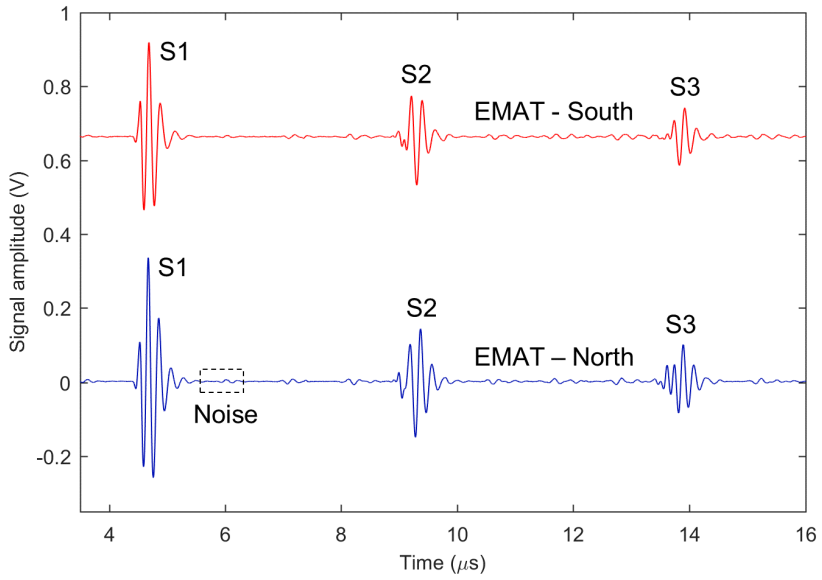

Figure 4.15: Signal amplitude on 6.8 mm thick magnetite coated mild steel sample (sample B) at 450 °C for EMATs used in field trial: (blue) EMAT-North and (red) EMAT-South, for the first three backwall echoes (S1, S2 and S3) with a label of the coherent noise region used to calculate the SNR.

To eliminate issues of variation in signal amplitude due to the magnetostriction mechanism on magnetite coated samples, the EMATs were compared on the 10.0 mm thick aluminium sample both before and after heating at room temperature, with the variac set to 100%; the results after heating are presented in Figure 4.16. The peak-to-peak voltage on aluminium for EMAT-North was 69 mV compared to 59 mV for EMAT-South, although due to difference in noise levels just after the first backwall echo (S1), there was only a slight difference in SNR with 28.4 dB for the EMAT-North and 28.3 dB for the EMAT-South. These results confirm there is a difference in performance between these two EMATs, and the variation in performance between the construction of this high temperature EMAT design needs to be further investigated.

The pipes used for this long-term field trial are pictured in Figure 4.17 along with the permanently installed high temperature EMATs. Although the EMAT was magnetically attached to the mild steel pipes, they were secured with jubilee clips to avoid any violations of health and safety procedures. Note that the BNC connectors were pointed away from the pipes to facilitated ambient air cooling, such that a temperature distribution was establish along the cable and the polymer components within the connector at the end of the cable were not destroyed.

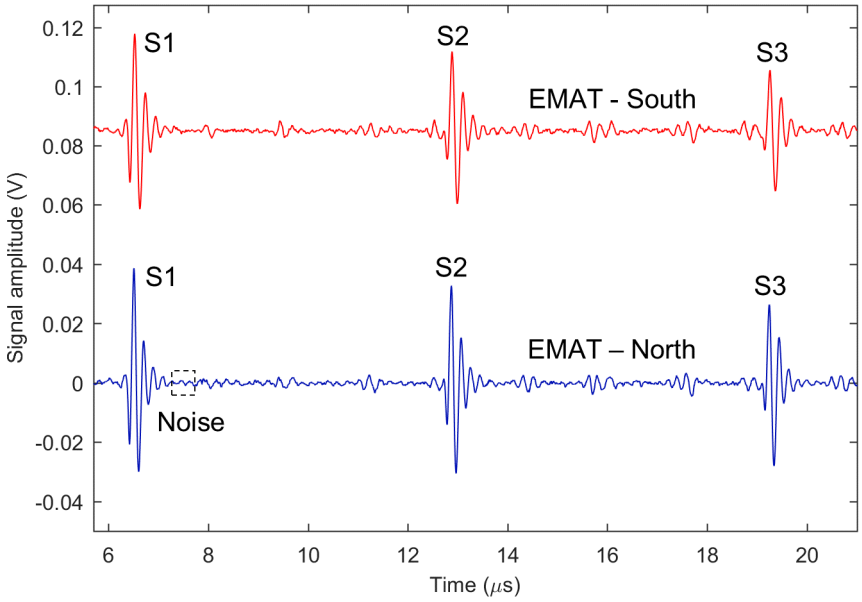

Figure 4.16: Signal amplitude on 10.0 mm thick aluminium sample at room temperature for EMATs used in field trial: (blue) EMAT-North and (red) EMAT-South, for the first three backwall echoes (S1, S2 and S3) with a label of the coherent noise region used to calculate the SNR.

Figure 4.17: Images of the EMAT pipe inspection locations for the field trial: (a) EMAT-North and (b) EMAT-South.

These pipe locations were chosen as these no pipe insulation was present. The EMATs were positioned adjacent to circumferential welds in the pipe. Limited information was provided about the pipe material and dimension (e.g. thickness) specifications. However, the pipes were mild steel and had developed a layer of magnetite (black) underneath the haematite (orange-brown), on which EMATs operate efficiently via the magnetostriction mechanism. The temperatures at the pipe outer surfaces were measured as 356 °C for the North location and 357 °C for the South location; it was expected that the temperature would not fluctuate higher than this. As such, the pipe temperature for both locations is referred to as $\approx 355\,^{\circ}\mathrm{C}$.

In order to record the high temperature performance of the EMAT on-site without a mains power supply, an alternative experimental set-up to that described in section 3.1 was adopted, which employed measurement and pulser-receiver systems that were able to operate on batteries. The ultrasound thickness measurement principle remained identical, in that a pulse-echo measurement was performed using the EMAT to generate shear waves which would reverberate within the pipe reflecting from the backwall. The battery-operated set-up involved the use of a conventional flaw detector (USM GO, General Electric) designed for use with piezoelectric transducers, which acts as both the pulser-receiver unit and a digital display of the waveform. Conventional flaw detectors, such as the one used here, typically do not have an averaging system, which is often required with EMATs to maximise the signal due to their relative inefficiency compared to piezoelectric transducers.

As such, an EMAT averaging adapter (GS2020, Sonemat Ltd.) was used, which provided increased signal amplitude via a 128 running average and automatic gain control (AGC). This set-up is similar to the one used for high temperature measurement on aluminium (see section 4.1.3), where the flaw detector provides the driving current to the EMAT and the averaging adapter computes averaging of the signal, which is then shown on the flaw detector display. The flaw detector used allowed the displayed waveform to be saved as an image file. As a digital oscilloscope could not be used (mains power supped required), additional units were added to the system to record the waveform in a text file for re-plotting. A high-precision PC-based oscilloscope (2207A, Pico Technologies, "picoscope"), was used alongside a LabVIEW programme on a laptop to record the waveform in a text file.

The rectified waveform presented in Figure 4.18 was recorded using the flaw detector (settings: high, broadband and 28.0 dB gain) with the EMAT-South after a period of 4 months at $\approx 355\,^{\circ}\mathrm{C}$, with gates over the first (green) and second (blue) backwall echoes. The A-scans recorded using the picoscope and laptop set-up for both the EMAT-North and EMAT-South are given in Figure 4.19.

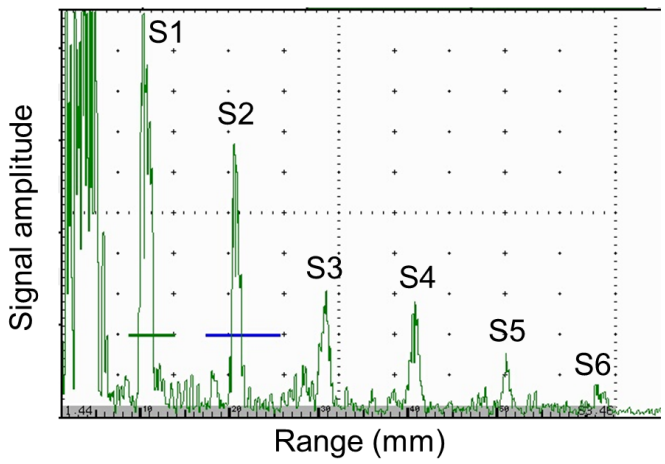

Figure 4.18: Waveform image recorded using a flaw detector and averaging adaptor for the EMAT-South location for field trial on an oil refinery magnetite coated steel pipe after 4 months at ≈ 355 °C, showing the first six backwall echoes (S1 - S6).

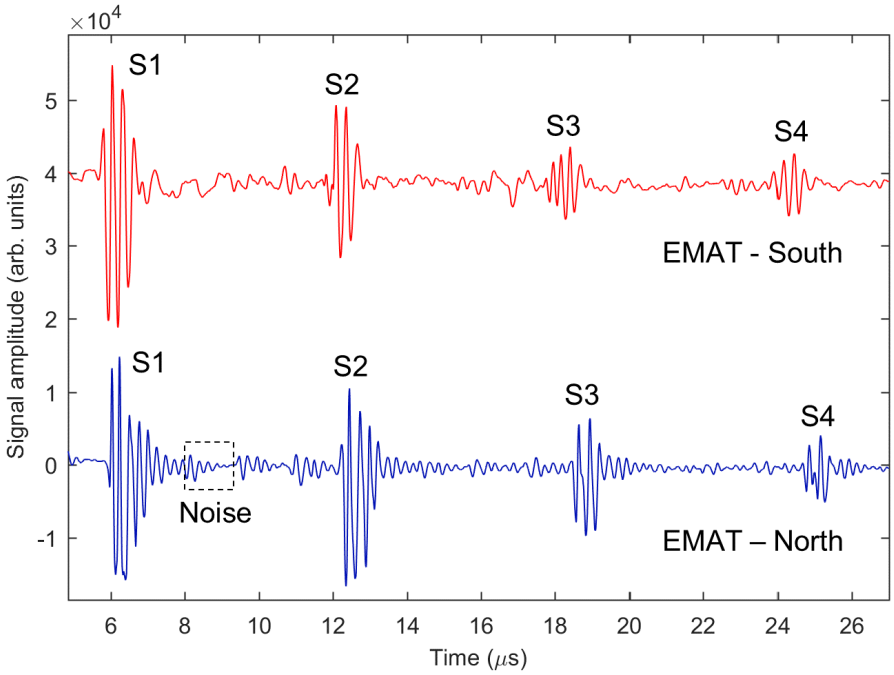

Figure 4.19: Signal amplitude after 4 months at ≈ 355 °C: (blue) EMAT-North and (red) EMAT-South, for the first three backwall echoes (S1, S2 and S3), with a label of the coherent noise region used to calculate the SNR.

After 4 months at $\approx 355\,^{\circ}\mathrm{C}$ the peak-to-peak signal amplitude and corresponding SNR of the first backwall echo (S1) for the EMAT-North was calculated at 3.05×10^4 (arb. units) and 16.8 dB, respectively, whilst the EMAT-South was found to be 3.60×10^4 (arb. units) and 20.2 dB, respectively. It is clear therefore, that the EMAT-South has a larger amplitude first backwall echo compared to the EMAT-North probe, however they are operating on different pipes, on which the magnetite coating is likely to have slightly varying properties, which could be where the difference in signal originates. Although, it is important to note that the signal amplitude of the second (S2) and third (S3) backwall echoes for the EMAT-North have larger amplitudes than those for the EMAT-South. Despite the slight differences in signal amplitude between the two EMATs, it is promising that the EMATs continue to perform well in a real engineering setting on magnetite coated steel after 4 months of continuous exposure to $\approx 355\,^{\circ}\mathrm{C}$ without active cooling.

It was expected that the EMATs would be removed from the refinery inspection and subject to laboratory furnace testing for comparative studies to investigate the high temperature performance of the EMAT under controlled conditions after the planned 6-month trial. Unfortunately, due to an unanticipated shutdown of the plant on which the EMATs were installed after approximately 5 months, one EMAT was lost and the other was damaged; this was due to a miscommunication between different teams working at the refinery. The damaged EMAT was intact except for the encapsulated coil, which was missing in its entirety, and it is not clear exactly how this occurred.

Fortunately, the permanent magnet was still in place, and the magnetic flux density was measured using a gaussmeter and compared to the recorded magnetic flux density before fabrication of the EMAT, effectively providing an estimation of the longer-term high temperature performance of the permanent magnet. The average magnetic flux density at a central location on the face of the magnet closest to the coil was measured to 4 significant figures to highlight the very slight difference, with a value of 0.3394 T before fabrication and a value of 0.3393 T after the field trial; although, the measurement was not this accurate, where 2 significant figures is more appropriate. Due to the error from the variation due to exact probe placement and constant small changes in the displayed value by the gaussmeter in the magnetic flux density measurement, it can be assumed that there has been no significant, if any, alteration to magnetic flux density of the permanent magnet (HT-PM550) due to 5 months continuous exposure of the EMAT to $\approx 355\,^{\circ}\mathrm{C}$. The electrical connection via the various brazed joints were also tested using a multimeter (72-7770, Tenma) and shown to maintain operation, along with the BNC connector.

4.3 Summary

This chapter provides a detailed account of the high temperature testing carried out using the EMAT design presented in this work. First, the high temperature performance on a magnetite coated mild steel sample (sample A) was reviewed in length (see section 4.1.1) for a temperature range of 25 °C to 450 °C. This work highlighted the non-linear relationship between signal amplitude and temperature when the magnetostriction mechanism is dominant on magnetite coated samples; greater signal amplitudes were measured at 450 °C compared to 25 °C, which was attributed to the non-linear relationship between magnetostrictive strain coefficients and the applied magnetic field of the biasing EMAT. The shear wave velocity and attenuation were reviewed for magnetite coated mild steel, and the values were comparable to those presented in the literature, where the velocity observes a steady decrease and the attenuation increases significantly at elevated temperatures.

The high temperature performance of the EMAT on a different magnetite coated steel sample (sample B) was also studied (see section 4.1.2), and it was shown that the signal amplitude also varied non-linearly with increasing temperature, although it exhibited a slightly different relationship than the previous sample; this work emphasised the difference in signal amplitude observed between different magnetite coated samples, which is likely due to varying properties of the magnetite coating (e.g. composition, degree of bonding and thickness).

Additionally, the high temperature performance of the EMAT on aluminium was tested, where the Lorentz force mechanism was the sole ultrasound generation and detection mechanism. Signals were obtained up to 350 °C, although with a much lower amplitude compared to the magnetite coated samples; these results emphasised the importance of the presence of magnetite coatings to improve the SNR of the EMAT at elevated temperatures.

Following this, a series of trials with varying degrees of sample-EMAT lift-off were performed on magnetite coated samples. The results confirmed that the EMAT signal amplitude decreases exponentially with increasing lift-off, however, even at relatively large lift-offs for EMATs, good SNR values were obtained due to the increase in signal gained on magnetite coated samples via the magnetostrictive mechanism. This work demonstrates the applicability of this EMAT design for high temperature scanning inspections.

The results from a preliminary long-term high temperature trial in the laboratory furnace validated the application of this EMAT for continuous monitoring applications, where over the course of 1 month no significant loss of signal was ob-

served on exposure to 450 °C. Subsequently, an industrial field trial of this EMAT design was carried out on high temperature magnetite coated mild steel pipeline in a refinery, where the EMATs were permanently installed to the pipelines which had a surface temperature of ≈ 355 °C. The EMATs maintained good performance after 4 months of continuous operation, confirming the suitability of this EMAT design for high temperature ultrasound thickness continuous monitoring applications.

Chapter 5

High Temperature EMAT: Conclusions

This chapter aims to provide a concise summary of the work presented in chapters 3 and 4. The main findings of the development and optimisation of the high temperature EMAT are presented in section 5.1, and the findings from a series of high temperature laboratory and industrial field trials using the EMAT are discussed in section 5.2. Finally, the various directions for future work on this project to improve the EMAT further and increase the technology readiness level (TRL) towards full commercialisation of this novel high temperature design by Sonemat Ltd. is reviewed in section 5.3.

5.1 Development of High Temperature EMAT

The objective of this EMAT project was to improve upon current commercially available high temperature EMATs for use at elevated temperatures, especially towards application in ultrasound thickness monitoring for continuous monitoring without the requirement of active cooling. It was established early on in the research that reaching temperatures of $\approx 550\,^{\circ}\mathrm{C}$ would be sufficient for a significant amount of high temperature pipelines in power generation and petrochemical industries, for which this high temperature EMAT was designed; this upper temperature limit formed the basis of the maximum operating temperature requirements to which the EMAT was specified in the initial design stages. The critical components of the bulk shear wave EMAT used in this work are the magnet, used to provide the static biasing magnetic field, and the coil, used to provide the dynamic magnetic field; therefore, these were the components which had to be altered compared to typical

room temperature EMATs to withstand continuous application at temperatures up to 550 °C. Additionally, as a large majority of industrial mild steel pipelines which operate continuously for long periods over 200 °C in a reducing atmosphere tend to develop a thin, well-adhered oxide surface coating (magnetite), which has been shown to greatly enhance EMAT efficiency, it was proposed that this high temperature EMAT could be designed to operate on these types of samples.

For the work presented in both chapters 3 and 4 a pulser-receiver system was used such that bulk shear waves were generated in the sample by the EMAT. A variac was attached to the pulser-receiver to control the maximum drive current though the coil to avoid saturation of the amplifier for use on magnetite coated mild steel samples, where the magnetostriction mechanism has the ability to generate ultrasound with significantly larger signal amplitude compared to the Lorentz force mechanism.

As it was estimated that operation up to temperatures of $\approx 550\,^{\circ}\mathrm{C}$ would be sufficient, the EMAT was constructed with a permanent magnet to avoid the use of bulky electromagnets. A high temperature permanent magnet (HT-PM) was selected due to its excellent magnetic properties at a maximum operating temperature of up to 550 °C. Two different grades of this high temperature permanent magnet (HT-PM450 and HT-PM550) were compared on aluminium and magnetite coated mild steel samples at room temperature, each with a different dimension and magnetic flux density values. It was found that the large cylindrical shape magnet, with the lowest measured magnetic flux density (0.25 T) performed best on magnetite coated steel, while it performed worst on aluminium. This result demonstrated the non-linear relationship between the signal amplitude of ultrasound generated from the magnetostriction mechanism with change in the applied magnetic flux density of the biasing magnetic field. The permanent magnet was exposed to 450 °C for a total of 1850 hours, and whilst a slight decrease in the magnetic flux density over this period was detected, it demonstrated the feasibility of application of this permanent magnet material for use in the high temperature EMAT.

For the EMAT coil, the optimisation and ceramic encapsulation of the EMAT coil was discussed in detail. The method of fabricating an EMAT coil capable of withstanding elevated temperatures continuously without cooling was adopted from previous work by Hernandez-Valle, by means of a hand wound bare copper coil with a fixed spacing such that ceramic adhesive was used to provide high temperature electrical insulation. Various coil parameters were tested, and the best performing coil was one constructed with a 0.20 mm diameter wire, with a 0.20 mm spacing and 20 turns; this was the coil design employed for the high temperature trials.

The methods used to assemble the final high temperature EMAT design were discussed, including incorporation of the permanent magnet and encapsulated coil within a stainless steel transducer housing and fabrication of a high temperature coaxial cable. Of key importance was the performance of the electrical connection at high temperature. Early trials demonstrated that a contact connection was not suitable for continuous application at elevated temperature due to oxidation of the contacting surface. Therefore, brazing was chosen as the method to electrically connect the live and ground wires to the coaxial cable and BNC connector, which was shown to be resistant to the effects of oxidation at high temperatures.

The performance of the final high temperature EMAT design was tested at room temperature on different materials, namely: aluminium, mild steel and magnetite coated mild steel. It was found that although a much lower driving current was used with the magnetite coated steel to avoid saturation of the amplifier, the signal amplitude was far greater compared to both aluminium and mild steel. This was attributed to the increased efficiency of the magnetostrictive mechanism on magnetite coated steels, whereby the oscillation of the ions/atoms in the sample bulk is generated by the oscillating strains of the coating itself, similar to the method in which piezoelectric transducers and magnetostrictive patch transducer operate.

5.2 Study of High Temperature EMAT Performance

Once the initial high temperature EMAT design was optimised at room temperature it was subject to intensive testing at elevated temperatures to investigate its high temperature performance, ultimately to demonstrate the feasibility of this EMAT design towards commercialisation for application in continuous thickness monitoring applications.

The high temperature performance on magnetite coated mild steel samples (samples A and B) were reviewed in length for a temperature range of 25 °C to 450 °C. This work highlighted the non-linear relationship between signal amplitude and temperature when the magnetostriction mechanism is dominant on magnetite coated samples; greater signal amplitudes were measured at 450 °C compared to 25 °C on sample A, which was attributed to the non-linear relationship between magnetostrictive strain coefficients and the applied magnetic field of the biasing EMAT. The shear wave velocity and attenuation were reviewed for magnetite coated mild steel, and the values were comparable to those presented in the literature, where the velocity observes a steady decrease and the attenuation increases significantly at elevated temperatures. It was found that the signal amplitude also varied in a non-

linearly with increasing temperature from sample B, however, it exhibited a slightly different relationship than sample A. This comparison emphasised the difference in signal amplitude observed between different magnetite coated samples, which is likely due to varying properties of the magnetite coating, such as composition, degree of bonding and thickness. Additionally, the high temperature performance of the EMAT on aluminium was tested, where the Lorentz force mechanism was the sole ultrasound generation and detection mechanism. Signals were obtained up to 350 °C, although with a much lower amplitude compared to the magnetite coated samples; these results emphasised the importance of the presence of magnetite coatings to improve the SNR of the EMAT at elevated temperatures.

A series of high temperature trials with varying degrees of sample-EMAT lift-off were performed on magnetite coated samples at 450 °C. The results confirmed that the EMAT signal amplitude decreases exponentially with increasing lift-off, however, even at relatively large lift-offs for EMATs, good SNR values were obtained due to the increase in signal gained on magnetite coated samples via the magnetostrictive mechanism; for example, on sample B at 8.0 mm lift-off the first backwall echo observed a SNR of 14.7 dB. This work demonstrated the applicability of this EMAT design for scanning inspections at elevated temperatures, where a distance between the sample and EMAT may be required to ensure smooth scanning and lift-off effects from slight variations along the sample surface can be ignored.

The results from a preliminary long-term high temperature trial in the laboratory furnace validated the application of this EMAT for continuous monitoring applications, where over the course of 1 month no significant loss of signal was observed on exposure to 450 °C. Subsequently, an industrial field of this EMAT design was carried out on high temperature magnetite coated mild steel pipeline in an oil refinery (Pembroke, Valero Energy), where the EMATs were permanently installed to the pipelines, which had a surface temperature of $\approx$ 355 °C. The EMATs maintained good performance after 4 months of continuous operation, confirming the suitability of this EMAT design for high temperature ultrasound thickness continuous monitoring applications.

5.3 Further Work

The research presented in this thesis on the high temperature EMAT design has demonstrated the definite potential for application in an industrial setting for ultrasound thickness by means of portable inspections or continuous monitoring at temperatures up to $\approx 500\,^{\circ}\mathrm{C}$. However, the work has highlighted areas for further research which may improve the long-term high temperature performance and provide further insight into the variability of signal amplitude on magnetite coated mild steel samples, specifically with regard to how this may impact signals observed on different pipelines in industry.

In the short-term, of key importance is improvement in the adhesion of the ceramic encapsulated coil within the transducer housing, specifically the adhesion of the alumina ceramic discs to the ceramic adhesive. This was highlighted by the industrial field trial at Pembroke refinery, where during an unexpected shutdown one EMAT was damaged such that the entire encapsulated coil was detached. In addition, the poor performance of the ceramic disc was established via feedback from a customer of Sonemat Ltd. who purchased an EMAT made using the same method as the EMATs for the field trial (HWS2035-VC, Sonemat); in this case, the front ceramic disc detached from the ceramic adhesive underneath, although the coil remained secured within the set ceramic adhesive, despite this the EMAT continued to operate well. This highlights the potential issue with adhesion of the ceramic discs to the ceramic adhesive, although both cases could be explained by use of excessive force, ideally the final EMAT probe would be relatively robust, especially for use in portable inspections. It has been proposed that this could be resolved by use of ceramic discs with increased roughness, assuming the poor adhesion is a factor of the reduced surface area between the relatively smooth disc and the adhesive. As roughening these discs has proven difficult, discussion with the manufacturer to ascertain whether discs with increased roughness can be supplied should be undertaken to improve EMAT durability.

It was apparent from the broken EMAT, that the method by which the magnet is secured in the transducer housing could be improved. Although the magnet was held in place within the housing after the trial, the grub screws were not tightly fixed against the magnet; this could have been due to thermal expansion effects. An initial redesign concept involves the use of a rim within the internal diameter of the transducer housing, on which the magnet could rest; this may also relieve stress from being exerted onto the encapsulated ceramic coil and further increase the durability of the EMAT. Furthermore, investigation into the effects of

thermal cycling on the durability of the EMAT would prove useful to access which components are susceptible to failure.

The results presented in this thesis have demonstrated the applicability of this EMAT design for high temperature inspection on magnetite coated steel samples, including use in a real engineering environment during the industrial field trials. However, the formation of the magnetostrictive magnetite coating, which provides increased EMAT efficiency at elevated temperatures, is known to vary significantly between different mild steel samples; this has the potential to cause issues during inspections where the coating (and resulting signal amplitude) may even vary significantly on the same pipe. Therefore, a further study on a more representative selection of magnetite coated mild steel pipelines will be crucial to understanding the variation in signal to be expected from these types of pipelines, especially at high temperature. More generally, there is clearly a drive to improve the performance of this EMAT design for materials on which the dominant ultrasound generation and detection mechanism is the Lorentz force, namely stainless steel, as this is also used in industry for a variety of high temperature components; this will involve further optimisation of the coil and magnet.

This research has focused on optimisation of the high temperature EMAT primarily for ultrasound thickness measurements, where of main importance was the signal amplitude of the sample backwall echoes. However, a study of the defect detection capabilities of the EMAT, especially at high temperature would prove interesting.

Chapter 6

Development of High Temperature Piezoelectric Transducers

This chapter details the development of a high temperature piezoelectric transducer. The experimental set-up of the ultrasound measurements is described in section 6.1. The process of selecting an appropriate waveguide for this transducer design is discussed in detail in section 6.2, including results from experimental measurements and finite element modelling. The high temperature transducer housing design is presented in section 6.3, along with a comparison of three different transducer housing designs. The comparison of two high Curie temperature piezoelectric materials used within the transducer housing design is provided in section 6.4. Finally, the performance of six different materials used as a piezoelectric element backing layer within this design is given in section 6.5.

6.1 Pulser-Receiver System

The ultrasound measurements presented in chapters 6 and 7 were obtained using the experimental set-up illustrated in Figure 6.1. A digital oscilloscope (DPO2014, Tektronix) was used to display and record ultrasound signals produced using an ultrasonic pulser-receiver (PR) (5099PR, Olympus); various different transducers and samples were used to record the data for this work, and these will be described within the text.

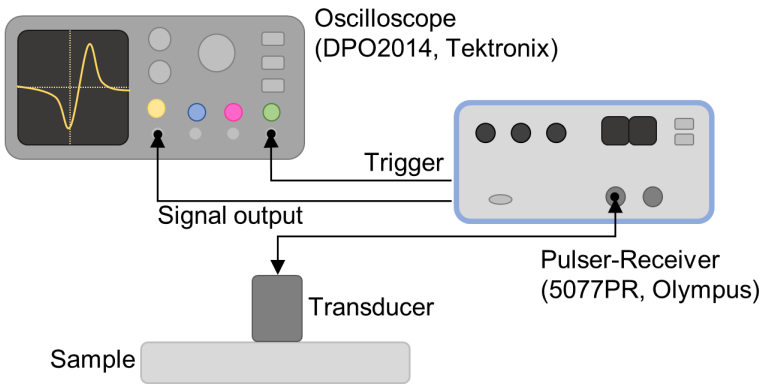

Figure 6.1: Schematic diagram of the experimental set-up used to obtain pulse-echo ultrasound measurements with the piezoelectric transducer.

The pulser section of the PR unit generates square wave (top hat shaped) electronic pulses of variable width and amplitude which are applied to the piezoelectric element in the transducer. The ultrasonic pulses are received after reflection from the waveguide end or sample (i.e. pulse-echo mode), and are amplified before the signal output is displayed on the oscilloscope. The external trigger is connected from the PR unit to the oscilloscope, providing a synchronizing trigger pulse.

There are a number of variable settings for the PR system, including: pulse repetition frequency (PRF), pulser voltage, transducer frequency, gain/attenuation, a low pass filter (LPF) and a high pass filter (HPF). The PRF was set to 200 Hz for all measurements within this work. The pulser voltage switch has four settings (100 V, 200 V, 300 V and 400 V) to select the optimum pulse amplitude for a particular transducer. The square wave (top hat shaped) excitation pulse width is generally chosen as that which corresponds most closely to half a time period of the natural resonant frequency of the transducer, having settings of 0.5 MHz, 1.0 MHz, 2-2.5 MHz, 3.5-4 MHz, 5-6 MHz, 7.5 MHz and 10 MHz. Gain or attenuation can be applied to the received signal, with up to 59 dB of (+) gain or 49 dB of (-) attenuation. The LPF switch can be set to pass the full bandwidth (1 kHz - 35 MHz), or to apply a 10 MHz cut-off frequency. The HPF switch can also be set to pass the full bandwidth or apply high pass filtering above 1 MHz. Different pulser voltage and transducer frequency settings have been used, and these will be reported with regard to the different measurements within this thesis.

The voltage pulse generated by the PR system, with a pulser voltage of 200 V and 5-6 MHz frequency, and was measured using a 100X high voltage oscilloscope probe (P5100, Tektronix), and the voltage pulse is shown in Figure 6.2(a), along with the frequency content in Figure 6.2(b), calculated by application of an FFT.

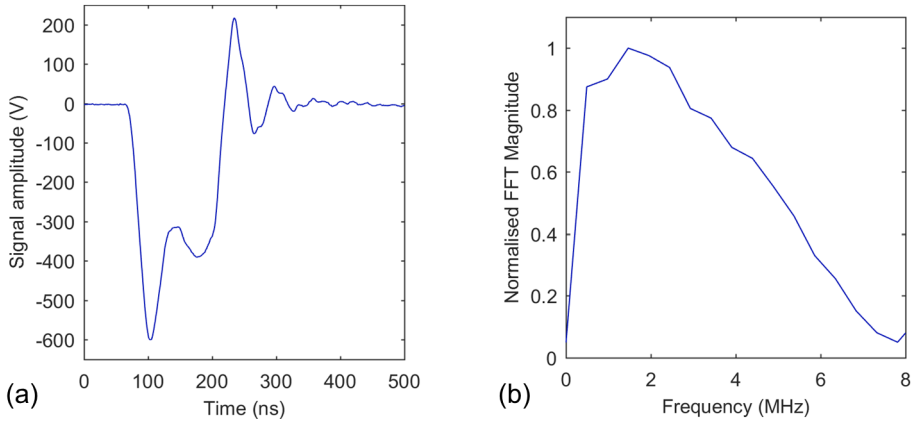

Figure 6.2: Olympus 5077PR square wave pulser-receiver with 400 V driving voltage, 5-6 MHz transducer frequency and 0 dB gain: (a) voltage pulse and (b) frequency spectrum.

6.2 Waveguide

The concept of waveguides with respect to application of piezoelectric transducers at elevated temperatures was discussed in section 1.5.4. Generally, waveguides (also referred to as delay lines or buffer rods) are used to thermally isolate the piezoelectric element from the hot sample, where a variable temperature profile along the waveguide is established during continuous monitoring. For portable inspections, the piezoelectric can be thermally shielded from a hot sample if a sufficiently short inspection time period is achieved, although this also depends on waveguide geometry, sample temperature and the piezoelectric material's T_C.

The high temperature piezoelectric transducer investigated in this work employs a relatively short waveguide, the design of which is described in section 6.3. Here, the waveguide provides a number of functions, including: a mass to which a compressive load can be applied across the piezoelectric disc, wear protection for the piezoelectric disc from contact with the sample and heat protection from a hot sample. It is important to note, the heat protection provided by the waveguide used in this work is dependent upon the physical coupling method used. If long term permanent installation is employed the temperature of the piezoelectric would likely be elevated due to the relatively large dimensions of the transducer, where heat can be conducted efficiently; the temperature of the piezoelectric during long term installation would likely be slightly lower than the sample, especially if a form of passive cooling was used. However, if the transducer is used for portable single-spot inspections, the heat conduction would be relatively inefficient over a short time period, such that the piezoelectric would be protected from the hot sample.

Since the piezoelectric transducer is intended for application at elevated temperatures, stainless steel (304) was selected as the waveguide material. Stainless steel is preferable to mild steel as mild steel exhibits much greater surface oxide formation at high temperatures, which can impede the transmission of ultrasound at the piezoelectric-waveguide boundary and at the waveguide-sample boundary.

A length of 60 mm was specified, such that all waveguides investigated would be identical in length. This waveguide length value was chosen to provide a suitable sample thickness measurement range for the transducer. This is the range in which backwall reflections from the end of the waveguide (as perfect coupling is unlikely to be achieved) will not interfere with the desired signals from the backwall of the sample, which are required for sample thickness measurements. For calculation of the required waveguide length, the sample was taken to be stainless steel of which a longitudinal wave velocity of 5900 m/s was assumed. A waveguide length of 60 mm would provide a thickness measurement from at least two sample backwall reflections (between waveguide backwall reflections) for samples up to 30 mm thick; the majority of high temperature pipelines used in the petrochemical and power generation industries fall below this wall thickness.

As described in section 1.5.4, the use of waveguides in piezoelectric transducers generates spurious echoes, here termed trailing echoes. These trailing echoes are formed due to the waveguide-air boundary effects, mainly mode conversion and reflection of diffracted edge waves originating from the ultrasound transducer, as depicted in Figure 6.3 [228], which propagates to the waveguide-air boundary at an oblique angle. The plane wave is the main longitudinal wave mode propagating along the waveguide. The mode converted signals generated along the length of the waveguide constructively and destructively interfere to form the trailing echoes.

The trailing echoes are considered undesirable in most inspection applications as they significantly decrease the SNR of desired signals due to interference with reflections from the sample. The arrival time delay difference, Δt, between trailing echoes for a cylindrical shaped (rod) waveguide can be defined by [97]:

$$\Delta t = D\sqrt{\frac{1}{v_S^2} - \frac{1}{v_L^2}}, \tag{6.1}$$

where D is the waveguide diameter and v_L and v_S are the longitudinal and shear wave velocity in the waveguide material, respectively.

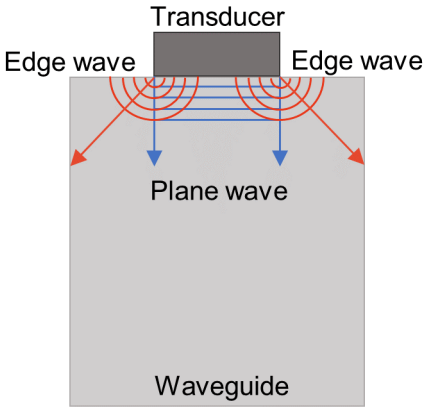

Figure 6.3: Schematic diagram illustrating the plane wave and edge waves generated by an ultrasound transducer operating on a waveguide, adapted from [228].

The use of large diameter, short waveguides can prevent the trailing echoes from forming, as over the propagation distance the waveguide can be assumed to be a semi-infinite space where waveguide-air boundary effects are negligible. However, for application on typical high temperature components used in industrial environments (e.g. pipelines) these waveguides could be impractical due to their weight and size and efficient physical coupling may be challenging due to the surface area of the transducer, especially with dry clamping methods for acoustic coupling, as large forces would be required to provide acoustic coupling. Moreover, depending upon the thickness of the inspected sample, the ultrasound echoes reflecting from the sample backwall may interfere with those reflecting from the interface between the delay line and the sample. The transducer design presented here makes use of a waveguide that is sufficiently long to avoid unwanted interference between reverberations within the sample and the waveguide, although this geometry introduces trailing echoes. The most successful methods reported for removing these undesired trailing echoes is via alteration of the waveguide-air boundary, these include: knurling, threading, tapering and cladding, as discussed in section 1.5.4.

For reference, the schematic diagram in Figure 6.4 illustrates the pathways of longitudinal ultrasound waves which propagate along the transducer waveguide when it is acoustically coupled to a sample and the corresponding labels which are used throughout. Here, W1, W2 and W3 denote the first, second and third waveguide backwall reverberations, respectively. Labels 4, 5, 6, 7 and 8 denote the first to fifth reverberations, respectively, of the wave within the sample which is transmitted across the interface from the initial wave generated by the piezoelectric element. As each of these reverberations interact with the waveguide-sample interface, the energy

transmitted propagates along the waveguide where it is detected by the piezoelectric element. Similarly, labels 9, 10, 11 and 12 denote the first to fourth reverberations, respectively, of the longitudinal wave within the sample which is transmitted across the interface when W1 is reflected from the waveguide end back to the interface.

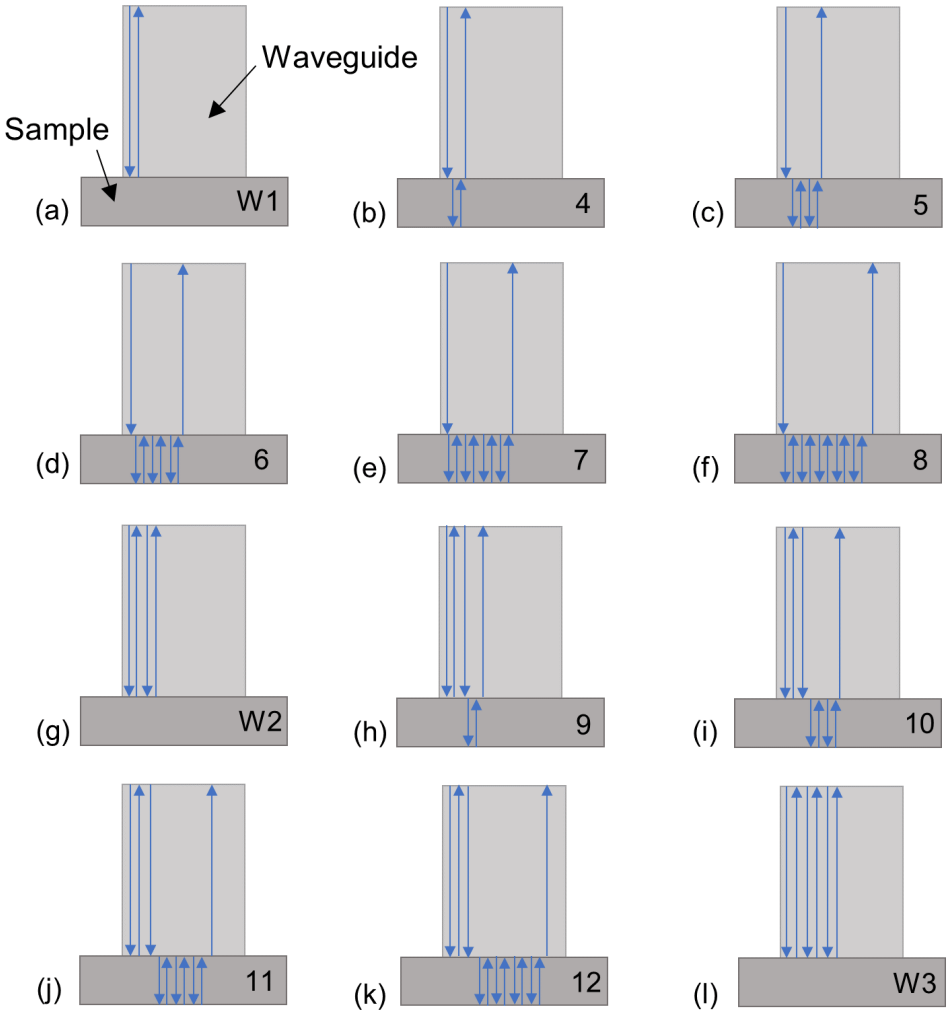

Figure 6.4: Schematic diagram illustrating the labelling of backwall echoes from the waveguide used throughout this thesis.

The following section describes finite element modelling to verify formation of these trailing echoes with the waveguide geometry used for this transducer design. This leads on to section 6.2.2 which details a number of different waveguide geometries investigated experimentally towards incorporation in the transducer design.

6.2.1 Finite Element Modelling

Finite element modelling of trailing echo formation in waveguides was performed using a commercial software package (PZFlex), which utilises an explicit time domain approach; the basic theory behind finite element modelling is detailed in section 2.5. The finite element model is structured to allow experimental validation of the results which are presented in section 6.2.2, such that it models the ultrasound signal output when a transducer is acoustically coupled to one end of the waveguide. The A-scan signal output from the model can be compared with that from the experimental data using a waveguide with identical geometry. Both 2D and 2D axisymmetric finite element models are described here to model the formation of trailing echoes in waveguides. The main stages in constructing a finite element model in PZFlex are as follows: model geometry, material properties, boundary conditions, finite element size and suitable driving input function to generate ultrasound.

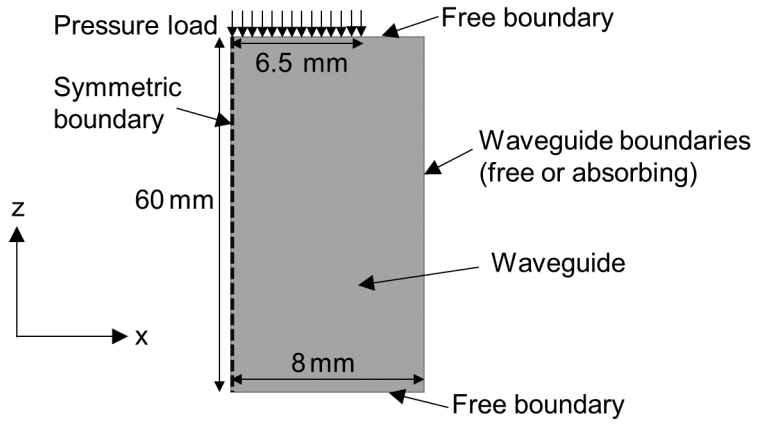

Figure 6.5: Schematic diagram of the 2D finite element model used in PZFlex to simulate the propagation of the ultrasonic waves within the waveguide.

The 2D finite element model geometry is illustrated in Figure 6.5, which is a cross-section of the cylindrical shaped waveguide used in the experimental validation. The waveguide has a radius of 8 mm and a length of 60 mm. The ultrasound transducer radius is 6.5 mm, as is the front face diameter of the transducer used in the experimental validation (V109, Panametrics Inc). The waveguide material properties were input for the stainless steel material used in the experiential validation, with a ρ of 7900 kg/m^3, a v_{L} of 5645 m/s, a v_{S} of 3100 m/s and the viscous damping parameter was not included to emphasise trailing echo effect in the 2D model. The upper (z-maximum) and lower (z-minimum) boundaries of the model are specified to be free, and the left-side boundary (x-minimum) is a symmetrical boundary since the model is axisymmetric. Two different 2D models were generated, one which de-

termined the right-side boundary (x-maximum) as free, thereby simulating a smooth waveguide-air boundary, and the other which determined the right-side boundary as absorbing, to simulate scattering and attenuation of the ultrasound interacting with the boundary. The absorbing boundary is a simplistic method to simulate the effect of the waveguide-air boundary features (e.g. knurling and thread patterns) which aim to scatter incident waves to avoid constructive and destructive interference of mode converted waves, which form trailing echoes, as these are difficult to model along the cubic elements used in PZFlex.

The finite element size was determined from the number of elements per wavelength and the minimum wavelength (1.22 mm), which calculated from the input function centre frequency (2.5 MHz) and lowest material ultrasound velocity of interest in the model (shear velocity at 3100 m/s). The number of elements per wavelength was chosen at 15, resulting in an element size of 80 μm.

PZFlex is capable of modelling the response of piezoelectric crystals to a particular electrical impulse, which provides full finite element modelling of the piezoelectric transducer. However, as the material properties of the commercial transducer components (i.e. piezoelectric material and backing material) are not known, and to minimise computational time, this was not implemented. A pressure load was used to simulate the piezoelectric transducer, such that it had similar characteristics to the output from the pulser-receiver unit used in the experimental validation, which was previously shown in Figure 6.2 from section 6.1. The output from a 2-cycle sine wave pressure load was found to most closely resemble the experimental A-scan data, the input function and its frequency spectrum are displayed in Figure 6.6(a) and 6.6(b), respectively.

It is important to note that a 2.5 MHz centre frequency for the pressure load was used in both the 2D and 2D axisymmetric models, yet the commercial transducer used in experimental validation has a centre frequency of approximately 5 MHz; it is assumed this will not to significantly impact the modelling of trailing echoes. This was done to avoid computational memory issues when running the model at higher frequencies, due to the decreased element size. The pressure load is applied along the y-direction, perpendicular to the waveguide surface to simulate the through thickness vibration mode of a piezoelectric element, in a line segment corresponding to the radius 6.5 mm of the piezoelectric element. The simulation time for the model was set to the minimum possible to observe the trailing echoes, and was set to 45 μs.

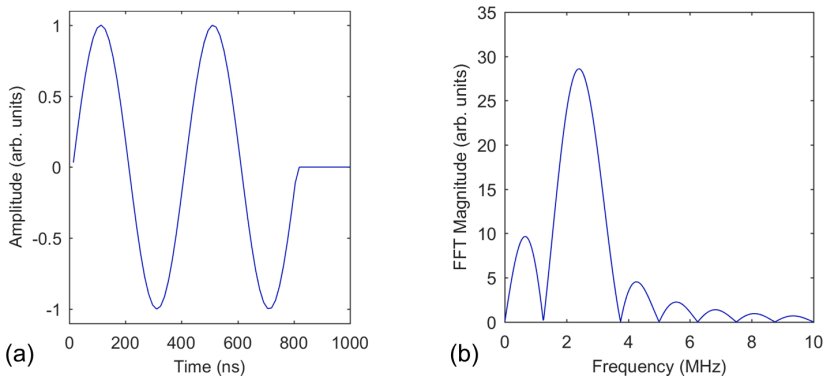

Figure 6.6: The simulated pressure load used as the input function in the 2D finite element models implemented in PZFlex: (a) 2 cycle sine wave input function and (b) its frequency spectrum showing a 2.5 MHz centre frequency.

The results from the model have been presented here as an A-scan, which can be compared to the experimental A-scan. The A-scans of the 2D models with a free waveguide-air boundary and an absorbing waveguide-air boundary are given in Figures 6.7 and 6.8, respectively. The A-scans are generated by calculating the average element z-velocity across the loading surface, to simulate the response from a piezoelectric transducer operating in pulse-echo mode. The experimental A-scan for a stainless steel (304) rod waveguide with the same geometry as that in the 2D model and a smooth waveguide-air boundary is presented in Figure 6.9, the data was measured using a 5 MHz, 13 mm diameter piezoelectric transducer (V109, Panametrics Inc.) with PR settings at 200 V and 5-6 MHz; more detail on experimental measurements with different waveguide geometries is given in section 6.2.2.

The first (W1) and second (W2) longitudinal echoes from the waveguide backwall and the trailing echoes (T1, T2, T3 and T4) are observable in Figure 6.7, where the first (T1) and second (T2) trailing echoes are clearly detectable, while the third (T3) and fourth (T4) trailing echoes are of lower amplitude, and there appears to be more noise around the baseline of the signal near these echoes. The initial signal at around at around zero time is the signal from the input pressure load. The time delay between the echoes from the 2D model is measured as 4.6 μs, which is close to both the delay calculated from equation 6.1 of 4.4 μs using the model input parameters, and the delay measured from the experimental data at 4.5 μs. Despite this, there appears to be more coherent noise in the baseline of the signal, arising from various mode converted signals, which do not appear in the baseline of the signal in the experimental A-scan. This most likely arises from the 2D nature of the model, which cannot fully simulate the response from the 3D boundary conditions in

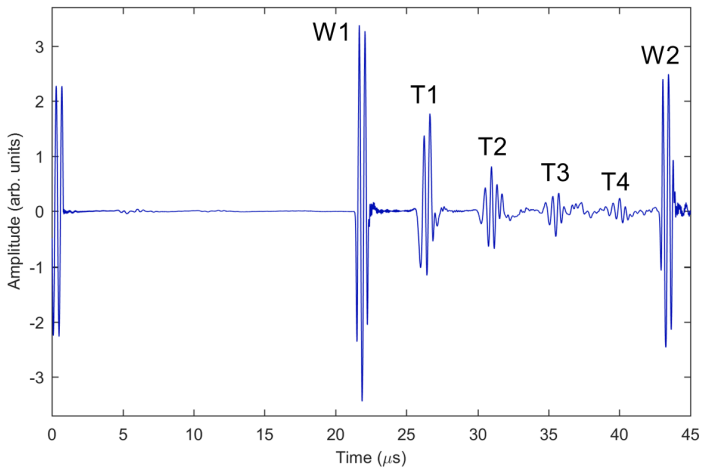

Figure 6.7: Simulated A-scan from the 2D model with a free waveguide-air boundary, showing element z-velocity against time, where the first (W1) and second (W2) waveguide backwall echoes and trailing echoes (T1, T2, T3 and T4) are observable.

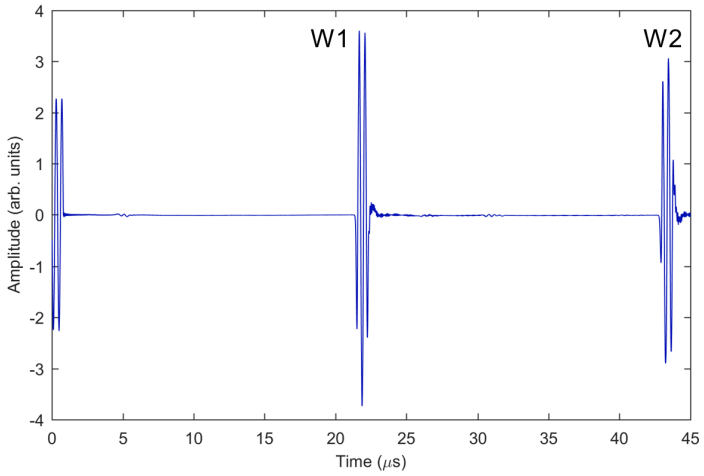

Figure 6.8: Simulated A-scan from the 2D model with an absorbing waveguide-air boundary showing element z-velocity against time, where the first (W1) and second (W2) waveguide backwall echoes are observable.

the experiment, such as the complete constructive and destructive interference of the various mode converted signals. The trailing echoes are not observable in the model with the absorbing waveguide-air boundary, as the ultrasound waves are absorbed on contact with the boundary (see Figure 6.8), and this result highlights that the nature of the trailing echo effect arises from the interaction of the ultrasound waves with the waveguide-air boundary.

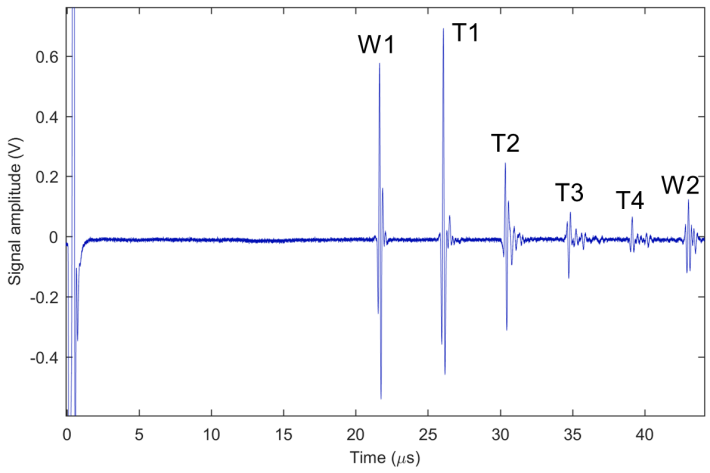

Figure 6.9: Experimental A-scan on a 16 mm diameter and 60 mm length stainless steel rod waveguide with a smooth waveguide-air boundary.

The set of images in Figures 6.10 and 6.11 represents the element y-velocity along the profile of the waveguide at different time periods (0.9 μs, 9.7 μs, 20.4 μs and 31.5 μs) for the 2D model with a free and absorbing waveguide-air boundary, respectively. Figures 6.10 and 6.11 (a), (b) and (c) show one complete round trip of the longitudinal wave from generation, propagation along the waveguide, reflection from the backwall to just before interaction at the transducer-waveguide interface (images 1-3), and the final image (d) shows the longitudinal wave just before the second reflection from the backwall. From the images in Figure 6.10 the W1 and W2 longitudinal backwall echoes are observable, along with the formation of trailing echoes T1 and T2. The images in Figure 6.11 highlight that trailing echoes are not established along the waveguide as the longitudinal wave propagates, due to absorption of the diffracted edge waves generated by the pressure load as they interact with the waveguide boundary.

To simulate the experimental conditions more accurately, a 2D axisymmetric model was performed in PZFlex, with parameters as close to the 2D model as possible for comparison. A schematic diagram of the 2D axisymmetric model geometry is given in Figure 6.12, where the cyln command was used in PZFlex to generate a cylindrical stainless steel waveguide and a cylindrical region of air above which interacts with the waveguide. The piezoelectric element radius (R_P) is 6.5 mm and the waveguide has a radius (R_W) of 8 mm with a length of 60 mm and is surrounded by a void. The model has two axis of symmetry (x-minimum and y-minimum) which reduces the computational time for the model significantly. All other boundaries

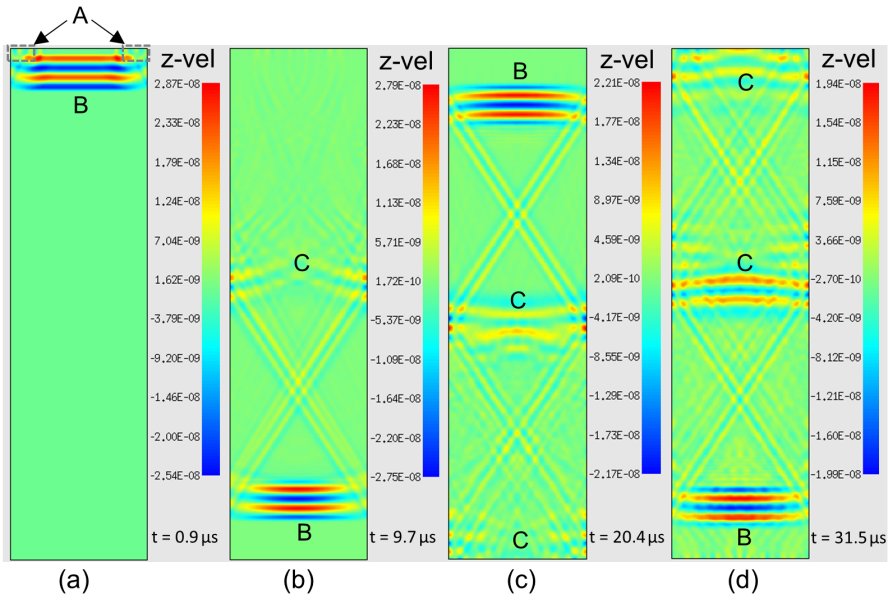

Figure 6.10: Simulated element z-velocity for the 2D model with a free boundary at time periods: (a) 0.9 μs, (b) 9.7 μs, (c) 20.4 μs and (d) 31.5 μs. Label A denotes the waves generated at the edges of the applied pressure load, B denotes the longitudinal waves which propagate along the waveguide to form W1 and W2, and C denotes the formation of trailing echoes.

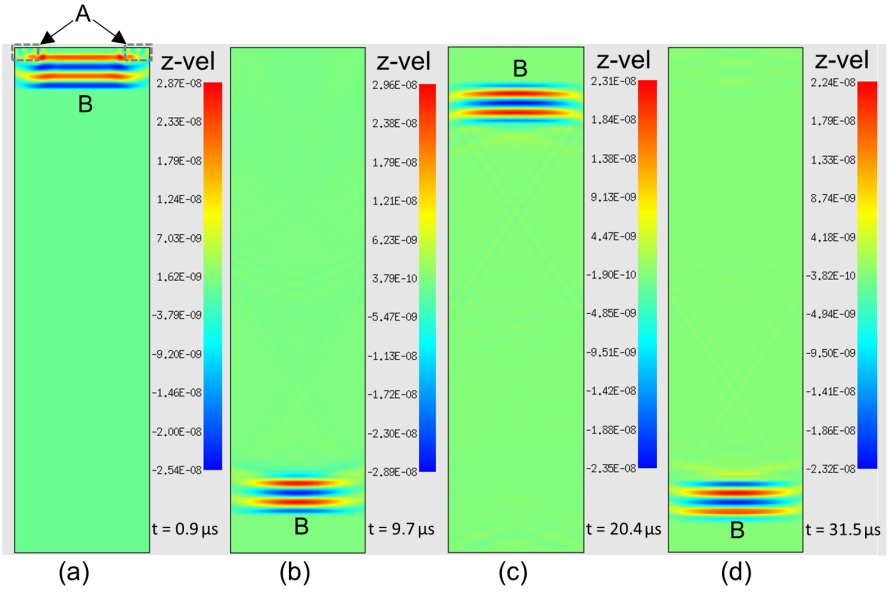

Figure 6.11: Simulated element z-velocity for the 2D model with an absorbing boundary at time periods: (a) 0.9 μs, (b) 9.7 μs, (c) 20.4 μs and (d) 31.5 μs. Label A denotes the waves generated at the edges of the applied pressure load and B denotes the longitudinal waves which propagate along the waveguide to form W1 and W2.

(x-maximum, y-maximum, z-minimum and z-maximum) are set to free boundaries, such that the 2D axisymmetric model simulates a cylindrical rod with a smooth waveguide-air boundary. It was not possible to set the waveguide boundary to absorbing, due to the nature of the clyn and the rectangular grid used in PZFlex. The same centre frequency, minimum wave speed and element size as described previously were used for the 2D axisymmetric model. Although, a different input function for the pressure load was found to more closely match the experimental results; as such, a Rickert wavelet input function with 8 sub-wavelets displayed in Figure 6.13 was used.

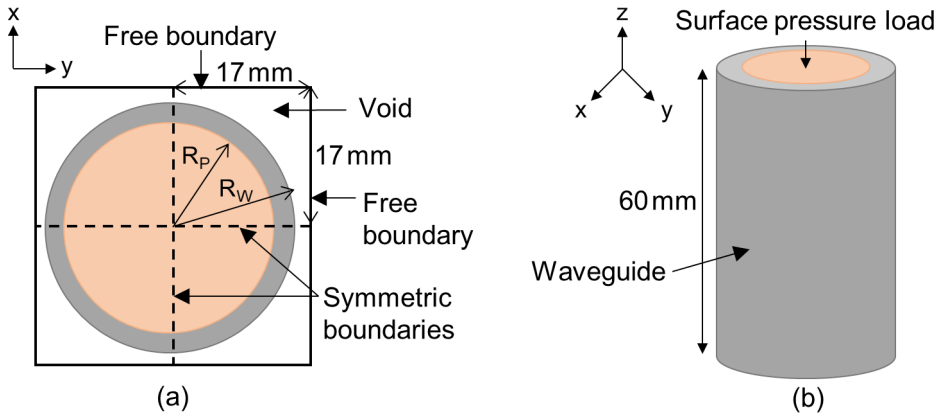

Figure 6.12: Schematic diagram of the 2D axisymmetric finite element model used in PZFlex to simulate the propagation of the ultrasonic waves within the waveguide.

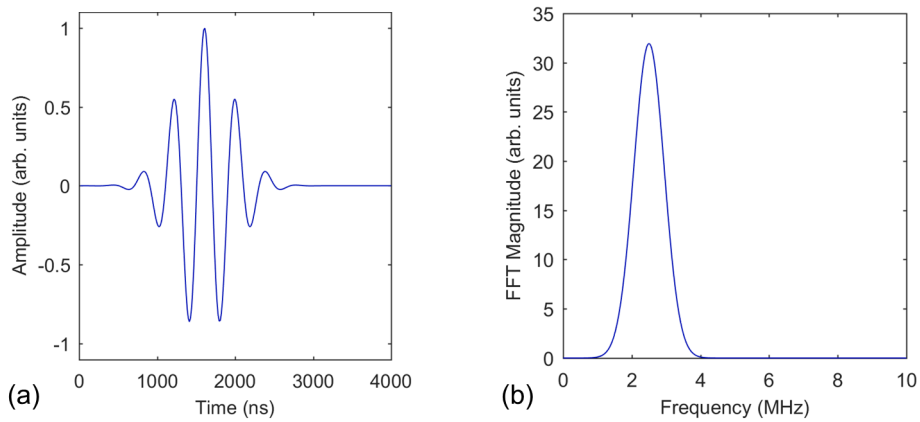

Figure 6.13: The simulated pressure load used as the input function in the 2D axisymmetric finite element models implemented in PZFlex: (a) Rickert wavelet with 8 sub-wavelets input function and (b) its frequency spectrum showing a 2.5 MHz centre frequency.

The A-scan from the 2D axisymmetric model is given in Figure 6.14, calculated from the average element z-velocity across the loading surface. The first (W1) and second (W2) longitudinal echoes from the waveguide backwall and the trailing echoes (T1, T2, T3 and T4) are observable, although the amplitude of T4 is small relative to the experimental A-scan. The first three trailing echoes are clearly identifiable from the baseline, with no spurious signals between the trailing echoes, again closely matching the experimental A-scan. This is likely due to the 2D axisymmetric model more accurately simulating the complete constructive and destructive interference of the mode converted waves across the circular cross-section of the waveguide as they propagate along the waveguide.

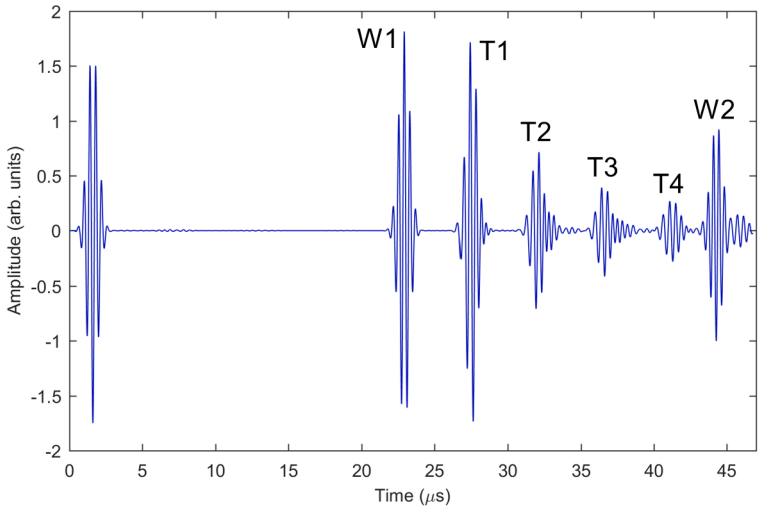

Figure 6.14: Simulated A-scan from the 2D axisymmetric model with a free waveguide-air boundary showing element z-velocity against time, where the first (W1) and second (W2) waveguide backwall echoes and trailing echoes (T1, T2, T3 and T4) are observable.

The set of images in Figure 6.15 represents the element z-velocity along the profile of the waveguide at different time periods (0.9 μs, 9.7 μs, 20.4 μs and 31.5 μs) for a 2D slice of the 2D axisymmetric model. Similarly to the images from the 2D free boundary model, the images show the formation of the W1 and W2 waveguide backwall echoes, along with the trailing echoes from the edge waves generated by diffraction from the pressure load mode converting at the waveguide-air boundary.

In the PZFlex analysis above, it is assumed that W1 and W2 can be approximated as bulk longitudinal waves which propagate along the waveguide. To investigate if this approximation holds, two finite element models were performed using for two cases: one where the waveguide is approximated as a bulk sample

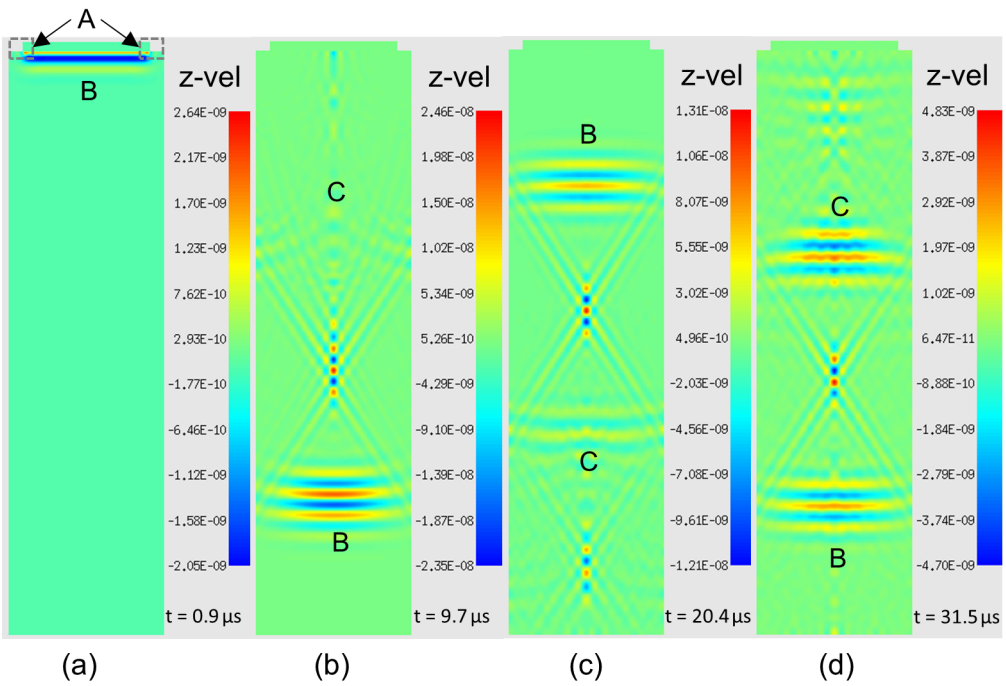

Figure 6.15: Simulated element z-velocity for the 2D axisymmetric model with a free boundary at time periods: (a) 0.9 μs, (b) 9.7 μs, (c) 20.4 μs and (d) 31.5 μs. Label A denotes the edge waves generated at the edges of the applied pressure load, B denotes the longitudinal waves which propagate along the waveguide to form W1 and W2 and C denotes the formation of trailing echoes.

(600 mm diameter), and the other where the waveguide (16 mm diameter) has absorbing boundaries. The 2D model geometry for the bulk case is given in Figure 6.16, where a central line of symmetry was used. The model geometry for the waveguide case is similar to that given in Figure 6.5 above, although a central line of symmetry was applied. Both models had identical input parameter, except the diameter of the waveguide and x-minimum boundary, and these input parameters where identical to the 2D model described above, excluding the input function which was the Rickert wavelet function used in the 2D axisymmetric model, as displayed in Figure 6.13.

The A-scan for the approximate bulk case and the waveguide with an absorbing boundary case are presented in Figures 6.17 and 6.18, respectively. It is clear that trailing echoes are absent from the A-scans from both modelling approaches, and this further indicates that the trailing echoes are formed as a result of the interaction of the longitudinal wave mode, generated by the pressure load, and the waveguide-air boundary. The time delay between the W1 and W2 echoes for both cases was measured, which was used to calculate the wave velocity. The wave veloc-

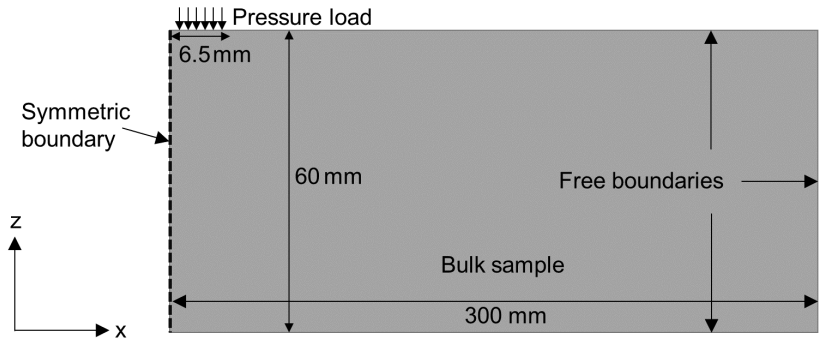

Figure 6.16: Schematic diagram of the 2D model used in PZFlex to simulate the propagation of the ultrasonic waves within the bulk.

ity for the approximate bulk case was calculated at 5659 m/s and the wave velocity for the waveguide with absorbing boundaries was calculated at 5670 m/s. The similarity between these velocity values indicates that the wave mode established within the waveguide with surface features, such as knurling and threading which act to scatter the waves at the waveguide-air boundary to prevent the formation of trailing echoes, can be approximated as a bulk longitudinal wave mode. The slight difference between these values and the input longitudinal velocity of the model is likely due to numerical dispersion.

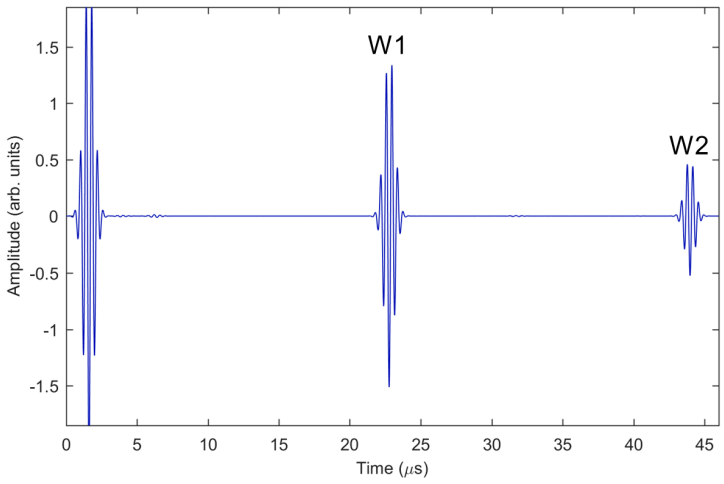

Figure 6.17: Simulated A-scan from the 2D model with the waveguide approximated as a bulk sample (600 mm diameter), showing element z-velocity against time, where the first (W1) and second (W2) waveguide backwall echoes are observable.

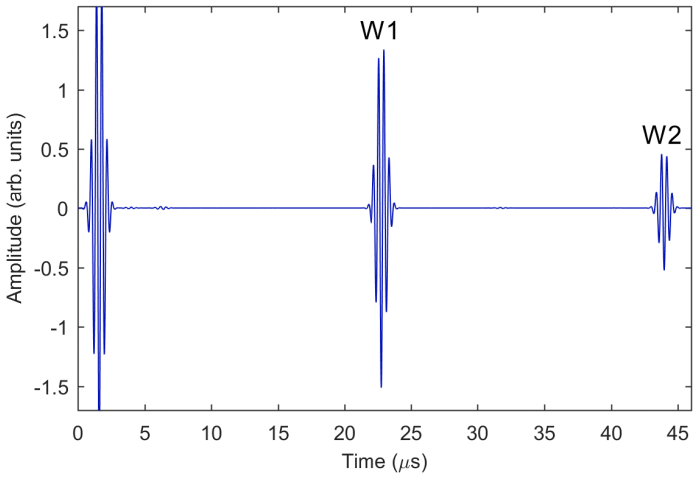

Figure 6.18: Simulated A-scan from the 2D model with an absorbing waveguide-air boundary showing element z-velocity against time, where the first (W1) and second (W2) waveguide backwall echoes are observable.

6.2.2 Experimental Comparison of Waveguides

This section describes the experimental results on comparison of different waveguide geometries, towards selection of appropriate waveguides for incorporation in the high temperature transducer design to effectively remove the trailing echoes. The presence of trailing echoes was observed experimentally using a stainless steel cylindrical shaped waveguide 16 mm in diameter and 60 mm in length, referred to within the remaining text as waveguide A, and pictured in Figure 6.19. The PR system described in section 6.1 was used to carry out a pulse-echo measurement in the waveguide using 200 V pulser voltage, 5-6 MHz transducer frequency and 0 dB amplifier gain. The measurements were made by coupling a commercial, single-element piezoelectric transducer with a 5 MHz centre frequency and a piezoelectric element diameter of 13 mm (V109, Panametrics Inc.) with a water-based ultrasonic couplant (SOUNDSAFE®, Diagnostic Sonar Ltd.) on the end of the waveguide.

The various different 60 mm long waveguides were fabricated, and their ability to remove trailing echoes was compared; descriptions of the waveguides are provided in Table 6.1 and images are given in Figure 6.19 and waveguide H is pictured in Figure 6.28. For all waveguides, both ends were flat, parallel to each other and polished. All waveguides are made from 304 stainless steel, however the original steel was sourced from different manufactures and will have undergone different processing methods, which is reflected in the amplitude values from the signals, as there are slight variations in velocity and attenuation.

Waveguides A and B are were produced from the same 16 mm diameter 304 stainless steel rod; waveguide A was not altered providing a uniform smooth waveguide-air boundary and waveguide B was knurled around the waveguide-air boundary. Waveguides C and D are were fabricated from the same 304 stainless steel 40 mm diameter rod, both with a taper from a diameter of 40 mm to 30 mm, giving a taper angle of 14 °. Waveguide D was altered such that 13 randomly distributed machined grooves of varying depth (up to ≈ 5 mm) were applied around the circumference of the waveguide-air boundary, leaving the remaining sections of the boundary smooth. Waveguides E, F and G were constructed from standard stainless steel M20 bolts from the same batch. A schematic diagram of the M20 bolts used for waveguides E, F and G cut to the correct length is shown in Figure 6.20, where L_T is the length of thread from the tail end towards the bolt head. Waveguide E has a thread all along the bolt length, whilst waveguide F has a thread approximately half way along the bolt length ($L_T = 25$ mm) and the hexagonal bolt head was removed for waveguide G such that $L_T = 35$ mm. Waveguide H was produced from a 304 stainless steel rod with a knurling pattern around the waveguide-air boundary, identical to that on waveguide B. The end face (i.e. the face interacting with a sample) of the waveguide was machined to fit the curve of an industrial pipe sample, whilst the front face (i.e. the face interacting with a piezoelectric disc or transducer) of the waveguide had four 10 mm deep holes, used to construct a transducer housing from the waveguide; this is described in more detail in section 6.3.

Table 6.1: Dimensions and descriptions of the waveguides, where D_W is the waveguide diameter. Note: all waveguides are 60 mm in length.

Waveguide	Dimensions (mm)	Description
A	$D_W = 16$	Rod - uniform smooth boundary
B	$D_W = 16$	Rod - knurled boundary
C	$D_{W1}= 40$, $D_{W2} = 30$	Rod - uniform smooth tapered boundary
D	$D_{W1} = 40$, $D_{W2} = 30$	Rod - uniform smooth tapered boundary with 13 randomly distributed groves along boundary
E	M20, $L_T = 47.5$	M20 bolt - hexagonal head, thread all along
F	M20, $L_T = 25$	M20 bolt - hexagonal head, thread part way along
G	M20, $L_T = 35$	M20 bolt - no head, thread part way along
H	$D_W = 40$	Rod - knurled boundary, curved end face

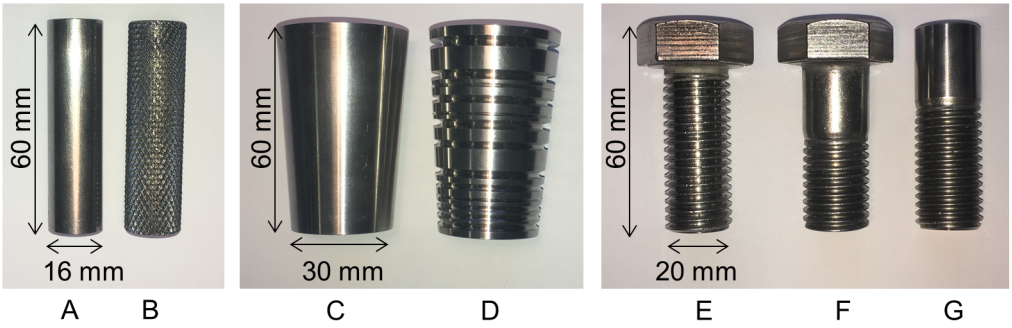

Figure 6.19: Images of the waveguides: A, B, C, D, E, F, and G.

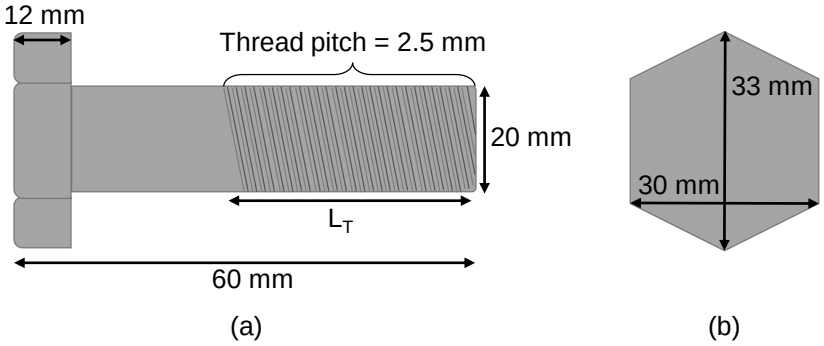

Figure 6.20: Schematic diagram of the M20 hexagonal head bolt dimensions, not to scale.

Table 6.2: Calculated SNR values for waveguides.

Waveguide	SNR (dB)
A	28.6
B	20.4
C	12.2
D	19.2
E	23.9
F	26.4
G	20.5
H	18.9

Pulse-echo measurements were carried out for each waveguide, and the resulting A-scans are provided in Figures 6.21 - 6.24, which are described in detail in the text below. The SNR was calculated for each waveguide as a figure of merit from the pulse-echo measurements, and the values are provided in Table 6.2. Within chapters 6 and 7, SNR is taken to be the SNR calculated using equation 2.78, where the maximum amplitude of the first waveguide backwall echo is compared with the maximum amplitude of a noise peak within a region of noise after the first waveguide backwall echo, as labelled in the A-scans. The term noise in this work refers to the noise floor of the signal, which is taken to be the signal that is observed outside of the regions where there is a clear backwall echo of interest. It is important to consider that the noise floor contains signals due to coherent noise, such as scattered signals from the patterned waveguide-air boundary, in addition to electrical noise. For comparison of the different waveguide geometries, calculating the SNR in this way determines the effect of waveguide geometries on the noise floor, and therefore the performance of the waveguide if incorporated in a transducer for use in ultrasound thickness monitoring.

The pulse-echo response from waveguides A (blue) and B (red) are shown in Figure 6.21, to highlight the effect of the knurling pattern on the formation of trailing echoes. For waveguide A, the first three backwall echoes (W1, W2 and W3) are identifiable, along with the with four trailing echoes (T1, T2, T3 and T4) between each waveguide backwall echo. The trailing echoes have a measured Δt of $\approx 4.5\,\mu$s, whilst the calculated Δt using equation 6.1 is $\approx 4.4\,\mu$s (assuming $v_L = 5645\,$m/s and $v_S = 3100\,$m/s [229]).

It is clear that all the waveguide geometries studied, excluding the simple rod, were able to alter the formation of trailing echoes to a certain extent. The knurling pattern on waveguide B was able to completely remove the trailing echoes from the signal; this is a result of the alternating pattern of angles at the waveguide-air boundary causing reflection and mode conversion from the edge of the sound field in such a way that that constructive interference does not occur and trailing echoes are not observed. However, the noise floor is elevated resulting in a decrease in the SNR from 28.6 dB found in waveguide A to 20.4 dB. This increase in noise can be attributed to the arrival of signals reflected and mode converted in multiple different pathways by the knurled pattern boundary, which do not totally destructively interfere, such that these much lower amplitude spurious echoes arrive at a spectrum of delay times in the signal. The noise floor using a knurled waveguide may be reducing the periodicity of the knurled pattern, where the increased randomness may contribute increased destructive interference of these scattered waves.

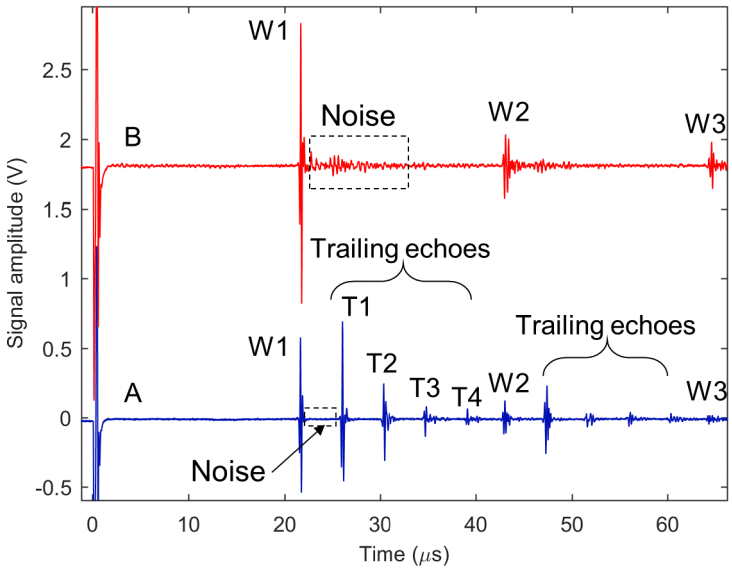

Figure 6.21: A-scan for waveguides A (blue) and B (red) showing the first three backwall echoes (W1, W2 and W3), and trailing echoes (T1, T2, T3 and T3), with a label of the coherent noise region used to calculate the SNR.

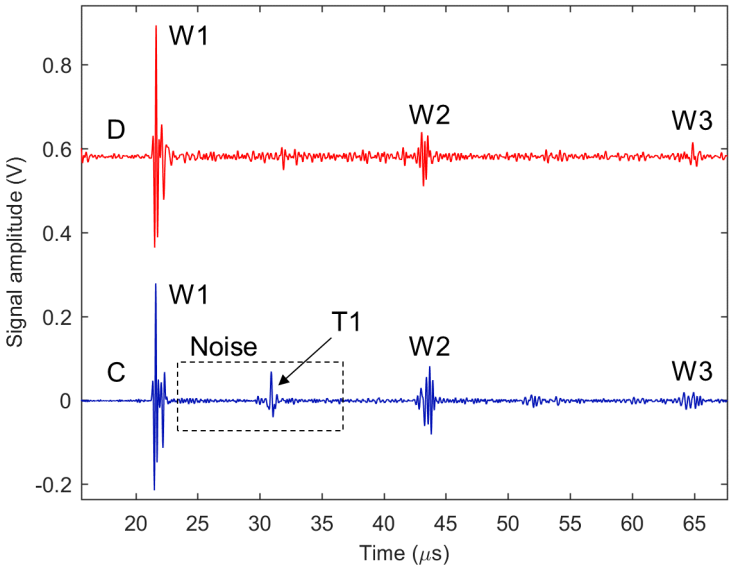

Figure 6.22: A-scan for waveguides C (blue) and D (red) showing the first three waveguide backwall echoes (W1, W2 and W3), with a label of the coherent noise region used to calculate the SNR.

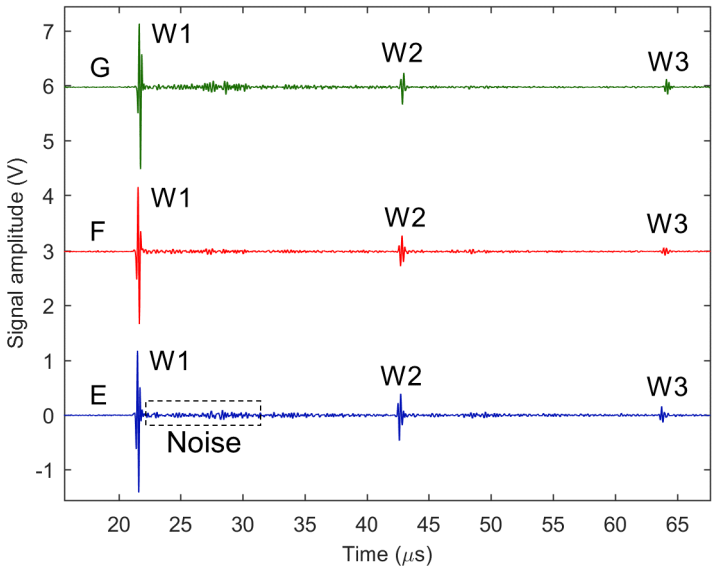

Figure 6.23: A-scan for waveguides E (blue), F (red) and G (green) showing the first three waveguide backwall echoes (W1, W2 and W3), with a label of the coherent noise region used to calculate the SNR.

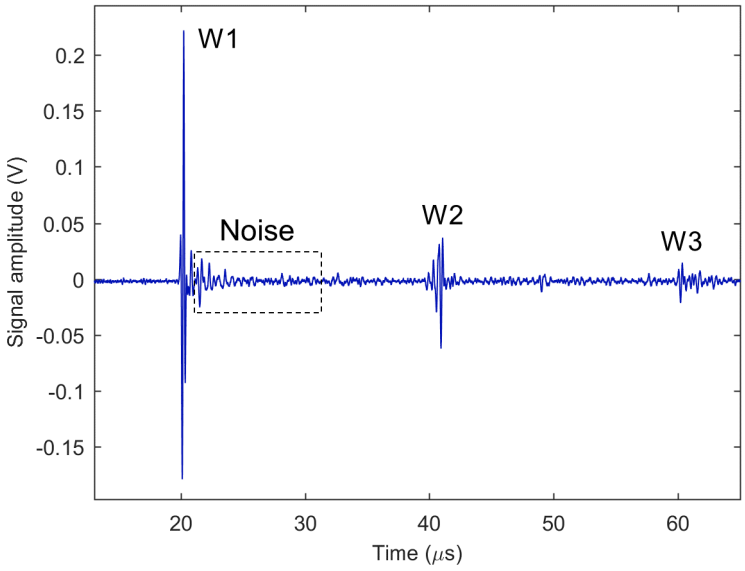

Figure 6.24: A-scan for waveguide H showing the first three waveguide backwall echoes (W1, W2 and W3), with a label of the coherent noise region used to calculate the SNR.

Waveguide C with the smooth boundary taper failed to completely remove the trailing echo, which can clearly be seen in the A-scan at 30.0 μs, giving a relatively low SNR of 12.2 dB. This result could have been improved by investigating different taper angles. Waveguide D appeared to perform much better than C, effectively removing the trailing echoes from the signal, with a greater SNR of 19.2 dB; thereby, highlighting the ability of such randomly orientated grooves to impede the constructive and destructive interference of the mode converted waves. However, both SNR for waveguides C and D are relatively low compared with the other waveguides.

All waveguides constructed from an M20 bolt (E, F and G) effectively removed trailing echoes from the signal, although there is a relatively significant difference between the calculated SNR values: waveguide G observed the lowest SNR at 20.5 dB, waveguide E observed a slightly higher SNR of 23.9 dB, whilst waveguide F observed the highest SNR of all waveguides tested (excluding the rod waveguide A) at 26.4 dB. Similarly to the knurled pattern waveguide B, the thread pattern at the waveguide-air boundary introduced varying angles resulting in mode conversion and reflection of the edges of the sound field, such that constructive interference did not occur and trailing echoes were not found.

Despite waveguides F and G having slightly different ratios of smooth to threaded boundaries, it is possible to draw the conclusion that the hexagonal bolt head geometry appears to decrease the noise floor, improving the SNR compared to no bolt head present; this is easily discernible via visual analysis of the A-scans in Figure 6.23. Moreover, it is possible to assume from these results that a waveguide which is part threaded (i.e. not threaded along the entire waveguide-air boundary) improves the SNR, compared to a waveguide which is threaded along the entire boundary.

Similarly to waveguide B, the knurled pattern on waveguide H effectively removed all the trailing echoes despite its curved end, yet this resulted in increased noise floor due to scattering, giving a SNR of 18.9 dB. Although the SNR is relatively low, the design is of interest for potential improved coupling, due to increased contact area, for inspection of curved samples (e.g. pipes).

In conclusion, for the length of waveguide used in this study, a knurling pattern (i.e. waveguides B and H) and a part threaded bolt with a hexagonal head (i.e. waveguide F) provide the greatest SNR with effective removal of the trailing echoes. Both of these waveguide types will be discussed in the next section with respect to incorporation into compression transducer designs.

6.3 High Temperature Transducer Design

The piezoelectric transducer design investigated within this study differs from conventional broadband transducers often used in the field of NDT; the design utilises a compressive force applied to the piezoelectric element, in addition to a backing material, to achieve acoustic coupling between the components and the desired damping characteristics via scattering, rather than a backing material attached to the piezoelectric element with an adhesive layer that primarily attenuates by absorption and scattering. For application at high temperature, the advantage of this design is in the ease of fabrication, where the use of polymer-based adhesive layers is not required, as these materials typically cannot survive high temperatures.

Application of compressive stress to the piezoelectric element is employed in sandwich type piezoelectric transducers (e.g. Langevin and Tonpliz transducers) which are widely used and their design theory is well developed [230]. Sandwich transducers have their piezoelectric elements arranged in stacks which are sandwiched between a head and tail mass with stressed applied via a central bolt. This configuration allows the transducer structure to have a longitudinal resonance, usually on the order of 1-100 kHz [230]. These types of transducers are commonly used in high power applications due to their high efficiency and large power output, for example: welding, cleaning, cutting and underwater acoustics.

On analysis of the literature, there appears to be limited published research on high frequency compression type piezoelectric transducers which employ a single piezoelectric element, specifically towards application in NDT and at high temperatures; as such, the work presented in chapters 6 and 7 aims to provide insight into the use of this compression type transducer design for ultrasound thickness monitoring at high temperatures. The remainder of this section provides a detailed review of the transducer compression design, the different transducer housings used within this study and the effects of compressive stress on the transducer performance.

6.3.1 Compression Transducer Assembly

All transducers in the experimental work use a 10 mm diameter piezoelectric disc as a proof of concept model, however the design can be easily adapted to house piezoelectric discs of different diameters, depending on the application requirements. For example, larger discs may be required to provide greater ultrasound energy output in challenging applications with highly attenuative components.

The schematic diagram in Figure 6.25 illustrates a close up view of this high temperature transducer design where the components are assembled and a

compressive force is applied with a central bolt. All components were machined from 304 stainless steel, except the central bolt, ceramic insulator, backing material and piezoelectric disc. Three transducers were constructed in this work and they have slightly different compression design and waveguide geometry; the schematic diagram in Figure 6.25 is the relevant design for the 30 mm diameter knurled flat end waveguide transducer (Tx1) and the 40 mm diameter knurled curved end waveguide transducer (Tx3), while the M20 bolt flat end waveguide transducer (Tx2) has a slightly different compression design, as explained in section 6.3.2.

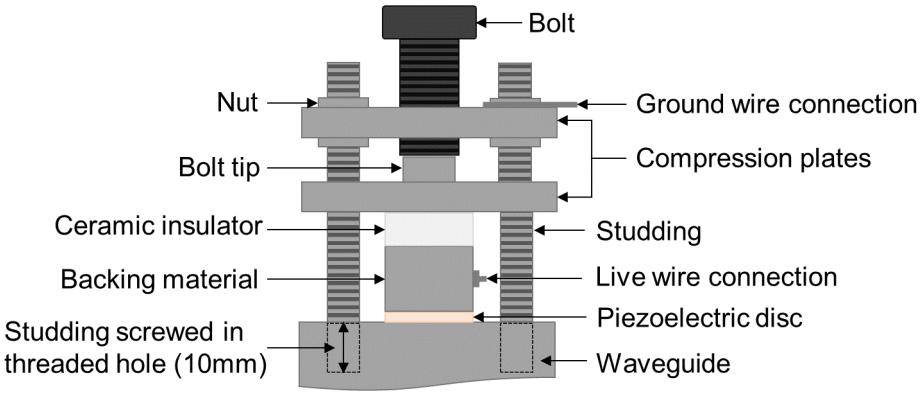

Figure 6.25: Schematic diagram of the transducer assembly design, not to scale.

The dimensions included in this description are for the 30 mm diameter knurled flat end waveguide transducer. The high tensile steel grade M8 central bolt, which has a flat machined end, is screwed into the M8 threaded hole in the top compression plate, which is locked in place via nuts on either side. The bolt end fits into a machined groove on the bottom compression plate, to ensure the correct central alignment; the bottom compression plate is free to move up and down with the central bolt. The compression plates are 8 mm thick and 30 mm in diameter. There are four threaded rods (termed studding) that are 4 mm in diameter, which connect the compression plates and central bolt to the waveguide via four 4 mm diameter and 10 mm deep threaded holes drilled into the waveguide, which is 60 mm in length. The location and dimensions of the threaded holes on the waveguides for Tx1 and Tx3 are shown in the schematic diagram in Figure 6.26. This is the system through which the compressive force is applied to the piezoelectric disc.

An insulating material is required in the current design to prevent short circuiting, such that the piezoelectric disc is properly electrically connected to generate and receive ultrasound. A machinable ceramic material was used, a glass ceramic termed Macor® (Corning, Inc.), due to its electrical insulating properties, high tem-

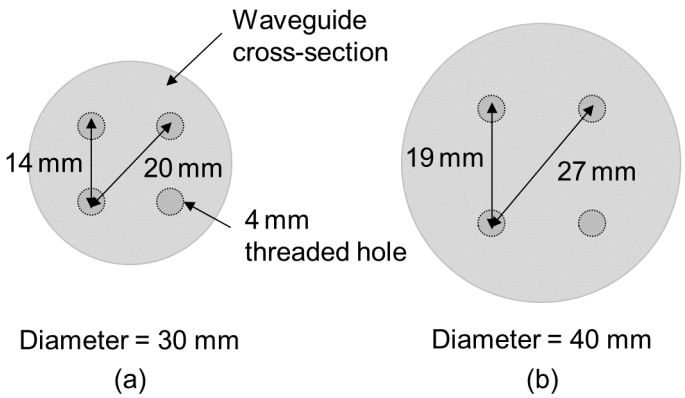

Figure 6.26: Schematic diagram of location and dimensions of the four threaded holes in the waveguide: (a) Tx1 and (b) Tx3.

perature performance and excellent machinability. The ceramic parts were 10 mm in diameter and machined to 8 mm at the top to fit into the groove on the bottom side of the bottom compression plate, again to ensure correct alignment of the compressive force.

The ceramic is connected to the backing material via compression. Different high temperature backing materials, all 10 mm in diameter were investigated within this transducer design, the results of which are detailed in section 6.5. High temperature metallic materials were chosen, such that they could withstand high temperature and large compressive stresses. The backing material front and back faces were machined to be as flat as possible, by hand polishing using different grit papers down to 1200 grit on a flat glass substrate.

The backing material is connected to the piezoelectric disc via compression, without the use of an adhesive materials. Different commercially available polycrystalline piezoelectric materials were used within this design, including PZT and high temperature piezoelectric materials, which are discussed in more detail in 6.4. All piezoelectric materials have a thin silver electrode layer on their front and back surfaces, to facilitate electrical connection.

Electrical connection is established within this transducer design by physical contact of electrical materials via the compression from the central bolt. The live electrical connection is made to the back face of the piezoelectric element, by contact with the conductive metallic backing material. The live wire is electrically connected to the backing material via clamping of the wire around a screw threaded into the backing material, or via a second conductive backing material at the back face of the backing material, with a threaded screw hole, which is clamped to the live wire; the

second backing material is used for backing materials which are difficult to machine a threaded hole. The ground electrical connection is made via clamping a wire around the washer and nut which connects the studding to the top compression plate. This electrical connection makes contact with the front face of the piezoelectric element via compression contact with the piezoelectric disc and the waveguide.

6.3.2 Different Transducer Designs

As described above, three different transducers were constructed in this work with slightly different compression designs and waveguide geometries, as follows: a 30 mm diameter knurled flat end waveguide transducer referred to as Tx1 within the text, see Figure 6.27(a), an M20 bolt flat end waveguide transducer referred to as Tx2 within the text, see Figure 6.27(b), and a 40 mm diameter knurled curved end waveguide transducer referred to as Tx3 within the text, see Figure 6.28. Table 6.3 displays the details of the three transducers for reference.

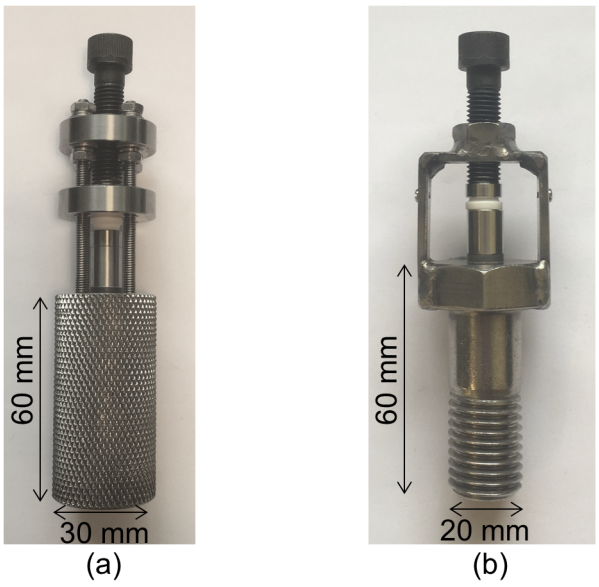

Figure 6.27: Side view photographs of transducer assembly designs: (a) 30 mm diameter knurled flat end waveguide transducer (Tx1) and (b) M20 bolt flat end waveguide transducer (Tx2).

The compression design of Tx2 is different to Tx1 and Tx3 in that compression plates and studding were not used to apply the compressive stress across the transducer components via the central bolt. The design was simpler as the stress was applied directly from the machined bolt tip to the ceramic insulator, through

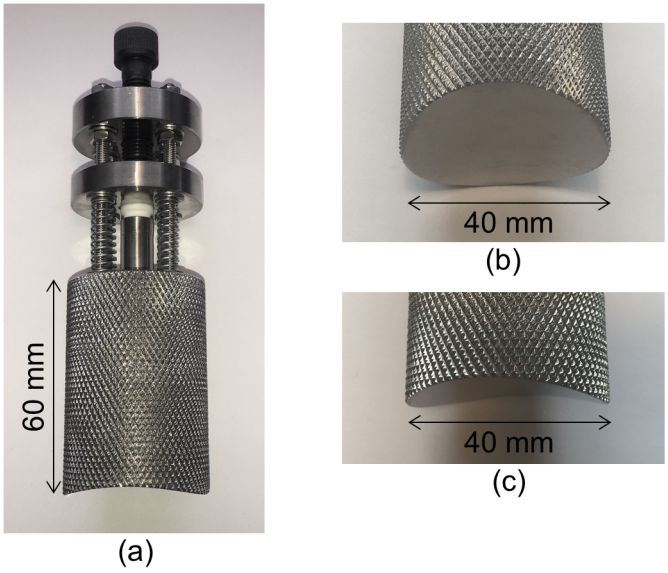

Figure 6.28: Photographs of Tx3 transducer assembly design which has a 40 mm diameter knurled curved end waveguide: (a) side view, (b) waveguide end view, and (c) waveguide end curved profile view.

Table 6.3: Description of the different transducer assembly designs.

Transducer	Waveguide Diameter (mm)	Description
Tx1	30	Knurled waveguide - flat end
Tx2	20	M20 hexagonal bolt waveguide (F) - flat end
Tx3	40	Knurled waveguide (H) - curved end

which it was transferred to the backing material and piezoelectric disc. The central bolt was connected to the waveguide via a frame (32 mm in length, 34 mm wide and 2.5 mm thick), with a central M8 nut serving as a threaded hole, which was welded together and to the hexagonal head of the M20 bolt waveguide. The M20 bolt waveguide is identical to waveguide F discussed in section 6.2.2.

The compression design of Tx3 is essentially the same as that described for Tx1 above, although the dimensions of the compression plates are larger, and springs were laid over the studding to prevent the bottom compression plate falling onto the waveguide during insertion of the various components. The waveguide for Tx3 is identical to the waveguide H discussed in section 6.2.2.

6.3.3 Effect of Stress on Ultrasonic Signals

Piezoelectric materials exhibit domain depolarization outside of certain environmental limits, including thermal depoling, electric depoling and mechanical depoling. Mechanical depoling describes the stress induced change in the polarisation state of a poled polycrystalline piezoelectric material, resulting in full or partial loss of the preferable polarisation orientation, and therefore the piezoelectric properties. The stresses required to result in mechanical depoling are often large, and it has been observed that a cycle of relatively low stress levels can result in an increase in the d_{33}, depending on the type of piezoelectric material [231].

It was observed during initial testing of this transducer design, that the signal amplitude decreased upon successive loading of the same piezoelectric disc by the central bolt, indicating mechanical depoling. To measure the effect of multiple rounds of compression on the same piezoelectric disc, the Tx3 housing was used with a 10 mm diameter 8.5 MHz PZT disc (PI Ceramic, PIC181) with a porous stainless steel foam backing material (see section 6.5). Six rounds of compression were applied, whereby for each round the disc was inserted into the transducer housing, the central bolt was tightened with a torque wrench set to 15 Nm and the signal recorded using the PR set-up descried in 6.1 (200 V, 5-6 MHz and 0 dB). After each round of compression the disc was removed from the housing. The peak-to-peak voltages of the first waveguide backwall at each round of compression are presented in the bar chart in Figure 6.29, and the values are given in Table 6.4. It was observed that the peak-to-peak voltage decreased over the first five rounds of compression from 1.79 V to 0.93 V, with a slight increase to 0.95 V on round six.

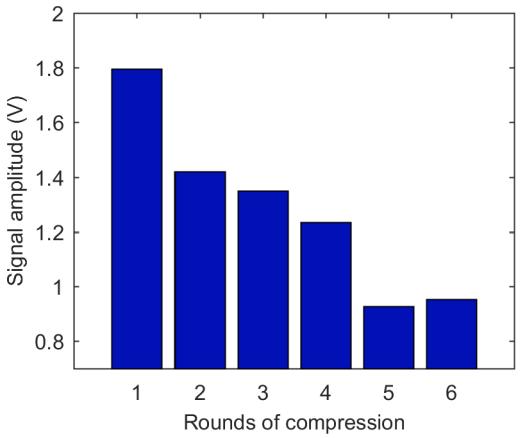

Figure 6.29: Signal amplitude (peak-to-peak voltage) of first waveguide backwall echo (W1) for multiple rounds of compression.

Table 6.4: Pk-Pk voltage of first waveguide backwall echo (W1) for six rounds of compression.

Round	Pk-Pk voltage (V)
1	1.79
2	1.42
3	1.35
4	1.23
5	0.93
6	0.95

In addition, the piezoelectric constant, d_{33}, was measured using a d_{33} meter (YE2730A, APC International, Ltd.) before and after the rounds of compression; the average d_{33} before was measured as 353×10^{-12}C/N and the average d_{33} after was measured as a decreased value of 233×10^{-12}C/N. Both the decrease in peak-to-peak voltage and d_{33} due to the stress applied within the transducer housing indicate mechanical depoling of the piezoelectric disc. As such, care must be taken when comparing the performance of the transducer, for example between different backing materials, to ensure the difference in performance is not due to mechanical depoling by multiple round of compressions. Therefore, within this work, as-supplied unstressed piezoelectric discs are used to compare transducer performance.

In order to provide a measurement of the change in the signal peak-to-peak voltage and SNR during the increase of stress via tightening the central bolt, the signal was recorded at multiple intervals during tightening. For this measurement, the transducer housing Tx3 was used with a 10 mm diameter lead metaniobate (PN) disc (Piezo Kinetics, Inc.) and a porous stainless steel foam backing (see section 6.5), using the PR system detailed in 6.1 (200 V, 5-6 MHz and 0 dB). The peak-to-peak voltage and SNR are displayed in the bar charts in Figure 6.30(a) and 6.30(b), respectively.

An increase in both the peak-to-peak voltage and SNR is observed by increasing the stress applied via the central bolt, where the peak-to-peak voltage continues to increase to a maximum value of 0.31 V, yet the SNR reaches a maximum at the ninth increment at 28.5 dB dropping slightly to 27.5 dB, and this may indicate depoling of the piezoelectric domains.

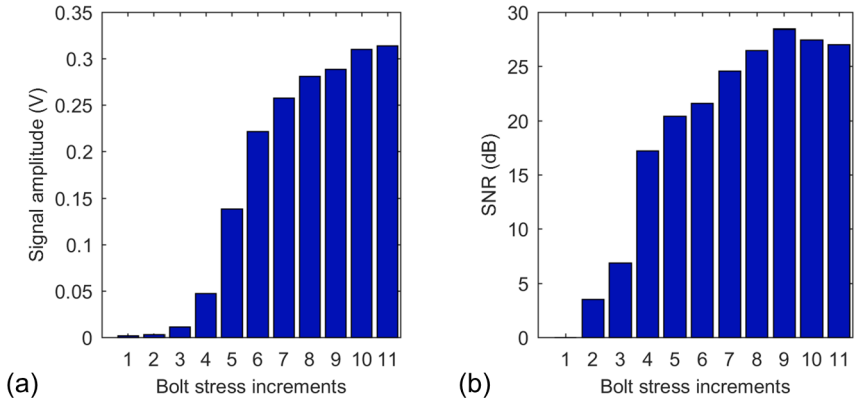

Figure 6.30: Effect of incremental increase of stress via tightening of the central bolt on Tx3 for the first waveguide backwall echo (W1): (a) peak-to-peak voltage and (b) SNR.

6.3.4 Transducer Performance at Room Temperature

The performance of the three different transducers (Tx1, Tx2 and Tx3) were compared at room temperature, using ultrasound pulse-echo measurements with the experimental setup described in section 6.1 (at 100 V, 5-6 MHz and -10 dB), where the transducers were coupled to the samples using a water-based ultrasonic couplant (SOUNDSAFE®, Diagnostic Sonar Ltd.). Commercially available PZT piezoelectric discs with 0.4 mm at $\approx$ 5.5 MHz centre frequency (Piezo Kinetics, Inc.), and pressed porous 316 stainless steel foam (Goodfellow), with 10 mm diameter and 15 mm thickness (see section 6.5 for details on backing materials), were used with each transducer design.

Two stainless steel samples were used, one flat and the other a section from a stainless steel pipe. The flat steel sample is pictured in Figure 6.31(a) which has 60 mm diameter and 9.8 mm thickness. The curved stainless steel pipe section is pictured in Figure 6.31(b), the original pipe has an outer diameter of 108 mm and the pipe section has a thickness of 6.2 mm. This pipe section used to achieve the curved end of waveguide H used in Tx3; the outer edges of the waveguide were machined to sit slightly above the pipe, to ensure good coupling across the central area of the waveguide curved end and the pipe section. The samples and waveguide end faces were hand polished down to 2500 grit. The performance was also compared with no sample present, using the signal reverberating within the waveguide, such that the effects of varying coupling parameters would not be present.

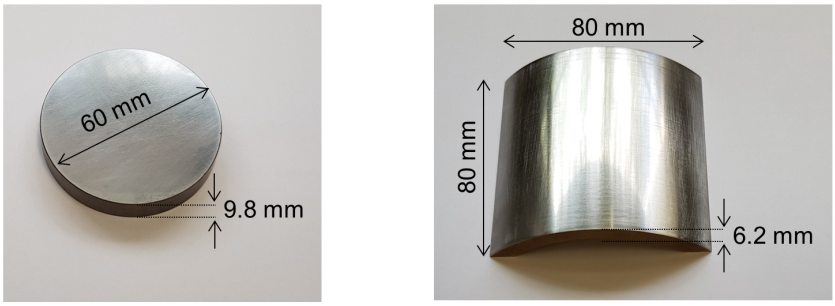

Figure 6.31: Photographs of stainless steel samples: (a) flat sample and (b) curved pipe section.

The A-scans with no sample present are given in Figure 6.32, with the flat sample in Figure 6.33, and with the curved sample in 6.34; Table 6.5 lists the corresponding peak-to-peak voltages and SNRs. Note for the "no sample" case the first waveguide backwall echo (W1) was taken, whereas for the case with a coupled sample the first sample backwall echo (4) was taken. Tx3 could not be tested on the flat sample due to the curvature, and the Tx2 data is not present in Figure 6.34 for the curved sample comparison, as no sample backwall echoes were detected.

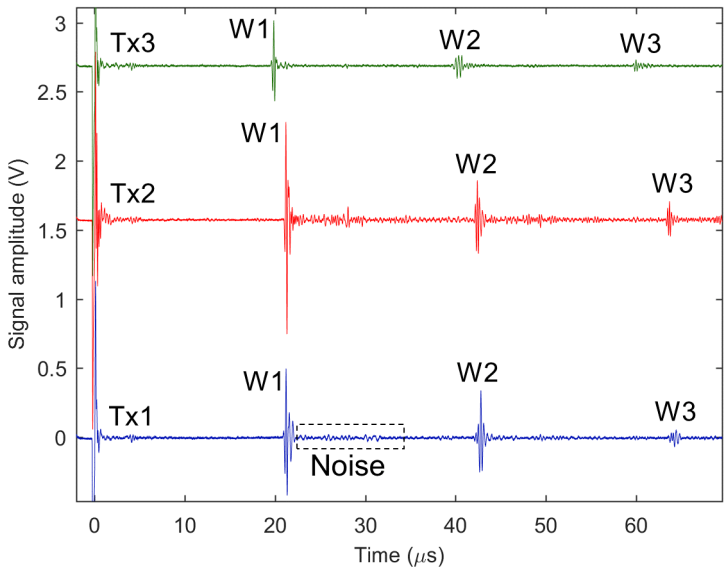

Figure 6.32: Signal amplitude at room temperature with no sample present for three different transducer assembly designs: Tx1 (blue), Tx2 (red) and Tx3 (green), with a label of the coherent noise region used to calculate the SNR.

For the case with no sample present, the peak-to-peak voltage is greatest for Tx2 at 1.53 V, compared to 0.920 V for Tx1 and 0.57 V for Tx3. However, when considering the SNR, Tx1 has a greater SNR of 22.7 dB compared to Tx2 at 19.4 dB, with 19.1 dB for Tx3. The SNR for Tx2 is less than expected due to raised noise floor from scattering of trailing echo signals by the thread pattern.

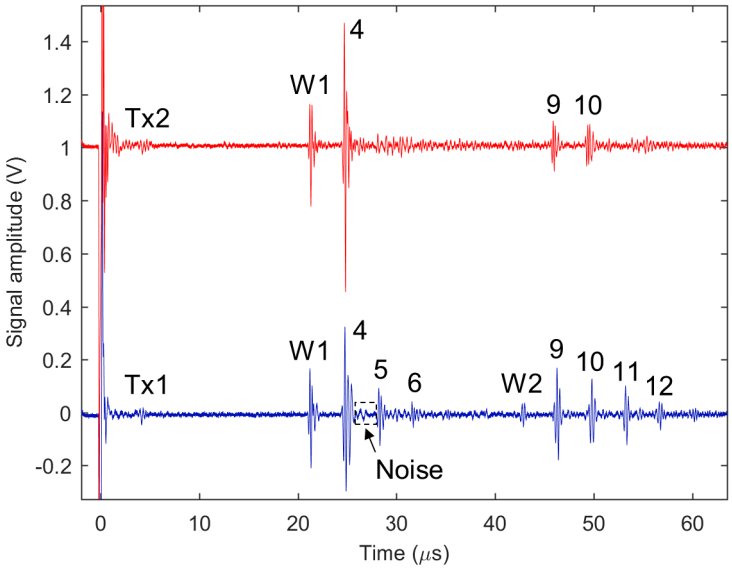

Figure 6.33: Signal amplitude at room temperature with coupling to the flat stainless steel sample for transducer assembly designs: Tx1 (blue) and Tx2 (red), with a label of the coherent noise region used to calculate the SNR.

On the flat sample (see Figure 6.33), for the first sample backwall echo (4), the peak-to-peak voltage for Tx2 is the greatest at 1.02 V compared to 0.62 V for Tx1. For this case, the SNR for Tx2 is slightly greater at 20.3 dB compared to 19.4 dB for Tx1; this is likely due to the region from which the maximum noise value was found, which was the region between sample backwall echoes, rather than the relatively high maximum scattering noise signal found with no sample. There is a greater number of sample backwall echoes (i.e. echoes 4, 5, 6, 9, 10, 11 and 12) for Tx1 than Tx2, which would be more favourable for use in inspections.

On the curved sample (see Figure 6.34), Tx3 clearly performed better than Tx1 with a peak-to-peak voltage of 0.31 V for Tx3 compared to 0.10 V for Tx1 and SNR for Tx3 of 13.4 dB compared to 8.14 dB for Tx1. Tx3 performed well on the curved sample as the curvatures matched, allowing increased coupling area, and therefore, more ultrasound energy can be coupled from the waveguide into the sample.

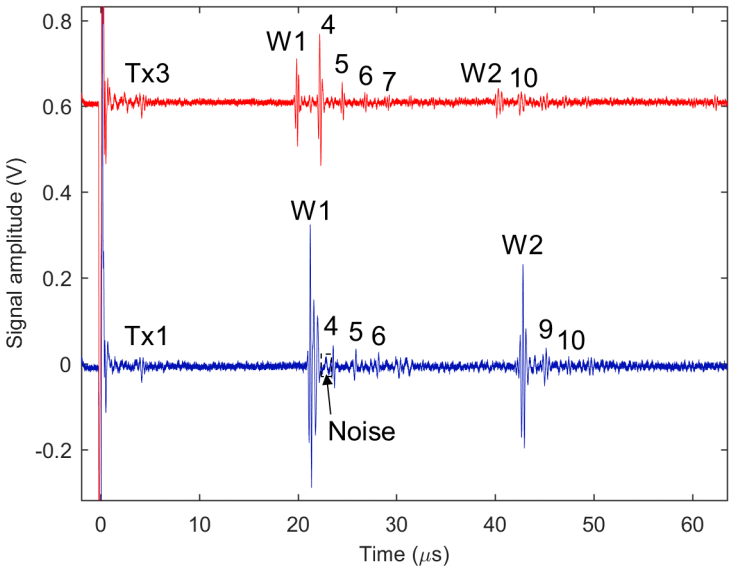

Figure 6.34: Signal amplitude at room temperature with coupling to the curved stainless steel sample for transducer assembly designs: Tx1 (blue) and Tx3 (red), with a label of the coherent noise region used to calculate the SNR.

Table 6.5: Pk-Pk voltage and SNR values from the transducer assemblies for no sample present (echo W1), and for flat and curved stainless steel samples (echo 4).

Transducer	No Sample		Flat Sample		Curved Sample	
	Pk-Pk (V)	SNR (dB)	Pk-Pk (V)	SNR (dB	Pk-Pk (V)	SNR (dB)
Tx1	0.92	22.7	0.62	19.4	0.10	8.14
Tx2	1.53	19.4	1.02	20.3	-	-
Tx3	0.59	19.1	-	-	0.31	13.4

6.4 High Temperature Piezoelectric Materials

This transducer design, detailed in section 6.3 above, can be used with a wide range of piezoelectric materials, here, the use of high temperature materials is of interest for application of ultrasound thickness measurements at elevated temperatures. Two commercially available piezoelectric materials with higher T_C than PZT were compared with this transducer design at room temperature, namely; lead metaniobate ($PbNb_2O_6$, PN) and bismuth titanate ($Bi_4Ti_3O_{12}$, BIT). These piezoelectric materials were discussed in section 1.5.1, along with other high temperature piezoelectric materials. PN has a T_C of $\approx 570\,^{\circ}C$, whilst BiT has a higher T_C of $\approx$

675 °C. Both piezoelectric materials were disc shaped with a diameter of 10 mm and thin silver electrodes deposited on each side. The PN (Piezo Kinetics, Inc.) were 0.33 mm thick, whilst BiT (Meggitt) 0.40 mm were thick.

The piezoelectric discs were characterised using electric impedance analysis, described in section 2.3.2, using an impedance analyser (4294A, Agilent). Figure 6.35(a) shows the impedance magnitude of a sample PN disc, whilst Figure 6.35(b) displays the phase, both across a frequency range of 4-6 MHz. Figure 6.36(a) shows the impedance magnitude of a sample BiT disc, whilst 6.36(b) displays the phase, both across a frequency range of 3-5 MHz. The peak in both figures is the first fundamental through thickness resonance, which is at ≈ 5 MHz for PN and ≈ 4.1 MHz for BiT. As expected, the phase angle away from resonance is close to -90 °, since piezoelectric elements generally behave as capacitors, which have an ideal purely capacitive phase angle of -90° between the voltage and current. The increase in the phase angle at resonance signifies the energy dissipation as the piezoelectric disc becomes more inductive. The peak phase angle is 38° for PN and 85° for BiT. The BiT appears to have various resonances occurring around the fundamental through thickness resonance, observed as many smaller peaks; these are likely due to harmonic resonances from radial and flexural modes of the disc.

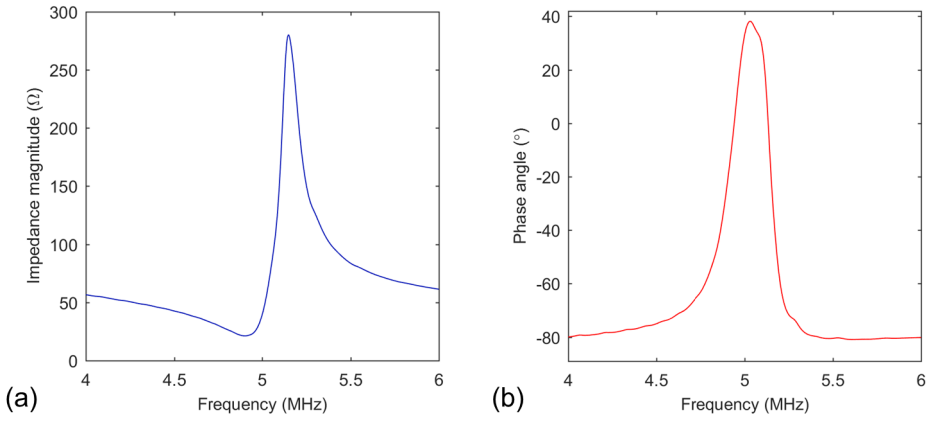

Figure 6.35: Electrical impedance of a lead metaniobate (PN) disc: (a) impedance magnitude and (b) phase.

The piezoelectric constant, d_{33}, was measured using a d_{33} meter (YE2730A, APC International, Ltd.). The discs were measured without any pre-stress, which could potentially change the polarization and lead to lower d_{33} values. PN was found to exhibit an average d_{33} value of 76×10^{-12}C/N , and BiT has an average d_{33} value of 20×10^{-12}C/N. These values agree with those reported in the literature [49, 50].

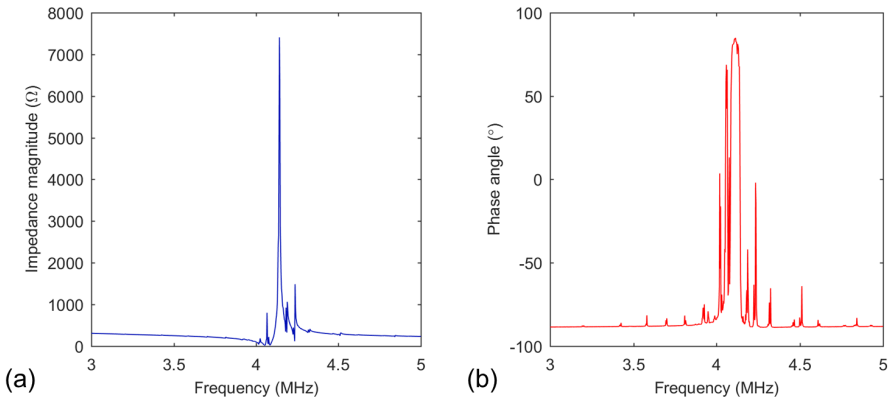

Figure 6.36: Electrical impedance of a bismuth titanate (BiT) disc: (a) impedance magnitude and (b) phase.

Table 6.6: Measured and calculated parameters of W1 for PN and BiT.

Material	d_{33} ($\times 10^{-12}$C/N)	Pk-Pk (V)	SNR (dB)	f_C (MHz)	BW (%)
PbNb	76	0.946	24.2	3.4	47
BiT	20	0.190	25.9	3.4	33

The ultrasonic performance of the two piezoelectric disc materials were compared in the Tx1 transducer housing (30 mm diameter knurled flat end waveguide transducer), using a pressed porous 316 stainless steel foam (Goodfellow), with 10 mm diameter and 15 mm thickness backing material (see 6.5 for details on backing materials). The PR system described in section 6.1 was used (200 V, 5-6 MHz and 0 dB), and the discs were compared with no samples present, to eliminate coupling effects. The A-scans in Figure 6.37 show the first three waveguide backwall echoes with no sample present for the PN and BiT discs, respectively. An FFT was applied to the first backwall echo to generate the frequency spectrum, given in Figure 6.38(a) and 6.38(b) for PN and BiT, respectively. Table 6.6 displays the data measured and calculated for PN and BiT for the first waveguide backwall echo, including: d_{33}, peak-to-peak voltage, SNR, centre frequency and bandwidth.

PN produces a greater peak-to-peak voltage than BiT, 0.946 V compared to 0.190 V, corresponding to the greater d_{33} value of PN compared to BiT. Despite this, the SNR for BiT is slightly greater at 25.9 dB compared to 24.2 dB. Both PN and BiT had a calculated centre frequency of 3.4 MHz, indicating the frequency content is dominated by the PR driving pulse. BiT exhibited a greater 3 dB bandwidth at 47% compared to 33% for PN. These results are promising for use of both PN and BiT in this transducer housing design for high temperature application.

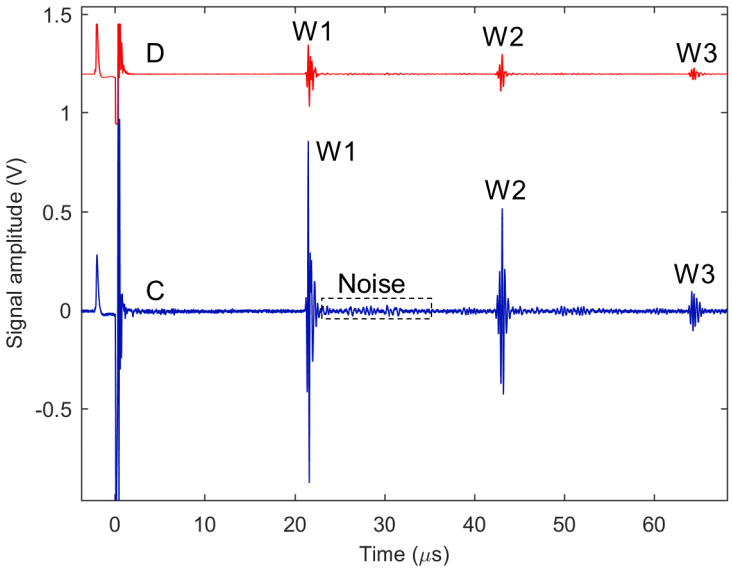

Figure 6.37: Signal amplitude at room temperature for Tx1 transducer housing with PN (blue) and BiT (red) piezoelectric discs showing waveguide backwall echoes (W1, W2 and W3), with a label of the coherent noise region used to calculate the SNR.

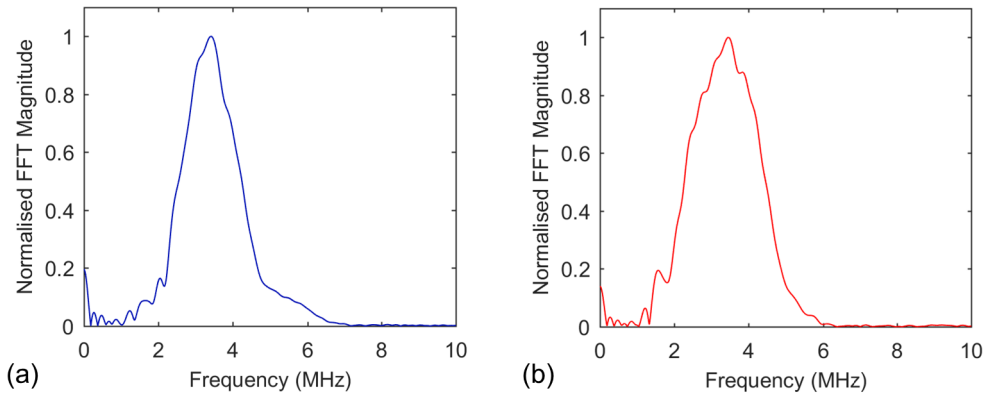

Figure 6.38: First waveguide backwall echo (W1) FFT magnitude spectrum: (a) PN, (b) BiT.

6.5 Backing Materials

A number of different metallic backing materials were investigated towards assessing their ability to effectively damp the vibrations of the piezoelectric disc and scatter reflections emitting from the piezoelectric disc back face. Electrically conductive materials were chosen to ensure a good electrical connection to the piezoelectric disc for the live wire, within the transducer housing design. All backing materials

chosen have high melting temperatures, to withstand the elevated temperatures in high temperature applications. The backing materials compared are listed, labelled *a* - *f*, with thickness and descriptions in Table 6.7, photographs of each are pictured in Figure 6.39 and the corresponding sound velocity, density and acoustic impedance values are given in Table 6.8. The longitudinal velocity was calculated (to 3 significant figures) using the time delay measured from a pulse-echo generated via coupling a 5 MHz commercial piezoelectric transducer (V109, Panametrics Inc.) coupled to the backing block with a liquid couplant (SOUNDSAFE®, Diagnostic Sonar Ltd.), using the experimental setup detailed in section 6.1. The density was calculated (to 3 significant figures) using the water immersion method using Archimedes principle using:

$$\rho_s = \rho_w \left(\frac{m_1}{m_1 - m_2} \right), \tag{6.2}$$

where ρ_s is the density of the sample, ρ_w is the density of water, m_1 is the dry mass and m_2 is the mass when the material is submerged under water.

Table 6.7: Backing material thickness and description.

Backing Material	Thickness (mm)	Description
a	12.0	Stainless steel
b	12.0	Brass
c	12.0	Porous tungsten
d	15.0	Porous stainless steel foam
e	13.0	Stainless steel with machined features: 1 mm D holes, circumferential ridges and a cone-shaped rear face
f	16.0	3 mm thick *d* at front face with *e* at the rear face

Backing materials *a* and *b* were machined from a larger blocks of 304 stainless steel and brass, respectively. Backing material *c* was formed from a commercially available porous tungsten materiel (Spectra-Mat, Inc), which was ordered at the specified geometry from the manufacturer, as tungsten is difficult to machine; the as-manufactured porosity of *c* was 18% (82% of tungsten by weight), with a density of 14140 kg/m^3. Backing material *d* was constructed from a commercially available porous 316 stainless steel foam (FE243840, Goodfellow), which was purchased as a 150 mm × 150 mm × 12.7 mm (W×L×D) sheet. As-supplied, the foam bulk density was 550 kg/m^3 with 93% porosity with 24 pores/cm. The foam was not able to support the compressive stress exerted by the transducer house design in the

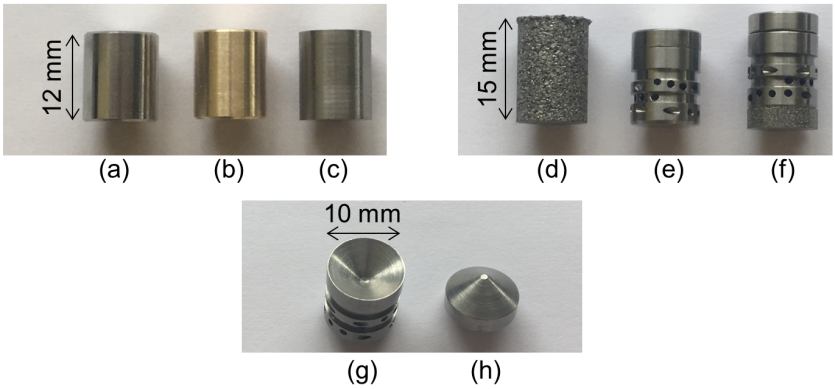

Figure 6.39: Images of backing material: (a) stainless steel - *a*, (b) brass - *b*, (c) porous tungsten - *c*, (d) porous stainless steel - *d*, (e) stainless steel with machined features - *e*, (f) porous foam backed with machined stainless steel - *f*, (g) top view of backing material *e* without cone back and (h) view of cone in backing material *e*.

Table 6.8: Backing material longitudinal velocity, density and acoustic impedance.

Backing Material	Longitudinal velocity, v_L (m/s)	Density, ρ (kg/m^3)	Acoustic Impedance, Z (MRayl)
a	5750	7940	45.6
b	4410	8400	37.1
c	4370	14100	61.8
d	-	3600	-
e	-	5980	-
f	5750	7940	45.6

as-supplied state without deformation, such that it was subject to a pressing in a uniaxial press to produce a much denser stainless steel foam. The supplied foam sheet was machined into a number of 10 mm diameter cylinders (12.7 mm in height), which were inserted into a 10 mm cylindrical die to form a backing material with a density of 3600 kg/m^3. The final backing material was 10 mm in diameter and 15 mm in height, able to withstand the stress exerted within the transducer compression design. Backing material *e* was machined from a 304 stainless steel cylindrical block, having three features to improve scattering of ultrasound, including: ridges around the circumference, randomly orientated 1 mm diameter through-holes and a cone shaped back (see Figures 6.39(g) and (h)). Backing material *f* was made from two parts, the first which interfaced with the piezoelectric disc is a 3 mm thick piece of pressed stainless steel foam (same material as *d*) pressed to a density of 5980 kg/m^3, and the same machined stainless steel used for backing material *e*.

Table 6.9: First waveguide backwall echo (W1) measured and calculated parameters for the different backing materials.

Backing Material	PkPk (V)	SNR (dB)	f_C (MHz)	BW (%)
a	0.63	6.8	2.6	35
b	0.66	10.8	2.6	35
c	0.66	10.7	3.0	46
d	1.42	23.7	2.7	34
e	0.42	10.2	2.5	36
f	0.87	19.2	2.7	37

The backing materials were machined to 10 mm in diameter, to compare their effectiveness at damping a 10 mm, 5.5 MHz PZT disc (Piezo Kinetics, Inc.), within the Tx1 transducer housing. The ultrasound performance of each backing material was compared by fabricating the transducer with a fresh PZT disc each time in the Tx1 transducer housing, and using the PR setup described in section 6.1 (200 V, 5-6 MHz and 0 dB). The ultrasound reverberating within the waveguide was used to compare between the backing materials, to eliminate coupling effects if a sample was used. Figures 6.40(a) - (f) display the A-scan of the first two backwall echoes (W1 and W2) for all backing materials, and Figures 6.41(a) - (f) show the calculated FFT magnitude from W1 for all backing materials. The measured and calculated ultrasound parameters from the W1 are presented in Table 6.9.

The peak-to-peak voltage of all the backing materials was the greatest, by a significant margin at 1.42 V, for backing material *d*, followed by backing material *f* at 0.870 V. Backing materials *a*, *b* and *c* observed similar peak-to-peak voltage values at 0.633 V, 0.664 V and 0.662 V, respectively. The lowest peak-to-peak voltage was observed for backing material *e* at 0.419 V. However, the peak-to-peak voltages do not directly correspond to the SNR values, as the coherent noise level varies significantly between the different backing materials. Backing material *d* calculated the highest SNR value at 23.7 dB, followed by backing material *f* at 19.2 dB. Backing materials *b*, *c* and *e* calculated similar SNR values at 10.8 dB, 10.7 dB and 10.2 dB, respectively. The lowest SNR was calculated for backing material *a* at 6.83 dB. It is also evident that for backing materials *a*, *b* and *c* there are clear signal peaks in the region between the electrical noise, created by the driving pulse, and the first backwall echo (W1); these are likely a result of reverberations within the backing material, as these materials are not sufficiently attenuative to absorb or scatter the ultrasound signal which radiates from the back face of the piezoelectric disc.

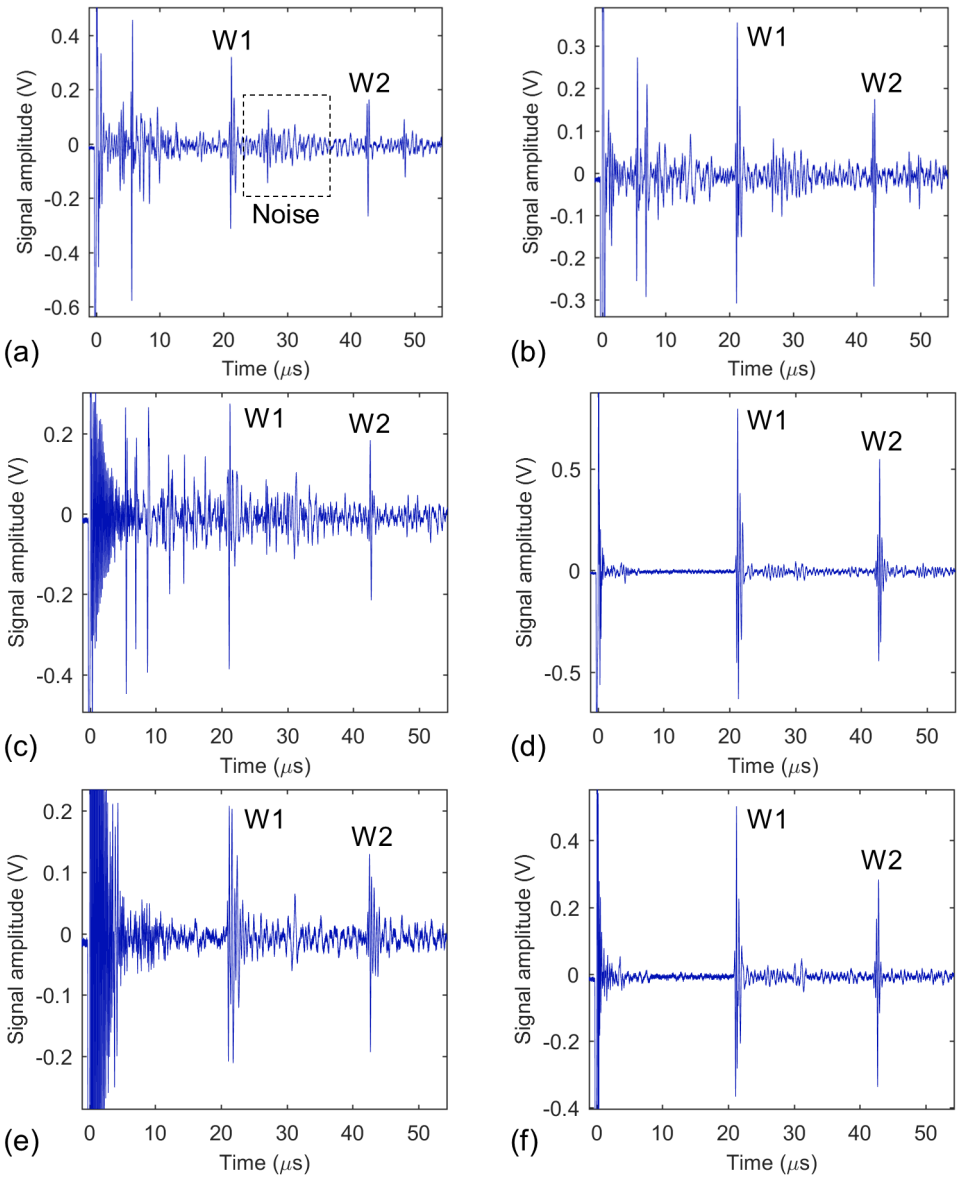

Figure 6.40: Signal amplitude showing first two backwall echoes (W1 and W2) of all backing materials: a) stainless steel - *a*, b) brass - *b*, c) porous tungsten - *c*, d) porous stainless steel *d*, e) stainless steel with machined features - *e* and f) porous stainless steel (front) and stainless steel with machined features (rear, i.e. *e*), with a label of the coherent noise region used to calculate the SNR.

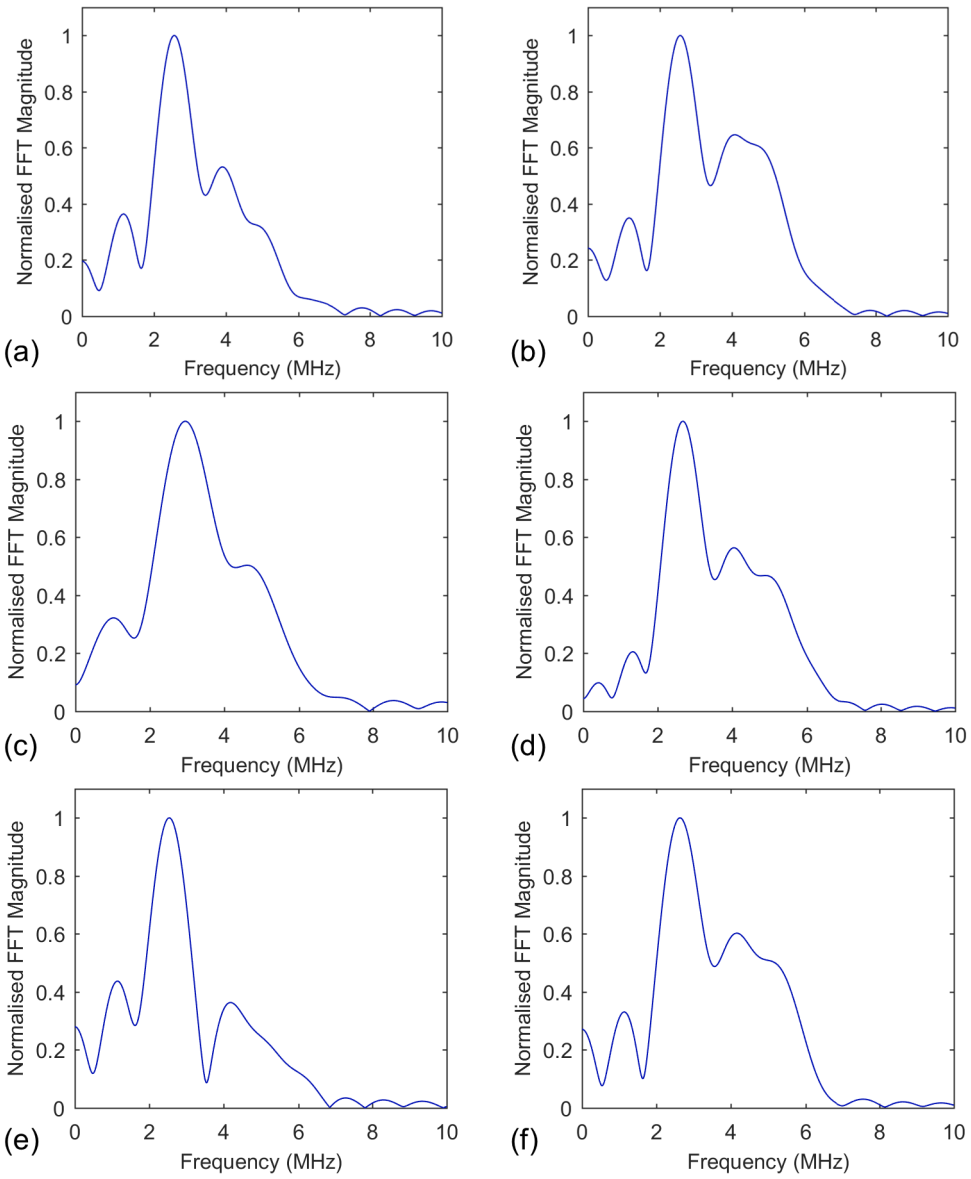

Figure 6.41: Waveguide first backwall echo (W1) FFT magnitude spectrum for all backing materials: a) stainless steel - *a*, b) brass- *b*, c) porous tungsten - *c*, d) porous stainless steel - *d*, e) stainless steel with machined features - *e* and f) porous stainless steel (front) and stainless steel with machined features (rear, i.e. *e*).

The centre frequency for backing material c was the highest at 3.0 MHz. The centre frequencies for the other backing materials were similar at 2.6 MHz, 2.6 MHz, 2.6 MHz, 2.7 MHz, 2.5 MHz, and 2.7 MHz for backing materials *a*, *b*, *d*, *e* and *f*, respectively. The bandwidth of backing material c, porous tungsten, was the greatest at 46 %, whilst the bandwidth for the other backing materials *a*, *b*, *d*, *e* and *f* were similar at 35 %, 35 %, 34 %, 36 % and 37 %, respectively.

To confirm the origin of the different echoes observed from the backing material signals displayed in Figure 6.40, a PZFlex model was constructed in 2D to represent the transducer Tx1 assembly with two different types of backing materials, to model the results from backing materials *a* and *d*. To model material *d* a homogeneous material was assumed with a single equivalent set of material parameters. The model geometry used is given in Figure 6.42, and other model input parameters were identical to those described in detail in section 6.2.1 for PZFlex 2D modelling of the waveguide, excluding the longitudinal velocity value in the Tx1 transducer waveguide, which was input as the experimentally measured value of 5601 m/s, and a Rickert wavelet was the input function chosen for the pressure load.

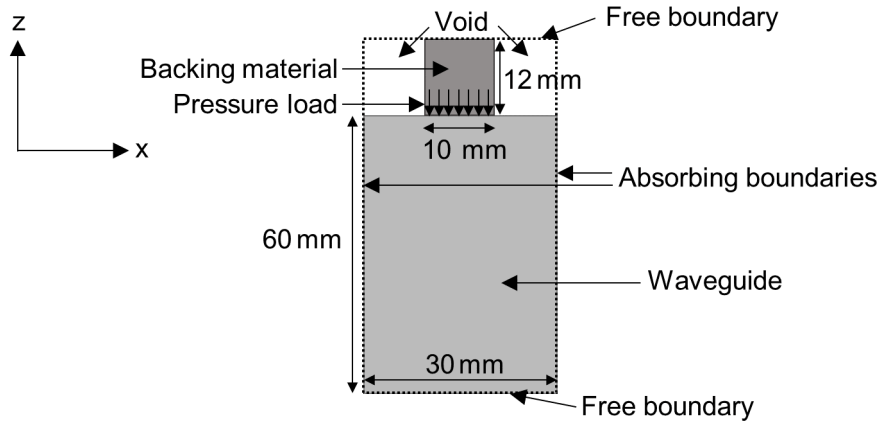

Figure 6.42: Schematic diagram of the 2D finite element model used in PZFlex to simulate the propagation of the ultrasonic waves within a simplified interpretation of the Tx1 transducer assembly, showing the backing material and knurled waveguide approximated by absorbing boundaries.

The material input parameters for backing material *a* as stainless steel were $\rho = 7395\,\mathrm{kg/m^3}$, $\mathrm{v_L} = 5751\,\mathrm{m/s}$ and $\mathrm{v_S} = 3100\,\mathrm{m/s}$, and for backing material *d* as highly attenuative stainless steel $\rho = 7395\,\mathrm{kg/m^3}$, $\mathrm{v_L} = 5751\,\mathrm{m/s}$ and $\mathrm{v_S} = 3100\,\mathrm{m/s}$). PZFlex models attenuation by specifying viscous damping parameters for a linear elastic material to convert it to a viscoelastic material, using an attenuation factor (dB/m) at a specified centre frequency, for longitudinal (α_L) and shear

(α_S) waves. The attenuation factor used to model backing material a was taken as the value for stainless steel, given by the built in PZFlex general material file, such that $\alpha_L = 0.3\,\mathrm{dB/m}$ and $\alpha_S = 1.2\,\mathrm{dB/m}$. The attenuation factor used to model backing material d was taken as the value for a highly attenuative tungsten-araldite composite (25 % volume fraction tungsten powder) backing, given by the built in PZFlex general material file, such that $\alpha_L = 290\,\mathrm{dB/m}$ and $\alpha_S = 870\,\mathrm{dB/m}$; this material was chosen as a simple method to model a highly attenuating material, despite the fact that this material will attenuate more by a combination of absorption and scatter, rather than the stainless steel foam, which is predicted to attenuate ultrasound predominantly via scattering, as it would be difficult to accurately model the complex nature of the porosity in the stainless steel foam.

Similarly to the waveguide modelling results, the A-scans presented were generated by calculating the average element y-velocity across the loading surface, to simulate the response from a piezoelectric transducer operating in pulse-echo mode; the resulting A-scan with stainless steel as the backing material is given in Figure 6.43, and the results with the attenuative material are given in Figure 6.44.

Considering the differences between the experimental conditions and the 2D model, such as the compressional stress on the piezoelectric disc exerted by the central bolt, the knurled pattern on the waveguide-air boundary and the difference in material properties between the attenuative backing and the stainless steel foam, there is a good correlation between the experimental and simulated A-scans. For the stainless steel backing material a, in both the experimental and simulated data there is a high amplitude, well defined echo at $\approx 6\,\mu$s, which can be identified as the first backwall echo from the rear face of the backing material, originating from the ultrasound energy which coupled into the backing material at the point when the pressure load is applied. This is followed in both A-scans by a region of lower amplitude peaks, identified as various reflected and scattered bulk waves from the backing material air boundary, which are not attenuated within the backing material. The first waveguide backwall echo (W1) is visible in both A-scans at $\approx 22\,\mu$s, followed by another backwall echo from the rear of the backing material at $\approx 27\,\mu$s, and then a region of lower amplitude peaks resulting from various reflected and scattered bulk waves within the backing material.

For the stainless steel foam backing material d, in both the experimental and simulated data there are two well defined echoes at $\approx 22\,\mu$s and $44\,\mu$s, which can be identified as the first waveguide backwall echo (W1) and second waveguide backwall echo (W2), respectively. In both A-scans there are no distinctive backwall echoes from the rear face of the backing material, as reflected and scattered bulk

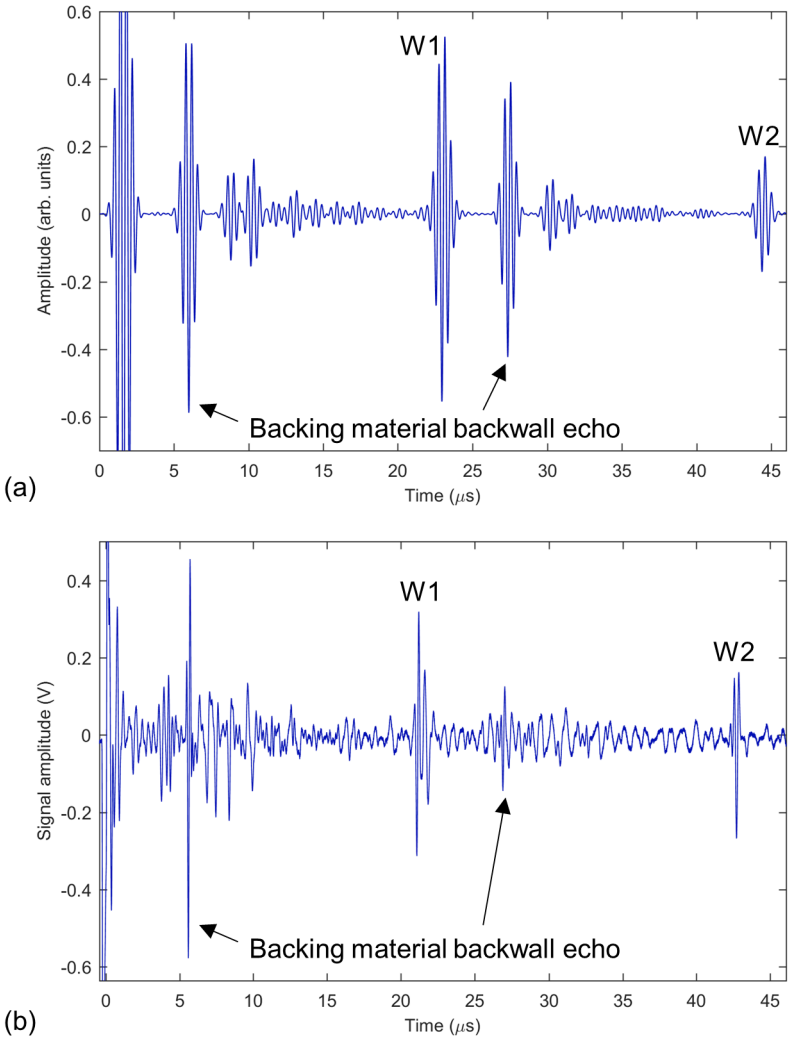

Figure 6.43: Backing material *a*: (a) simulated A-scan from the 2D model showing element z-velocity against time and (b) experimental signal amplitude, where the first (W1) and second (W2) waveguide backwall echoes are observable, alongside backing material backwall reflections and regions of noise from scattered wave modes within the backing material.

waves within the backing material are attenuated. The main difference between the experiential and simulated data is the increased coherent noise level after W1 and W2 visible for backing material *d*, and this is due to the scattered waves caused by the knurled waveguide-air boundary, which disrupts the constructive and destructive interference that results in trailing echoes along the waveguide (as described in section 6.2.2); the absorbing boundary does not aim to fully mode the scattering behaviour of the knurled boundary, only the removal of the trailing echoes.

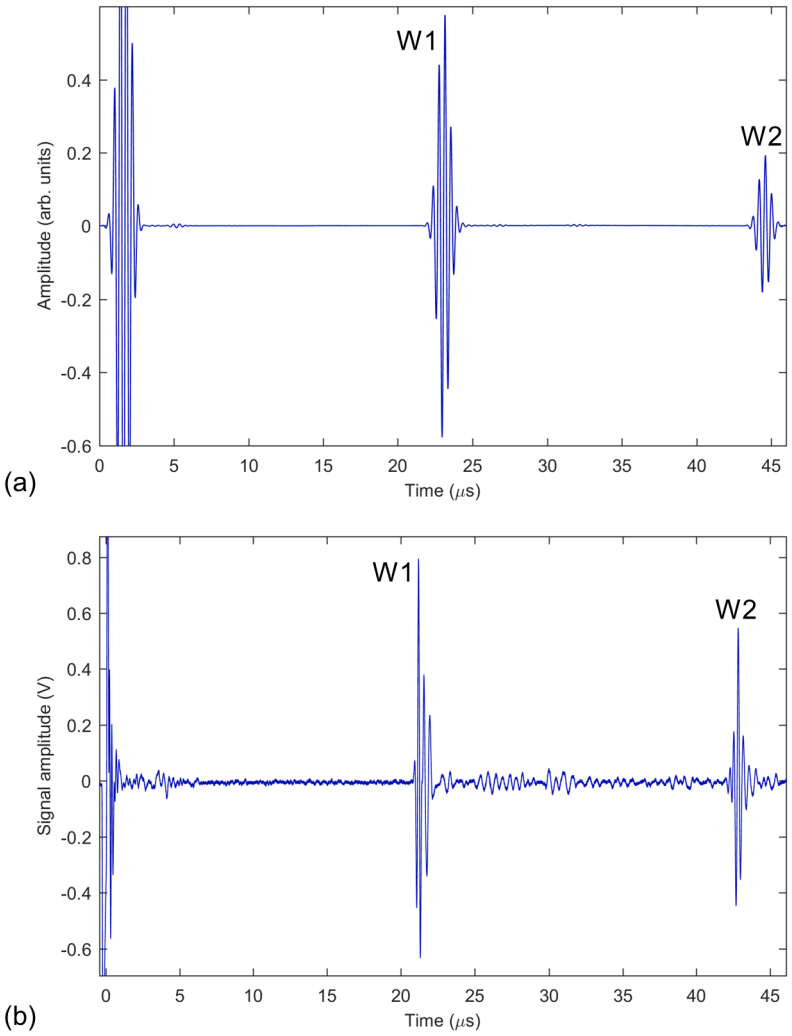

Figure 6.44: Backing material *d*: (a) Simulated A-scan from the 2D model showing element z-velocity against time and (b) experimental signal amplitude, where the first (W1) and second (W2) waveguide backwall echoes are observable.

The difference in noise level between the backing materials can be predominantly attributed to the relative difference between their attenuative properties, where attenuation of backing materials *a*, *b*, *c* and *d* is not sufficient to remove undesirable reverberations, reflections and scattering of wave modes within the backing material to efficiently reduce the coherent noise floor of the signal. Backing materials *d* and *f*, for which the highly scattering stainless steel foam interfaces the back of the piezoelectric disc, are more able to attenuate these undesirable signals. It was expected that the as-manufactured porosity in backing material *c* would have

resulted in a high degree of scattering centres, and that the random orientation of drilled holes backing material *e* would also provide sufficient scattering centres to attenuate the ultrasound waves within the backing material. However, it is evident from these results that the porous structure within the stainless steel foam provides a much greater degree of attenuation, presumably due to a vast number of scattering centres.

The highest SNR values were calculated for backing material *d*, followed by *f*, as a combination of the attenuative stainless steel foam scattering the undesirable signals, and the increased peak-to-peak voltage measured for both *d*, followed by *f*, compared to the other materials. It is thought that the increase observed for the peak-to-peak voltage of W1 for *d* and *f* is a result of increased contact area between the piezoelectric disc and the backing material, as it was recognised earlier from Figure 6.30a in section 6.3.3 that increase in stress on the piezoelectric disc increased the peak-to-peak voltage. The increase in contact area may be due to the ability of the stainless steel foam material to more readily plastically deform at the interface, resulting in increased conformity of the surfaces at the interface, as opposed to the other backing materials which are more rigid. With this reasoning, it could assumed that the other backing materials would have relatively similar peak-to-peak voltages, which is true for backing materials *a*, *b* and *c*. Yet, the peak-to-peak voltage for backing material *e* is lower than expected, as it would be expected to be similar to that of backing material *a* as they are machined from the same batch of 304 stainless steel; however, this difference is assumed to be due to a difference in the surface roughness, such that *e* has a lower contact area with the piezoelectric disc, resulting in a lower stress on the disc and a decrease in the peak-to-peak voltage.

According to these results, the porous stainless steel foam (backing material *d*) will was used for evaluating the performance of the transducer both at room temperature and at elevated temperatures, as detailed in chapter 7.

6.6 Summary

This chapter presents an overview of the design, modelling, fabrication and room temperature testing of the high temperature piezoelectric transducer assembly. The ultrasound transducer pulser-receiver system and experimental setup used to generate, measure and record the data presented in this chapter were discussed for reference, including the settings used to make all measurements (see section 6.1).

This chapter included a detailed analysis of the waveguide incorporated in this high temperature transducer design. The waveguide is an integral component within the transducer design, as it provides a mass to which a compressive load can be applied across the piezoelectric disc, wear protection for the piezoelectric disc from contact with the sample and a degree of heat protection from a hot sample. However, as a waveguide of 60 mm length was chosen, the issue of trailing echoes has to be addressed within the design to prevent them from interfering with desired echoes from the sample (refer to section 6.2). Both 2D and 2D axisymmetric finite element modelling of the waveguide was performed in PZFlex to investigate the trailing echo formation (see section 6.2.1), the absence of trailing echoes with an absorbing waveguide-air boundary and the confirmation that the predominant longitudinal wave mode propagating along the waveguide could be approximated as a bulk longitudinal wave.

Alongside this, an experimental investigation was performed to draw a comparison between different waveguide geometries, towards selection of appropriate waveguides for incorporation in the high temperature transducer design to effectively remove the trailing echoes (see section 6.2.2). It was determined that a waveguide with a knurled pattern along its boundary gave the greatest SNR when including the coherent noise level generated by the scattering of waves by the knurled boundary, followed by a M20 hexagonal head bolt with a thread pattern along half the bolt tail and a knurled waveguide with a curved end-face that conformed to the radius of curvature of a pipe sample. These three waveguides were incorporated in to the transducer design to form three different transducer assemblies which were compared at room temperature (detailed in to section 6.3.2).

The piezoelectric transducer design investigated within this study differs from conventional broadband transducers often used in the field of NDT; the design utilises a compressive force applied to the piezoelectric element to achieve acoustic coupling between the transducer components. On analysis of the literature, there appeared to be limited published research on high frequency compression type piezoelectric transducers which employ a single piezoelectric element, specifically towards

application in NDT and at high temperatures; as such, the work presented in this chapter and chapter 7 aimed to provide insight into the use of this transducer design for ultrasound thickness monitoring at high temperatures.

The transducer assembly design and role of internal components was discussed at length in section 6.3.1. It was shown that all components (waveguide, piezoelectric disc and backing material) are acoustically coupled under compressive stress from a central bolt, negating the need for adhesive layers, such that all components are able to withstand high temperatures continuously without cooling (depending upon the T_C of the piezoelectric element). This type of transducer is suitable for both portable and permanent high temperature inspections, and the piezoelectric element chosen can be tailored depending upon the application requirements. It was found that the signal amplitude increased with increase in torque applied to the central bolt (see section 6.3.3). Although, multiple round of compression on the same piezoelectric disc resulted in depoling, such that comparisons made of the design (e.g. between different assembly designs, piezoelectric materials, and backing materials) must all use a non-stressed piezoelectric disc from the same batch and supplied, otherwise changes in the signal amplitude may be due to depoling of the piezoelectric material.

In this chapter, two commercially available piezoelectric materials with high T_C values were compared with this transducer design at room temperature, namely; lead metaniobate (PN) and bismuth titanate (BIT). It was found that although lead metaniobate observed a much higher piezoelectric constant (d_{33}) than bismuth titanate, the resulting SNR from the first waveguide backwall echo were similar. Highlighting the capability of this transducer design to work efficiently with a range of different piezoelectric materials; the choice of piezoelectric material can be tailored to the requirements of the application.

Finally, a number of different metallic backing materials were investigated in this chapter, towards assessing their ability to effectively damp the vibrations of the piezoelectric disc and scatter reflections emitting from the piezoelectric disc back face. Electrically conductive materials were chosen to ensure a good electrical connection to the piezoelectric disc for the live wire, within the transducer housing design. Additionally, all backing materials studied exhibit high melting temperatures, to withstand the elevated temperatures in high temperature applications. It was found that a backing material formed from a commercially available porous stainless steel foam, further pressed to form a denser foam, provided the greatest SNR of all the backing materials for use in the transducer assembly. It was concluded that the foam material performed best due it its ability to effectively

attenuate ultrasound wave emitting from the rear face of the piezoelectric disc; the highly attenuative properties of this material are attributed to scattering, rather than absorption, and it was presumed that the porous nature of the foam resulted in a large number of scattering centres. As a result of these trials, the stainless steel foam was used in high temperature trials of this transducer design, as detailed in the following chapter.

Chapter 7

High Temperature Performance of Piezoelectric Transducers

This chapter provides an overview of the high temperature testing of the compression-type piezoelectric transducer design introduced in chapter 6. The results of a trial using a hot plate and commercial high temperature liquid couplants are presented in section 7.1. This leads onto a review of a series of high temperature furnace trials performed in section 7.2. First, the dry coupling clamping setup used to maintain acoustic coupling at elevated temperatures is detailed in section 7.2.1. The results of high temperature trials using both aluminium foil (see section 7.2.2) and nickel foil (see section 7.2.4) to improve coupling efficiency at the transducer-sample interface are discussed. The longer-term high temperature performance of the transducer is reviewed in section 7.2.5, along with the high temperature performance of the transducer assembly with no sample present in section 7.2.6. Finally, a preliminary high temperature trial using a pipe clamping setup is discussed in section 7.2.7.

7.1 Hot Plate Trial

This section details the high temperature performance of the transducer design in trials using a hot plate to supply the heat to the sample. The hot plate trials differ to the high temperature trials using a furnace, as described in section 7.2, in that there is a temperature distribution between the transducer, which is at room temperature at the start of the trial, and the hot sample, rather than both the sample and transducer being heated to temperature in the furnace.

The aim of studying the performance of this transducer design using a hot plate setup is to model portable type high temperature inspections carried out in industry, where high temperature couplants are often used for a short period of time to obtain a reading. These types of inspections typically require cooling of the transducer between inspections, depending on the length of operation time at the maximum operating temperature of the transducer, as specified by the manufacturer; for example, high temperature dual element transducers (e.g. D790-SM) sold by Olympus [232] are rated for use up to 500 °C, although the recommended duty cycle for temperatures between 90 °C - 500 °C is less than ten seconds with one minute air cooling between measurements.

As described in section 1.5.3, for short term applications at elevated temperatures, high temperature couplants can be used to achieve acoustic coupling between the transducer and sample. The couplants used in these hot plate trials are proprietary pastes and fluids manufactured by Olympus (H-2, a thick grease [233]), Sonotech (Pyrogel®, a thick gel 100 [234]) and Echo Ultrasonics (EchoTherm Extreme™ a very thick paste [235]). Table 7.1 displays the maximum operating temperature and auto ignition temperature for each couplant used. The autoignition-temperature is the temperature above which the couplant can auto-ignite, and has important repercussions for the safety of any high temperature inspection carried, particularly in an industrial environment. Therefore, care must be taken that the couplant chosen has a greater auto-ignition temperature than the temperature of the inspection to avoid fires. The hot plate trials were carried out at 350 °C, which is lower than the auto-ignition temperatures for each of the couplants used, and is also within their operating temperature range.

Table 7.1: Ultrasound couplant maximum operating and auto-ignition temperatures.

Couplant	Operating Range (°C)	Auto-Ignition Temperature (°C)
EchoTherm Extreme™	-40 - 675	732
Pyrogel® 100	-45 - 429	479
Olympus H-2	Up to 398	417 - 449

For the trials, the hot plate (PC-400D, Corning) was set to 450 °C, as this corresponded to a surface temperature of ≈ 350 °C on the flat, 9.8 mm thick, stainless steel sample, described in section 6.3.4, when placed in the centre of the hot plate; the surface temperature of the sample was measured using a K-type thermocouple probe. The pulser-receiver system detailed in 6.1 was used (400 V, 7.5 MHz and

0 dB). The transducer Tx1 (detailed in section 6.3.1) was assembled with a 4 MHz BiT piezoelectric disc (described in section 6.4), and a stainless steel foam backing material (discussed in section 6.5).

The following procedure was repeated for each high temperature measurement taken using the hot plate, to ensure repeatability. Before each measurement, the temperature was recorded at the centre of the sample surface, and a small bead of couplant was placed directly at the centre of the waveguide face on the transducer. Then, the transducer was pushed down onto the centre of the hot sample with a uniform force, in order to evenly spread the couplant towards the edge of the waveguide face. The transducer was moved back and forth slightly over the surface to obtain the thinnest uniform layer of couplant as possible, to increase the transmission of ultrasound; the resulting waveform was recorded using the oscilloscope. After each measurement, the couplant was removed from the sample and allowed to reach temperature, and the transducer waveguide was placed into a small beaker of water to cool the transducer to room temperature before the next measurement. Due to the variability of the signal observed with each couplant, as a result of the degree of coupling (effected by layer thickness, force etc.) each couplant was tested three times.

The maximum signal obtained from each high temperature couplant are displayed in Figure 7.1, where Olympus H-2 is in blue, Pyrogel® 100 is in red and EchoTherm Extreme™ is in green; the corresponding peak-to-peak voltage, SNR, centre frequency and bandwidth of the first sample backwall echo (4) at $\approx 350\,^{\circ}\mathrm{C}$ are presented in Table 7.2.

Table 7.2: Measured and calculated parameters of the first sample backwall echo (4) for each high temperature couplant at $\approx 350\,^{\circ}\mathrm{C}$.

Couplant	Pk-Pk Voltage (V)	SNR (dB)	f_C (MHz)	BW (%)
EchoTherm Extreme	0.09	14.5	3.8	60
Pyrogel 100	0.19	20.0	3.9	56
Olympus H-2	0.26	23.7	3.9	58

From the results above, it is clear that transducer Tx1 is able to produce well defined signals suitable for portable high temperature thickness measurements using high temperature couplants, at least under the conditions specified in this trial. The results also show that the effectiveness of the high temperature couplant has a significant impact on the peak-to-peak voltage and SNR of the first sample backwall signal (4), where the Olympus H-2 couplant appeared to perform best

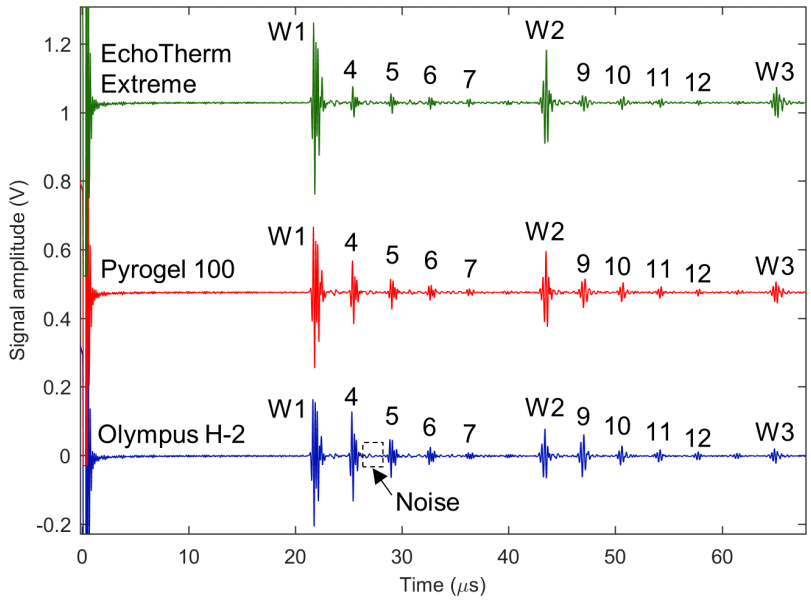

Figure 7.1: Signal amplitude using the hot plate on the flat stainless steel sample with a surface temperature of 350 °C for each high temperature couplant used: (blue) Olympus H-2, (red) Pyrogel® 100 and (green) EchoTherm Extreme™, with a label of the coherent noise region used to calculate the SNR.

with a SNR of 23.7 dB, compared to 20.0 dB with Pyrogel® 100 and 14.5 dB with EchoTherm Extreme™. Unlike the other couplants, the Olympus H-2 couplant was quick to burn off and form a thin brown layer on the sample surface if left on for more than 20-30 seconds. Figure 7.2 displays the signal amplitude results with the EchoTherm Extreme™ couplant, with a focus on showing the shape of the signals, which is not as clear in Figure 7.1.

To study changes in transducer performance before and after the hot plate trial, the signal amplitude produced with no sample present was recorded at room temperature before and after. The signal amplitudes are given in Figure 7.3, along with the corresponding peak-to-peak voltage, SNR, centre frequency and bandwidth of the first waveguide backwall echo (W1) displayed in Table 7.3. There appears to be no significant change in signal amplitude between the transducer before and after the hot plate trial, although there is a very slight increase in the peak-to-peak voltage after at 0.68 V compared to 0.67 V; this could be attributed to an improvement in the coupling at the waveguide-piezoelectric disc interface, due to the heat from the hot plate trial, however, the 0.01 V difference could be within the quantisation error from the digitisation of the signal by the oscilloscope.

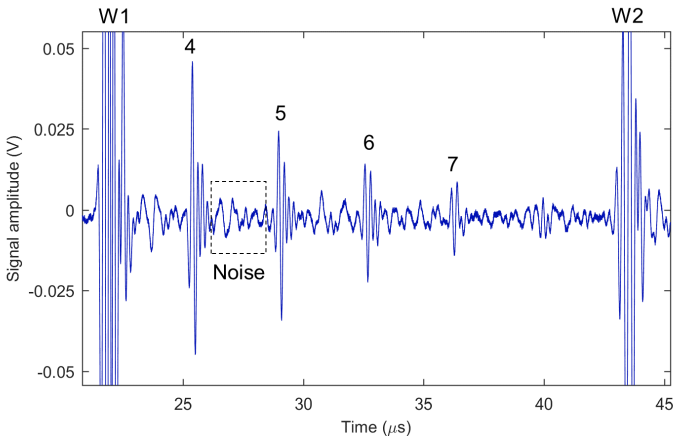

Figure 7.2: Signal amplitude of the first sample backwall echo (4) using the EchoTherm Extreme™ high temperature couplant, with a label of the coherent noise region used to calculate the SNR.

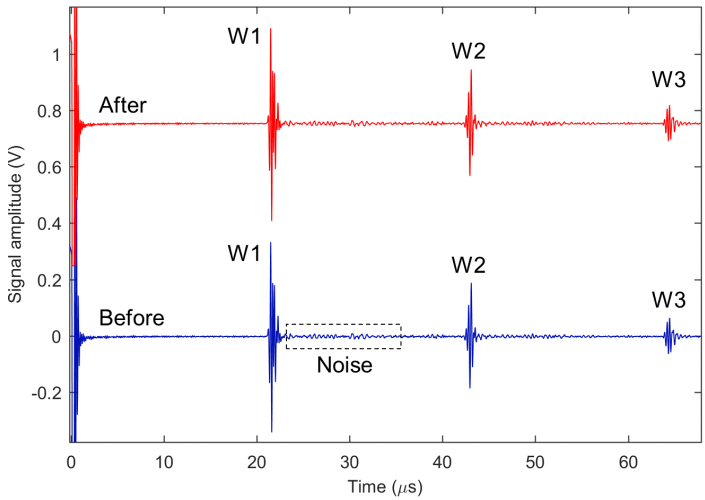

Figure 7.3: Signal amplitude of Tx1 transducer assembly before (blue) and after (red) the hot plate trial at ≈ 350 °C, with a label of the coherent noise region used to calculate the SNR.

Table 7.3: Measured and calculated parameters of the first waveguide backwall echo (W1) of Tx1 with no sample present before and after the hot plate trial at ≈ 350 °C.

	Pk-Pk Voltage (V)	SNR (dB)	f_C (MHz)	BW (%)
Before	0.67	28.7	4.8	26
After	0.68	29.1	4.7	26

A trial was performed to measure the temperature distributions across the waveguide whilst the transducer was in contact with a hot sample. The hot plate was set to 550 °C the maximum temperature setting, corresponding to a surface temperature on the flat stainless steel sample of ≈ 425 °C. The Tx1 transducer, with a BiT piezoelectric disc and stainless steel foam backing material, was placed on the hot sample surface without a couplant present. From the moment it was placed on the surface the temperature of the waveguide-piezoelectric interface on the transducer was recorded every 10 seconds for 3 minutes, using an infra-red thermometer (68, Fluke); the result of this trial is presented in Figure 7.4.

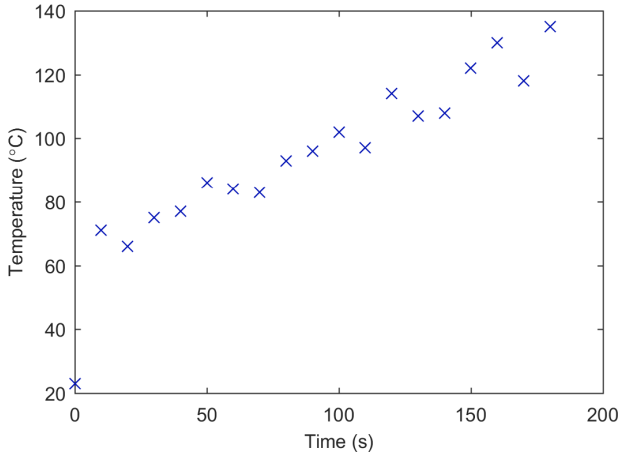

Figure 7.4: Temperature at waveguide-piezoelectric disc interface when the transducer was placed on the flat sample with a surface temperature of 425 °C.

This result demonstrates that after 3 minutes the temperature at the waveguide-piezoelectric interface reached 135 °C. Thus, this transducer assembly design is potentially suited for use in portable type thickness measurement inspections, even with the use of lower T_C piezoelectric materials. If the temperature distribution across the waveguide was further characterised with samples at different temperatures, either experimentally or via thermal distribution modelling, the type of piezoelectric material and corresponding maximum transducer-sample contact time could be selected for a particular portable type inspection application, with the required cooling time between measurements.

7.2 Laboratory Furnace Trials

Following the hot plate trials, a series of high temperature trials were performed where the sample and entire transducer were heated in a furnace (Pyro Therm Furnaces, ITEMP 14/15). The aim of these trials was to evaluate the high temperature performance of the transducer under conditions similar to those found in permanent inspections, in which the transducer is attached to the hot sample continuously without any form of active cooling. In all trials described below, unless otherwise stated, the sample and transducer were placed in the furnace, which was then allowed to reach the allocated temperature, and a 3-hour dwell was used to ensure the sample and transducer had reached temperature before taking a measurement. For all furnace trials discussed within this section, the pulser-receiver system detailed in 6.1 was used (400 V, 7.5 MHz and 0 dB, unless otherwise stated), along with transducer Tx1 assembled with a BiT disc and a stainless steel foam backing. The transducer and pulser-receiver system were connected via a high temperature coaxial cable, which consisted of a ceramic fibre cable as the inner sheath over a bare copper wire, which extend through a small, thermally insulated hole in the furnace door.

The temperature at the sample surface was recorded using a K-type thermocouple clamped to the sample. On heating, the furnace temperature was lower than the sample surface temperature, and the measured temperature from the thermocouple is inserted in brackets in each table for the results below. The temperature difference was attributed to a thermal gradient established within the furnace, where the lower furnace regions are warmer due to the position of the heating elements. The furnace thermocouple is fixed at the top of the furnace, whereas the sample was placed at the base of the furnace.

7.2.1 Dry Coupling Setup

As detailed in section 1.5.3, there are a number of methods to achieve physical coupling between the transducer and sample in high temperature applications, including: brazing, welding, solder, dry coupling, ceramic adhesives, or direct deposition of the piezoelectric material via sol-gel methods or other chemical deposition techniques. There are critical factors to consider when adopting a long-term coupling method, such as achieving good ultrasound transmission at the transducer-specimen interface, safety and material compatibility, long term thermal stability and ability of the interface to withstand thermal cycling. Each coupling method has advantages and disadvantages, and its use may be limited depending upon the high temperature application.

For the laboratory furnace trials in this work, dry coupling using a clamp was selected as the preferred physical coupling technique. Dry coupling creates an interface between the transducer and sample to improve acoustic coupling by joining them under high pressure, and thereby reducing the air pockets which result of the surface roughness of both interfaces; this is commonly improved by addition of a soft metal foil between the transducer and sample. The disadvantages of this system are mainly problems arising with long term use at high temperature, thermal expansion effects and the requirement for very high pressures, for instance it has been stated in the literature that $\approx 300\,\mathrm{MPa}$ [89] is required to remove air at the interface, even between highly polished surfaces. However, as these test are performed in a laboratory environment where the surfaces of the sample and transducer waveguide can be highly polished, this was seen as a viable option. Moreover, the nature of the dry coupling method provides a simple method for carrying out repeat measurements with the same transducer using different samples or metal foils, unlike other permanent coupling techniques, such as brazing, welding, ceramic adhesives and direct deposition of piezoelectric materials.

The dry coupling clamping setup used in these trials is shown in Figure 7.5, for transducer Tx1 coupled to the 9.8 mm thick, flat, stainless steel sample, with a 0.1 mm thick nickel foil at the interface. The clamp design is relatively simple and compact in order for it to fit inside the laboratory furnace. All components, except the high tensile steel M8 bolt, were machined from 304 stainless steel. The flat base plate is connected to the clamped bar via two lengths of 10 mm diameter studding, which were screwed into threaded holes in the plate and held tight with a washer and nut. The clamped bar was fixed in place using the studding via a nut and washer on either side. The M8 bolt is screwed into a threaded through-hole in the centre of the clamped bar; this bolt locks into the head of the central compression bolt on the transducer, such that tightening the M8 bolt exerts a force across the transducer-sample interface. The torque applied to the M8 bolt can be controlled by use of a torque wrench with a suitable scale bar.

Care was taken when applying torque using this setup, as it was apparent that the 4 mm diameter studding used within the transducers was the weakest link, as the studding deformed due to a large torque (35 Nm) being applied. As a result of this, the torque applied to the M8 bolt for the furnace trials below was set at 25 Nm to avoid deformation. However, it should be noted, that if the transducer design were to be altered, which would allow it to withstand a greater torque, there could be a greater degree of physical coupling between the transducer and sample than observed within these trials.

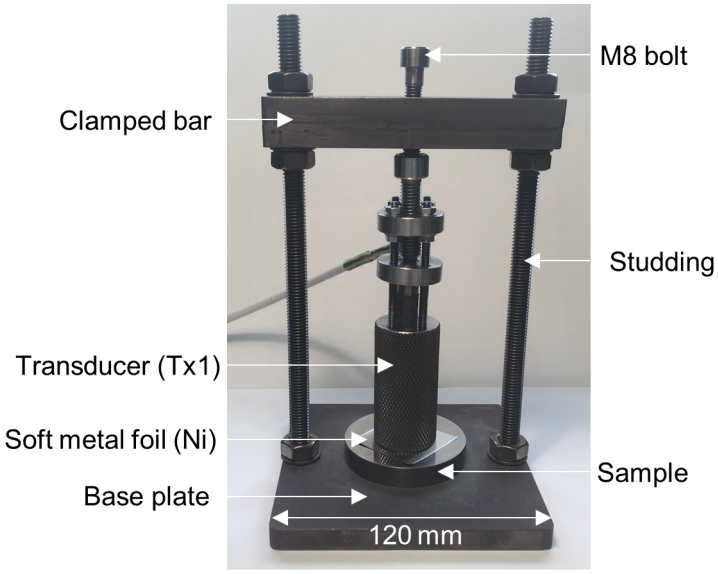

Figure 7.5: Image of the dry coupling clamping setup used in the furnace trials.

7.2.2 Aluminium Foil Coupling

The first series of furnace trials using the Tx1 transducer assembly were carried out with aluminium foil (Caterwrap 500) with a thickness of 0.015 mm ± 0.001 mm, measured with an electronic micrometer (293-766-30, Mitutoyo), which was positioned at the transducer-sample interface within the dry coupling clamping setup. The purpose of the aluminium foil as to act as a coupling layer between the transducer and sample surfaces, which despite both being hand polished on a flat sheet of glass down to 2500 grit, will have microscopic surface roughness in the form of pits and grooves. When the transducer and sample are mounted under pressure within the clamping setup, it is expected that the relatively soft aluminium foil will deform and act to fill in the air gaps at the voids when the microscopically rough surfaces meet, thereby increasing ultrasound transmission between the transducer and sample.

In the first furnace trial the transducer and flat stainless steel sample (see section 6.3.4) were mounted into the clamping setup with the aluminium foil and the bolt was tightened using a torque wrench (AVT300A, Britool) to 25 Nm. A measurement was taken before the trial, and then the entire setup was heated in the furnace. The furnace was set to 425 °C and the setup was left to dwell for 3 hours, after which a measurement was taken. The furnace was cooled slowly, and once the system had completely cooled to room temperature a further reading was taken.

Table 7.4: Measured and calculated parameters of first sample backwall echo (W1) with aluminium foil as a dry coupling layer under clamping at various temperatures.

Temperature (°C)	Pk-Pk Voltage (V)	SNR (dB)	f_C (MHz)	BW (%)
RT (before)	0.09	14.3	2.6	116
425 (452)	0.34	25.2	3.7	54
RT (after)	0.47	28.4	4.7	24

The data in Figure 7.6 shows the measured signal amplitude at room temperature before the measurement, at 425 °C and after cooling down to room temperature; the corresponding measured and calculated ultrasound parameters for the first sample backwall echo (4) are given in Table 7.4. A closer view of the measured signal amplitude before the trial is presented in Figure 7.7, such that the shape of the relatively low amplitude sample reverberations are more readily observed. The FFT magnitude of the first sample backwall echoes (4) are displayed in Figure 7.8 for each of the measurements.

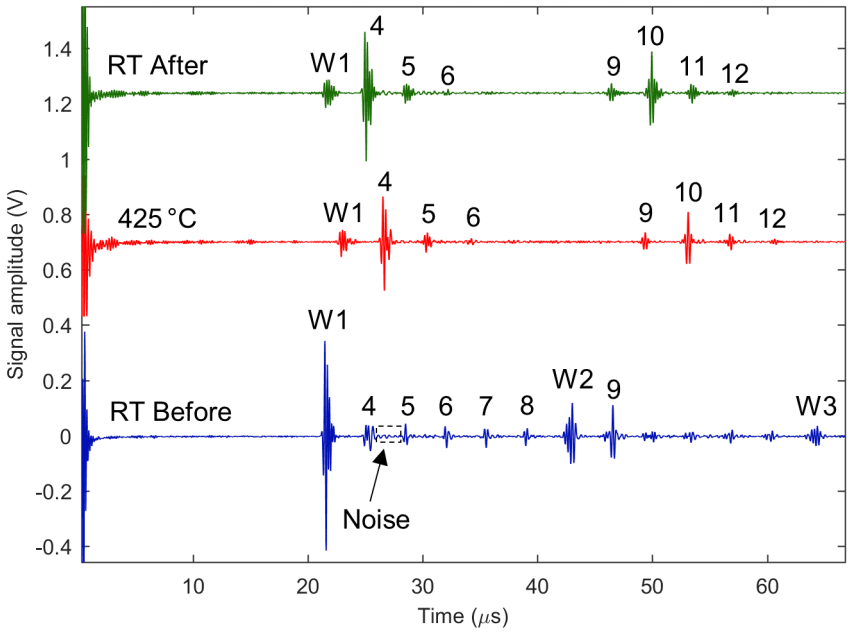

Figure 7.6: Signal amplitude of transducer assembly dry clamped with aluminium foil on the flat stainless steel sample for: (blue) room temperature before heating, (red) 425 °C, and (green) room temperature after heating, with a label of the coherent noise region used to calculate the SNR.

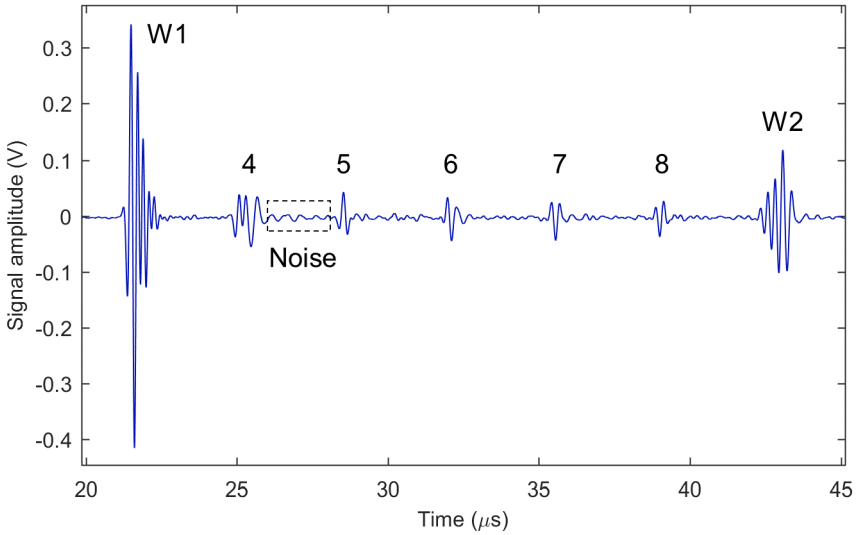

Figure 7.7: Signal amplitude of transducer assembly dry clamped with aluminium foil on the flat stainless steel sample for room temperature before heating, with a label of the coherent noise region used to calculate the SNR.

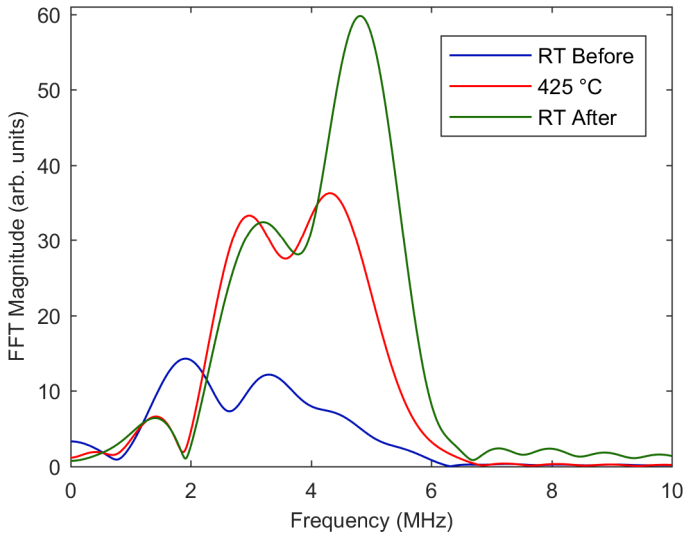

Figure 7.8: Sample first backwall echo (4) FFT magnitude spectrum for the first furnace trial: (blue) room temperature before heating, (red) 425 °C, and (green) room temperature after heating.

On analysis of the results from the first trial, it is evident that the transducer is able to generate ultrasound signals within the sample, both at room temperature and 425 °C, which are sufficiently large to calculate the thickness of the sample. However, the coupling efficiency between the transducer and sample appears to

increase as the temperature of the setup is elevated, owing to the fact that both the peak-to-peak voltage and SNR of the first sample backwall echo (4) increase from room temperature before heating (from 0.09 V and 14.3 dB) on heating to 425 °C (to 0.34 V and 25.2 dB). This increase in coupling efficiency is maintained on cooling, as both the room temperature peak-to-peak voltage and SNR are much larger after cooling than before (at 0.47 V and 28.4 dB).

The observed increase in the transmission coefficient is not likely to be due to changes in the acoustic impedance at increased temperature, especially since the increase in transmission coefficient is maintained on cooling to room temperature. It is likely due to an increase in the contact area at the transducer-sample interface, possibly due to increased plastic deformation of the foil at temperature. The effect of the coupling layer transmission coefficient is discussed further using a finite element model in section 7.2.3, to show how the change in coupling causes a change in the relative amplitudes of the sample reverberations. Also, it is not possible to determine any change in performance of the transducer, that may have resulted from depoling of the BiT piezoelectric disc, due to the change in transmission coefficient. To avoid the effect of the transmission coefficient on evaluating the performance of the transducer at temperature a series of longer-term trials were done with no sample present, as discussed in section 7.2.6.

The frequency content of the signal also appears to change on heating and subsequent cooling. The centre frequency increases from 2.6 MHz to 3.7 MHz and then 4.8 MHz for room temperature before, at 425 °C and room temperature after, respectively. Correspondingly, the bandwidth of the signal also decreases. This could indicate that the compressive stress exerted on the piezoelectric through the central bolt was decreased; this could be a result of thermal expansion of the thread and bolt, potentially in both the transducer assembly and the clamp.

After the first trial, a second trial was done without altering the setup (i.e. the transducer and sample were left in the same clamping setup as the first trial). The furnace was set to a range of temperatures between room temperature and 325 °C, and again at each temperature a 3-hour dwell was used. The data for the second trial is present in Figure 7.9 for each of the temperatures, including the room temperature result on cooling. The corresponding measured and calculated ultrasound properties of the first sample backwall echo (4) are given in Table 7.5. The FFT magnitude of the first sample backwall echoes (4) are displayed in Figure 7.10 for each of the measurements.

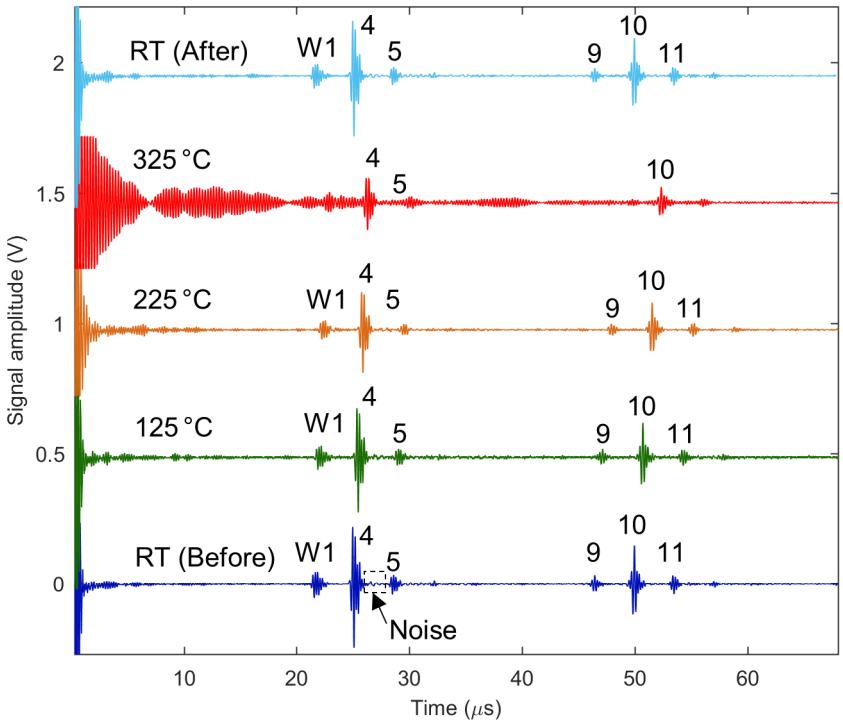

Figure 7.9: Signal amplitude of transducer assembly dry clamped with aluminium foil on the flat stainless steel sample for: (blue) room temperature before heating, (green) 125 °C, (orange) 225 °C, (red) 325 °C, and (light blue) room temperature after heating, with a label of the coherent noise region used to calculate the SNR.

Table 7.5: Measured and calculated parameters of first sample backwall echo (4) with aluminium foil as a dry coupling layer under clamping at various temperatures.

Temperature (°C)	Pk-Pk Voltage (V)	SNR (dB)	f_C (MHz)	BW (%)
RT (before)	0.46	27.3	4.7	24
125 (132)	0.40	24.3	4.6	24
225 (240)	0.31	23.7	4.5	25
325 (346)	0.20	18.4	4.3	24
RT (after)	0.44	28.6	4.7	24

From the results for the second trial with aluminium foil, it appears that the coupling efficiency between the transducer and sample is not significantly changed, unlike the first trial. More noticeable is the resonance seen along the waveform for the data at 325 °C, increasing the noise floor of the signal, quite different to the

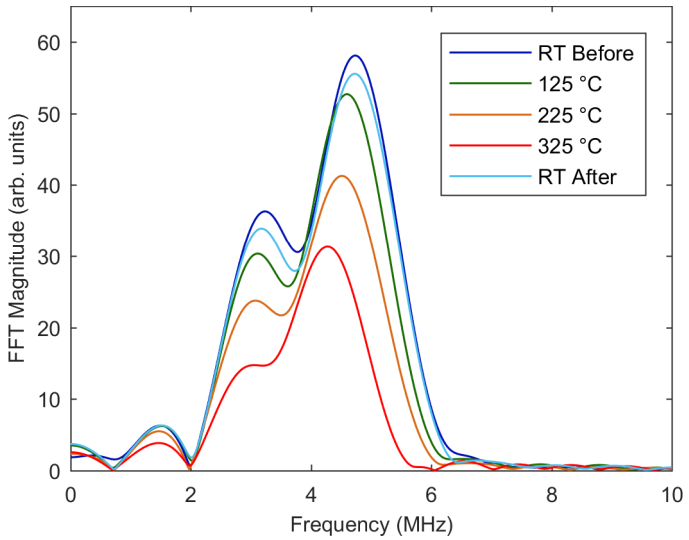

Figure 7.10: Sample first backwall echo (4) FFT magnitude spectrum for the second furnace trial: (blue) room temperature before heating, (green) 125 °C, (orange) 225 °C, (red) 325 °C, and (light blue) room temperature after heating.

waveform for the trial trail at 425 °C. Also, note that at 325 °C both the peak-to-peak voltage at 0.20 V and SNR 18.4 dB are lower for the first sample backwall echo (4) compared to the first trial at 425 °C. It is assumed that this loss in signal is due to increased thermal expansion of the bolts, which exert the compressive stress on the transducer central bolt and the clamping setup, since the whole setup was heated for much longer in second trial, with a total time at elevated temperature of 9 hours. The resonance observed in the signal at 325 °C is reversed on cooling to room temperature, although the peak-to-peak voltage after cooling is slightly lower than before.

In conclusion, the transducer assembly within the dry coupling setup is able to produce sufficient signals for thickness measurements with aluminium foil on the flat stainless steel sample. However, there appears to be an issue with thermal expansion of the two bolts within the assembly. This could possibly be improved by using stainless steel bolts rather than high tensile steel bolts; as such, all further furnace trials discussed in this chapter are done using stainless steel bolts in the transducer assembly and the dry coupling clamp setup.

7.2.3 PZFlex Modelling of Couplant Layer

As described briefly in the above, preliminary trials using the dry coupling setup with the furnace at elevated temperatures appeared to show an increase in the relative amplitude of waveguide and sample backwall echoes, likely a result of change in the reflection and transmission coefficients at the waveguide-foil-sample interface. This section aims to explain the origin of the resulting echoes in the measured waveforms and the change in their relative amplitudes at elevated temperatures, by describing the reflection coefficient for solid surfaces contacting at an interface. Following this, a finite element model to simulate the effect on the signal output of different interface properties, and results were compared to the experimental data.

The reflection coefficient, R_{12}, was introduced in section 2.1.4 for the case with perfect contact at the interface between two materials, and this value can be calculated using equation 2.28 provided, repeated here for reference:

$$R_{12} = \frac{Z_1 - Z_2}{Z_1 + Z_2} \tag{7.1}$$

The equation above cannot be used to calculate the reflection coefficient with real engineering surfaces, as these are typically rough with an associated surface roughness. At an interface between two rough materials the contact occurs between asperities, such that the true contact area can be considerably lower than the apparent contact area [89]. The schematic diagram in Figure 7.11(a) represents the experimental setup where two rough surfaces contact to form a boundary, in this case the waveguide from the transducer is material 1 and the sample is material 2, without a metal foil present. The incident wave, I, is partially reflected, R, and partially transmitted, T. As indicated in the diagram, the contact points occur at positions where the surface roughness of each material meets, resulting in air pockets along the boundary, which result in almost total reflection of the incident wave due to the large mismatch between the acoustic impedance of steel and air.

The individual air pockets will scatter the incoming wave, producing reflected and transmitted waves which are net result of numerous wave-scatterer interactions at the boundary. The shape of the air pockets and their size relative to the ultrasound wavelength dictates the scattering regime which occurs at the interface. If the size of the air pockets are much smaller than the wavelength, which is assumed in this work as the ultrasound wavelength is $\approx 1.5\,\text{mm}$ and typical air pockets at the interface can be on the order of 5-50 μm [89]. Although, the size of the air pockets varies depending upon the surface roughness values, as the materials are polished down to 2500 grit in these experiments, this approximation is predicted to be valid in

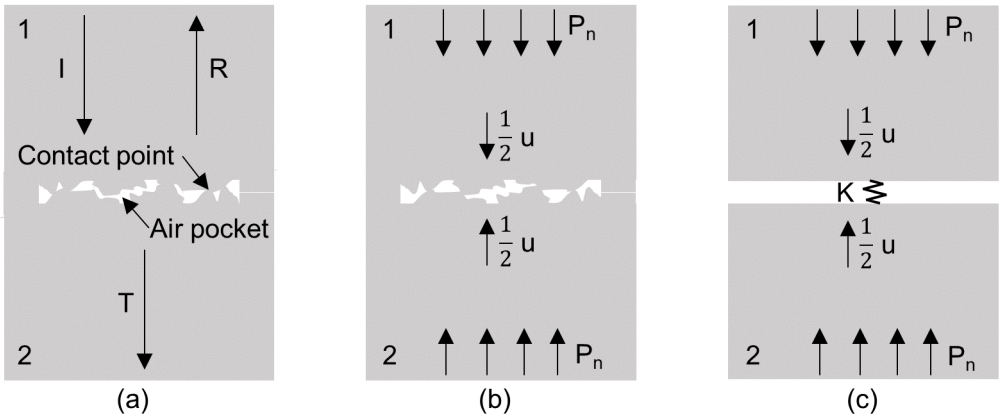

Figure 7.11: Schematic diagram of partially contacting solid interfaces (materials 1 and 2) by a spring: (a) experimental setup, (b) static model of the interface and (c) spring model of the interface, adapted from [89].

this case. The mass term in a mass-spring model of a partially contacting interface has been found to be negligible [236]. In addition to this, the damping of an interface layer can be considered to have an insignificant effect on the reflection coefficient [237]. Therefore, in this frequency region ($\approx$ 4 - 5 MHz), it can be approximated that the stiffness of the interface dictates the reflection coefficient [89].

A static model [89], shown in Figure 7.11(b), can be used to represent this system, where a nominal contact pressure (applied load divided by nominal contact area), P_n, is applied which results in a displacement of the interface, u. A schematic of the spring model of this system is given in Figure 7.11(c) [89]. For this type of interface, the stiffness per unit area, K, can be represented by the change of average pressure with change in the displacement of the interface (i.e. average interfacial separation), given by equation 7.2. Following this, the reflection coefficient, R_{12}, at a partially contacting interface can be expressed by equation 7.3. If materials 1 and 2 are identical, this relationship reduces to the expression in equation 7.4.

$$K = -\frac{\mathrm{d}P_n}{\mathrm{d}u} \tag{7.2}$$

$$R_{12} = \frac{Z_1 - Z_2 + i\omega\left(Z_1 Z_2 / K\right)}{Z_1 + Z_2 + i\omega\left(Z_1 Z_2 / K\right)} \tag{7.3}$$

$$R_{12} = \frac{1}{\sqrt{1 + \left(2K/\omega Z\right)^2}} \tag{7.4}$$

Applying this model between the frequency range 4 - 17 MHz it has been shown [89] that as the interfacial stiffness increases (i.e. greater real contact area), the ultrasound transmission efficiency across the interface increases, thereby decreasing the reflection coefficient. The reflection coefficient was shown to increase with increasing frequency due to increased scattering. This spring model of partially contacting interfaces is invalid if the wavelength is proportional to the average interfacial separation.

The model described above is useful in certain situations, but it is difficult to predict the change in reflection coefficient at the interface with the experimental setup and conditions in this work, due to the effect of elevated temperatures and the presence of a thin metal foil layer at the interface, which renders the model invalid as it is comparable in thickness to the wavelength [238]. However, using this model, it appears the increased temperature results in an increase in the real contact area between the waveguide and the sample, perhaps through a number of mechanisms, thereby increasing the interface stiffness and decreasing the reflection coefficient.

Following this, a 2D model was executed in PZFlex to obtain waveforms from a waveguide coupled to a steel sample via an interface. The model was performed for two cases: one represented poor acoustic coupling (i.e. high R_{12}), while the other represented good acoustic coupling (i.e. low R_{12}). A schematic diagram of the model is given in Figure 7.12, where a stainless steel waveguide is coupled via a coupling layer to a stainless steel sample.

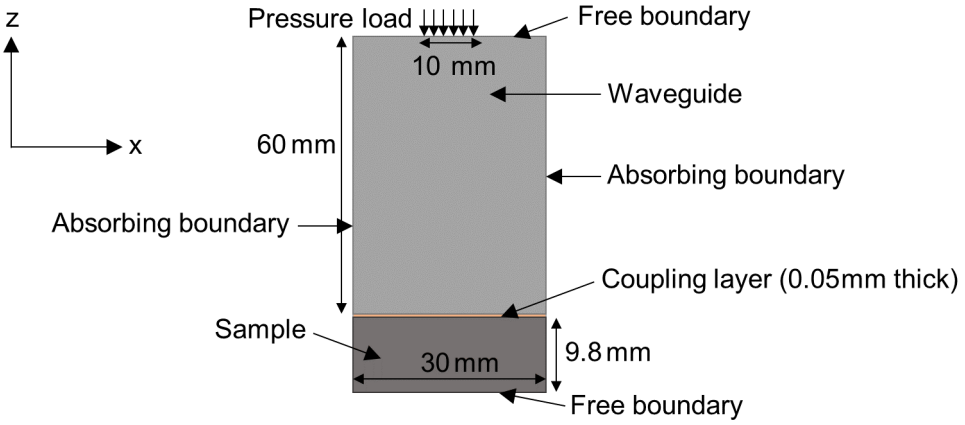

Figure 7.12: Schematic diagram of the 2D finite element model used in PZFlex to simulate the propagation of the ultrasound waves when the transducer is acoustically coupled to the sample with a solid a coupling layer.

For this model, the frequency was set to 4 MHz, and with a minimum wave velocity of 1000 m/s and 15 elements per wavelength, corresponding to an element size of 16.7 μm. A Rickert wavelet was used as the input pressure load. The coupling layer material properties to represent poor coupling were $\rho = 2000\,\mathrm{kg/m^3}$ $\mathrm{v_L} = 2000\,\mathrm{m/s}$, $\mathrm{v_S} = 1000\,\mathrm{m/s}$, while the coupling properties for good coupling were $\rho = 6000\,\mathrm{kg/m^3}$ $\mathrm{v_L} = 4000\,\mathrm{m/s}$, $\mathrm{v_S} = 2500\,\mathrm{m/s}$. The material properties of the stainless steel waveguide and sample were both $\rho = 7900\,\mathrm{kg/m^3}$ and $\mathrm{v_S} = 3200\,\mathrm{m/s}$. The $\mathrm{v_L}$ was measured experimentally for both and set these values, giving 5601 m/s for the waveguide and 5673 m/s for the sample.

The results from the model are presented as an A-scan, by calculating the average element z-velocity across the loading surface, which can be compared to the experimental A-scans. The A-Scan from the model with poor coupling is shown in Figure 7.13(a), and the corresponding experimental A-scan with the aluminium foil before heating is repeated for reference below in Figure 7.13(b). The A-Scan from the model with good coupling is shown in Figure 7.14(a), and the corresponding experimental A-scan with the aluminium foil before heating is repeated for reference below in Figure 7.14(b).

There is good agreement between the experimental and simulated data, highlighting that the change in the relative amplitudes of the echoes in the signals is due to a change in the interface properties, leading to different reflection and transmission coefficients; this is likely as a result of the elevated temperatures on the contact area at the interface between the transducer waveguide, metal foil and the sample. For the case with poor coupling, relating to the case when the transducer, aluminium foil and sample are loaded into the dry clamping setup before heating, the two waveguide backwall echoes (W1 and W2) are clearly distinguishable above the noise floor, as are the sample echoes (4, 5, 6, 7 and 8), although these are of relatively low amplitude. Moreover, it is apparent particularly from the model results, as the noise floor is much lower, that the low amplitude echoes after W2 are not simply sample backwall echoes; these echoes appear elongated compared to the previous sample backwall echoes, and this is as there is interference between the continued reverberations of ultrasound trapped within the sample (due to a high R_{12} at the interface), and the onset of further reverberations caused by the transmission ultrasound from a second longitudinal wave interacting with the interface.

For the case with good coupling, relating to the case when the transducer, aluminium foil and sample are loaded into the dry clamping setup once the temperature has been increased, the first waveguide backwall echoes (W1) is distinguishable above the noise floor but at a much lower amplitude compared to the poor coupling

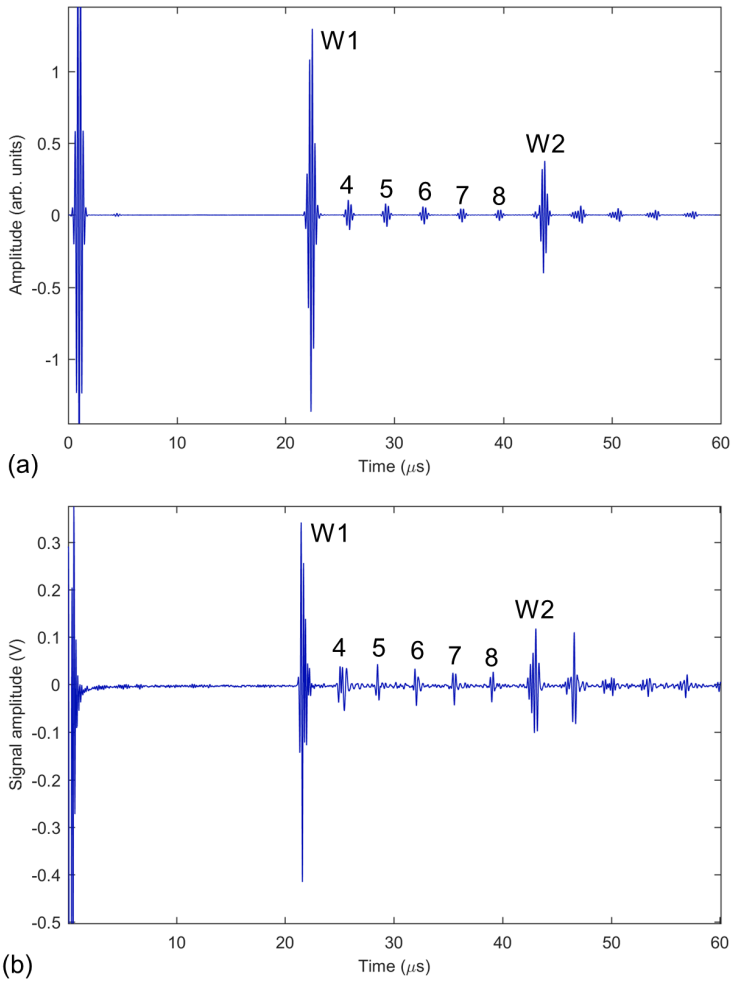

Figure 7.13: Signal amplitude showing the waveguide backwall echoes (W1 and W2) and sample backwall echoes (4, 5, 6, 7 and 8) for: (a) 2D PZFlex model with a poor coupling layer (high R_{12}) between the transducer and sample, and (b) transducer assembly dry clamped with aluminium foil on the flat stainless steel sample at room temperature before heating.

case. This is as a greater portion of the energy from the initial longitudinal wave generated by the piezoelectric disc is transmitted into the sample, as the reflection coefficient is decreased on increasing temperature. The low amplitude of W1 leads to total loss of the second backwall echo (W2), which is not distinguishable above the noise floor from the experimental data, although it appears with a very low amplitude in the simulation. Another difference in the signals with good coupling, is that fewer sample backwall echoes are detectable, as a greater portion of the sound transmitted into the sample from the initial wave is transmitted across the interface

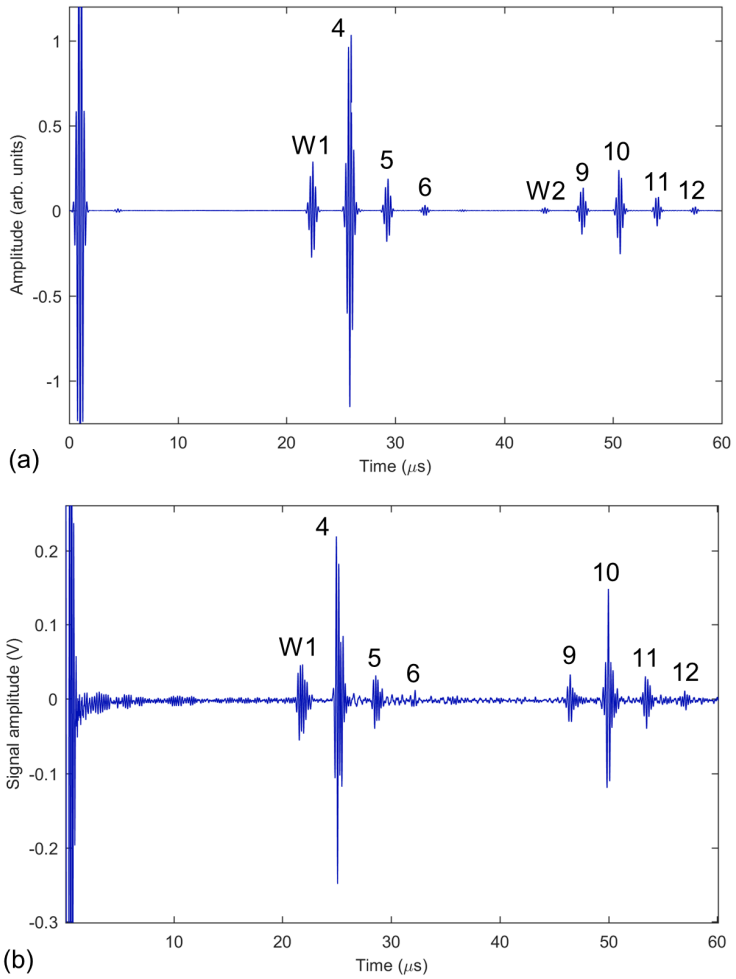

Figure 7.14: Signal amplitude showing the waveguide backwall echoes (W1 and W2) and sample backwall echoes (4, 5, 6, 9, 10, 11 and 12) for: (a) 2D PZFlex model with a good coupling layer (low R_{12}) between the transducer and sample, and (b) transducer assembly dry clamped with aluminium foil on the flat stainless steel sample at room temperature after heating.

back into the waveguide; this leads to a much higher amplitude for the first sample backwall echo (4), and lower amplitudes for the other sample backwall echoes which are observable (5 and 6), resulting in no interference between the first and second set of sample reverberations, as that seen with poor coupling. The decreased reflection coefficient at the interface result in the relatively high amplitude of the sample backwall echo (10), as it originated from the subsequent transmission and reflection of sample backwall echo 4, whilst the other sample backwall echoes (9, 11 and 12) are relatively small.

7.2.4 Nickel Foil Coupling

Following on from the furnace trials with aluminium foil, trials with nickel foil (N188217, Advent Research Materials Ltd.) with a thickness of 0.100 mm ± 0.001 mm, measured using an electronic micrometer, acting to improve the coupling efficiency between the transducer and sample in the dry coupling setup were carried out. From the preliminary trials, it was concluded that the thermal mismatch at elevated temperatures between the high tensile steel bolts, both in the transducer assembly and dry clamping setup, and the stainless steel components may result in loss of compressive stress on the piezoelectric disc. Therefore, for the remainder of the trials discussed, stainless steel bolts were used in both the transducer assembly and dry coupling setup, in an attempt to overcome this issue.

Prior to the trials with nickel foil, the following re-assembly of the setup was required: polishing of both waveguide faces, polishing of the sample and an unstressed BiT disc was placed in the transducer. The nickel foil was placed between th transducer and flat stainless steel sample and compressed in the dry coupling setup, then placed in the furnace. Polishing was required due to the thin oxide layer which developed on the stainless steel surfaces. Measurements were made at room temperature before the trial, then at 125 °C, 225 °C, 325 °C and 425 °C, with a 3-hour dwell at each temperature, and then the system was allowed to cool and another room temperature measurement was taken; the results of this trial are presented in Figure 7.15. The corresponding measured and calculated ultrasound parameters for the first sample backwall echo (4) are given in Table 7.6. The FFT magnitude of the first sample backwall echoes (4) are displayed in Figure 7.16 for each of the measurements.

Similarly to the aluminium foil, the coupling efficiency between the transducer waveguide and the sample appears to increase at elevated temperatures, as the peak-to-peak amplitude of the first sample backwall echo (4) tends to increase relative to the waveguide backwall echo (W1). However, despite this improvement in coupling, the peak-to-peak voltage of the first sample backwall echo (4) does not change significantly between 125 °C - 425 °C; this could be due to the increase in coupling being offset by the reduction in the signal amplitude from temperature related changes to piezoelectric constants of the disc (e.g. decrease d_{33} value). The change in SNR between different temperatures is significant, where the SNR is higher for at 325 °C and 425 °C than the room temperature before, despite it having a greater peak-to-peak voltage; this is a result of the decrease in the peak amplitude of the noise floor level at higher temperatures. A slightly higher peak-to-peak voltage after heating at 0.34 V was measured compared to 0.32 V before heating, although the

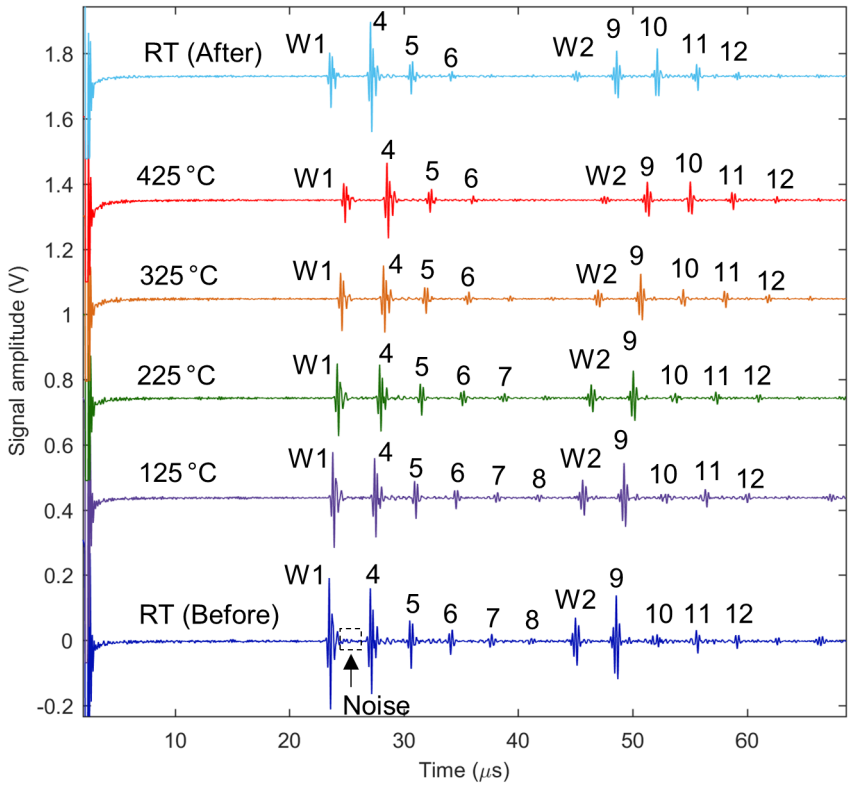

Figure 7.15: Signal amplitude of transducer assembly dry clamped with nickel foil on the flat stainless steel sample for: (blue) room temperature before heating, (purple) 125 °C, (green) 225 °C, (orange) 325 °C, (red) 425 °C and (light blue) room temperature after heating, with a label of the coherent noise region used to calculate the SNR.

corresponding SNR was significantly larger at 28.6 dB after heating compared to 23.5 dB before, again due to the decrease in the peak noise floor value measured after heating; these results indicate that the increase in coupling efficiency is maintained on cooling, due to the heat induced changes in the physical properties at the interface.

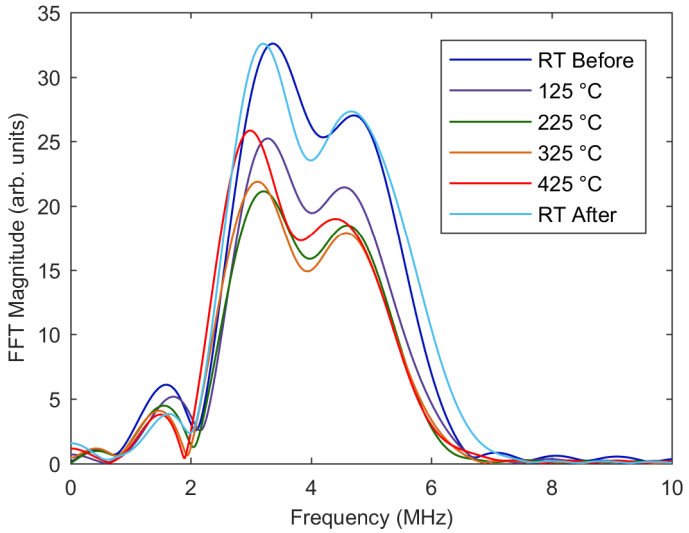

Figure 7.16: Sample first backwall echo (4) FFT magnitude spectrum for the furnace trial with nickel foil on the flat stainless steel sample: (blue) room temperature before heating, (purple) 125 °C, (green) 225 °C, (orange) 325 °C, (red) 425 °C and (light blue) room temperature after heating.

Table 7.6: Measured and calculated parameters of first sample backwall echo (4) with nickel foil as a dry coupling layer under clamping at various temperatures.

Temperature (°C)	Pk-Pk Voltage (V)	SNR (dB)	f_C (MHz)	BW (%)
RT (before)	0.32	23.5	4.0	71
125 (124)	0.24	22.5	3.9	68
225 (225)	0.20	20.0	3.9	75
325 (326)	0.21	25.4	3.8	77
425 (433)	0.23	27.1	3.6	72
RT (after)	0.34	28.6	4.0	79

The increase in coupling efficiency at the interface (i.e. decrease in R_{12}) observed at elevated temperatures renders it difficult to use the data with the transducer coupled to a sample to compare the signal output of the transducer before and after heating. Therefore, after heating, the transducer was removed from the clamping setup and the waveform with no sample was measured, then compared to the waveform measured with no sample present before heating. It was immediately apparent on observing the waveform with no sample present after heating that the signal was not what was expected due to the significant reverberation and loss of distinguishable backwall echoes, perhaps due to loss of compressive stress

on the piezoelectric disc by the central transducer bolt. To investigate if this was the case, the torque wrench was used and set to 25 Nm and applied to the central transducer bolt, which had evidently lost tension; the resulting waveform with no sample present was measured, and is hereby referred to as re-tightened. The no sample present data is presented in Figure 7.17, and the corresponding measured and calculated ultrasound parameters for the first waveguide backwall echo (W1) are given in Table 7.7, although no data is included for the case with no sample present with no heating without re-tightening as there is no clear W1 echo present.

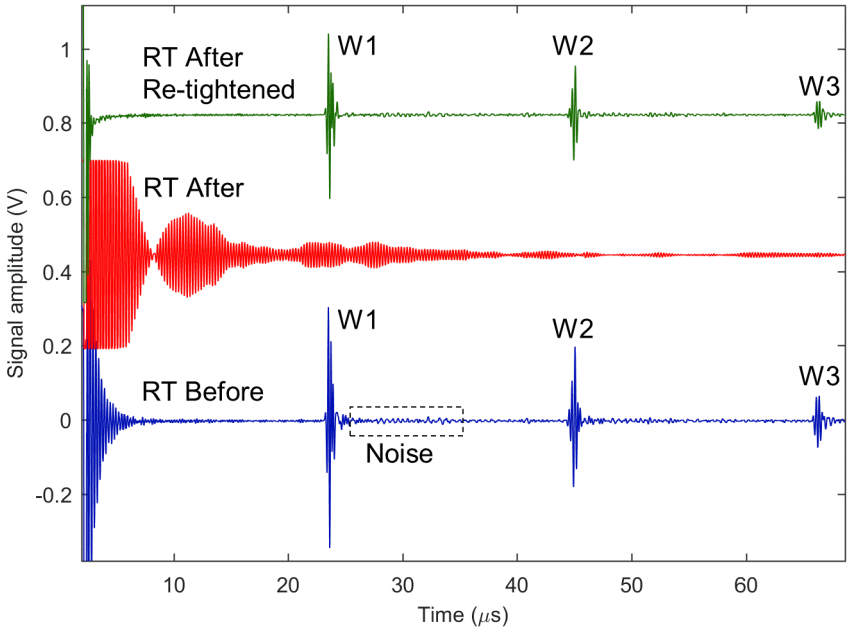

Figure 7.17: Signal amplitude of transducer assembly with no sample present: (blue) room temperature before heating, (red) room temperature after heating and (green) room temperature after heating after re-tightening of the central bolt, with a label of the coherent noise region used to calculate the SNR.

Table 7.7: Measured and calculated parameters of first waveguide backwall echo (W1) with no sample present for the transducer before heating and after heating re-tightened.

Measurement Taken	Pk-Pk Voltage (V)	SNR (dB)	f_C (MHz)	BW (%)
Before	0.65	30.0	4.5	71
After	0.45	28.6	4.0	79

It appears that the thermal expansion and subsequent contraction of the transducer central bolt when compressed within the dry coupling setup does not result in the same stress state, such that the central bolt becomes slack after heating, resulting in significant resonance of the piezoelectric disc; this was confirmed by re-tightening of the transducer central bolt, where the echoes reappear in the waveform. However, it is clear that there is a reduction in the signal peak-to-peak voltage of the W1 echo before heating from 0.65 V to 0.45 V after heating to 425 °C. This loss in signal could be attributed to both temperature related effects of the piezoelectric constants of the element, or a stress induced decrease due to multiple applications of stress on the piezoelectric disc (as observed in section 6.3.3). The next section describes long term trials carried out in an attempt to isolate the effect of temperature on the transducer performance.

7.2.5 Longer-Term Performance

This section details longer-term trials performed, without the presence of a sample, to investigate the effect of temperature on transducer performance. For these trials, the Tx1 transducer assembly was used, with a new BiT disc and a stainless steel foam backing material, and both transducer waveguide ends were re-polished. The transducer was placed in an alternative furnace, which is designed for long term testing, and this was set to 500 °C, although data was taken at room temperature before and after testing as a it was not possible to position a coaxial cable to record data at an elevated temperature with furnace used here. The PR system described in section 6.1 was used (200 V, 7.5 MHz and 0 dB). Three heating rounds were applied to the transducer with the transducer subject to 500 °C continuously for 72 hour (3 day) intervals between cooling to room temperature for measurement; the results are presented in Figure 7.18 with the corresponding measured and calculated ultrasound parameters for the first waveguide backwall echo (W1) are given in Table 7.8.

Table 7.8: Measured and calculated parameters of first waveguide backwall echo (W1) with no sample present for the transducer at room temperature after a number of hours at 500 °C.

Time at 500 °C (hours)	Pk-Pk Voltage (V)	SNR (dB)	f_C (MHz)	BW (%)
0	0.38	30.2	4.0	65
72	0.28	25.9	4.0	56
144	0.28	26.6	4.2	51
216	0.27	27.2	4.3	49

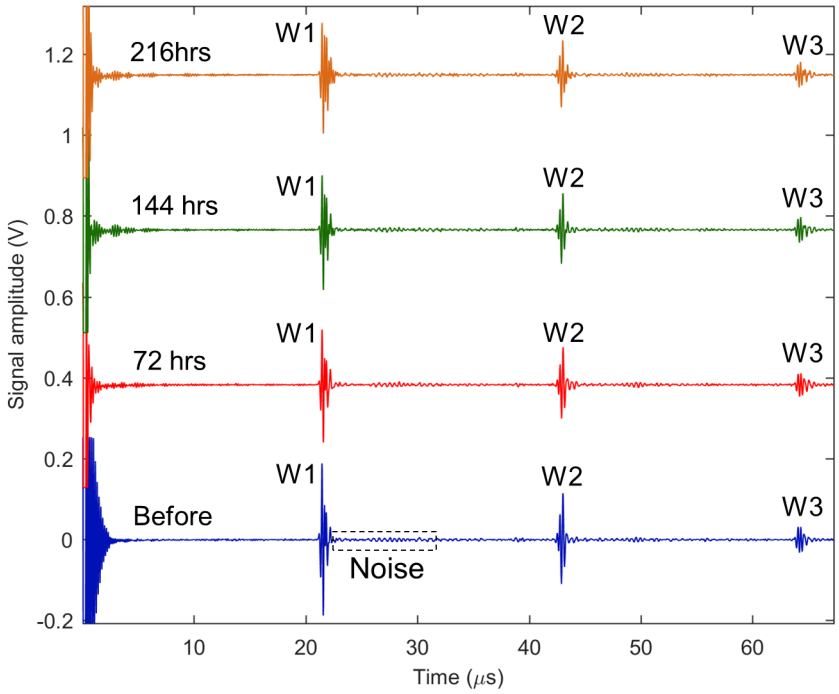

Figure 7.18: Signal amplitude of transducer assembly with no sample present at room temperature, showing the first three waveguide backwall echo (W1, W2 and W2) after a number of hours held at 500 °C in a furnace: (blue) before heating, (red) 72 hours (3 days), (green) 144 hours (6 days) and (orange) 216 hours (9 days), with a label of the coherent noise region used to calculate the SNR.

The main conclusion drawn from these long term trials was that on initial exposure to high temperatures the peak-to-peak amplitude decreases, here from 0.38 V to 0.28 V, likely due to change in the piezoelectric properties of the disc as a result of various complex depoling processes exhibited at elevated temperatures below the Curie temperature of BiT ($\approx$ 675 °C), which have been previously investigated for bismuth titanate in the published literature [239, 240]. However, the stress and thermal cycling related effects on the piezoelectric disc, especially at elevated temperature, cannot be ignored, these too may have resulted in depoling of the piezoelectric disc. Despite this initial decrease, over the trial period investigated (total of 216 hours) there appeared to be no significant change in the peak-to-peak voltage, suggesting stabilisation of the piezoelectric properties. The results confirm that the central transducer bolt is able to undergo thermal expansion and contraction with no clear loss in tension when not within the dry clamping setup.

7.2.6 Performance with No Sample Present

The final trial in this section aimed to measure transducer performance at high temperatures with no sample present (i.e. the transducer is not fixed within the dry clamping setup). The Tx1 transducer assembly was used with a new BiT disc and both transducer waveguide ends were polished down to 2500 grit. The transducer was placed into the furnace and heated to 425 °C and a 6-hour dwell was applied to ensure the transducer assembly had reached temperature. On measuring the waveform at 425 °C it was clear that the signal was lost, likely due to lose of tension in the central bolt. To confirm this, the transducer was removed from the furnace whilst still hot and the central bolt was re-tightened. The transducer was placed back in the furnace and the resulting waveform was recorded. The results of this trial are given in Figure 7.19, along with the corresponding measured and calculated ultrasound parameters for the first waveguide backwall echo (W1) in Table 7.9.

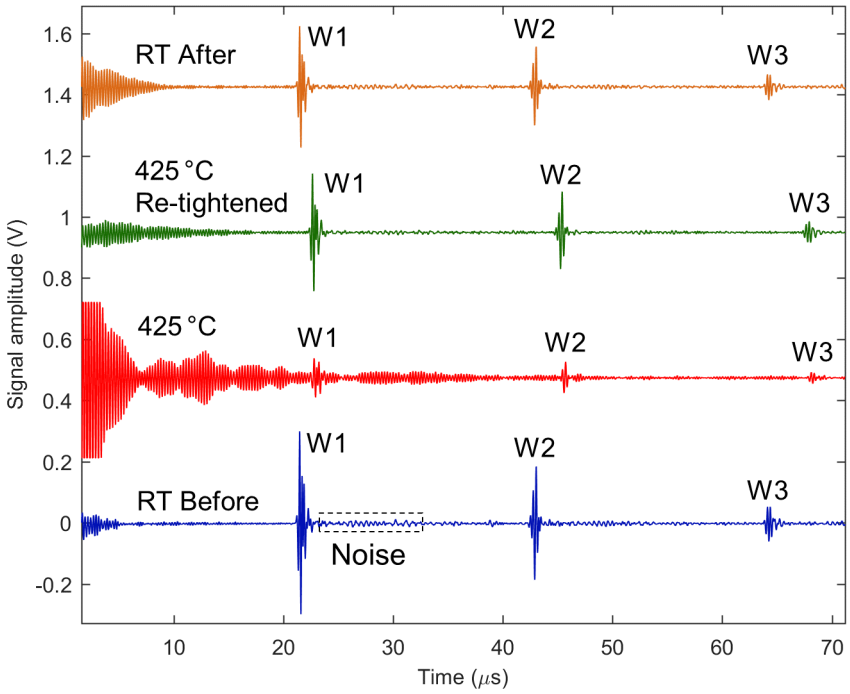

Figure 7.19: Signal amplitude of transducer assembly with no sample present for: (blue) room temperature before heating, (red) 425 °C, and (green) room temperature after heating, with a label of the coherent noise region used to calculate the SNR.

Table 7.9: Measured and calculated parameters of first waveguide backwall echo (W1) with no sample present.

Temperature (°C)	Pk-Pk Voltage (V)	SNR (dB)	f_C (MHz)	BW (%)
RT (Before)	0.60	27.4	4.6	31
425 (449)	0.13	8.7	4.4	22
425 (449) Re-tightened	0.38	26.9	3.7	68
RT (After)	0.40	26.9	4.0	56

The results from the high temperature trial with no sample present highlight the predominant issue with the current demonstration of this type of compression transducer design, which is maintaining the compressive force across the piezoelectric disc at elevated temperatures with the effects of thermal expansion on the stainless steel assembly. Although the first, second and third waveguide backwall echoes (W1, W2 and W3) are identifiable in the waveform at 425 °C, there is a large amount of resonance along the waveform, increasing the noise floor and significantly reducing SNR. For W1, once the central bolt on the transducer was re-tightened, the peak-to-peak voltage increased from 0.13 V to 0.38 V, providing a large increase in SNR from 8.7 dB to 26.9 dB. Although it is noted the peak-to-peak voltage and SNR are less at 425 °C even when re-tightened compared to room temperature, as a result of change in the piezoelectric coefficients with increasing temperature and application of another round of stress (as detailed in 6.3.3), likely due to depoling of the piezoelectric disc.

7.2.7 Preliminary Trial on Stainless Steel Pipe

This section presents the results of a preliminary trial using an alternative dry clamping method, designed for use on pipe samples. The clamping setup introduced in section 7.2.1 worked well with transducer Tx1 on flat samples at elevated temperatures, however, it failed to produce good signals on curved samples, without huge amounts of torque. The Tx1 transducer design failed to withstand high torques (> 40 Nm) without deformation of the studding. The difficulty in obtaining good signals on curved samples with this transducer design is mainly due to the significantly reduced contact area between the end of the waveguide and the sample, such that effectively there is a line contact at the interface rather than a larger circular area. This results in less ultrasound energy penetrating into the sample, which causes greater reflection of ultrasound back to the waveguide, and much lower

signals reflecting from the backwall of the sample. Good signals were achieved with transducer Tx3 using liquid coupling, however, due to the increased contact area at the curved waveguide to pipe interface, it was not possible to obtain sufficient signals at torques below the deformation threshold of the studding within the transducer assembly.

The dry coupling clamping setup designed for use with pipe samples, with a U-shaped clamp fixed around the bend of the pipe, is given in Figure 7.20; the transducer used here is Tx2 (see section 6.3.2) which has an M20 bolt with part of the bolt tail threaded, and this thread was used to connect the transducer to the clamp block. The clamp block (50 mm×40 mm×100 mm, W×D×L) is connected to the U-shaped clamp rod (10 mm diameter, with thread on the ends) by two M10 threaded holes. For this trial a BiT ($\approx$ 4.0 MHz) piezoelectric disc was used, along with the same stainless steel foam backing as in the trials discussed above. The central bolt on the Tx2 transducer was tightened to 25 Nm.

For this preliminary trial on a curved sample a stainless steel pipe sample was used, which has an outer diameter of 37.5 mm and a wall thickness of 6.0 mm. Nickel foil (0.10 mm thickness) was used to improve the coupling at the transducer-sample interface. The clamping setup was positioned in the furnace, and heated to 425 °C, the resulting A-scans before heating, at 425 °C and after heating at room temperature are presented in Figure 7.21; the corresponding measured and calculated parameters of the first sample backwall echo (4) are given in Table 7.10.

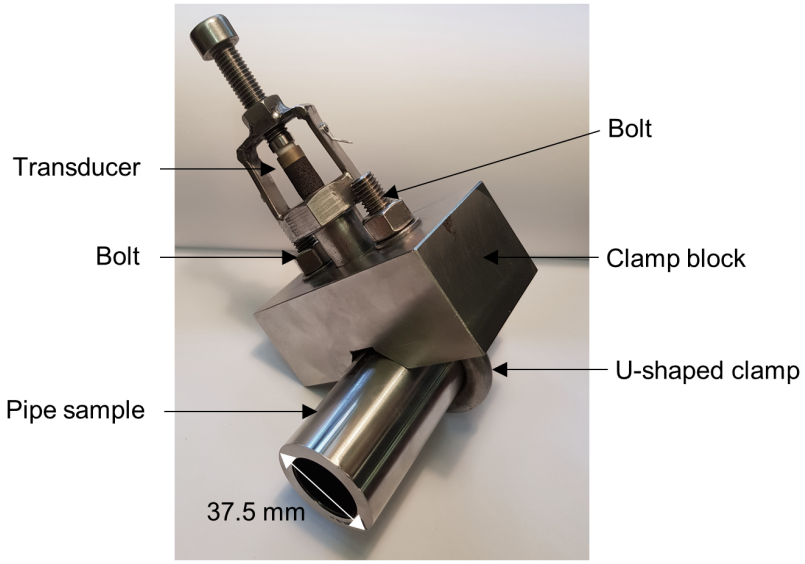

Figure 7.20: Image of the dry coupling clamping setup used in the furnace trial with the stainless steel pipe sample.

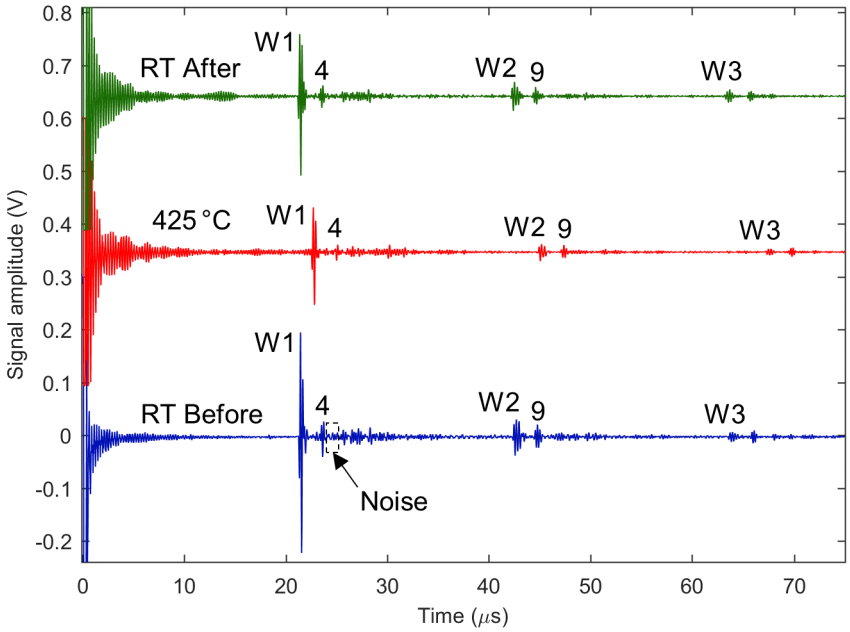

Figure 7.21: Signal amplitude using Tx2 transducer with nickel foil in pipe clamp with a stainless steel pipe sample: (blue) room temperature before heating, (red) 425 °C, and (green) room temperature after heating, with a label of the coherent noise region used to calculate the SNR.

Table 7.10: Measured and calculated parameters of first sample backwall echo (4) with Tx2 transducer using pipe clamp.

Temperature (°C)	PkPk- Voltage (V)	SNR (dB)	f_C (MHz)	BW (%)
RT (Before)	0.067	12.3	4.3	64
425 (454)	0.030	6.6	4.1	63
RT (After)	0.043	10.1	4.5	43

The results from this preliminary trial highlight the difficulty in obtaining high amplitude signals with good SNRs, especially compared to use with flat samples, due to the greatly decreased contact area. It also demonstrated the effect of scattered signals as a result of the threaded pattern on the M20 bolt waveguide (on Tx2), which tend to interfere and reduce the SNR of the desired signals from the backwall of the sample. Despite this, backwall echoes from the pipe sample were detected (i.e. echoes 4 and 9), which could be used to calculate the thickness of the pipe sample. The peak-to-peak voltage of the first sample backwall echo (4) before

heating was 0.067 V with a SNR of 12.3 dB, which reduced to 0.030 V with 6.6 dB at 425 °C. Unlike earlier trials with the flat sample, it appears that the coupling efficiency failed to significantly improve with increasing temperature, where the ratio between W1 and 4 after heating does not vary compared to before heating.

It is important to note that unlike the Tx1 transducer, the Tx2 transducer continued to operate at high temperatures despite thermal expansion effects. As was described in section 7.2.6, the Tx1 transducer failed to perform well at high temperatures with no sample present and when not within the clamping setup, as the central transducer bolt lost tension, reducing the compressive stress on the piezoelectric disc, resulting in significant resonance across the waveform and greatly reduced signal amplitude and SNR. However, this preliminary trial indicates that with the Tx2 transducer at elevated temperature thermal expansion of the bolt and welded structure do not result in significantly reduced compressive stress across the piezoelectric disc.

7.3 Summary

This chapter presents an analysis of laboratory based high temperature performance of the high temperature piezoelectric transducer assembly. Initially, the performance at elevated temperatures was studied using a hot plate to supply the heat to the sample (see section 7.1). The hot plate trials differ to furnace trails, as there is a temperature distribution between the transducer and the hot sample, which aims to model portable type high temperature inspections carried out in industry, where high temperature couplants are often used for a short period. The results highlighted that the Tx1 transducer assembly is able to produce well defined signals suitable for portable high temperature thickness measurements using commercially available high temperature couplants, under the conditions specified in this trial.

Following this, a series of high temperature trials were performed where the sample and entire transducer were heated in a furnace (see section 7.2). The aim of these trials was to evaluate the high temperature performance of the transducer under conditions similar to those found in permanent inspections, in which the transducer is attached to the hot sample continuously without any form of active cooling. The high temperature acoustic coupling method used during the furnace trials was discussed in section 7.2.1. Achieving good ultrasound transmission at the transducer-specimen interface, safety and material compatibility, long term thermal stability and ability of the interface to withstand thermal cycling are important factors to consider when adopting a high temperature coupling technique. For the furnace trials, dry coupling using a clamp was selected, primarily because the nature of the dry coupling method provides a simple method for carrying out repeat measurements with the same transducer using different samples or metal foils, unlike other permanent coupling techniques. Although the main disadvantage of this system is the need for very high pressures at the transducer-sample interface.

The first series of furnace trials were carried out using a very thin aluminium foil to improve the acoustic coupling at the transducer-sample interface (see section 7.2.2). These trials showed that the transducer is able to generate ultrasound signals within the sample at room temperature and 425 °C which are adequate for thickness measurements. It was found that the coupling efficiency at the transducer-sample interface appears to improve with increasing temperature, and this effect was maintained on cooling. However, subsequent trials with this setup resulted in increased resonance along the noise floor of the signal, which was attributed to thermal expansion of the bolts within the transducer assembly and the clamping setup. This could possibly be improved by using stainless steel bolts rather than high tensile

steel bolts; as such, all further furnace trials were performed using stainless steel bolts in both the transducer assembly and the dry coupling clamp setup.

It was noted that the apparent increase in coupling efficient at the transducer-sample interface resulted in a change in their relative amplitudes of the reflected echoes in the signal; the effect of the change in coupling efficiency was discussed in section 7.2.3. The effect was described by consideration of the contact area at the interface between two rough solid surfaces (the transducer waveguide face and the sample surface) with a thin metal foil between, and the application of high pressure. A static model was described, and with application to this study, it was proposed that the increased temperature results in an increase in the real contact area at the interface, through a number of mechanisms, thereby increasing the interface stiffness and decreasing the reflection coefficient (i.e. increasing coupling efficiency). A finite element model to simulate the effect on the signal output of different interface properties was compared to the experimental data, and there was good agreement between the simulated and experimental data.

Further furnace trials were discussed with the use of stainless steel bolts and a thin nickel foil at the transducer-sample interface (see section 7.2.4). Similarly to the trials with aluminium foil, the coupling efficiency observed an increase at increasing temperatures, and the signals are of sufficient amplitude for ultrasound thickness monitoring. Although the increase in coupling efficiency proved useful for increased signals at high temperatures, it was difficult to directly compare the performance of the transducer before and after heating when the transducer is coupled to the sample. Therefore, after heating the transducer was removed from the clamping setup and the waveform with no sample was measured, then compared to the waveform measured with no sample present before heating. It was immediately apparent with no sample present after heating that the signal was significantly altered, with substantial reverberation along the waveform and loss of distinguishable backwall echoes, attributed to loss of compressive stress on the piezoelectric disc by the central transducer bolt. This was further confirmed by re-tightening of the transducer central bolt, wherein the transducer proceeded to perform as before, the resonance was lost and the backwall echoes from the waveguide returned, although with a lower amplitude primarily due to a combination of temperature and stress related depoling of the piezoelectric disc.

Longer-term trials were then performed with the transducer, without the presence of a sample, to investigate the effect of temperature on transducer performance (see section 7.2.5). The transducer was subject to 500 °C for a total of 216 hours, and its performance on cooling to room temperature was measured at

intervals during this period. On initial exposure to high temperatures the signal amplitude decreased, most likely due to change in the piezoelectric properties of the disc as a result of various complex depoling processes exhibited at elevated temperatures below the Curie temperature of BiT. Despite this, over the trial period investigated there appeared to be no significant change in the signal amplitude, suggesting stabilisation of the piezoelectric properties. The results confirm that the central transducer bolt is able to undergo thermal expansion and contraction with no clear loss in tension when not within the dry clamping setup.

The final trial discussed in this section aimed to measure the performance of the transducer at high temperatures with no sample present (see section 7.2.6). The results with no sample present highlight the predominant issue with the current demonstration of this type of compression transducer design, that is maintaining the compressive force across the piezoelectric disc at elevated temperatures despite thermal expansion. Although the waveguide backwall echoes were detectable in the waveform at high temperature, there is significant resonance along the waveform, increasing the noise floor and significantly reducing SNR.

Finally, the results of a preliminary high temperature trial using an alternative dry clamping method and the Tx2 transducer assembly, was designed for use on pipe samples (see section 7.2.7). The clamping setup when first introduced worked well on flat samples, however, it failed to generate signals on curved samples (i.e. pipes), without the application of large torque, which resulted in deformation of the Tx1 transducer assembly. The difficulty in obtaining signals on curved samples is primarily due to the reduced contact area, which is essentially a line contact here, thereby reducing the amount of ultrasound which can be coupled into the sample. The pipe clamping setup utilised a U-shaped clamp fixed around the pipe to produce the high pressures required at the transducer-sample interface. Although the sample backwall signals obtained at high temperature are generally lower than those obtained with the flat sample, they were of sufficient amplitude for thickness measurements. This trial also highlighted that the Tx2 transducer assembly was much less susceptible than that Tx1 transducer assembly to the effects of thermal expansion and the subsequent loss of signal.

Chapter 8

High Temperature Piezoelectric Transducers: Conclusions

This chapter presents a summary of the work presented in chapters 6 and 7. The main findings of the development and optimisation of the compression-type piezoelectric transducer at room temperature are presented in section 8.1, and the findings from a series of high temperature laboratory trials using the piezoelectric transducer are discussed in section 8.2. Finally, avenues of further work on this project to improve the high temperature performance of the compression-type piezoelectric transducer design are discussed in section 8.3.

8.1 Development and Optimisation of Compression-Type Piezoelectric Transducer

The aim of this project was to develop a piezoelectric transducer constructed from components which could all withstand long term exposure to elevated temperatures, whilst generating suitable signals for use in both portable inspections and continuous monitoring for thickness measurements, to detect corrosion and erosion, for example. The transducer design proposed varied significantly from transducer designs presented in the published literature. This section provides a review of chapter 6, which presented an overview of the design, modelling, fabrication and room temperature testing of the compression-type piezoelectric transducer assembly.

The piezoelectric transducer design investigated within this study differs from conventional broadband transducers often used in the field of NDT; the design

utilises a compressive force applied to the piezoelectric element to achieve acoustic coupling between the transducer components. On analysis of the literature, there appeared to be limited published research on high frequency compression type piezoelectric transducers which employ a single piezoelectric element, specifically towards application in NDT and at high temperatures; as such, the work presented in and chapters 6 and 7 aimed to provide insight into the use of this transducer design for ultrasound thickness monitoring at high temperatures.

Similarly to the project on EMAT transducers described in chapters 3 - 5, the piezoelectric transducer was designed for use in a pulse-echo mode, by which longitudinal backwall echoes reverberating within the sample could be used to calculate the sample thickness. The pulser-receiver system and experimental setup used to generate, measure and record all the data presented chapters 6 and 7 was detailed in section 6.1.

A detailed analysis of the waveguide incorporated in this compression-type piezoelectric transducer design was provided in section 6.2. The waveguide is an integral component within the transducer design, as it provides a mass to which a compressive load can be applied across the piezoelectric disc, wear protection for the piezoelectric disc from contact with the sample and a degree of heat protection from a hot sample. However, the waveguide length chosen for the transducer application resulted in generation and detection of trailing echoes in the waveform, which had to be addressed to prevent them from interfering with desired echoes from the sample. Both 2D and 3D Finite element modelling of the waveguide was performed to investigate the trailing echo formation (see section 6.2.1). The absence of trailing echoes with an absorbing waveguide-air boundary and the confirmation that the predominant longitudinal wave mode propagating along the waveguide could be approximated as a bulk longitudinal wave.

An experimental investigation was performed to compare various waveguide geometries, towards selection of suitable waveguides for use within the compression-type transducer design, which was able to effectively remove the trailing echoes (see section 6.2.2). It was determined that a waveguide with a knurled pattern along the boundary gave the greatest SNR, even when including the coherent noise level generated by waves scattered by the knurled boundary, followed by a M20 hexagonal head bolt with a thread pattern along half the bolt tail and a knurled waveguide with a curved end-face. These three waveguides were incorporated into the transducer design to form three different transducer assemblies, and their performance at room temperature was compared (detailed in to section 6.3.2). It was found that the knurled waveguide transducer assembly (Tx1) provided the greatest SNR followed

by the M20 bolt transducer (Tx2) on a flat sample; however, the knurled curved-end waveguide transducer (Tx3) provided the largest SNR on curved samples, owing to the increased surface contact at the transducer-sample interface.

The compression-type transducer assembly design and role of internal components was discussed at length in section 6.3.1. It was shown that all components (waveguide, piezoelectric disc and backing material) are acoustically coupled under compressive stress from a central bolt, negating the need for adhesive layers, such that all components are able to withstand high temperatures continuously without cooling. This type of transducer is suitable for both portable and permanent high temperature inspections, and the piezoelectric element chosen can be tailored depending upon the application requirements. It was found that the signal amplitude increased with increase in torque applied to the central bolt (see section 6.3.3). Although, multiple round of compression on the same piezoelectric disc resulted in depoling.

Two commercially available high Curie Temperature piezoelectric materials were compared with this transducer design at room temperature, namely; lead metaniobate (PN) and bismuth titanate (BIT). It was found that although lead metaniobate observed a much higher piezoelectric constant than bismuth titanate, the resulting SNR from the first waveguide backwall echo were similar. Highlighting the capability of this transducer design to work efficiently with a range of different piezoelectric materials; the choice of piezoelectric material can be tailored to the requirements of the application.

Various metallic backing materials were studied, and their ability to effectively damp the vibrations of the piezoelectric disc and scatter reflections from the piezoelectric disc back face were compared. Electrically conductive materials were chosen to ensure electrical connection to the piezoelectric disc. All backing materials studied exhibited high melting temperatures to withstand continuous exposure to high temperatures without cooling. A backing material formed from a commercially available porous stainless steel foam, further pressed to form a denser foam provided the greatest SNR, likely due to it its ability to effectively attenuate ultrasound waves emitting from the rear face of the piezoelectric disc. This was attributed to the highly attenuative properties of this material as a result of scattering, rather than absorption, and it was presumed that the porous nature of the foam resulted in a large number of scattering centres. Hence, the stainless steel foam was used in high temperature trials.

8.2 Study of High Temperature Piezoelectric Transducer Performance

This section provides an overview of the high temperature trials presented in chapter 7. The performance at elevated temperatures was investigated using a hot plate (see section 7.1). The hot plate trials differ to furnace trails, as there is a temperature distribution between the transducer and the sample, which aims to model portable-type high temperature inspections, where high temperature couplants are often used for a short period. The results showed that the Tx1 transducer assembly is able to produce well defined signals, suitable for thickness measurements using commercially available high temperature couplants.

Following this, various high temperature trials were performed where the sample and entire transducer were heated in a furnace (see section 7.2), to study transducer performance under conditions similar to those found in permanent inspections. The high temperature acoustic coupling method used during the furnace trials was discussed in section 7.2.1. For these furnace trials, dry coupling using a clamp was used, primarily as this allowed repeat measurements with the same transducer using different samples or metal foils, unlike other permanent coupling techniques. However, the main disadvantage of this was the requirement of very high pressures at the transducer-sample interface to achieve good acoustic coupling.

High temperature trials were performed with the clamping setup on flat stainless steel samples with the use of aluminium foil (see section 7.2.2) and nickel foil (see section 7.2.4); the foils were used to improve the coupling efficiency at the transducer-sample interface. The results from these trials demonstrated good SNR with application of this compression-type transducer design at high temperature, highlighting the capability of this piezoelectric transducer design to perform ultrasound thickness measurements at elevated temperatures. It was noted that the coupling efficiency increased significantly after exposure to elevated temperatures, and this was discussed in detail in section 7.2.3 with respect to the change in real contact area at the interface, along with a finite element model to show the effect of coupling efficiency on the relative amplitude of waveguide and sample backwall echoes.

However, on removal of the transducer from the clamping setup after these high temperature trials, it was immediately apparent with no sample present, that the signal was significantly altered, with substantial reverberation along the waveform and loss of distinguishable backwall echoes. This was attributed to loss of compressive stress on the piezoelectric disc by the central transducer bolt, as a

result of thermal expansion effects, further confirmed by re-tightening of the transducer central bolt. To further analyse this behaviour, a high temperature trial was performed with no sample present (see section 7.2.6), and this showed the same resonance and loss of signal effect, which again were resolved in part by re-tightening the bolt at high temperature. These results highlight the predominant issue with the current demonstration of this type-compression piezoelectric transducer design, that is maintaining the compressive force across the piezoelectric disc at elevated temperatures despite thermal expansion.

Longer-term high temperature trials were performed with the transducer (see section 7.2.5). The transducer was subject to 500 °C for a total of 216 hours, and its performance on cooling to room temperature was measured at intervals during this period. On initial exposure to high temperatures the signal amplitude decreased, most likely due to a combination of change in the piezoelectric properties of the disc as a result of various complex depoling processes exhibited at elevated temperatures below the Curie temperature of BiT and change in compressive stress applied by the central bolt due thermal expansion. Despite this, over the trial period investigated there appeared to be no significant change in the signal amplitude, suggesting stabilisation of the piezoelectric properties.

Finally, the results of a preliminary high temperature trial using an alternative dry clamping method and the Tx2 transducer assembly, was designed for use on pipe samples (see section 7.2.7). The clamping setup first introduced worked well on flat samples, however, it failed to generate signals on curved samples (i.e. pipes), without the application of large torque, which resulted in deformation of the Tx1 transducer assembly. The pipe clamping setup utilised a U-shaped clamp fixed around the pipe to produce the high pressures required at the transducer-sample interface. Although the sample backwall signals obtained at high temperature are generally lower than those obtained with the flat sample, they were of sufficient amplitude for thickness measurements. This trial also highlighted that the Tx2 transducer assembly was much less susceptible than that Tx1 transducer assembly to the effects of thermal expansion and the subsequent loss of signal.

8.3 Further Work

The research reviewed in this thesis on the high temperature compression-type piezoelectric transducer design has demonstrated its potential for application in ultrasound thickness measurement, by means of portable inspections or continuous monitoring at temperatures up to $\approx 500\,^{\circ}\mathrm{C}$. However, there is clearly further work required to improve the execution of the design, especially with regards to overcoming thermal expansion issues.

A detailed analysis on the effects of thermal expansion on the various metallic components of the transducer housing, both for transducer assemblies Tx1 and Tx2 could be carried out. Perhaps, a combination of the two assemblies designs would result in a transducer with greater resistance to thermal expansion effects, that is a knurled waveguide with a welded compression assembly, rather than studding. Ideally, the transducer should be designed such that thermal expansion of components at elevated temperatures fails to result in any change in the compressive stress applied across the piezoelectric disc. This may be achieved via the use of metallic springs set around the central transducer bolt. An improved compression-type transducer assembly should be subject to even longer-term high temperature trials to investigate if surface oxidation at the waveguide-piezoelectric disc interface and piezoelectric disc-backing material interface results in loss of electrical connection. Moreover, during these longer-term high temperature trials the potential effect of surface oxidation at the interface, including that of the foil (if gold foil is not used), and effect on acoustic coupling efficiency should be studied.

Ultimately for commercialisation of this piezoelectric transducer design, improved signals on curved surfaces is critical, as the majority of both portable inspection and permanent condition monitoring applications would be for used on high temperature pipelines. This could be achieved via a combination of factors, such as use of gold foil (which although more expensive is softer than both aluminium and nickel), improving the polishing method of the transducer waveguide end and sample prior to clamping, use of greater torque applied to the clamping design, or even use of an alternative coupling method (e.g. brazing/welding).

Bibliography

[1] G. Shen and T. Li, "Infrared thermography for high-temperature pressure pipe," *Insight-Non-Destructive Testing and Condition Monitoring*, vol. 49, no. 3, pp. 151–153, 2007.

[2] I. Atkinson, C. Gregory, S. P. Kelly, and K. J. Kirk, "Ultrasmart: Developments in Ultrasonic Flaw Detection and Monitoring for High Temperature Plant Applications," *Volume 9: Eighth International Conference on Creep and Fatigue at Elevated Temperatures*, no. August, pp. 573–585, 2007.

[3] R. Kažys, a. Voleišis, and B. Voleišien, "High temperature ultrasonic transducers : review," *Ultrasound*, vol. 63, no. 2, pp. 7–17, 2008.

[4] F. B. Cegla, P. Cawley, J. Allin, and J. Davies, "High-temperature ($> 500\,^{\circ}\mathrm{C}$) wall thickness monitoring using dry-coupled ultrasonic waveguide transducers," *IEEE Transactions on Ultrasonics, Ferroelectrics, and Frequency Control*, vol. 58, no. 1, pp. 156–167, 2011.

[5] "Sonemat Ltd., Coventry, UK." `http://www.sonemat.com/`. Accessed Online [10/12/2017].

[6] T. S. Newman and A. K. Jain, "A survey of automated visual inspection," *Computer vision and image understanding*, vol. 61, no. 2, pp. 231–262, 1995.

[7] L. Bruno and A. Poggialini, "Back to the future: From speckle to holography," *Optics and Lasers in Engineering*, vol. 45, no. 5, pp. 538–549, 2007.

[8] H. Shang and J. Gao, "Theories and industrial applications of optical interferometric NDT techniques: A review," *Insight-Non-Destructive Testing and Condition Monitoring*, vol. 51, no. 5, pp. 240–251, 2009.

[9] G. Grizzell, "Dye Penetrant Techniques for Flaw Detection: A Discussion of their Nature and Limitations," *Aircraft Engineering and Aerospace Technology*, vol. 36, no. 7, pp. 207–212, 1964.

[10] P. Prokhorenko, A. Sekerin, and A. Klornev, "a Quantitative Estimation of Penetrant Systems," *Nondestructive Testing and Evaluation*, vol. 13, no. 6, pp. 325–345, 1997.

[11] B. A. Auld and J. C. Moulder, "Review of advances in quantitative eddy current nondestructive evaluation," *Journal of Nondestructive evaluation*, vol. 18, no. 1, pp. 3–36, 1999.

[12] A. Sophian, G. Y. Tian, D. Taylor, and J. Rudlin, "Electromagnetic and eddy current NDT in weld inspection: A review," *Insight: Non-Destructive Testing and Condition Monitoring*, vol. 43, no. 5, pp. 302–306, 2001.

[13] J. García-Martín, J. Gómez-Gil, and E. Vázquez-Sánchez, "Non-destructive techniques based on eddy current testing," *Sensors*, vol. 11, no. 3, pp. 2525–2565, 2011.

[14] K. Bainton, "Characterizing defects by determining magnetic leakage fields," *NDT International*, vol. 10, no. 5, pp. 253–257, 1977.

[15] Z. D. Wang, Y. Gu, and Y. S. Wang, "A review of three magnetic NDT technologies," *Journal of Magnetism and Magnetic Materials*, vol. 324, no. 4, pp. 382–388, 2012.

[16] J. Krautkrämer and H. Krautkrämer, *Ultrasonic Testing of Materials*. Spring-Verlag, 4th ed., 1990.

[17] J. Blitz and G. Simpson, *Ultrasonic methods of non-destructive testing*, vol. 2. Springer Netherlands, 1995.

[18] B. W. Drinkwater and P. D. Wilcox, "Ultrasonic arrays for non-destructive evaluation: A review," *NDT & E International*, vol. 39, no. 7, pp. 525–541, 2006.

[19] W. N. Reynolds, "Thermographic methods applied to industrial materials," *Canadian Journal of Physics*, vol. 64, no. 9, pp. 1150–1154, 1986.

[20] V. P. Vavilov and D. D. Burleigh, "Review of pulsed thermal NDT: Physical principles, theory and data processing," *NDT & E International*, vol. 73, pp. 28–52, 2015.

[21] H. Kriesz, "Radiographic NDTa review," *NDT International*, vol. 12, no. 6, pp. 270–273, 1979.

[22] C. Nockemann, H. Heidt, and N. Thomsen, "Reliability in NDT: ROC study of radiographic weld inspections," *NDT & E International*, vol. 24, no. 5, pp. 235–245, 1991.

[23] M. S. Rapaport and A. Gayer, "Application of gamma ray computed tomography to nondestructive testing," *NDT & E International*, vol. 24, no. 3, pp. 141–144, 1991.

[24] A. Arnau and Others, *Piezoelectric transducers and applications*. Springer, 2008.

[25] M. Hirao and H. Ogi, *EMATs for Science and Industry: Noncontacting Ultrasonic Measurements*. Kluwer Academic Publishers, 2003.

[26] C. B. Scruby and L. Drain, *Laser ultrasonics. Techniques and Applications*. CRC Press, 1990.

[27] L. C. Lynnworth, *Ultrasonic measurements for process control: theory, techniques, applications*. Academic press, 2013.

[28] K. A. Fowler, G. M. Elfbaum, K. A. Smith, and T. J. Nelligan, "Theory and application of precision ultrasonic thickness gauging," *Insight*, vol. 38, no. 8, pp. 582–587, 1996.

[29] W. Luo and J. L. Rose, "Guided wave thickness measurement with EMATs," *Insight-Non-Destructive Testing and Condition Monitoring*, vol. 45, no. 11, pp. 735–739, 2003.

[30] D. I. Crecraft, "The measurement of applied and residual stresses in metals using ultrasonic waves," *Journal of Sound and Vibration*, vol. 5, no. 1, pp. 173–192, 1967.

[31] C. O. Ruud, "A review of selected non-destructive methods for residual stress measurement," *NDT International*, vol. 15, no. 1, pp. 15–23, 1982.

[32] W. Zhu, J. L. Rose, J. N. Barshinger, and V. S. Agarwala, "Ultrasonic guided wave NDT for hidden corrosion detection," *Journal of Research in Nondestructive Evaluation*, vol. 10, no. 4, pp. 205–225, 1998.

[33] A. Demma, P. Cawley, M. Lowe, A. G. Roosenbrand, and B. Pavlakovic, "The reflection of guided waves from notches in pipes: a guide for interpreting corrosion measurements," *NDT & E International*, vol. 37, no. 3, pp. 167–180, 2004.

[34] F. Lakestani, J.-F. Coste, and R. Denis, "Application of ultrasonic Rayleigh waves to thickness measurement of metallic coatings," *NDT & E International*, vol. 28, no. 3, pp. 171–178, 1995.

[35] Y. Fan, S. Dixon, R. S. Edwards, and X. Jian, "Ultrasonic surface wave propagation and interaction with surface defects on rail track head," *NDT & E International*, vol. 40, no. 6, pp. 471–477, 2007.

[36] S. Dixon, C. Edwards, and S. B. Palmer, "A laser–EMAT system for ultrasonic weld inspection," *Ultrasonics*, vol. 37, no. 4, pp. 273–281, 1999.

[37] Y. Javadi, H. S. Pirzaman, M. H. Raeisi, and M. A. Najafabadi, "Ultrasonic inspection of a welded stainless steel pipe to evaluate residual stresses through thickness," *Materials & Design*, vol. 49, pp. 591–601, 2013.

[38] I. G. Scott and C. M. Scala, "A review of non-destructive testing of composite materials," *NDT International*, vol. 15, no. 2, pp. 75–86, 1982.

[39] F. Aymerich and S. Meili, "Ultrasonic evaluation of matrix damage in impacted composite laminates," *Composites Part B: Engineering*, vol. 31, no. 1, pp. 1–6, 2000.

[40] C. C. H. Guyott, P. Cawley, and R. D. Adams, "The non-destructive testing of adhesively bonded structure: a review," *The Journal of Adhesion*, vol. 20, no. 2, pp. 129–159, 1986.

[41] R. D. Adams and P. Cawley, "A review of defect types and nondestructive testing techniques for composites and bonded joints," *NDT international*, vol. 21, no. 4, pp. 208–222, 1988.

[42] J. L. Rose, *Ultrasonic Waves in Solid Media*. Cambridge University Press, 1999.

[43] R. Turner, P. Fuierer, R. Newnham, and T. Shrout, "Materials for high temperature acoustic and vibration sensors: A review," *Applied Acoustics*, vol. 41, no. 4, pp. 299–324, 1994.

[44] D. Damjanovic, "Materials for high temperature piezoelectric transducers," *Current Opinion in Solid State and Materials Science*, vol. 3, no. 5, pp. 469–473, 1998.

[45] S. Zhang, R. Xia, L. Lebrun, D. Anderson, and T. R. Shrout, "Piezoelectric materials for high power, high temperature applications," *Materials Letters*, vol. 59, no. 27, pp. 3471–3475, 2005.

[46] S. Zhang and F. Yu, "Piezoelectric materials for high temperature sensors," *Journal of the American Ceramic Society*, vol. 94, no. 10, pp. 3153–3170, 2011.

[47] T. Stevenson, D. G. Martin, P. I. Cowin, A. Blumfield, A. J. Bell, T. P. Comyn, and P. M. Weaver, "Piezoelectric materials for high temperature transducers and actuators," *Journal of Materials Science: Materials in Electronics*, vol. 26, no. 12, pp. 9256–9267, 2015.

[48] D. Berlincourt, *Piezoelectric Crystals and Ceramics*, pp. 63–124. Boston, MA: Springer US, 1971.

[49] G. Goodman, "Ferroelectric properties of lead metaniobate," *Journal of the American Ceramic Society*, vol. 36, no. 11, pp. 368–372, 1953.

[50] H. S. Shulman, M. Testorf, D. Damjanovic, and N. Setter, "Microstructure, electrical conductivity, and piezoelectric properties of bismuth titanate," *Journal of the American Ceramic Society*, vol. 79, no. 12, pp. 3124–3128, 1996.

[51] B. Jaffe, W. R. Cook, and H. Jaffe, *Piezoelectric Ceramics*. Academic, 1971.

[52] C. M. Lueng, H. L. W. Chan, C. Surya, and C. L. Choy, "Piezoelectric coefficient of aluminum nitride and gallium nitride," *Journal of applied physics*, vol. 88, no. 9, pp. 5360–5363, 2000.

[53] K. Soejima, Junichiro, Sato, Kokichi, Nagata, "Preparation and Characteristics of Ultrasonic Transducers for High Temperature Using PbNb2O6," *Japanese Journal of Applied Physics*, vol. 39, no. 5B, pp. 3083–3085, 2000.

[54] Y.-M. Li, L. Cheng, X.-Y. Gu, Y.-P. Zhang, and R.-H. Liao, "Piezoelectric and dielectric properties of $PbNb_2O_6$-based piezoelectric ceramics with high Curie temperature," *Journal of materials processing technology*, vol. 197, no. 1, pp. 170–173, 2008.

[55] R. Kazys, A. Voleisis, R. Sliteris, B. Voleisiene, L. Mazeika, P. H. Kupschus, and H. A. Abderrahim, "Development of ultrasonic sensors for operation in a heavy liquid metal," *IEEE Sensors Journal*, vol. 6, no. 5, pp. 1134–1142, 2006.

[56] C. T. Searfass, *Characterization of bismuth titanate thick films fabricated using a spray-on technique for high temperature ultrasonic non-destructive evaluation.* PhD thesis, Pennsylvania State University, 2012.

[57] S. Burrows, K. McAughey, R. Edwards, and S. Dixon, "Solgel prepared bismuth titanate for high temperature ultrasound transducers," *RSC Advances*, vol. 2, no. 9, p. 3678, 2012.

[58] R. Hauser, L. Reindl, and J. Biniasch, "High-temperature stability of $LiNbO_3$ based SAW devices," in *Ultrasonics 2003 IEEE Symposium on*, vol. 1, pp. 192–195, 2003.

[59] A. Baba, C. T. Searfass, and B. R. Tittmann, "High temperature ultrasonic transducer up to 1000 °C using lithium niobate single crystal," *Applied Physics Letters*, vol. 97, no. 23, 2010.

[60] D. Parks, S. Zhang, and B. Tittmann, "High-temperature (> 500 °C) ultrasonic transducers: an experimental comparison among three candidate piezoelectric materials," *IEEE Transactions on Ultrasonics, Ferroelectrics and Frequency Control*, vol. 60, no. 5, pp. 1010–1015, 2013.

[61] A. Mohimi, T.-H. Gan, and W. Balachandran, "Development of high temperature ultrasonic guided wave transducer for continuous in service monitoring of steam lines using non-stoichiometric lithium niobate piezoelectric ceramic," *Sensors and Actuators A: Physical*, vol. 216, pp. 432–442, 2014.

[62] J. Hornsteiner, E. Born, and E. Riha, "Langasite for high temperature surface acoustic wave applications," *Physica Status Solidi (a)*, vol. 163, no. 1, 1997.

[63] L. O. Svaasand, M. Eriksrud, G. Nakken, and A. P. Grande, "Solid-solution range of $LiNbO_3$," *Journal of Crystal Growth*, vol. 22, no. 3, pp. 230–232, 1974.

[64] N. D. Patel and P. S. Nicholson, "High frequency, high temperature ultrasonic transducers," *NDT International*, vol. 23, no. 5, pp. 262–266, 1990.

[65] D. A. Stubbs and R. E. Dutton, "An ultrasonic sensor for high-temperature materials processing," *JOM Journal of the Minerals, Metals and Materials Society*, vol. 48, no. 9, pp. 29–31, 1996.

[66] R. Hou, D. Hutson, and K. J. Kirk, "Development of sputtered AlN thin-film ultrasonic transducers for durable high-temperature applications," *Insight* -

Non-Destructive Testing and Condition Monitoring, vol. 55, pp. 302–307, jun 2013.

[67] B. Reinhard, B. R. Tittmann, and A. Suprock, "Nuclear Radiation Tolerance of Single Crystal Aluminum Nitride Ultrasonic Transducer," *Physics Procedia*, vol. 70, pp. 609–613, 2015.

[68] K. Shimamura, H. Takeda, T. Kohno, and T. Fukuda, "Growth and characterization of lanthanum gallium silicate $La_3Ga_5SiO_{14}$ single crystals for piezoelectric applications," *Journal of Crystal Growth*, vol. 163, no. 4, pp. 388–392, 1996.

[69] H. Fritze and H. L. Tuller, "Langasite for high-temperature bulk acoustic wave applications," *Applied Physics Letters*, vol. 78, no. 7, pp. 976–977, 2001.

[70] H. Fritze, "High-temperature bulk acoustic wave sensors," *Measurement Science and Technology*, vol. 22, no. 1, p. 012002, 2011.

[71] H. Fritze, "High temperature piezoelectric materials: Defect chemistry and electro-mechanical properties," *Journal of Eectroceramics*, vol. 17, no. 2, pp. 625–630, 2006.

[72] S. Zhang, E. Frantz, R. Xia, W. Everson, J. Randi, D. W. Snyder, and T. R. Shrout, "Gadolinium calcium oxyborate piezoelectric single crystals for ultrahigh temperature ($\geq$1000 °C) applications," *Journal of Applied Physics*, vol. 104, no. 8, pp. 8–15, 2008.

[73] S. Zhang, X. Jiang, M. Lapsley, P. Moses, and T. R. Shrout, "Piezoelectric accelerometers for ultrahigh temperature application," *Applied Physics Letters*, vol. 96, no. 1, pp. 2–5, 2010.

[74] K. Kim, S. Zhang, W. Huang, F. Yu, and X. Jiang, "$YCa_4O(BO_3)_3$ (YCOB) high temperature vibration sensor," *Journal of Applied Physics*, vol. 109, no. 12, pp. 2009–2012, 2011.

[75] J. A. Johnson, K. Kim, S. Zhang, D. Wu, and X. Jiang, "High-temperature acoustic emission sensing tests using a Yttrium calcium oxyborate sensor," *IEEE Transactions on Ultrasonics, Ferroelectrics, and Frequency Control*, vol. 61, no. 5, pp. 805–814, 2014.

[76] H. Lee, S. Zhang, Y. Bar-Cohen, and S. Sherrit, "High Temperature, High Power Piezoelectric Composite Transducers," *Sensors*, vol. 14, no. 8, pp. 14526–14552, 2014.

[77] K. J. Kirk, R. Hou, N. Schmarje, N. M. Pragada, L. Torbay, and D. Hutson, "Investigation of high-temperature ultrasonic transducer design using lithium niobate piezocomposite," *Insight-Non-Destructive Testing and Condition Monitoring*, vol. 57, no. 4, pp. 193–199, 2015.

[78] M. Kobayashi and C.-K. Jen, "Piezoelectric thick bismuth titanate/lead zirconate titanate composite film transducers for smart NDE of metals," *Smart Materials and Structures*, vol. 13, no. 4, pp. 951–956, 2004.

[79] L. Li, S. Zhang, Z. Xu, F. Wen, X. Geng, H. J. Lee, and T. R. Shrout, "1–3 piezoelectric composites for high-temperature transducer applications," *Journal of Physics D: Applied Physics*, vol. 46, no. 16, p. 165306, 2013.

[80] C. S. Wu, Y. L. Liu, Y. C. Chiu, and Y. S. Chiu, "Thermal stability of epoxy resins containing flame retardant components: an evaluation with thermogravimetric analysis," *Polymer Degradation and Stability*, vol. 78, no. 1, pp. 41–48, 2002.

[81] R. Jain, P. Kukreja, A. K. Narula, and V. Chaudhary, "Studies of the curing kinetics and thermal stability of epoxy resins using a mixture of amines and anhydrides," *Journal of Applied Polymer Science*, vol. 100, no. 5, pp. 3919–3925, 2006.

[82] R. Boubenia, E. Rosenkrantz, F. Despetis, J. Y. Ferrandis, and Others, "Metal composite as backing for ultrasonic transducers dedicated to non-destructive measurements in hostile," in *IOP Conference Series: Materials Science and Engineering*, vol. 108, p. 12007, IOP Publishing, 2016.

[83] M. H. Amini, A. N. Sinclair, and T. W. Coyle, "A New High-Temperature Ultrasonic Transducer for Continuous Inspection," *IEEE Transactions on Ultrasonics, Ferroelectrics, and Frequency Control*, vol. 63, no. 3, pp. 448–455, 2016.

[84] H. Mrasek, D. Gohlke, K. Matthies, and E. Neumann, "High temperature ultrasonic transducers," *NDTnet*, vol. 1, no. 9, pp. 1–10, 1996.

[85] A. McNab, K. J. Kirk, and A. Cochran, "Ultrasonic transducers for high temperature applications," *Science, Measurement and Technology, IEE Proceedings-*, vol. 145, pp. 229–236, 1998.

[86] M. Kobayashi and C.-K. Jen, *Ultrasonic Transducers Materials and Design for Sensors, Actuators and Medical Applications*. Woodhead Publishing Limited, 2012.

[87] K. Muto and Y. Atsuta, "Applications of Brazed-Type Ultrasonic Probes for High and Low Temperature uses," *Nondestructive Testing and Evaluation*, vol. 7, no. 1-6, pp. 263–272, 1992.

[88] T. Arakawa, M. Tanosaki, and K. Yoshikawa, "On-line monitoring techniques of crack propagation using brazed-type ultrasonic sensors for high temperature use," tech. rep., ASM International, Materials Park, OH (United States), 1995.

[89] B. W. Drinkwater, R. S. Dwyer-Joyce, and P. Cawley, "A Study of the Interaction between Ultrasound and a Partially Contacting Solid–Solid Interface," in *Proceedings of the Royal Society of London A: Mathematical, Physical and Engineering Sciences*, vol. 452, pp. 2613–2628, The Royal Society, 1996.

[90] B. Butler, S. B. Palmer, and G. J. Primavesi, "Techniques for the generation of ultrasound for extended periods at high temperatures," *Ultrasonics*, vol. 17, no. 6, pp. 249–254, 1979.

[91] L. L. Hench and J. K. West, "The sol-gel process," *Chemical reviews*, vol. 90, no. 1, pp. 33–72, 1990.

[92] M. Kobayashi, T. R. Olding, M. Sayer, and C. K. Jen, "Piezoelectric thick film ultrasonic transducers fabricated by a sol-gel spray technique," *Ultrasonics*, vol. 39, no. 10, pp. 675–680, 2002.

[93] D. A. Stubbs and R. E. Dutton, "High-temperature ultrasonic sensor for in-situ monitoring of hot isostatic processing," in *SPIC*, no. November 1996, pp. 165–172, 1996.

[94] C.-K. Jen, J.-G. Legoux, and L. Parent, "Experimental evaluation of clad metallic buffer rods for high temperature ultrasonic measurements," *NDT&E International*, vol. 33, no. 3, pp. 145–153, 2000.

[95] K. Wang, H. T. Chien, T. W. Elmer, W. P. Lawrence, D. M. Engel, and S. H. Sheen, "Development of ultrasonic waveguide techniques for under-sodium viewing," *NDT & E International*, vol. 49, pp. 71–76, 2012.

[96] H. Viumdal and S. Mylvaganam, "Enhancing signal to noise ratio by fine-tuning tapers of cladded/uncladded buffer rods in ultrasonic time domain reflectometry in smelters," *Ultrasonics*, vol. 54, no. 3, pp. 894–904, 2014.

[97] M. Redwood, *Mechanical waveguides*. Pergamon Press, 1960.

[98] R. N. Thurston, "Elastic waves in rods and clad rods," *The Journal of the Acoustical Society of America*, vol. 64, no. 1, pp. 1–37, 1978.

[99] A. Sather, "Ultrasonic Buffer-Rod Technique for the High-Temperature Measurement of the Elastic Moduli of Short Specimens," *The Journal of the Acoustical Society of America*, vol. 43, no. 6, p. 1291, 1968.

[100] T. Maruyama, M. Eto, and T. Oku, "Elastic modulus and bend strength of a nuclear graphite at high temperature," *Carbon*, vol. 25, no. 6, pp. 723–726, 1987.

[101] C. A. Youngdahl and W. A. Ellingson, "Development of ultrasonic techniques for remote monitoring of erosive wear in coal-conversion systems," tech. rep., Argonne National Lab., IL (USA), 1978.

[102] C.-K. Jen, C. Neron, A. Miri, H. Soda, A. Ohno, and A. McLean, "Fabrication and characterization of continuously cast clad metallic buffer rods," *The Journal of the Acoustical Society of America*, vol. 91, no. 6, pp. 3565–3570, 1992.

[103] C.-K. Jen and J.-G. Legoux, "High performance clad metallic buffer rods," in *Ultrasonics Symposium, 1996. Proceedings., 1996 IEEE*, vol. 1, pp. 771–776, IEEE, 1996.

[104] C.-K. Jen, L. Piche, and J. F. Bussiere, "Long isotropic buffer rods," *The Journal of the Acoustical Society of America*, vol. 88, no. 1, pp. 23–25, 1990.

[105] L. C. Lynnworth and Y. Liu, "Ultrasonic path bundle and systems." US Patent 5,962,790, 1999.

[106] L. C. Lynnworth, Y. Liu, and J. A. Umina, "Extensional bundle waveguide techniques for measuring flow of hot fluids," *IEEE Transactions on ultrasonics, ferroelectrics, and frequency control*, vol. 52, no. 4, pp. 538–544, 2005.

[107] A. M. Heijnsdijk and J. M. Van Klooster, "Ultrasonic waveguide." US Patent 6,400,648, 2002.

[108] F. B. Cegla, A. J. C. Jarvis, and J. O. Davies, "High temperature ultrasonic crack monitoring using SH waves," *NDT & E International*, vol. 44, no. 8, pp. 669–679, 2011.

[109] M. Laws, S. N. Ramadas, L. C. Lynnworth, and S. Dixon, "Parallel strip waveguide for ultrasonic flow measurement in harsh environments," *IEEE transactions on ultrasonics, ferroelectrics, and frequency control*, vol. 62, no. 4, pp. 697–708, 2015.

[110] M. Laws, *Low Frequency Strip Waveguide Array for Flow Measurement in Hostile Environments*. PhD thesis, University of Warwick, 2015.

[111] "Ionix Advanced Technologies Ltd.." url-http://www.ionixadvancedtechnologies.co.uk. Accessed Online: [12/02/2018].

[112] "KANDE International Ltd.." `http://www.kande.net/`. Accessed Online [12/02/2018].

[113] I. Atkinson, S. Kelly, P. Lay, and C. Brett, "On-line flaw growth monitoring in high temperature plant," in *BALTICA VIII - International Conference on Life Management and Maintenance for Power Plants*, (Helsinki), 2010.

[114] "Permasense Ltd.." `http://www.permasense.com`. Accessed Online: [12/02/2018].

[115] H. A. Wheeler, "Formulas for the skin effect," *Proceedings of the IRE*, vol. 30, no. 9, pp. 412–424, 1942.

[116] M. Gori, S. Giamboni, E. D'Alessio, S. Ghia, and F. Cernuschi, "EMAT transducers and thickness characterization on aged boiler tubes," *Ultrasonics*, vol. 34, pp. 339–342, jun 1996.

[117] S. Dixon, C. Edwards, S. B. Palmer, and P. Crowther, "Electromagnetic acoustic transducers for testing power station boiler tubes," in *Review of Progress in Quantitative Nondestructive Evaluation*, vol. 18B, pp. 1995–2000, 1999.

[118] C. Kittel, *Introduction to solid state physics*. Hoboken: J. Whiley & Sons, Inc., 2005.

[119] J. F. Hernandez-Valle, *Pulsed-electromagnet EMAT for high temperature applications*. PhD thesis, 2011.

[120] "DuPont." `http://www.dupont.com`. Accessed Online [24/01/2018].

[121] F. Hernandez-Valle and S. Dixon, "Pulsed electromagnet EMAT for ultrasonic measurements at elevated temperatures," *Insight - Non-Destructive Testing and Condition Monitoring*, vol. 53, no. 2, pp. 96–99, 2011.

[122] P. T. Cole, "The generation and reception of ultrasonic surface waves in mild steel at high temperatures," *Ultrasonics*, vol. 16, no. 4, pp. 151–155, 1978.

[123] K. R. Whittington, "Ultrasonic testing at high temperatures," *Physics in Technology*, vol. 9, no. 2, p. 62, 1978.

[124] H. Yamaguchi, K. Fujisawa, R. Murayama, K. Hashimoto, R. Nakanishi, A. Kato, H. Ishikawa, T. Kadowaki, and I. Sato, "Development of hot seamless tube wall thickness gauge by electromagnetic acoustic transducer," *Transactions of the Iron and Steel Institute of Japan*, vol. 26, no. 1, pp. 61–68, 1986.

[125] F. Hernandez-Valle and S. Dixon, "Initial tests for designing a high temperature EMAT with pulsed electromagnet," *NDT&E International*, vol. 43, pp. 171–175, mar 2010.

[126] T. Uchimoto, T. Takagi, G. Dobmann, and S. Ogata, "Development and Performance Evaluation of High Temperature Electromagnetic Acoustic Transducer [Abstract]." Review of Progress in Quantitative Nondestructive Evaluation, Atlanta 2016, `http://lib.dr.iastate.edu/qnde/2016/abstracts/192/`.

[127] C. Edwards and S. B. Palmer, "Wideband electromagnetic acoustic transducers utilising neodymium iron boron permanent magnets," *IEEE Transactions on Magnetics*, vol. 26, no. 5, pp. 2080–2084, 1990.

[128] E. de Lacheisserie, M. Schlenker, and D. Gignoux, *Magnetism: Materials and applications*. Springer, 2005.

[129] M. T. Thompson, "Practical issues in the use of NdFeB permanent magnets in maglev, motors, bearings, and eddy current brakes," *Proceedings of the IEEE*, vol. 97, no. 11, pp. 1758–1767, 2009.

[130] J. F. Liu and M. H. Walmer, "Thermal Stability and Performance Data for SmCo 2:17 High-Temperature Magnets on PPM Focusing Structures," *IEEE Transactions on Electron Devices*, vol. 52, no. 5, pp. 899–902, 2005.

[131] D. M. Boyd, P. D. Sperline, B. D. Droney, J. F. Jackson, and J. R. Cook, "In-plant demonstration of high-temperature EMAT system on continuous caster strand," in *Review of Progress in Quantitative Nondestructive Evaluation*, pp. 1091–1097, Springer, 1989.

[132] S. Lee and B. Ahn, "EMAT Application at High Temperature," *Nondestructive Testing and Evaluation*, vol. 7, no. 1-6, pp. 253–261, 1992.

[133] S. Dixon, C. Edwards, J. Reed, and S. B. Palmer, "Using EMATs to measure the wall thickness of hot galvanizing kettles," *Insight*, vol. 37, no. 5, pp. 368–370, 1995.

[134] S. Burrows, Y. Fan, and S. Dixon, "High temperature thickness measurements of stainless steel and low carbon steel using electromagnetic acoustic transducers," *NDT & E International*, vol. 68, pp. 73–77, 2014.

[135] M. Hirao and H. Ogi, "An SH-wave EMAT technique for gas pipeline inspection," *NDT&E International*, vol. 32, pp. 127–132, apr 1999.

[136] A. Raghavan and C. E. S. Cesnik, "Review of guided-wave structural health monitoring," *Shock and Vibration Digest*, vol. 39, no. 2, pp. 91–116, 2007.

[137] M. Kogia, T. H. Gan, W. Balachandran, M. Livadas, V. Kappatos, I. Szabo, A. Mohimi, and A. Round, "High temperature shear horizontal electromagnetic acoustic transducer for guided wave inspection," *Sensors (Switzerland)*, vol. 16, no. 4, pp. 1–16, 2016.

[138] S. J. Davies, C. Edwards, G. S. Taylor, and S. B. Palmer, "Laser-generated ultrasound: Its properties, mechanisms and multifarious applications," *Journal of Physics D: Applied Physics*, vol. 26, no. 3, pp. 329–348, 1993.

[139] G. Alers, "Noncontact Ultrasonic Sensors for High Temperature Process Control," *Intelligent Processing of Materials and Advanced Sensors*, pp. 85–101, 1986.

[140] D. M. Boyd and P. D. Sperline, "Noncontact temperature measurements of hot steel bodies using an electromagnetic acoustic transducer (EMAT)," in *Review of Progress in Quantitative Nondestructive Evaluation*, pp. 1669–1676, Springer, 1988.

[141] A. Idris, C. Edwards, and S. B. Palmer, "Acoustic wave measurements at elevated temperature using a pulsed laser generator and an electromagnetic acoustic transducer detector," *Nondestructive Testing and Evaluation*, vol. 11, no. 4, pp. 195–213, 1994.

[142] I. Baillie, P. Griffith, X. Jian, and S. Dixon, "Implementing an ultrasonic inspection system to find surface and internal defects in hot, moving steel using EMATs," *Insight-Non-Destructive Testing and Condition Monitoring*, vol. 49, no. 2, pp. 87–92, 2007.

[143] I. Baillie, *The development of a laser-EMAT system suitable for on-line inspection in the continuous casting plant: innovation report.* PhD thesis, University of Warwick, 2008.

[144] C. A. Calder, E. C. Draney, and W. W. Wilcox, "Noncontact measurement of the elastic constants of plutonium at elevated temperatures," *Journal of Nuclear Materials*, vol. 97, pp. 126–136, 1981.

[145] R. J. Dewhurst, C. Edwards, A. D. W. McKie, and S. B. Palmer, "A remote laser system for ultrasonic velocity measurement at high temperatures," *Journal of Applied Physics*, vol. 63, no. 4, pp. 1225–1227, 1988.

[146] C. Scruby and B. Moss, "Non-contact ultrasonic measurements on steel at elevated temperatures," *NDT&E International*, vol. 26, no. 4, pp. 177–188, 1993.

[147] R. J. Dewhurst and Q. Shan, "Modelling of confocal Fabry-Perot interferometers for the measurement of ultrasound," *Measurement Science and Technology*, vol. 5, no. 6, pp. 655–662, 1994.

[148] A. Cand, J. P. Monchalin, and X. Jia, "Detection of in-plane and out-of-plane ultrasonic displacements by a two-channel confocal Fabry-Perot interferometer," *Applied Physics Letters*, vol. 64, no. 4, pp. 414–416, 1994.

[149] H. Nakano and S. Nagai, "Crack Measurements by Laser Ultrasonic at High Temperatures," vol. 2540, pp. 2540 – 2542, 1993.

[150] J.-P. Monchalin, C. Néron, J. F. Bussière, P. Bouchard, C. Padioleau, R. Héon, M. Choquet, J.-D. Aussel, G. Durou, and J. A. Nilson., "Laser-ultrasonics: from the laboratory to the shop floor," *Advanced Performance Materials*, vol. 5, no. 1-2, pp. 7–23, 1998.

[151] D. Lévesque, S. E. Kruger, G. Lamouche, R. Kolarik, G. Jeskey, M. Choquet, and J.-P. Monchalin, "Thickness and grain size monitoring in seamless tube-making process using laser ultrasonics," *NDT&E International*, vol. 39, no. 8, pp. 622–626, 2006.

[152] R. Quintero, F. Simonetti, P. Howard, J. Friedl, and A. Sellinger, "Noncontact laser ultrasonic inspection of Ceramic Matrix Composites (CMCs)," *NDT&E International*, vol. 88, no. May 2016, pp. 8–16, 2017.

[153] C. H. Yeh and C. H. Yang, "Material characterization for Zircaloy claddings in elevated temperatures using a laser ultrasound technique," *IEEE International Ultrasonics Symposium, IUS*, pp. 265–268, 2012.

[154] D. W. Schindel, L. Zou, M. Sayer, and D. A. Hutchins, "The Design and Characterization of Micromachined Air-Coupled Capacitance Transducers," *IEEE Transactions on Ultrasonics, Ferroelectrics, and Frequency Control*, vol. 42, no. 1, pp. 42–50, 1995.

[155] I. Ladabaum, X. Jin, H. T. Soh, A. Atalar, and B. T. Khuri-Yakub, "Surface micromachined capacitive ultrasonic transducers," *IEEE Transactions on Ultrasonics, Ferroelectrics, and Frequency Control*, vol. 45, no. 3, pp. 678–690, 1998.

[156] D. W. Schindel and D. A. Hutchins, "Applications of micromachined capacitance transducers in air-coupled ultrasonics and nondestructive evaluation," *IEEE Transactions on Ultrasonics, Ferroelectrics, and Frequency Control*, vol. 42, no. 1, pp. 51–58, 1995.

[157] I. J. O'Sullivan and W. M. D. Wright, "Ultrasonic measurement of gas flow using electrostatic transducers," *Ultrasonics*, vol. 40, no. 1, pp. 407–411, 2002.

[158] B. T. Khuri-Yakub and Ö. Oralkan, "Capacitive micromachined ultrasonic transducers for medical imaging and therapy," *Journal of Micromechanics and Microengineering*, vol. 21, no. 5, p. 54004, 2011.

[159] O. Oralkan, A. S. Ergun, J. A. Johnson, M. Karaman, U. Demirci, K. Kaviani, T. H. Lee, and B. T. Khuri-Yakub, "Capacitive micromachined ultrasonic transducers: Next-generation arrays for acoustic imaging?," *IEEE Transactions on Ultrasonics, Ferroelectrics, and Frequency Control*, vol. 49, no. 11, pp. 1596–1610, 2002.

[160] A. G. Bashford and D. A. Hutchins, "Non-destructive evaluation of green-state ceramics using micromachined air-coupled capacitance transducers," *Ultrasonics*, vol. 36, no. 1-5, pp. 121–126, 1998.

[161] W. M. Wright and D. A. Hutchins, "Monitoring of binder removal from injection molded ceramics using air-coupled ultrasound at high temperature," *IEEE Transactions on Ultrasonics, Ferroelectrics, and Frequency Control*, vol. 46, no. 3, pp. 647–653, 1999.

[162] A. Schröder, S. Harasek, M. Kupnik, M. Wiesinger, E. Gornik, E. Benes, and M. Gröschl, "A capacitance ultrasonic transducer for high temperature applications," *Ultrasonics, Ferroelectrics and Frequency Control, IEEE Transactions on*, vol. 51, no. 7, pp. 896–907, 2004.

[163] Y. Y. Kim and Y. E. Kwon, "Review of magnetostrictive patch transducers and applications in ultrasonic nondestructive testing of waveguides," *Ultrasonics*, vol. 62, pp. 3–19, 2015.

[164] S. H. Cho, H. W. Kim, and Y. Y. Kim, "Megahertz-range guided pure torsional wave transduction and experiments using a magnetostrictive transducer," *IEEE transactions on ultrasonics, ferroelectrics, and frequency control*, vol. 57, no. 5, 2010.

[165] A. Ashish, P. Rajagopal, K. Balasubramaniam, A. Kumar, B. P. Rao, and T. Jayakumar, "Development of Magnetostriction Based Ultrasonic Transducer For In-situ High Temperature Inspection," *NDE-2015*, 2015.

[166] T. Heo and S. H. Cho, "Thin-Plate-Type Embedded Ultrasonic Transducer Based on Magnetostriction for the Thickness Monitoring of the Secondary Piping System of a Nuclear Power Plant," *Nuclear Engineering and Technology*, vol. 48, no. 6, pp. 1404–1411, 2016.

[167] B. Lebrun, Y. Jayet, and J.-C. Baboux, "Pulsed eddy current signal analysis: application to the experimental detection and characterization of deep flaws in highly conductive materials," *NDT&E International*, vol. 30, no. 3, pp. 163–170, 1997.

[168] A. McNab and J. Thomson, "An eddy current array instrument for application on ferritic welds," *NDT&E International*, vol. 28, no. 2, pp. 103–112, 1995.

[169] X. Chen and T. Ding, "Flexible eddy current sensor array for proximity sensing," *Sensors and Actuators, A: Physical*, vol. 135, no. 1, pp. 126–130, 2007.

[170] J. Vetterlein, H. Klümper-Westkamp, T. Hirsch, and P. Mayr, "Eddy current testing at high temperatures for controlling heat treatment processes," in *Proceedings of International Symposium of Non Destructive Testing in Civil Engineering*, 2003.

[171] T. Kasuya, T. Okuyama, N. Sakurai, H. Huang, T. Uchimoto, T. Takagi, Y. Lu, and T. Shoji, "In-situ eddy current monitoring under high temper-

ature environment," *International Journal of Applied Electromagnetics and Mechanics*, vol. 20, no. 3, 4, pp. 163–170, 2004.

[172] R. Urayama, T. Uchimoto, and T. Takagi, "Application of EMAT/EC dual probe to monitoring of wall thinning in high temperature environment," *International Journal of Applied Electromagnetics and Mechanics*, vol. 33, no. 3, 4, pp. 1317–1327, 2010.

[173] H. Klümper-Westkamp, H.-W. Zoch, W. Reimche, and F. W. Bach, "High temperature resistant eddy current sensor for in situ monitoring the material microstructure development of steel alloys during heat treatment–bainite sensor," *Procedia Engineering*, vol. 25, pp. 1605–1608, 2011.

[174] T. Uchimoto, T. Takagi, T. Kasuya, and T. Shoji, "Quantitative monitoring of crack propagation in high temperature environment using eddy current testing," *Hozengaku*, vol. 12, no. 2, pp. 77–83, 2013.

[175] "Emerson Electric Co., St. Louis, MO, USA." `https://www.emerson.com/en-us`. Accessed Online [10/12/2017].

[176] "Omni Instruments Ltd., Dundee, UK." `http://www.omniinstruments.co.uk/`. Accessed Online [10/12/2017].

[177] "Micro-Elipson UK Ltd., Birkenhead, UK." `www.micro-epsilon.co.uk`. Accessed Online [10/12/2017].

[178] G. Van Drunen and V. S. Cecco, "Recognizing limitations in eddy-current testing," *NDT International*, vol. 17, no. 1, pp. 9–17, 1984.

[179] S. Bagavathiappan, B. B. Lahiri, T. Saravanan, J. Philip, and T. Jayakumar, "Infrared thermography for condition monitoring–a review," *Infrared Physics & Technology*, vol. 60, pp. 35–55, 2013.

[180] N. P. Avdelidis, B. C. Hawtin, and D. P. Almond, "Transient thermography in the assessment of defects of aircraft composites," *NDT & E International*, vol. 36, no. 6, pp. 433–439, 2003.

[181] D. Wu and G. Busse, "Lock-in thermography for nondestructive evaluation of materials," *Revue générale de thermique*, vol. 37, no. 8, pp. 693–703, 1998.

[182] G. Y. Tian, J. Wilson, L. Cheng, D. P. Almond, E. Kostson, and B. Weekes, "Pulsed Eddy Current Thermography and Applications," in *New Developments in Sensing Technology for Structural Health Monitoring* (S. C.

Mukhopadhyay, ed.), pp. 205–231, Berlin, Heidelberg: Springer Berlin Heidelberg, 2011.

[183] D. J. Titman, "Applications of thermography in non-destructive testing of structures," *NDT&E International*, vol. 34, no. 2, pp. 149–154, 2001.

[184] T. Sakagami and S. Kubo, "Applications of pulse heating thermography and lock-in thermography to quantitative nondestructive evaluations," *Infrared Physics & Technology*, vol. 43, no. 3, pp. 211–218, 2002.

[185] J. H. Kim, K. H. Yoo, M. G. Na, J. W. Kim, and K. S. Kim, "On-power detection of pipe wall-thinned defects using IR thermography in NPPs," *Nuclear Engineering and Technology*, vol. 46, no. 2, pp. 225–234, 2014.

[186] J. D. Achenbach, "Wave Propagation in Elastic Solids," 1973.

[187] A. P. French, *Vibrations and waves*. Chapman and Hall, 1991.

[188] B. A. Auld, *Acoustic fields and waves in solids vol. 1*. Krieger Publishing, 1990.

[189] S. Essex, *Ultrasonic characterisation of rolled aluminium and steel sheet correlated with electron backscatter diffraction measurements*. PhD thesis, University of Warwick, 2009.

[190] J. D. N. Cheeke, "Fundamentals and applications of ultrasonic waves," 2002.

[191] F. A. Silber and C. Ganglbauer, "Ultrasonic testing of hot welds," *Non-Destructive Testing*, vol. 3, no. 6, pp. 429–432, 1970.

[192] E. H. F. Date, M. Atkins, and G. V. Beaton, "Measurement of the elasticity and ultrasound velocities of steel," *Ultrasonics*, vol. 9, no. 4, pp. 209–214, 1971.

[193] D. Fleisch, *A Student's Guide to Maxwell's Equations*. Cambridge University Press, 2008.

[194] S. Dixon and X. Jian, "Eddy current generation enhancement using ferrite for electromagnetic acoustic transduction," *Applied Physics Letters*, vol. 89, no. 19, p. 193503, 2006.

[195] X. Jian and S. Dixon, "Enhancement of EMAT and eddy current using a ferrite back-plate," *Sensors and Actuators A: Physical*, vol. 136, no. 1, pp. 132–136, 2007.

[196] K. Kawashima, "Quantitative calculation and measurement of longitudinal and transverse ultrasonic wave pulses in solid," *IEEE Transactions on Sonics and Ultrasonics*, vol. 31, no. 2, pp. 83–93, 1984.

[197] S. Dixon, C. Edwards, and S. B. Palmer, "High accuracy non-contact ultrasonic thickness gauging of aluminium sheet using electromagnetic acoustic transducers," *Ultrasonics*, vol. 39, no. 6, pp. 445–453, 2001.

[198] C. Rouge, A. Lhémery, and D. Ségur, "Modal solutions for SH guided waves radiated by an EMAT in a ferromagnetic plate," in *Journal of Physics: Conference Series*, vol. 353, p. 12014, IOP Publishing, 2012.

[199] E. W. Lee, "Magnetostriction and magnetomechanical effects," *Reports on Progress in Physics*, vol. 18, no. 1, p. 184, 1955.

[200] K. Linnemann, S. Klinkel, and W. Wagner, "A constitutive model for magnetostrictive and piezoelectric materials," *International Journal of Solids and Structures*, vol. 46, no. 5, pp. 1149–1166, 2009.

[201] S. Lanceros-Méndez and Others, *Magnetoelectric Polymer-based Composites: Fundamentals and Applications*. John Wiley & Sons, 2017.

[202] R. M. Bozorth, *Ferromagnetism*. Van Nostrand, Princeton, 1951.

[203] G. Engdahl, *Handbook of giant magnetostrictive materials*. San Diego: Academic Press, 2000.

[204] R. B. Thompson, "Mechanisms of electromagnetic generation and detection of ultrasonic Lamb waves in iron-nickel alloy polycrystals," *Journal of Applied Physics*, vol. 48, no. 12, pp. 4942–4950, 1977.

[205] R. B. Thompson, "A model for the electromagnetic generation of ultrasonic guided waves in ferromagnetic metal polycrystals," *IEEE Transactions on Sonics and Ultrasonics*, vol. 25, no. 1, pp. 7–15, 1978.

[206] A. Wilbrand, "Emus-probes for bulk waves and Rayleigh waves. Model for sound field and efficiency calculations," in *New Procedures in Nondestructive Testing*, pp. 71–80, Springer, 1983.

[207] A. Wilbrand, "Quantitative modeling and experimental analysis of the physical properties of electromagnetic-ultrasonic transducers," *Review of Progress in Quantitative Nondestructive Evaluation*, vol. 7, pp. 671–678, 1987.

[208] H. Ogi, "Field dependence of coupling efficiency between electromagnetic field and ultrasonic bulk waves," *Journal of Applied Physics*, vol. 82, no. 8, pp. 3940–3949, 1997.

[209] I. D. Kiteley, *A study of EMAT (electromagnetic acoustic transducer) operation on ferromagnetic metals*. PhD thesis, University of Warwick, 1999.

[210] R. Ribichini, *Modelling of electromagnetic acoustic transducers*. PhD thesis, Imperial College London, 2011.

[211] S. Dixon, C. Edwards, and S. B. Palmer, "High accuracy non-contact ultrasonic thickness gauging of aluminium sheet using electromagnetic acoustic transducers," *Ultrasonics*, vol. 39, no. 6, pp. 445–453, 2001.

[212] M. D. G. Potter and S. Dixon, "Ultrasonic texture measurement of sheet metals: An integrated system combining Lamb and shear wave techniques," *Nondestructive Testing and Evaluation*, vol. 20, no. 4, pp. 201–210, 2005.

[213] M. Hirao, H. Ogi, and H. Fukuoka, "Resonance EMAT system for acoustoelastic stress measurement in sheet metals," *Review of Scientific Instruments*, vol. 64, no. 11, pp. 3198–3205, 1993.

[214] J. F. Nye, *Physical properties of crystals: their representation by tensors and matrices*. Oxford university press, 1985.

[215] "IEEE Standard on Piezoelectricity," *Sponsored by the Standards Committee of the IEEE Ultrasonics, Ferroelectrics and Frequency Control Society*, 1988.

[216] R. S. C. Cobbold, *Foundations of biomedical ultrasound*. Oxford University Press, 2006.

[217] P. R. Hoskins, K. Martin, and A. Thrush, *Diagnostic ultrasound: physics and equipment*. Cambridge University Press, 2010.

[218] J. K. J. Kim, B. Grisso, J. Kim, D. S. H. D. S. Ha, and D. Inman, "Electrical modeling of Piezoelectric ceramics for analysis and evaluation of sensory systems," *2008 IEEE Sensors Applications Symposium*, pp. 122–127, 2008.

[219] S. Sherrit, H. D. Wiederick, B. K. Mukherjee, and M. Sayer, "An accurate equivalent circuit for the unloaded piezoelectric vibrator in the thickness mode," *Journal of Physics d: applied physics*, vol. 30, no. 16, p. 2354, 1997.

[220] M. J. Guan and W. H. Liao, "On the equivalent circuit models of piezoelectric ceramics," *Ferroelectrics*, vol. 386, no. 1, pp. 77–87, 2009.

[221] G. D. Klapel and P. N. Shive, "High-temperature magnetostriction of magnetite," *Journal of Geophysical Research*, vol. 79, no. 17, pp. 2629–2633, 1974.

[222] B. M. Moskowitz, "High-temperature magnetostriction of magnetite and titanomagnetites," *Journal of Geophysical Research: Solid Earth*, vol. 98, no. B1, pp. 359–371, 1993.

[223] R. Ribichini, P. B. Nagy, and H. Ogi, "The impact of magnetostriction on the transduction of normal bias field EMATs," *NDT & E International*, vol. 51, pp. 8–15, 2012.

[224] E. P. Papadakis, L. C. Lynnworth, K. A. Fowler, and E. H. Carnevale, "Ultrasonic attenuation and velocity in hot specimens by the momentary contact method with pressure coupling, and some results on steel to 1200 C," *The Journal of the Acoustical Society of America*, vol. 52, no. 3B, pp. 850–857, 1972.

[225] S. Dixon, M. P. Fletcher, and G. Rowlands, "The accuracy of acoustic birefringence shear wave measurements in sheet metal," *Journal of Applied Physics*, vol. 104, no. 11, p. 114901, 2008.

[226] "Sonomatic Ltd.." `http://www.vsonomatic.com/`. Date Accessed:[12/09/2018].

[227] "Valero Energy Corporation." `https://www.valero.com/en-us`. Date Accessed:[12/09/2018].

[228] F. Foudzi, "Development of Polygonal Buffer Rods for Ultrasonic Pulse-Echo Measurements with High Signal-to-Noise Ratio," 2016.

[229] "Velocity of Sound in Various Media." `http://www.rfcafe.com/references/general/velocity-sound-media.htm`. Accessed Online [17/02/2018].

[230] J. L. Butler and C. H. Sherman, *Transducers and arrays for underwater sound*. Springer, 2016.

[231] Y. Li, Y. Sun, and F. Li, "Domain texture dependent fracture behavior in mechanically poled/depoled ferroelectric ceramics," *Ceramics International*, vol. 39, no. 8, pp. 8605–8614, 2013.

[232] Olympus, "NDT Instruments - Dual Element." https://www.olympus-ims.com/en/ultrasonic-transducers/dualelement/#!cms[tab]=%2Fpanametrics-ndt-ultrasonic%2Fdualelement%2Foverview. Date Accessed: [15/07/2018].

[233] Olympus, "Ultrasonic Couplants." https://www.olympus-ims.com/en/applications/ultrasonic-couplant/. Date Accessed: [15/07/2018].

[234] Magnaflux, "Wide Temperature Range Ultrasonic Couplant." https://magnaflux.com/Magnaflux/Products/Ultrasonic-Couplants/Pyrogel.htm. Date Accessed: [15/07/2018].

[235] EchoUltrasonics, "EchoTherm Extreme." https://www.echoultrasonics.com/products/high-temperature-couplants/echotherm-extreme/. Date Accessed: [15/07/2018].

[236] J.-M. Baik and R. B. Thompson, "Ultrasonic scattering from imperfect interfaces: a quasi-static model," *Journal of Nondestructive Evaluation*, vol. 4, no. 3-4, pp. 177–196, 1984.

[237] T. P. Pialucha, *The reflection coefficient from interface layers in NDT of adhesive joints*. PhD thesis, University of London, 1992.

[238] B. Drinkwater and P. Cawley, "Measurement of the frequency dependence of the ultrasonic reflection coefficient from thin interface layers and partially contacting interfaces," *Ultrasonics*, vol. 35, no. 7, pp. 479–488, 1997.

[239] H. Yan, H. Zhang, M. J. Reece, and X. Dong, "Thermal depoling of high Curie point Aurivillius phase ferroelectric ceramics," *Applied Physics Letters*, vol. 87, no. 8, p. 82911, 2005.

[240] Y. Hiruma, H. Nagata, and T. Takenaka, "Thermal depoling process and piezoelectric properties of bismuth sodium titanate ceramics," *Journal of Applied Physics*, vol. 105, no. 8, p. 84112, 2009.